Micromechanical Modelling of Wood and Fibre Properties

Persson, Kent

2000

Document Version:
Publisher's PDF, also known as Version of record

Link to publication

Citation for published version (APA):
Persson, K. (2000). *Micromechanical Modelling of Wood and Fibre Properties*. [Doctoral Thesis (monograph), Structural Mechanics]. Division of Structural Mechanics, Lund Institute of Technology.

Total number of authors:
1

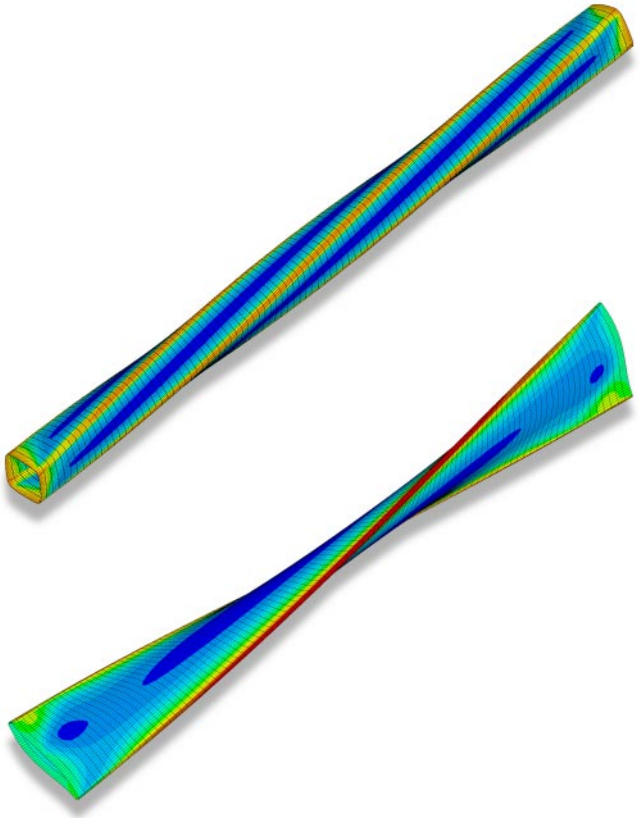

MICROMECHANICAL MODELLING OF WOOD AND FIBRE PROPERTIES

KENT PERSSON

Department
of
Mechanics
and
Materials

Structural Mechanics

Doctoral Thesis

Department of Mechanics and Materials
Structural Mechanics

ISRN LUTVDG/TVSM--00/1013--SE (1-223)
ISBN 91-7874-094-0 ISSN 0281-6679

MICROMECHANICAL MODELLING OF WOOD AND FIBRE PROPERTIES

Doctoral Thesis by
KENT PERSSON

Printed by KFS i Lund AB, Lund, Sweden, October 2000.

For information, address:
Division of Structural Mechanics, LTH, Lund University, Box 118, SE-221 00 Lund, Sweden.
Homepage: http://www.byggmek.lth.se

ACKNOWLEDGMENTS

The research presented in this thesis was carried out at the Division of Structural Mechanics, Lund University. The thesis represents results from studies within a wood research programme supported by Södra Timber AB and research conducted within the framework of the Forest Products Industry Research College (FPIRC). The financial support provided by Södra Timber AB and the Forest Products Industry Research College programme sponsored by the Foundation for Strategic Research (SSF), is greatfully acknowledged.

I would like to thank my supervisor Professor Hans Petersson for starting up and guiding me through the research project as well as giving many valuable comments on the manuscript.

A number of persons who were involved in the experimental work in the project is gratefully acknowledged. The laboratory work performed at the division was mainly carried out by Rizalina Brillante and Bertil Enquist. The microstructural measurements were performed in co-operation with Magnus Nilsson and Dr. Bohumil Kučera. I would like to thank Fridberg Stefansson for his laboratory assistance and for the cooperation we had during the period of his masters thesis.

I want to thank Dr. Ola Dahlblom and Dr. Christer Nilsson for their proofreading of the original manuscript and for their comments on it and Prof. Thomas Thörnqvist for his comments on parts of the manuscript from a forestery perspective. I also want to thank Bo Zadig for his skillful drawing of some of the more complicated figures in the report and my colleagues at the Division of Structural Mechanics for their support and for making our coffee breaks pleasant.

Finally, I want to express my gratitude to my family - Monica, Alfred and Ludvig - for their patience and support during the course of the work.

Lund October 2000

Kent Persson

ABSTRACT

Wood is a material with mechanical properties that vary markedly, both within a tree and among trees. Moisture changes lead to shrinkage or swelling and modify the mechanical properties. In the present study both experimental and numerical work concerning the stiffness and the hygroexpansion properties of wood and of fibres and variations in them is presented.

The experimental work involves both characterizing the structure of wood at the microstructural level and the testing of clear-wood specimens. The experiments at the microstructural level provide valuable information concerning the cellular structure of wood, information needed for modelling wood on the basis of its microstructure. Deformations in the microstructure due to loading, as characterized by use of a SEM, was also studied. The longitudinal modulus of elasticity, three hygroexpansion coefficients and the density along the radius from pith to bark in the stem were determined by the testing of clear wood specimens. The longitudinal modulus of elasticity and the three shrinkage coefficients were shown to vary considerably along the radial direction of the stem.

Models based on the microstructure for determining the stiffness and shrinkage properties of wood are proposed. The models investigated include the chain of modelling from the mechanical properties of the chemical constituents of the cell wall to the average mechanical properties of a growth ring. The models are based mainly on results of the experiments that were performed. Models of the microfibril in the cell wall as well as models of the cellular structure of wood were developed with the aim of determining the stiffness and shrinkage properties of wood from simply a few key parameters. Two models of the cellular structure of wood were investigated. In one of these, the structure was composed of irregular hexagonal cells, whereas in the other the cell structures were obtained from micrographs. Parametric studies performed by use of the hexagonal cell model are presented. The results of these studies showed the parameters governing the stiffness and the hygroexpansion properties of wood to be the microfibril angle of the S$_2$-layer, density and the properties of the chemical constituents.

An introductory study of the nonlinear behaviour of cell structures was also carried out. The results of numerical analyses of the deformations in cell structures that occur in compression loading in the radial and tangential directions are presented.

The mechancial behaviour of chemically unaltered fibres of simplified geometrical shape was also studied in a preliminary way by means of micromechanical modelling. Three-dimensional finite element models of straight fibres of undeformed and of collapsed cross-sectional shape were involved. Both the force-displacement relationship and the moisture-induced deformations needed for characterization the behaviour of the fibre were determined. The results of simulations of the stiffness behaviour of fibres revealed two unique coupled deformation modes: coupling between extension and twist and coupling between in-plane bending and out-of-plane shear deformation. The deformation modes obtained were shown to be dependent on the value of the microfibril angle in the S_2-layer.

Keywords:
Wood, Fibre, Simulation, Stiffness, Hygroexpansion, Density, Microfibril angle

CONTENTS

1. INTRODUCTION

1.1. Background

Products made from biological materials such as wood and paper products often have a complex mechanical behaviour. Although such materials have been utilised for thousands of years, full knowledge of their mechanical behaviour has yet to be achieved. They often vary in their properties from sample to sample and exhibit a nonlinear mechanical behaviour at higher loading. Moisture changes lead to shrinkage or swelling and modify the mechanical properties. Wood and paper materials also show a loading-rate dependency, such as creep and viscoelasticity.

In modern forestry management, which is highly mechanised, new problems have appeared, such as those of selecting the right trees for different purposes. In the past, such tasks were performed by skilled craftsmen who selected which trees in the forests were to be used for different purposes. Since the grading of wood is now carried out at sawmills, certain highly useful information concerning growth location that could lead to better grading is no longer available. Under such conditions, obtaining more thorough knowledge of relations between the growth characteristics and the mechanical properties of wood and fibres can help to improve the selection of trees as well as grading considerably. The value of both wood and paper products could be increased if quality estimates of the wood and fibres in a log were made.

Wood and paper are materials with great potential since the raw material from which they are obtained is cheap, environmentally friendly and represents renewable materials. Being easy both to form and to assemble at a construction site, wood is frequently the most preferable construction material. However, unless wood is selected, used and treated properly, problems of crack development, deformation due to moisture changes, low timber strength and stiffness may occur. Better knowledge of the mechanical behaviour of wood is important if such problems are to be avoided and new applications of wood discovered. Also, better knowledge of the behaviour of the wood material is needed if the increasingly powerful computer simulation tools that are becoming available are to be adequately utilised in analysing complex wood structures.

Wood is a material that, although formed by nature, can be strongly influenced by silvicultural treatment. In regard to its structural behaviour, wood has both advantages and disadvantages. It is a highly oriented material with properties that differ in the three main directions. In the strongest direction, the stiffness and strength are great, greater than for most other materials if strength is considered in relation to material weight. In the other two directions, on the other hand, wood is relatively soft and weak. This can result in cracking and can cause structural failures. Because of wood having differing properties in different directions, a large number of parameters need to be taken into account in an analysis if the mechanical behaviour is to be adequately described. Reducing these to just a few key parameters, sufficient for determining the quality of wood, would be of great interest.

In the paper-making process the raw material of wood is processed to yield a structure made up of fibres. The logs are cut into chips which are treated chemically and/or mechanically so as to produce fibres with properties suitable for paper-making. The fibre structure that forms the paper sheet can be optimised by using computer simulations of fibre networks. To be able to perform meaningful simulations of the paper properties through fibre network models, it is essential to have full knowledge of the properties of the fibres.

Problems related to the structural behaviour of wood are often due to its mechanical properties being highly variable. Trees growing in the forest are subjected to considerable natural variation in growth conditions, such as in type of soil, nature of the terrain and climatic conditions, the latter varying from day to day. The mechanical properties of wood are strongly affected by all of these factors. The boards sawn from different trees of the same type often differ very much in their properties. The mechanical properties also vary substantially within the tree, since the wood that a tree formed at different ages can differ considerably in its properties, especially during the juvenile phase of growth. In addition, the climatic conditions from one year to another can differ very much, affecting the yearly growth increment. Growth is also strongly affected by silvicultural treatment, such as by cleaning and thinning.

1.2. Scope

Wood and paper are materials each with their own intrinsic structural hierarchy. This means that structural levels involving basic structural components can be found on various scales. The basic structural levels for wood and paper are shown in Figure 1.1. The structure of wood can be divided into the homogeneous wood level, the cell structure level, the cell wall level and the microfibril level. Paper can be divided into the paper sheet level, the fibre network level, the fibre level, the cell wall level and the microfibril level. The two levels at the smallest scale for paper and for wood are thus similar. Other levels than those mentioned above can be distinguished as well, such as the molecular level, the board level and the end-use level. At each level the structural components are regarded as being homogeneous. It is the homogeneous properties of these components and the geometric structure at each level then that determines the equivalent homogeneous properties of the structural component at the next level.

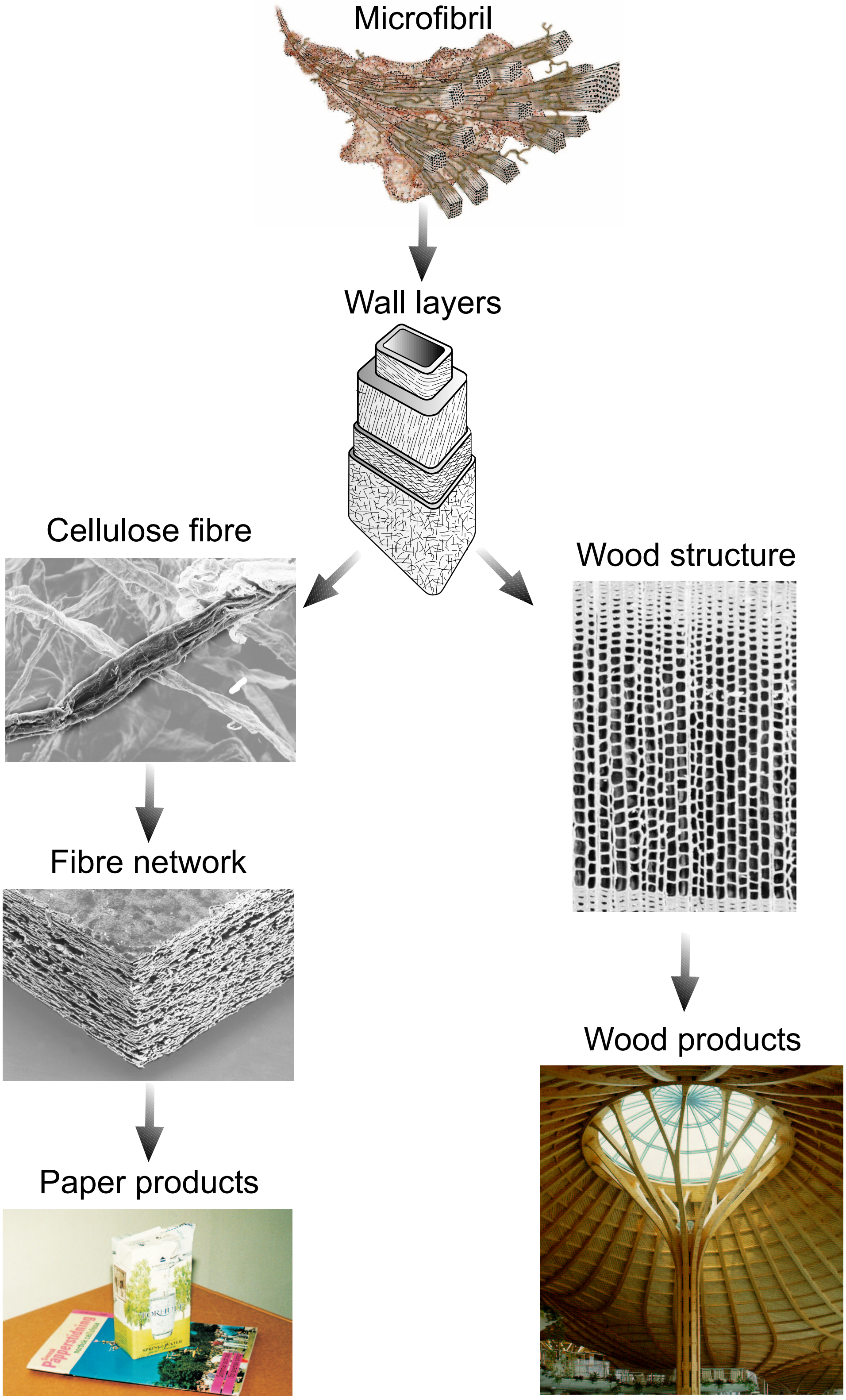

Figure 1.1: *Different structural scales of wood and paper from the ultrastructure to large structural systems.*

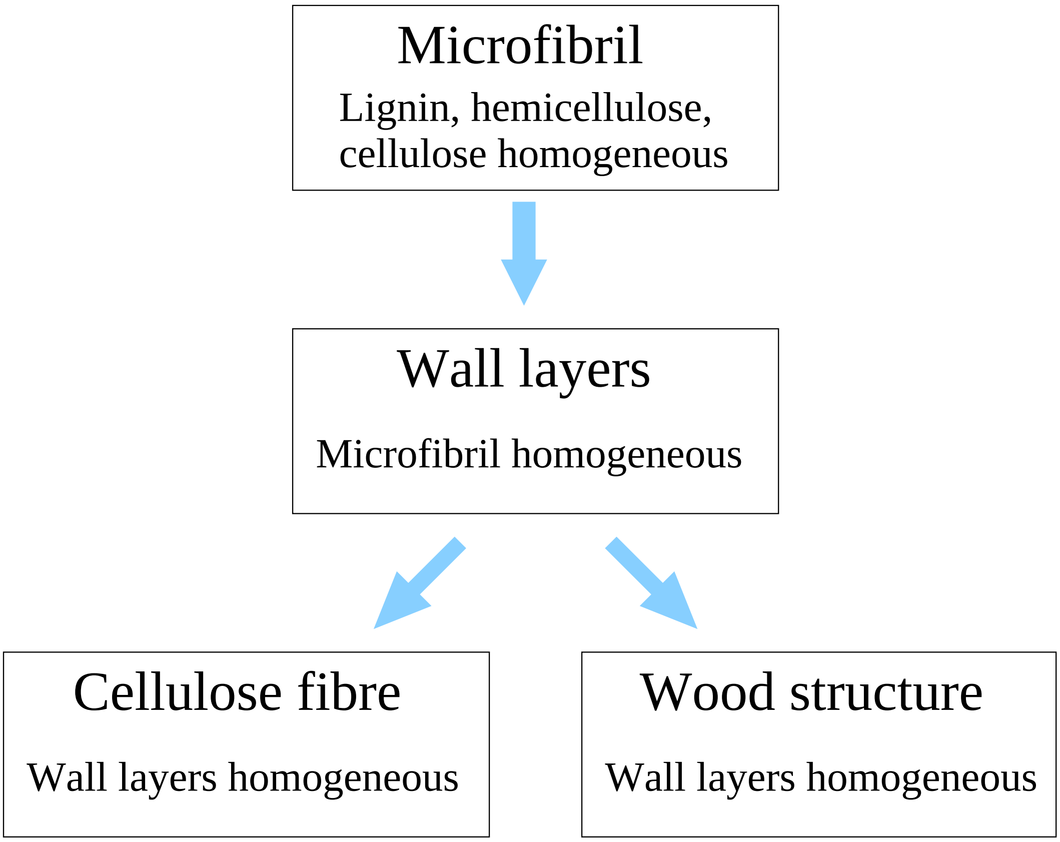

Figure 1.2: *The structural scales investigated in the present study. The arrows represent models for determining homogeneous properties on the next larger scale.*

The present study focuses on the mechanical properties of clear wood and wood fibres of Norway Spruce. Figure 1.2 shows the structural scales that are investigated in this study. The mechanical properties of clear wood are governed by the shape of the cellular structure and the properties of the various layers of the fibre wall. Thus, knowing the cellular structure of wood and the properties of the fibre wall allows the properties of wood to be determined. The mechanical properties of the individual fibres can be determined in a similar way, the fibre properties being governed by the geometry of the fibre and the properties of the various layers in the fibre wall. The mechanical properties of the layers in the fibre wall are governed by the properties of the chemical constituents and by the microfibril structure. If proper models of the microstructure of wood and fibres are developed, variations in mechanical properties can be determined by use of computer simulations. Moreover, at the microstructural level the important parameters governing the mechanical properties of wood and fibres can be determined by use of these models. The present work is concerned with the development of models, allowing the resulting stiffness and shrinkage parameters, as well as variations in these parameters, to be determined. Special attention is directed at examining variations related to the radial position within the tree. In modelling the mechanical properties of wood, thorough knowledge of the cellular structure is necessary. It is also of interest to compare the theoretically obtained properties with experimental results. Accordingly, experiments have been carried out to determine the physical properties both for microstructural sized specimens and for clear wood specimens. In modelling the mechanical properties of wood and of fibres, the complete chain of relationships from the microstructural level up to the level of large structural systems is of interest. The properties of wood determined in this study can be used in models of boards and planks, Ormarsson [48] and in numerical studies of defibration processes, as described by Holmberg [30]. The properties of the fibres that are determined can be used in fibre network models of the paper sheet, Heyden [27].

1.3. Outline

In Chapter 2 certain basic facts concerning the different levels of the cellular structure of wood, the mechanical properties of the chemical constituents and certain properties found at the macrostructural level are discussed. In Chapter 3 some of the basic properties of wood are derived experimentally from clear-wood specimens so as to investigate how the mechanical properties vary within the tree. In addition, measurements aimed at characterizing the features of the cellular structure of wood experimentally, as well as observations of deformation processes within the microstructure, made with the aid of a scanning electron microscope, are presented. Various models of microstructural formations derived from experimental results are discussed in Section 3.5. In Chapter 4 various mathematical methods for deriving the average mechanical properties of wood from the microstructure are presented. The equivalent stiffness and shrinkage properties of a periodic material are obtained by use of a homogenisation procedure in which the equations are solved by means of the finite-element method. In Section 5.2 the equivalent properties of the cell wall layers are derived from the properties of the chemical constituents. The cell-wall properties determined are then used in Sections 5.3, 5.4 and 5.5 to develop structural models for the cell wall and for cellular wood structures, these being used to determine the equivalent mechanical properties of clear wood. Determination of the equivalent properties at the different levels is carried out by means of the methods described in Chapter 4. Numerical studies based on the models developed in Chapters 4 and 5 are presented in Chapter 6. In Section 6.2 a parametric study is reported in which the influence of the density and the microfibril angle of the S_2-layer on the stiffness and shrinkage properties of wood are determined. In Section 6.3 the equivalent mechanical properties along the radius of a tree are determined on the basis of certain basic measurements. In Chapter 7 introductory studies of the nonlinear behaviour of wood under large compressional deformations are reported. In Chapter 8 the basic mechanical behaviour of fibres is analysed. Models of fibres are developed that are utilised in analysing the collapse of the fibre cross-section and in determining the stiffness properties of fibres. In Chapter 9, finally, the experimental and the modelling results are discussed and concluding remarks are made involving in part suggestions for future work.

2. WOOD

2.1. General Remarks

In Sweden, the most common conifers are Norway spruce (*Picea abies*) and Scots pine (*Pinus sylvestris*). The analyses, experiments and discussions in this report relate only to spruce. However, most of the results achieved in the testing and in the analyses are probably valid for other conifers as well, since the internal structure of all of them is similar. Spruce was chosen for the investigation since spruce is the most important conifer for providing structural timber and fibres for paper-making and since the forests in southern Sweden contain about 70% spruce.

Studying the interior of wood generally reveals it to have a complex, inhomogeneous structure. A number of features at each level in the hierarchic structure of wood which can be defined need to be considered in characterizing its mechanical properties. One distinguishes between macrostructural and microstructural structural levels in wood. The present study deals with the properties of clear wood, inhomogeneities such as knots are not being considered. The clear wood is regarded as representing the macrostructural level. The levels in the hierarchy below that level are referred to as the microstructural levels. Sometimes the structures below the fibre level are referred to as the ultrastructural levels. In the next section the structural and mechanical properties of wood and fibres at both a macro- and microstructural level are discussed briefly. Where no specific references are given, and for further reading about the structure of wood, see e.g. Kollman and Côté [35], Bodig and Jayne [9] and Dinwoodie [20].

2.2. Structural Levels of Wood

2.2.1. Macrostructural level

If the cross section of a log is examined, Figure 2.1, different types of wood can be identified. The growth rings, which appear as alternating light and dark rings, the lighter rings being earlywood and the darker rings latewood, are the most obvious. Earlywood is formed during the spring and early summer, whereas latewood grows during the summer. For conifers in Sweden the distance between two adjacent growth rings, called the ring width, is normally from 1 up to 10 mm, and for very fast growing wood it is even greater. Radial growth in a tree occurs in the cambium, located between the stem and the bark, in which wood cells are formed during the growth season.

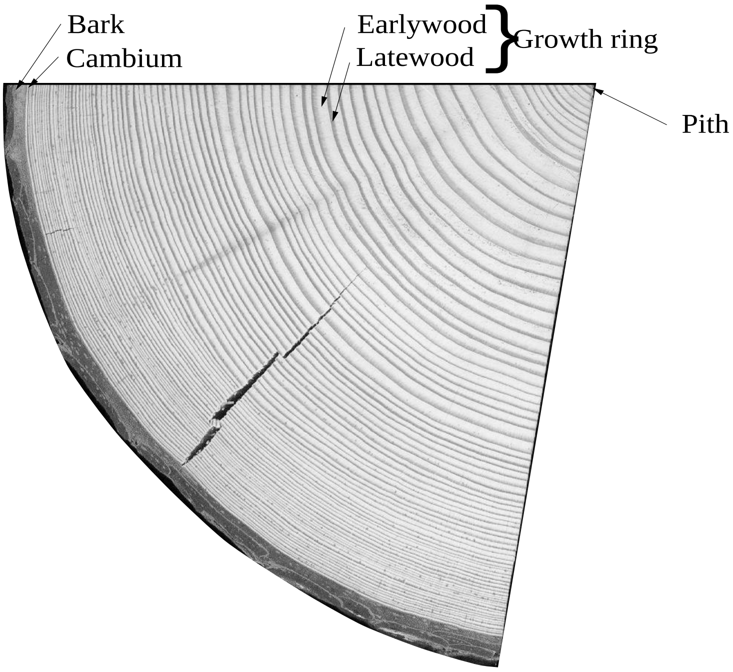

Figure 2.1: *Cross section of a log showing features revealed by the naked eye.*

The area around the centre of the log, termed the pith, consists of juvenile wood formed during the first few years along the entire length of a tree, Kyrkjeeide [39]. In softwood, the juvenile wood consists of the first 15-20 growth rings. Juvenile wood is characterized by lower stiffness, greater longitudinal shrinkage, lower tangential shrinkage and lower density than mature wood. The wood material in the outer growth rings of the stem, called the sapwood, provides for transportation of liquid up in the tree. The wood material inside the sapwood, where liquid transportation no longer occurs, is called the heartwood. This region can be recognised through the absence of living cells and through its containing deposits of chemical substances called extractives, which prevent the wood from being attacked by fungi or by insects. Extractives also seal the pores of the wood cells, making the wood material less permeable. For some species, the deposits give the heartwood a darker colour. In softwoods there are about 8% extractives in the heartwood and about 3% in the sapwood. In tree stems that have been subjected to bending forces caused by wind or gravitation, abnormal wood called compression wood may be found in certain parts of the tree.

Since a tree stem grows in a cylindrical manner, the different properties of wood can be related to the three principal directions of growth. In the Cartesian coordinate system that has been adopted, one coordinate axis is in the longitudinal direction, the other two axes being located radially and tangentially to the growth rings in the cross section of the stem. The common names for the three directions

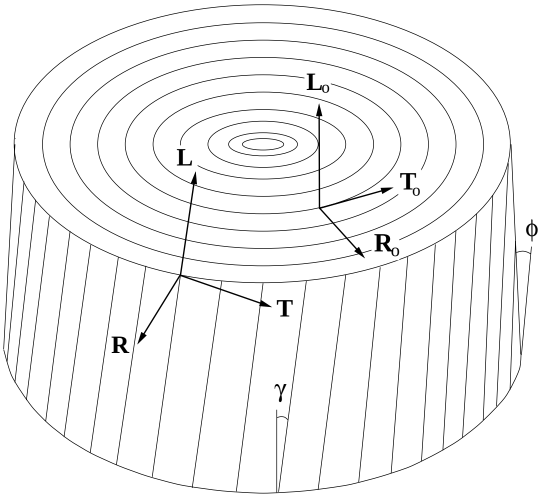

Figure 2.2: *The main directions used for the tree stem and for the fibres are expressed by the $L_0R_0T_0$-coordinate system being aligned with the tree and the LRT-coordinate system with the fibres. The spiral growth angle is denoted by γ and the conical angle by ϕ.*

are L for the longitudinal direction, R for the radial direction and T for the tangential direction. However, due to spiral growth and to that the stem often having a conical shape, the fibres in the stem are seldom fully aligned in the main directions of the tree stem cylinder. This is important, since the mechanical properties of clear wood are described with reference to the fibre direction and not to the longitudinal direction in the cylinder of a tree. It is necessary, therefore, when dealing with structural timber, to define two coordinate systems. One is a global coordinate system in which the longitudinal axis L_0 is parallel to the pith of the stem, the radial direction being termed the R_0-axis and the T_0-axis being perpendicular to both L_0 and R_0. A second, local coordinate system is introduced with the main directions L, R and T, Figure 2.2, in which L is oriented in the longitudinal direction of the fibres, and R and T are oriented in the cross-fibre directions. The spiral growth angle, i.e. the deviation between the two axes L and L_0, is normally less than 5° but varies within the stem. This angle is normally high in the juvenile wood and decreases along the radius in the stem, to often have an opposite angle near the bark, Säll et al. [66], Dahlblom et al. [15],[16] and Ormarsson [48].

2.2.2. Wood cell level

Softwoods are composed of two types of cells, termed tracheids and parenchyma cells. Tracheids are long slender cells which most of the tree consists of, as much as 95% of the cells in a tree being tracheids. In this report the term cell or fibre will often be used instead of the longer and more correct term tracheid. Those tracheids that are formed during the early growth season when fluid transport from the root to the needles is high, have thin walls and large cavities (lumen). Such tracheids, which form the earlywood part of the growth ring, are of low density. In the later part of

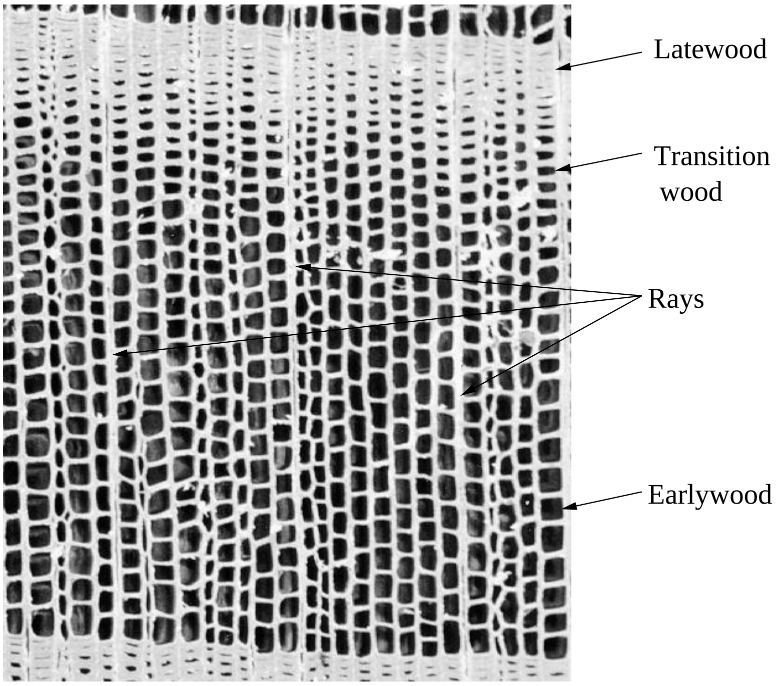

Figure 2.3: *Cell structure of an annual ring (Picea abies).*

the growth season the tree builds latewood, which has tracheids with thick walls. The transition phase in the growth ring from earlywood to latewood is sometimes called transitionwood, Figure 2.3.

A tracheid is about 1 mm long near the pith, increasing in the 15-20th growth ring in the juvenile wood to about 3-4 mm and remaining constant throughout the mature wood, Atmer and Thörnquist [5]. The tracheids are about 30-40 μm in diameter in the earlywood and about 20-30 μm in the latewood.

In the radial direction there are wood rays organised into bands of cells. The rays extend radially from the pith to the bark, serving mainly to provide radial liquid transport and food storage in the trunk. Ray cells consist primarily of thin-walled parenchyma cells that are shorter and wider than tracheids. The volume percentage of the ray cells in Norway spruce is about 7%, but due to the parenchyma cells being wider and having thinner walls and thus being of lower density, the weight percentage is only about 2-3%, Perilä et al. [56]. Since the ray cells are aligned perpendicular to the tracheids, they also serve to reinforce the wood in the radial direction. The rays thus increase the stiffness of the wood in the radial direction.

Parenchyma cells are also found in resin ducts, which are large sparsely distributed cavities oriented mainly in the longitudinal direction and surrounded by parenchyma cells. Due to their sparse distribution, resin ducts have little influence on the mechanical properties of wood. Thus, their influence can normally be neglected.

Pit pores are found almost entirely in the radially oriented cell walls between the lumens of adjacent cells. These allow liquid to flow between the cells and from the cells to the rays. Since they occur frequently, the pores may weaken the radially oriented cell walls and decrease the radial stiffness of the wood.

2.2.3. Cell wall

The cell wall, see Figure 2.4, consists mainly of the primary wall (P) and of the secondary wall, the latter being composed of three layers (S_1, S_2 and S_3). Sometimes, an additional layer is distinguished, the so-called warty layer, a very thin layer inside the S_3-layer. The middle lamella is not regarded as a cell-wall layer, since it acts primarily as a bonding medium, holding the cells together. The primary and secondary walls can be regarded as fibre-reinforced composites. The layers of these walls consists of cellulosic chains located in a hemicellulose and lignin matrix that forms thread-like units called microfibrils. Several different descriptions of the size and shape of the microfibrils are to be found in the literature, for example Salmén [61], Fengel [21], Preston [57] and Kerr and Goring [33]. A common characteristic of all the models of the microfibrils that have been proposed is that the cellulosic chains and the hemicellulose are closely associated, the hemicellulose binding several cellulosic chains to form larger blocks. Lignin acts as a matrix material, surrounding the blocks of cellulose and hemicellulose. Figure 2.5 shows a microfibril model proposed by Salmén [61]. The length of the cellulose molecules in the wood microfibril has been measured to be approximately 3500-5000 nm, whereas their width has been determined to be 2-4 nm, the shape of the cross-section of the microfibril being nearly square, O'Sullivan [49].

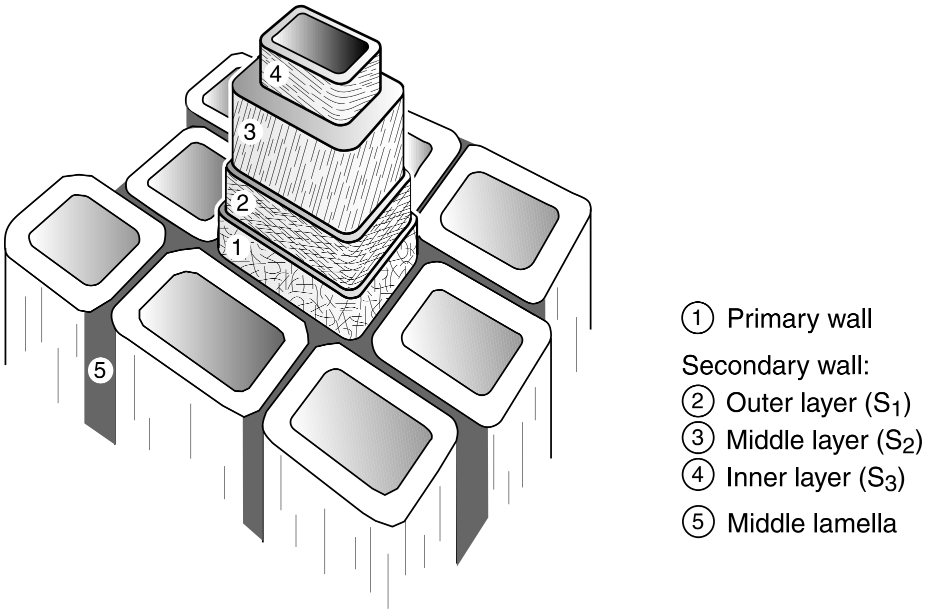

Figure 2.4: *Schematic drawing of the layers in the cellular structure of wood.*

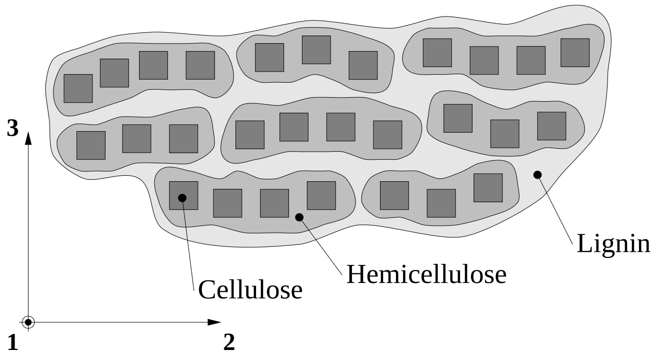

Figure 2.5: *Schematic organisation and coordinate directions of the microfibrils in the cell wall. The 1-axis is the longitudinal direction in the microfibril, the 2-axis is the tangential direction in the microfibril and the 3-axis is the direction normal to the cell wall.*

Cellulose is the major chemical component of wood, its volumetric content in softwood being about 40-45%. It is a crystalline polymer with short amorphous regions. The crystallinity of wood cellulose ranges from 67 to 90%. The crystalline regions in the cellulose chains do not absorb water and can thus be regarded as being independent of moisture change. In the amorphous regions, certain absorption that can alter the physical properties may occur.

Hemicelluloses are a group of materials that are non-cellulosic polysaccharides. The different hemicelluloses are assumed here to have equal properties and are treated as a single unified type of material. Hemicellulose has a low degree of polymerisation and crystallinity, giving it a low stiffness and a high moisture absorption capacity. The hemicellulose in wood accounts for about 30% of the cell-wall volume. Lignin, in turn, is a complex compound having a three-dimensional molecular structure. It is amorphous and possesses moisture- and temperature-dependent properties. The volumetric content of lignin in the cell wall of wood amounts to about 30%. All the cell-wall layers except the middle lamella consist of microfibrils but differ in how they are organised, and also in their thicknesses and in the fractions of the various chemical constituents they contain, see Table 2.1.

The chemical composition of the various cell wall layers is shown in Figure 2.6. The primary wall is a very thin layer in which the microfibrils are loosely packed and are randomly oriented. Since the cellulose content is only about 12% in there, the primary wall will have a low stiffness. The primary wall and the middle lamella are similar in their chemical composition and are often treated as a single compound layer. The secondary wall, in turn, consists of three layers. Nearest the primary wall lies the S_1-layer, where the microfibrils are oriented in a direction 50° to 70° from the longitudinal cell axis. The microfibrils lie in several lamellae. They have a crossed orientation, being alternately wound to the left and right around the cell in a helical pattern. Table 2.2 shows the inclination of the microfibril angle relative to the longitudinal cell axis for the different cell-wall layers.

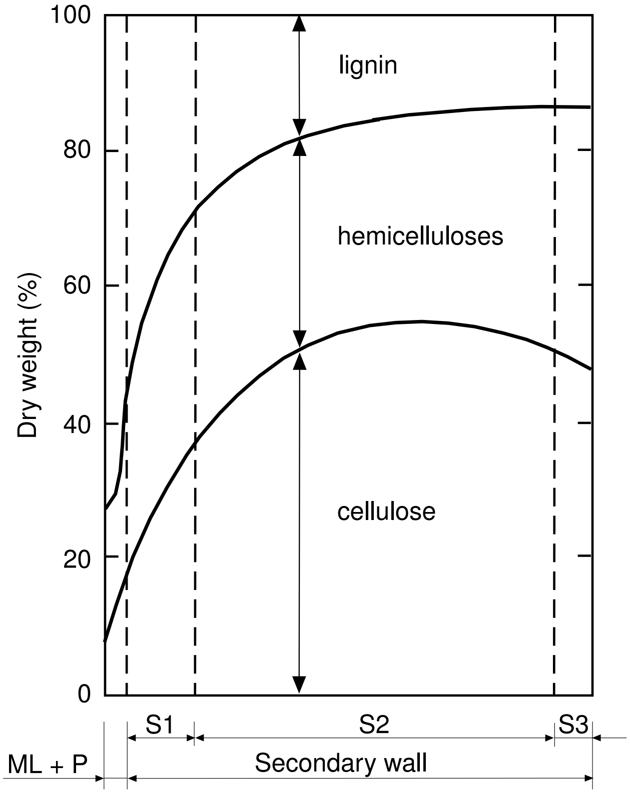

Figure 2.6: *Chemical composition of the different layers of the cell wall, Panshin and deZeeuw [8].*

The S_2-layer is the most dominant layer, making up about 70-80% of the thickness of the cell wall. The angle between the microfibril direction and the longitudinal cell direction in the S_2-layer, referred to as the microfibril angle, varies within the range of about 5° to 45°. Although some reports state that the microfibril angles in the radial and the tangential cell walls differ, these are assumed in the present investigation to be the same. The highest values for the microfibril angle are found in juvenile wood and in compression wood. The S_3-layer is the inner layer of the

Table 2.1: *Volumetric fractions of the chemical constituents and thicknesses of the cell wall layers, Fengel [21], Kollman [35].*

Cell wall layer	Thickness, μm		Chemical contents, %		
	Earlywood	Latewood	Cellulose	Hemicellulose	Lignin
ML	0.5	0.5	12	26	62
P	0.1	0.1	12	26	62
S_1	0.2	0.3	35	30	35
S_2	1.4	4.0	50	27	23
S_3	0.03	0.04	45	35	20

Table 2.2:*Microfibril angle of the cell wall layers, Dinwoodie[3], Sahlberg et al. [22].*

Cell wall layer	Microfibril angle, $\varphi°$	
	Earlywood	Latewood
P	Random	Random
S_1	±50-70	±50-70
S_2	10-40	0-30
S_3	60-90	60-90

secondary cell wall. It has a microfibril angle of between 60° and 90°. The S_3-layer has been found to be oriented approximately perpendicular to the S_2-layer. The microfibrils follow the orientation of their respective layer, but where they are interrupted by the pit area they sweep around it in a stream-like fashion. A thickening of the cell wall around the pits occurs. This arrangement of the microfibrils around the pits contributes to decreasing the weakening effect of the pits.

2.3. Properties and Behaviour of Wood

2.3.1. Density

The density of wood is an important property to consider since the stiffness, strength and shrinkage properties are all dependent on the density. Lignin and hemicellulose are material constituents of wood that absorb water and swell, which affects the volume and the weight of a wood sample. There are several ways of defining the density of wood. A common measure of density, employed in this report, is the oven-dry weight of the wood divided by its volume in the green condition, i.e.

$$\rho = \frac{m_0}{V_G} \tag{2.1}$$

where m_0 is the weight in the oven-dry condition and V_G is the volume in the saturated condition. Another measure is the oven-dry weight divided by the volume in the oven-dry condition, in which there may still be a small amount of bound water left within the cell walls. The density can also be defined as the oven-dry weight divided by the volume at a specified moisture content. The density of clear wood specimens of Norway spruce grown in Sweden is about 350 - 600 kg/m^3, as will be shown later in this study.

Since the earlywood and latewood walls differ in their cross-sectional shape and thickness, the density of the wood varies considerably over a growth ring. Figure 2.7 shows the fraction of the cell wall area to the total area over a few growth rings. The bulk density of the cell wall is assumed to be about 1500 kg/m^3 for dry plant cell walls, Kollman et al. [35]. For earlywood and latewood, the average densities can be expressed as the cell wall area ratio S of a cross section, multiplied by the bulk density of the cell wall.

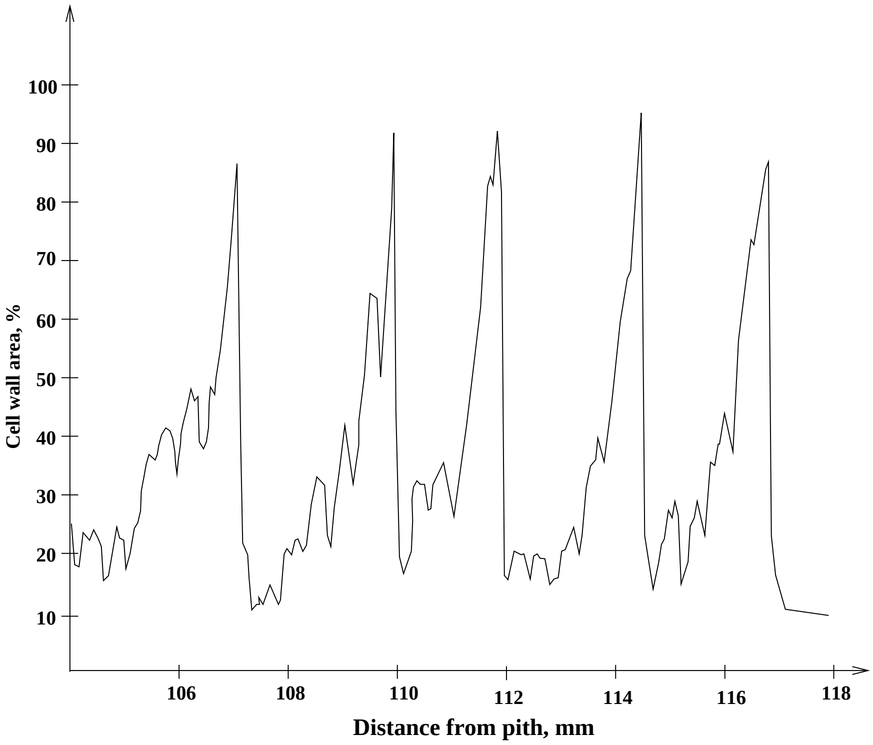

Figure 2.7: *Variation in density over a few growth rings in the radial direction in spruce, Wigge [70].*

The average density, ρ_r, of a growth ring can be calculated by integrating the curve shown in Figure 2.7 as

$$\rho_r = \frac{1}{l_r} \int_0^{l_r} \rho(x) dx \tag{2.2}$$

where l_r is the growth ring width. The density function $\rho(x)$ can be approximated by dividing the density curve over the growth ring into three regions: the earlywood, the transitionwood and the latewood regions, see Figure 2.8. The earlywood and latewood regions can be assumed to be of linearly increasing density, whereas the density function for the transitionwood has an exponential form. The densities of the earlywood, transitionwood and latewood regions of a growth ring can be represented by the average values ρ_e, ρ_t and ρ_l for the respective regions. The width of the transitionwood region l_t is considered to be a fraction of the growth-ring width l_r,

$$l_t = s l_r \tag{2.3}$$

If the length ratio s is assumed to be constant, the transition from earlywood to latewood is more abrupt for wood with small growth rings than for fast-grown wood with large growth rings. On the basis of the assumptions made above, the average density ρ_r of a growth ring is

$$\rho_r = \rho_e + (\rho_t - \rho_e)s + (\rho_l - \rho_e)\frac{l_l}{l_r} \tag{2.4}$$

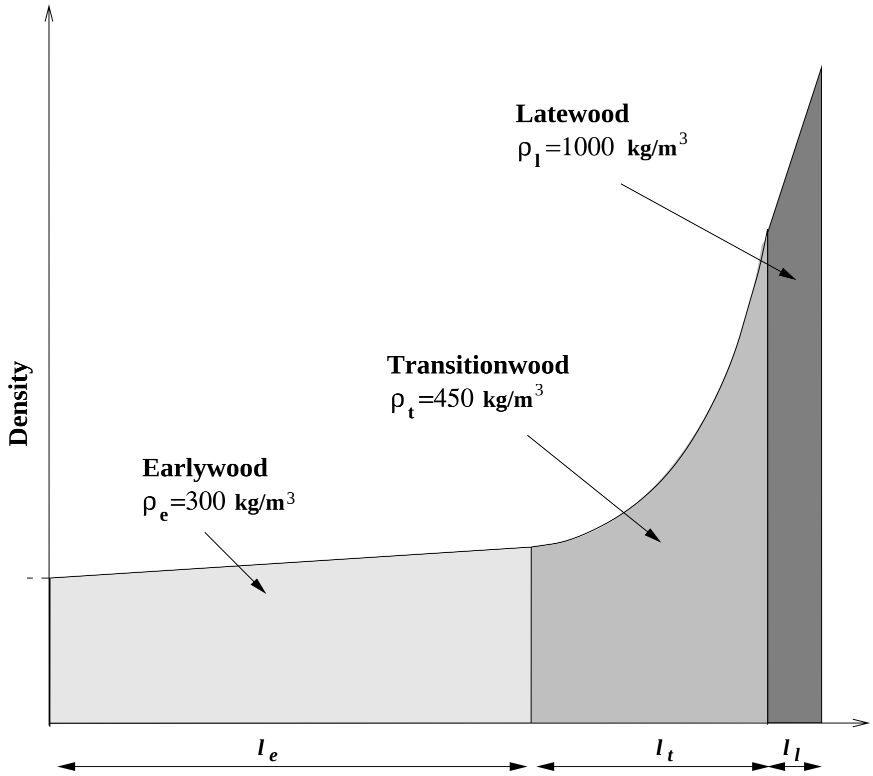

Figure 2.8: *Density over a growth ring divided into three different regions of differing average density.*

where l_l is the width of the latewood region of the growth ring.

In the present study, the width of the latewood region, l_l, is assumed to be constant of about 0.2 mm. The average densities for the earlywood, the transitionwood and the latewood are set to 300 kg/m^3, 450 kg/m^3 and 1000 kg/m^3, respectively. The transitionwood fraction as determined by the ratio s is set to 0.2. Inserting these values into Eq.(2.4) yields a relation between the average density, ρ_r, of the growth ring and the growth ring width l_r. The relation is shown in Figure 2.9.

2.3.2. Stiffness properties

Wood is a porous material with mechanical behaviour that is influenced by loading rate, duration of loading and such environmental factors as temperature and humidity. Wood is frequently regarded as a homogeneous material, that below the limit of proportionality shows a linear elastic orthotropic material behaviour. Its constitutive behaviour in this region can be described by Hooke's generalised law as a linear elastic orthotropic material. An orthotropic material possesses different properties with respect to three perpendicular symmetric planes. The three principal directions for wood are the longitudinal direction L, the radial direction R and the tangential direction T. These are the principal orthotropic directions, which vary

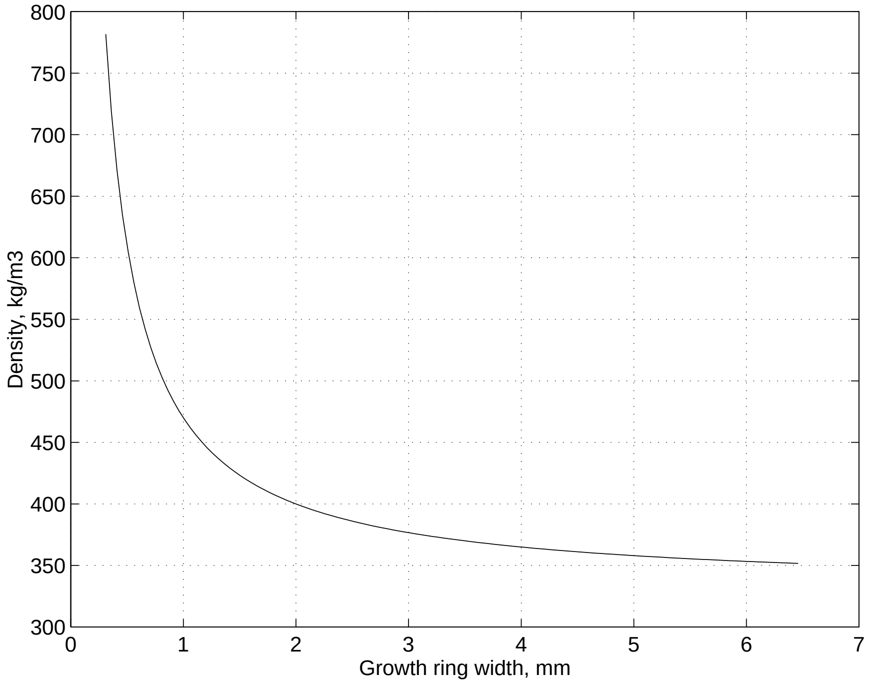

Figure 2.9: *Theoretical relation of average density to growth-ring width, Eq.(2.4).*

in the stem of a tree due to its cylindrical growth, conical shape and spiral growth. If the wood sample studied is small the L,R,T-coordinate system can be regarded as a Cartesian coordinate system. Hooke's generalised law for an orthotropic material can be written by use of matrix notation as

$$\begin{bmatrix} \epsilon_{LL} \\ \epsilon_{RR} \\ \epsilon_{TT} \\ \gamma_{LR} \\ \gamma_{LT} \\ \gamma_{RT} \end{bmatrix} = \begin{bmatrix} \frac{1}{E_L} & -\frac{\nu_{RL}}{E_R} & -\frac{\nu_{TL}}{E_T} & 0 & 0 & 0 \\ -\frac{\nu_{LR}}{E_L} & \frac{1}{E_R} & -\frac{\nu_{TR}}{E_T} & 0 & 0 & 0 \\ -\frac{\nu_{LT}}{E_L} & -\frac{\nu_{RT}}{E_R} & \frac{1}{E_T} & 0 & 0 & 0 \\ 0 & 0 & 0 & \frac{1}{G_{LR}} & 0 & 0 \\ 0 & 0 & 0 & 0 & \frac{1}{G_{LT}} & 0 \\ 0 & 0 & 0 & 0 & 0 & \frac{1}{G_{RT}} \end{bmatrix} \begin{bmatrix} \sigma_{LL} \\ \sigma_{RR} \\ \sigma_{TT} \\ \tau_{LR} \\ \tau_{LT} \\ \tau_{RT} \end{bmatrix} \tag{2.5}$$

or more briefly as

$$\boldsymbol{\epsilon}^e = \mathbf{C}\boldsymbol{\sigma} \tag{2.6}$$

or as the inverse relation

$$\boldsymbol{\sigma} = \mathbf{D}\boldsymbol{\epsilon}^e, \quad \mathbf{D} = \mathbf{C}^{-1} \tag{2.7}$$

where $\boldsymbol{\epsilon}^e$ is the elastic strain vector, $\boldsymbol{\sigma}$ is the stress vector and $\boldsymbol{D}$ is the material stiffness matrix. The parameters of the material stiffness matrix $\boldsymbol{D}$ are three moduli of elasticity, E_L, E_R and E_T, three moduli of shear, G_{LR}, G_{LT} and G_{RT}, and six Poisson's ratios, ν_{LR}, ν_{LT}, ν_{RL}, ν_{RT}, ν_{TL} and ν_{TR}. For uniaxial cases, the first index of Poisson's ratio denotes the loading direction and the second index the strain direction. The material is assumed to be linear elastic, resulting in the material stiffness matrix $\mathbf{D}$ being symmetric. Thus,

$$\frac{\nu_{RL}}{E_R} = \frac{\nu_{LR}}{E_L}, \quad \frac{\nu_{TL}}{E_T} = \frac{\nu_{LT}}{E_L}, \quad \frac{\nu_{TR}}{E_T} = \frac{\nu_{RT}}{E_R} \tag{2.8}$$

Due to this symmetry, there are nine independent parameters describing the stiffness of the orthotropic material.

Since the fibres in the stem are mainly oriented in the longitudinal direction, the strength and stiffness are considerably greater in this direction than in the two directions perpendicular to the longitudinal direction. However, there is also a difference in stiffness between the radial and tangential directions. The stiffness in the radial direction is about 1.5 times higher than the stiffness in the tangential direction. This difference is due mainly to the cellular structure is differing in the tangential and in the radial directions and to the presence of radially oriented ray cells that acts as reinforcement in the latter direction. The stiffness coefficients vary markedly. Common values for Norway spruce (Picea Abies), at around 12% of moisture content, are shown in Table 2.3.

Normally, the principal orthotropic directions do not coincide with the global coordinate system that is chosen. For an anisotropic material such as wood, a transformation of the stiffness matrix must thus be made in order to determine the material stiffness with reference to the global directions. The transformation for a vector $\mathbf{P}$ described in a local LRT-coordinate system to a global xyz-coordinate

Table 2.3: *Typical values of stiffness coefficients of spruce at 12% moisture content.*

Parameter	Measurements Ref. [11], [26]
E_L, MPa	13500 - 16700
E_R, MPa	700 - 900
E_T, MPa	400 - 650
G_{LR}, MPa	620 - 720
G_{LT}, MPa	500 - 850
G_{RT}, MPa	29.0 - 39.0
ν_{RL}	0.018 - 0.030
ν_{TL}	0.013 - 0.021
ν_{TR}	0.24 - 0.33

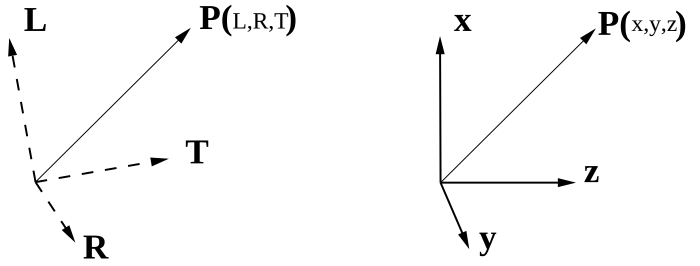

Figure 2.10: *A vector* **P** *in a local LRT-coordinate system and in a global xyz-coordinate system.*

system, as shown in Figure 2.10, is given by

$$\begin{bmatrix} L \\ R \\ T \end{bmatrix} = \mathbf{A^T} \begin{bmatrix} x \\ y \\ z \end{bmatrix} \tag{2.9}$$

The orthogonal transformation matrix **A** is given by

$$\mathbf{A} = \begin{bmatrix} a_L^x & a_R^x & a_T^x \\ a_L^y & a_R^y & a_T^y \\ a_L^z & a_R^z & a_T^z \end{bmatrix} \tag{2.10}$$

where a_{local}^{global} denotes the direction cosines between the local and global directions, respectively. The transformation of the stress vector $\boldsymbol{\sigma}$ and the strain vector $\boldsymbol{\epsilon}$ with reference to the local material directions, into the stress vector $\hat{\boldsymbol{\sigma}}$ and the strain vector $\hat{\boldsymbol{\epsilon}}$, with reference to the global directions, is made by the transformations

$$\hat{\boldsymbol{\sigma}} = \mathbf{G}^T \boldsymbol{\sigma} \tag{2.11}$$

$$\boldsymbol{\epsilon} = \mathbf{G}\, \hat{\boldsymbol{\epsilon}} \tag{2.12}$$

where **G** is the transformation matrix for a transformation between the local and the global coordinate systems as given by

$$\mathbf{G} = \begin{bmatrix} a_L^x a_L^x & a_L^y a_L^y & a_L^z a_L^z & a_L^x a_L^y & a_L^z a_L^x & a_L^y a_L^z \\ a_R^x a_R^x & a_R^y a_R^y & a_R^z a_R^z & a_R^x a_R^y & a_R^z a_R^x & a_R^y a_R^z \\ a_T^x a_T^x & a_T^y a_T^y & a_T^z a_T^z & a_T^x a_T^y & a_T^z a_T^x & a_T^y a_T^z \\ 2a_L^x a_R^x & 2a_L^y a_R^y & 2a_L^z a_R^z & a_L^x a_R^y + a_L^y a_R^x & a_L^z a_R^x + a_L^x a_R^z & a_L^y a_R^z + a_L^z a_R^y \\ 2a_T^x a_L^x & 2a_T^y a_L^y & 2a_T^z a_L^z & a_T^x a_L^y + a_T^y a_L^x & a_T^z a_L^x + a_T^x a_L^z & a_T^y a_L^z + a_T^z a_L^y \\ 2a_R^x a_T^x & 2a_R^y a_T^y & 2a_R^z a_T^z & a_R^x a_T^y + a_R^y a_T^x & a_R^z a_T^x + a_R^x a_T^z & a_R^y a_T^z + a_R^z a_T^y \end{bmatrix} \tag{2.13}$$

which is defined in terms of the direction cosines according to Eq.(2.10).

The transformation of **D** in Eq.(2.7), expressed in terms of the local material directions, to a matrix $\hat{\mathbf{D}}$, expressed in terms of the global coordinate directions, can be written by use of Eqs.(2.11) and (2.12) as

$$\hat{\mathbf{D}} = \mathbf{G}^T \mathbf{D}\, \mathbf{G} \tag{2.14}$$

2.3.3. Nonlinear properties

When wood is subjected to loading above the limit of proportionality, irreversible changes in the material take place and the force-displacement relation becomes nonlinear. For wood loaded in tension these changes are small up to the point where fracture occurs. In compression, wood behaves in a highly nonlinear way due to its porous nature. In Figure 2.11 uniaxial stress-strain relationships are shown for dry wood loaded in tension and in compression in different directions. In compression the response can be characterized, for all three directions, by an initial linear elastic region followed by a plateau region and finally by a rapidly increasing stress region. Compression in the tangential direction gives a continuously increasing curve directly after the elastic region. Compression in the radial direction gives a curve with an almost constant stress plateau region following a small notch in the stress curve after the linear region has been passed. The yield stresses produced by compression in the tangential and the radial directions are about equal. The yield stress in the longitudinal direction, however, is considerably higher than in the radial and tangential directions and the plateau region is serrated due to buckling and crushing of the fibres. The presence of a plateau region in compression loading is due to instabilities and to local buckling in the microstructure, see Holmberg [30] and Stefansson [65]. Compression loading in the tangential direction gives rise to buckling of the latewood regions into the surrounding earlywood regions, whereas compression loading in the radial direction leads to cell wall buckling of the thin-walled earlywood cells. The stress corresponding to the limit of proportionality for wood in tension is very close to the ultimate stress limit. For compression in the

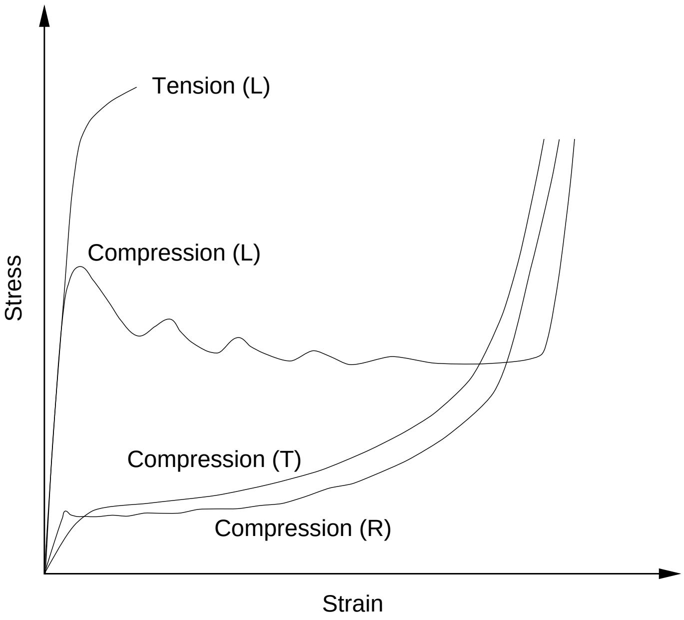

Figure 2.11: *Typical stress-strain curves for wood loaded in compression in the longitudinal, radial and tangential directions and for tension in the longitudinal direction.*

longitudinal direction, the yield stress for wood at 12 % moisture content is about 40-60 MPa, whereas in the radial and tangential directions it is about 3-5 MPa. For higher moisture contents the yield stresses decrease. The mechanical response of wood is also dependent on the loading rate. If wood is to be studied under high loading rates or for loading of very long duration, viscoelasticity or creep must be considered.

2.3.4. Hygroexpansion properties

Wood is a material clearly affected by moisture changes. Shrinkage or swelling occur when the moisture content of wood below the fibre saturation point is altered. The fibre saturation point is defined as the point at which, as the moisture content increases, the cell wall ceases to absorb additional water. For spruce, this occur at a moisture content slightly less than 30%. The moisture content w is defined as

$$w = \frac{m_{H_2O}}{m_0} = \frac{m_w - m_0}{m_0} \tag{2.15}$$

where m_{H_2O} is the weight of the water, m_0 is the weight of the wood in an oven-dry condition and m_w is the weight of the wood at the moisture content w. To include hygroexpansion in the constitutive model, hygroexpansion strains are added to the elastic strains

$$\boldsymbol{\epsilon} = \boldsymbol{\epsilon}^e + \boldsymbol{\epsilon}^s \tag{2.16}$$

where $\boldsymbol{\epsilon}^e$ denotes the elastic strains and $\boldsymbol{\epsilon}^s$ the hygroexpansion strains. The hygroexpansion in wood is assumed to be orthotropic. Linear orthotropic hygroexpansion $\boldsymbol{\epsilon}^s$ can be expressed in terms of moisture change as

$$\boldsymbol{\epsilon}^s = \begin{pmatrix} \alpha_L \\ \alpha_R \\ \alpha_T \\ 0 \\ 0 \\ 0 \end{pmatrix} \Delta w \tag{2.17}$$

where α_i are the hygroexpansion coefficients in the three principal orthotropic directions and Δw is the change in moisture content. This relation is valid below the fibre saturation point. The constitutive relations, including the hygroexpansion strains, are obtained by inserting Eq.(2.16) into Eq.(2.7), yielding

$$\boldsymbol{\sigma} = \mathbf{D}\boldsymbol{\epsilon} - \mathbf{D}\boldsymbol{\epsilon}^s \tag{2.18}$$

If the principal orthotropic directions do not coincide with the global coordinate system, the transformation matrix $\mathbf{G}$ used in Eq.(2.14) must be employed, resulting in

$$\hat{\boldsymbol{\sigma}} = \mathbf{G}^T\mathbf{D}\,\mathbf{G}\,\hat{\boldsymbol{\epsilon}} - \mathbf{G}^T\mathbf{D}\boldsymbol{\epsilon}^s \tag{2.19}$$

Table 2.4: *Typical values of hygroexpansion coefficients of Spruce.*

Parameter	Measurements Ref. [35]
α_L	0.00 - 0.02
α_R	0.17 - 0.22
α_T	0.33 - 0.40

The stresses $\hat{\boldsymbol{\sigma}}$ and the strains $\hat{\boldsymbol{\epsilon}}$ refer to the global coordinate system whereas $\mathbf{D}$ and $\boldsymbol{\epsilon}^s$ are given in the local material coordinate system. The volumetric shrinkage from the green to the dry condition is about 10% with a linear relationship between the volumetric shrinkage and the moisture content from a moisture content of approximately 25% to 0%, Kollman [35], the change in volume ΔV between two specific moisture contents, can within this range be calculated as

$$\Delta V = 0.4 \Delta w V_0 \tag{2.20}$$

where V_0 is the volume in a dry condition and Δw is the change in moisture content. This relation can be useful for calculating densities for volumes defined under different moisture conditions.

The magnitude of the hygroexpansion coefficients in spruce is dependent upon the moisture content and also on the location within the stem. The dimensional changes due to moisture changes are largest in the tangential direction and lowest in the longitudinal direction. Typical hygroexpansion coefficients for spruce are shown in table 2.4. It should be noted that negative longitudinal hygroexpansion coefficients have also been reported, see Kollman [35].

2.4. Properties of Fibres and the Fibre wall

The mechanical properties of individual fibres have not been studied very thoroughly. There are very large variations in the mechanical properties of fibres. Fibres can be divided into two major categories: untreated fibres with their original properties, such as in wood, and treated fibres such as those found in paper. Untreated fibres found in the stem include both earlywood fibres with a relatively thin S_2-layer and latewood fibres with an S_2-layer that is thick in relation to the total thickness of the fibre wall. The fibres in paper are either chemical or mechanical pulps although there is often a mixture of both. In chemical pulp, the fibres are separated by dissolving the lignin by chemical means. In mechanical pulp, the fibres are separated by mechanical processes such as refining or grinding.

The stiffness and shrinkage properties of the fibres in paper depend on several factors. First, the fibres in trees differ due to genetic factors and the growing conditions when the fibres were formed. The factors influencing this include, the tree species from which the fibres originate, the location of the fibre within the tree and tension/compression during growth. Secondly, during the pulping and paper-making processes the original properties of the fibres are changed. The pulping process affects such things as the chemical composition and the morphology of the fibre walls, the collapse of fibres, reduction in fibre length and development of fines, curling and kinking, see Mohlin [44] and Paavilainen [55]. What changes occur depends on how the fibres are treated, both chemically and mechanically. The chemical pulping process dissolves almost all layers of the fibre structure except the S_2-layer. The chemical composition and the properties of the chemical constituents are also affected. The mechanical pulping process produces a greater degree of change in the morphology of the fibre.

Due to the various matters just mentioned, the stiffness and shrinkage properties of fibres vary to a high degree. Measurements must thus be made on very large numbers of fibres so as to adequately characterize their properties and distribution. However, due to the difficulties involved in measuring on such a small scale, the amount of experimental data on the stiffness of fibres found in the literature is very limited. Some measurements of the modulus of elasticity of fibres in the longitudinal direction are reported in the literature. Page et al. [53] measured the longitudinal stiffness of individual chemical pulp fibres as a function of the microfibril angle of the S_2-layer, showing that the stiffness decreased with an increase in microfibril angle, Figure 2.12.

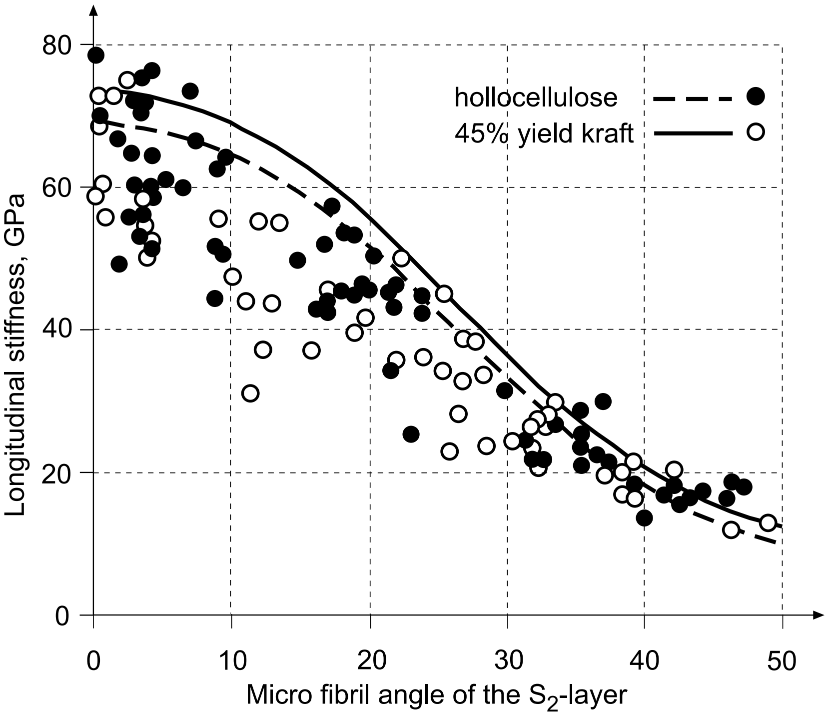

Figure 2.12: *Longitudinal stiffness of single wood pulp fibres as a function of the microfibril angle of the* S_2*-layer, from Page et al. [53].*

There is little experimental data available for the radial and tangential directions. Bergander [8] has performed measurements on native wood fibres to determine the stiffness properties of the radially oriented fibre wall in tension. The results of these measurements range from about 700 MPa to 3000 MPa for different fibres. The transverse stiffness in compression has been measured by Hartler et al. [25] for sulfite and sulfate pulp fibres, being found to be about 600 MPa.

2.5. Properties of Chemical Constituents

2.5.1. General remarks

As mentioned earlier, the chemical constituents of the cell wall are cellulose, hemicellulose and lignin. Several investigations aimed at determining the stiffness properties and shrinkage coefficients of these constituents have been carried out, from which the properties presented in this section have been adapted. Some of the stiffness parameters referred to in the following are measured values, some are calculated from molecular models and the remaining ones are estimated on the basis of the behaviour of similar materials. The values given here will be employed as a first estimate in structural modelling of wood and fibres. Some of these values are questionable, and are discussed further later in the thesis. There are problems involved in measuring the properties of the chemical constituents of wood. For example, during the process of isolating lignin and hemicelluloses from wood, changes in the molecular structure occur which influence the properties. More and better experimental stiffness and shrinkage data for all three constituents are needed.

2.5.2. Stiffness properties of cellulose

Native cellulose, i.e. cellulose of form I, is a highly crystalline material having stiffness properties that are considered to be independent of moisture changes. Some investigations show that cellulose is anisotropic but here it is assumed that cellulose can be regarded as being a transversely isotropic material. A transversely isotropic material is isotropic in one plane and has a different stiffness in the direction normal to this plane. Cellulose has a high stiffness in the longitudinal fibril direction and can be regarded as isotropic with respect to directions in the plane crossing the fibril direction. The stiffness matrix can for a symmetric transversely isotropic material, in which the 23-plane is isotropic, be written as

$$\boldsymbol{D}_C = \begin{bmatrix} D_{11} & D_{12} & D_{12} & 0 & 0 & 0 \\ D_{12} & D_{22} & D_{23} & 0 & 0 & 0 \\ D_{12} & D_{23} & D_{22} & 0 & 0 & 0 \\ 0 & 0 & 0 & D_{44} & 0 & 0 \\ 0 & 0 & 0 & 0 & D_{44} & 0 \\ 0 & 0 & 0 & 0 & 0 & \frac{1}{2}(D_{22} - D_{23}) \end{bmatrix} \qquad (2.21)$$

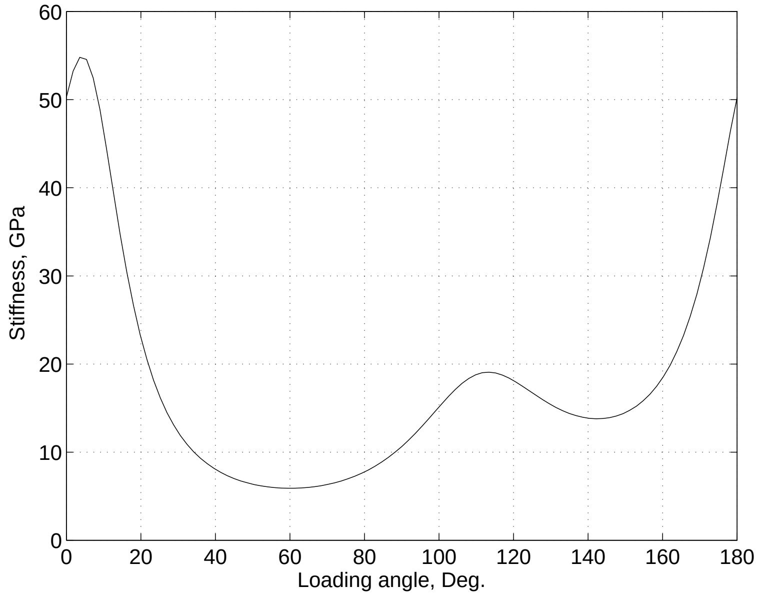

Figure 2.13: *Uniaxial stiffness of cellulose in cross longitudinal directions versus direction of loading in the cross directional plane, data from Tashiro et al. [68].*

where the components of $\boldsymbol{D}_C$ are found by inverting a matrix similar to the one given in Eq.(2.5) but expressed in a 123-coordinate system according to Figure 2.5. A transversely isotropic material thus has five independent stiffness coefficients. The five coefficients chosen here are two moduli of elasticity, one modulus of shear and two Poisson's ratios.

The modulus of elasticity in the longitudinal direction E_{11} has been determined experimentally, Sakurada et al. [60], Nishino et al. [47] and Matsuo et al. [43] and been estimated by molecular modelling by Tashiro et al. [67],[68]. The measurements were made by loading cellulose fibres and measuring the crystal elongation by x-ray diffraction. As pointed out by Mark [41], the values obtained from x-ray diffraction measurements are probably somewhat too low since the load is applied in the longitudinal fibre direction and thus deviates somewhat from the directions of the cellulose chains in the fibre wall. The properties obtained from molecular models are probably too high since they are calculated at low temperatures, where the thermal motion of the molecules are neglected. The stiffness parameters in the cross longitudinal direction, the moduli in shear and the Poisson's ratios have been estimated through molecular modelling by Mark [42], Tashiro et al. [67],[68] and have also been estimated by Cave [12]. Tashiro et al. [68] determined the full three-dimensional elastic stiffness matrix for cellulose. The calculated material stiffness for cellulose microfibrils was found to be anisotropic. Figure 2.13 shows the calculated stiffness of cellulose normal to the longitudinal direction for varying angles of loading in the cross longitudinal plane. If the microfibrils are oriented randomly around the longitudinal axis in the cell wall, the mean cross directional stiffness will be the mean value of the function shown in Figure 2.13, yielding E_{22}=17.7 GPa.

Table 2.5: *Stiffness coefficients of native cellulose.*

Coefficient	Value	Method and Reference
E_{11}, GPa	135	Measured, Sakurada et al. [60]
	138	Measured, Nishino et al. [47]
	140	Measured, Matsuo et al. [43]
	168	Molecular model, Tashiro et al. [68]
E_{22}, GPa	17.7	Molecular models, Tashiro et al. [68]
	27	Molecular model, Mark [41]
	18	Estimated, Cave [12]
G_{12}, GPa	4.4	Molecular model, Mark [41]
	5.1	Molecular model, Tashiro et al. [68]
ν_{21}	0.011	Molecular model, Mark [41]
	<0.005	Molecular model, Tashiro et al. [68]
	0.047	Estimated, Cave [12]
ν_{32}	0.52	Molecular model, Tashiro et al. [68]
	0.48	Estimated, Cave [12]

The moduli of shear can be evaluated in the same manner, arriving at $G_{12}=G_{13}=5.1$ GPa and $G_{23}=5.8$ GPa. In Table 2.5 stiffness coefficients for cellulose that are found in the literature are shown.

As already indicated, the fact that cellulose contains small amorphous regions that can absorb water and change the stiffness properties somewhat is not considered in the present study. Table 2.6 shows the range of stiffness coefficients chosen for the cellulose used for modelling purposes later in the study.

Table 2.6: *Range of stiffness coefficients of cellulose employed in this study.*

Coefficient	Value
E_{11}, GPa	130.0 - 170
E_{22}, GPa	15.0 - 20.0
G_{12}, GPa	3.0 - 6.0
ν_{21}	0.01
ν_{32}	0.50

2.5.3. Stiffness properties of hemicellulose

Hemicelluloses are materials strongly affected by moisture changes, their stiffness properties decreasing with increasing moisture content up to the point of saturation. Cousins [14] measured the stiffness of isolated hemicellulose at various moisture contents by use of a ball indentation test. During the isolation of hemicellulose,

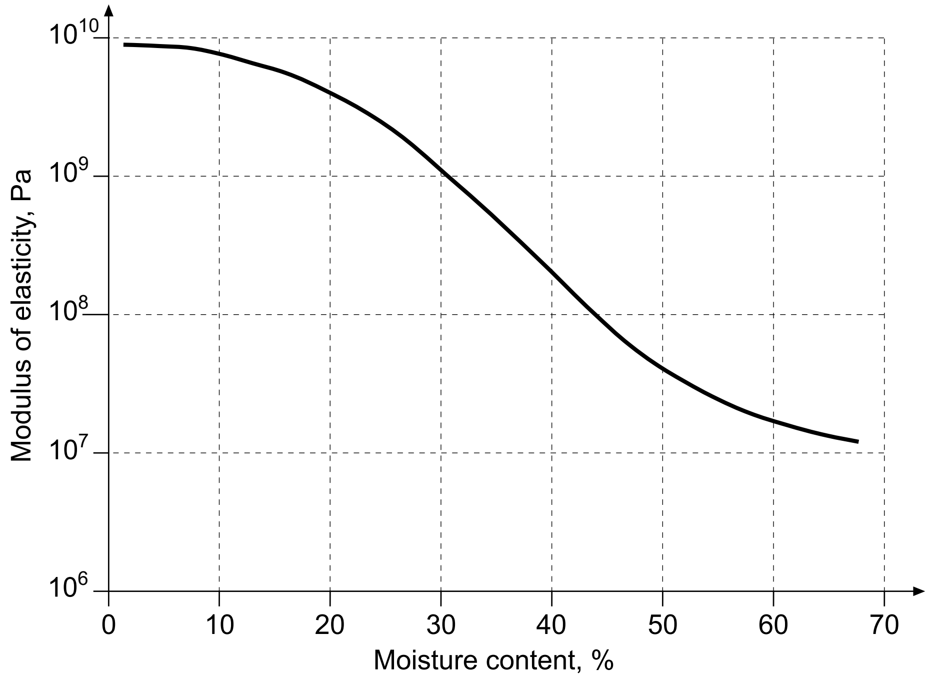

Figure 2.14: *Modulus of elasticity of hemicellulose at different moisture contents, from Cousins [14].*

there is an unknown alteration of the molecular arrangement, the material behaviour becoming isotropic. As pointed out by Cousins, the hemicellulose molecules tend to be aligned with the cellulose chains, suggesting that the material can be regarded as transversely isotropic, allowing it to be described by five coefficients. The modulus of elasticity of isolated hemicellulose at different moisture contents is shown in Figure 2.14, based on measurements by Cousins. The modulus of elasticity ranges from 8 GPa at a low moisture content down to about 10 MPa at a moisture content of about 70%. In the modelling part of this thesis, the properties of wood are determined at a moisture content of 12%, corresponding to wood conditioned at a relative humidity of 60 %. The moisture content of isolated hemicellulose as a function of the relative humidity was measured by Cousins [14], see Figure 2.15. From the results of Cousins, shown in Figure 2.14 and 2.15, the modulus of elasticity of isolated hemicelluloses at 60 % RH can be determined to be about 4.5 GPa. Since hemicellulose is assumed to be transversely isotropic, the longitudinal modulus of elasticity must be higher and the cross directional stiffness lower than 4.5 GPa. On basis of the measurements by Cousins, Cave [12] suggested the moisture dependent three-dimensional elastic

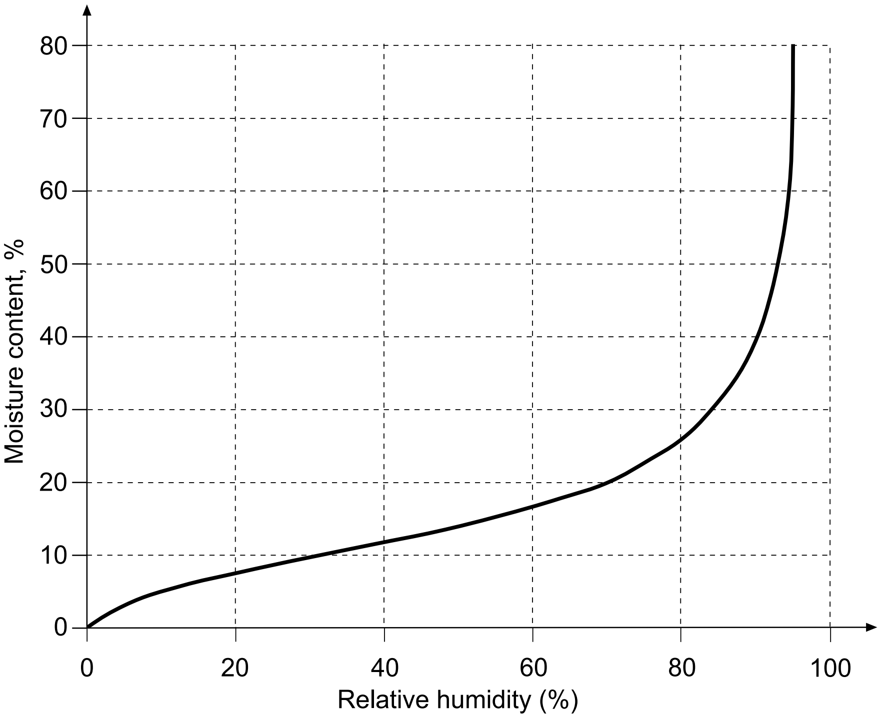

Figure 2.15: *Moisture content of isolated hemicellulose at different RH values, from Cousins [14].*

stiffness matrix $\mathbf{D}_H(w)$ for hemicellulose to be

$$\boldsymbol{D}_H(w) = \begin{bmatrix} 8 & 2 & 2 & 0 & 0 & 0 \\ 2 & 4 & 2 & 0 & 0 & 0 \\ 2 & 2 & 4 & 0 & 0 & 0 \\ 0 & 0 & 0 & 1 & 0 & 0 \\ 0 & 0 & 0 & 0 & 1 & 0 \\ 0 & 0 & 0 & 0 & 0 & 1 \end{bmatrix} c_H(w)\, GPa \tag{2.22}$$

where $c_H(w)$ is a moisture dependent function fitted to the experimental data reported by Cousins [14] that is shown in Figure 2.14. The longitudinal stiffness was assumed to be twice the cross-directional stiffness. In the thesis, several stiffness values will be employed in the modelling and stiffness values giving higher degree of orthotropy than two, as was suggested by Cave, will be examined. Table 2.7 shows the range of stiffness coefficients chosen for hemicellulose at 60% RH, used for modelling purposes later in the study.

2.5.4. Stiffness properties of lignin

Lignin is an amorphous material regarded as having isotropic stiffness properties that are moisture dependent. The stiffness of an isotropic material can be described by two coefficients. Here one modulus of elasticity and one Poisson's ratio are chosen to represent the stiffness. The modulus of elasticity of isolated lignin has been measured

Table 2.7: *Range of stiffness coefficients of hemicellulose at 60% RH employed in this study.*

Coefficient	Value
E_{11}, GPa	14.0 - 18.0
E_{22}, GPa	3.0 - 4.0
G_{12}, GPa	1.0 - 2.0
ν_{21}	0.1
ν_{32}	0.40

by Srinivasan [64] and Cousins [13], the latter author also having characterized its moisture dependency. Srinivasan measured the modulus of elasticity of air dried lignin to 2.0 GPa on rods of electrochemically prepared lignin that also contained hemicellulose in small amounts. The modulus of elasticity of isolated periodate lignin at different moisture contents, obtained from measurements by Cousins [13], is shown in Figure 2.16. The modulus of elasticity was measured to 5.5 GPa at a low moisture content, increasing to 6.5 GPa at a 4% moisture content and decreasing to about 3 GPa at a moisture content of 20% or higher. In the modelling part of the thesis, the properties of wood at a moisture content of 12% are of primary interest. The moisture content of isolated lignin as a function of relative humidity

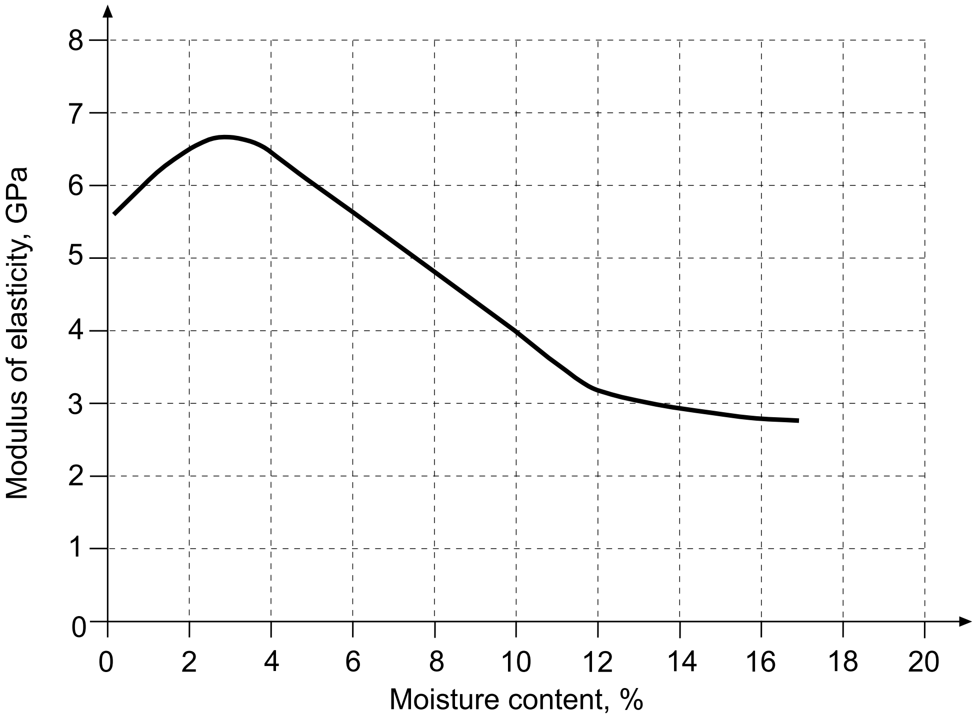

Figure 2.16: *Modulus of elasticity of lignin at different moisture contents, from Cousins [13].*

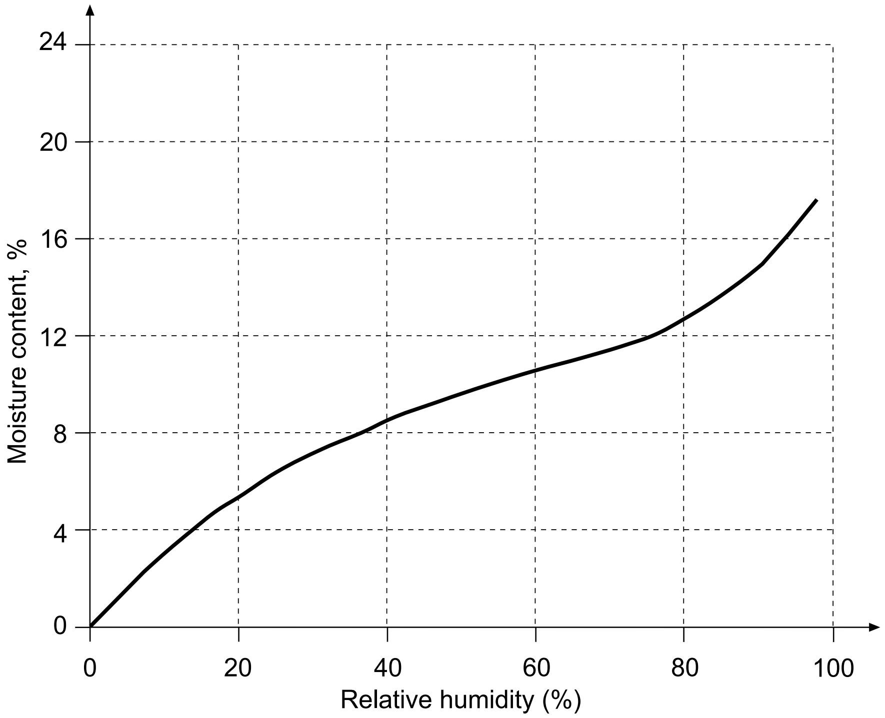

Figure 2.17: *Moisture content of isolated lignin at different RH values, from Cousins [13].*

was measured by Cousins [13], see Figure 2.17. From the results shown in Figures 2.16 and 2.17, the modulus of elasticity of periodate lignin at 60% RH can be determined to be about 3.5 GPa.

On the basis of measurements reported by Cousins, Cave [12] suggested the moisture-dependent elastic stiffness matrix $\mathbf{D}_L(w)$ for lignin to be

$$\mathbf{D}_L(w) = \begin{bmatrix} 4 & 2 & 2 & 0 & 0 & 0 \\ 2 & 4 & 2 & 0 & 0 & 0 \\ 2 & 2 & 4 & 0 & 0 & 0 \\ 0 & 0 & 0 & 1 & 0 & 0 \\ 0 & 0 & 0 & 0 & 1 & 0 \\ 0 & 0 & 0 & 0 & 0 & 1 \end{bmatrix} c_L(w)\, GPa \tag{2.23}$$

where $c_L(w)$ is a moisture-dependent function fitted to the experimental data that Cousins [13] reported, shown in Figure 2.16. Table 2.8 shows the range of stiffness coefficients chosen for lignin and used for modelling purposes later in the study.

2.5.5. Hygroexpansion properties of the chemical constituents

The hygroexpansion properties of the chemical constituents of wood have, to the authors knowledge, not been studied experimentally. Cave [12] has estimated the hygroexpansion properties of hemicellulose and lignin. Cellulose is assumed to be independent of moisture changes and therefore not shrink or swell due to variations

Table 2.8: *Range of stiffness coefficients of lignin at 60% RH employed in this study.*

Coefficient	Value
E, GPa	2.0 - 3.5
ν	0.33

in moisture content. For hemicellulose, Cave [12] assumed that no shrinkage occurs in the longitudinal direction and that in the cross-longitudinal plane the shrinkage is isotropic. According to Cave [12], the hygroexpansion strain for hemicellulose is approximated by

$$\Delta\boldsymbol{\epsilon}^{s}_{H} = \begin{bmatrix} 0 \\ {}^{1}/_{2} \\ {}^{1}/_{2} \\ 0 \\ 0 \\ 0 \end{bmatrix} \epsilon^{\circ}_{H}(\Delta w_b) \tag{2.24}$$

and the hygroexpansion strain for lignin is assumed to be isotropic as

$$\Delta\boldsymbol{\epsilon}^{s}_{L} = \begin{bmatrix} {}^{1}/_{3} \\ {}^{1}/_{3} \\ {}^{1}/_{3} \\ 0 \\ 0 \\ 0 \end{bmatrix} \epsilon^{\circ}_{L}(\Delta w_b) \tag{2.25}$$

The parameters $\Delta\epsilon^{\circ}_{H}$ and $\Delta\epsilon^{\circ}_{L}$ are related to the volumetric shrinkage of hemicellulose and lignin, respectively. These two parameters are functions of w_b which are the bound fractions of the sorbed water w. Cave [12] suggests that the volumetric shrinkage be set equal to the volume of released bound water. The parameters are directly coupled then to the volume of water absorbed by the hemicellulose and the lignin, respectively. The parameters can be written then as

$$\begin{aligned} \epsilon^{\circ}_{H}(\Delta w_b) &= \Delta w_{bH}(w_b) \\ \epsilon^{\circ}_{L}(\Delta w_b) &= \Delta w_{bL}(w_b) \end{aligned} \tag{2.26}$$

where Δw_{bH} and Δw_{bL} are the change in the bound water content of the hemicellulose and the lignin, respectively. A scaling constant b, which is introduced, determines the relation between the moisture content w and the bound water fraction w_b, where

$$w_b = b\, w \tag{2.27}$$

The scaling constant b is less than 1 if the hygroexpansion is less than the volume of water released.

Since cellulose is not considered to absorb water, the bound water w_b in the wood needs to be divided between the hemicellulose and the lignin. The bound water w_b is suggested by Cave [12] to be partitioned between the hemicellulose and lignin in the ratio of 2.6:1, so that

$$\Delta w_{b_H} = 2.6 \Delta w_{b_L} \tag{2.28}$$

The change in the total amount of bound water can be written as

$$\Delta w_b = f_H \Delta w_{b_H} + f_L \Delta w_{b_L} \tag{2.29}$$

where f_H and f_L are the weight fractions of hemicellulose and lignin in wood. By combining Eqs (2.26), (2.27), (2.28) and (2.29), one can write

$$\begin{aligned} \epsilon_H^{\circ}(\Delta w_b) &= b\, \frac{2.6}{f_L + 2.6 f_H} \Delta w \\ \epsilon_L^{\circ}(\Delta w_b) &= b\, \frac{1}{f_L + 2.6 f_H} \Delta w \end{aligned} \tag{2.30}$$

According to Dinwoodie [20], the weight fractions of hemicellulose and lignin are set to f_L=30% and f_H=25%. The constant b is here set to 1, all the sorbed water in the cell wall being assumed to be bound water. Substituting Eqs (2.30) into Eqs (2.24) and (2.25) yields

$$\Delta \boldsymbol{\epsilon}_H^s = \boldsymbol{\alpha}_H (\Delta w) \tag{2.31}$$

$$\Delta \boldsymbol{\epsilon}_L^s = \boldsymbol{\alpha}_L (\Delta w) \tag{2.32}$$

where

$$\boldsymbol{\alpha}_H = \begin{bmatrix} 0 \\ {}^1\!/_2 \\ {}^1\!/_2 \\ 0 \\ 0 \\ 0 \end{bmatrix} \cdot \frac{2.6}{0.30 + 2.6 \cdot 0.25} = \begin{bmatrix} 0 \\ 1.368 \\ 1.368 \\ 0 \\ 0 \\ 0 \end{bmatrix} \tag{2.33}$$

$$\boldsymbol{\alpha}_L = \begin{bmatrix} {}^1\!/_3 \\ {}^1\!/_3 \\ {}^1\!/_3 \\ 0 \\ 0 \\ 0 \\ 0 \end{bmatrix} \cdot \frac{1}{0.30 + 2.6 \cdot 0.25} = \begin{bmatrix} 0.351 \\ 0.351 \\ 0.351 \\ 0 \\ 0 \\ 0 \end{bmatrix} \tag{2.34}$$

The hygroexpansion coefficients as determined in Eqs (2.33) and (2.34) will be used later in the modelling of cell wall hygroexpansion.

2.6. Relation Between Mechanical Properties, Density and Microfibril Angle

As discussed earlier in this chapter, the modulus of elasticity depends on the microfibril angle in the S$_2$-layer that varies considerably along the radius of the tree. For normal wood, the angle is large in the juvenile wood and considerably smaller in the mature wood. Although this angle is difficult to measure, it is essential to know its value when modelling the mechanical properties of wood. One of the basic ideas in the present study is that the mechanical properties of wood are governed primarily by the density and by the microfibril angle of the S$_2$-layer. The microfibril angle, however, is much more difficult to measure than measuring the density and the longitudinal modulus of elasticity. Finding an approximate formula for estimating the microfibril angle on the basis of measured values for the density and the longitudinal modulus of elasticity would be of great aid in further micromechanical modelling.

Since it is assumed here that a unique relation exists between the density, the longitudinal modulus of elasticity and the microfibril angle, it should be possible to formulate this relationship in a simple approximate way. Making certain assumptions regarding the stiffness of the S$_2$-layer and employing the transformation rule given in Eq.(2.14), one can show that

$$cos(\varphi) \approx \left(\frac{\dfrac{\rho_o}{\beta \rho_r} \dfrac{E_L}{D_{11}^{S_2}} - 0.13}{0.872} \right)^{1/4} \tag{2.35}$$

where E_L is the longitudinal modulus of elasticity, ρ_r is the average density and φ is the average microfibril angle of the S$_2$-layer. In addition, the constant ρ_o is the cell wall bulk density, the constant β is the fraction of the wood mechancially active in the longitudinal direction, and the constant $D_{11}^{S_2}$ is the stiffness of the S$_2$-layer in the longitudinal microfibril direction. These three constants are chosen as ρ_o=1500 kg/m^3, β =0.77 and $D_{11}^{S_2}$=74.0 GPa. The detailed derivation of Eq.(2.35) and the motivation for the choice of the values of the three constants just given are provided in Appendix A. The relationship shown in Eq.(2.35) can be rewritten for an unknown longitudinal modulus of elasticity as

$$E_L \approx \frac{\beta \rho_r}{\rho_o} D_{11}^{S_2} \left(0.872 \ \cos^4(\varphi) + 0.13 \right) \tag{2.36}$$

In Figure 2.18 the longitudinal modulus of elastictity as obtained using Eq.(2.36) is shown in varying the microfibril angle from 0° to 45° and the density from 350 to 550 kg/m^3. As already indicated, earlier, the microfibril angle is about 10° for normal wood and it can be as high as 45° for juvenile wood and compression wood. The longitudinal modulus of elastictity otained, as shown in Figure 2.18, varies from about 4 GPa for large microfibril angles and low density to about 20 GPa for small

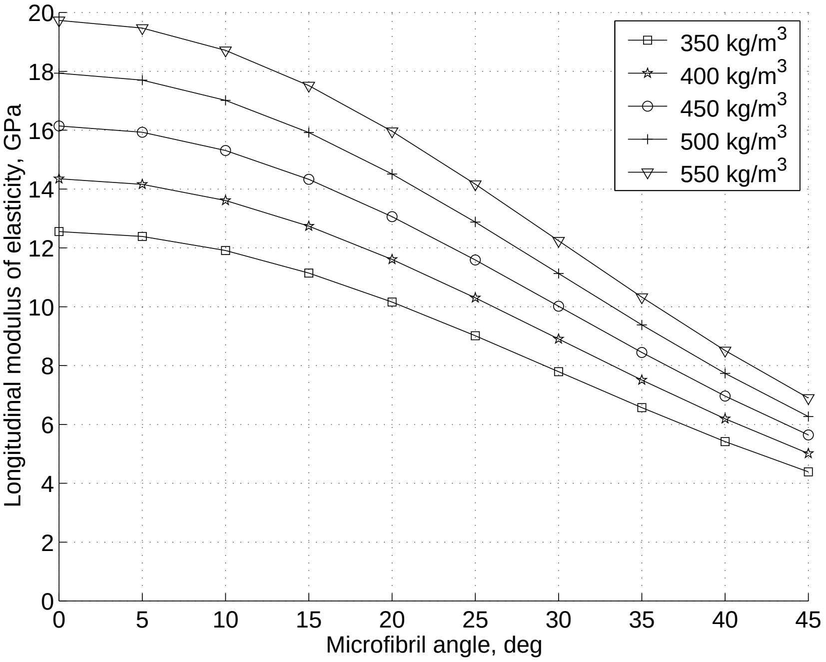

Figure 2.18: *Simplified theoretical relation between the longitudinal modulus of elasticity, the density and the microfibril angle of the S_2-layer.*

microfibril angles and high density. The results shown are values commonly found for spruce wood. Although Eq.(2.35) is only an approximate estimate, the results indicate that the variation in the mechanical properties of wood may be very large. Obviously, further study of the relationship between the microfibril angle, density and the mechanical properties of wood is highly important.

3. EXPERIMENTAL DETERMINATION OF WOOD PROPERTIES

3.1. Experimental Introduction

The experiments to be presented in this chapter are of two categories, those at a microstructural level and those for the testing of clear-wood specimens. The experiments at the microstructural level provide an understanding of how the microstructure is built up and of how it behaves under loading. A characterization of the microstructure is presented in Section 3.2. A study of deformations in the microstructure due to loading is presented in Section 3.3. Testing of clear wood aims at determining the mechanical parameters and their dependency upon the position in the trunk. The experimental setup and results of testing are presented in Section 3.4. From measurements at the micro- and macroscopical levels, certain important relationships are established. These are discussed in Section 3.5 and are later used for modelling the mechanical parameters of wood.

The specimens used in the investigation were taken from a total of 11 trees (Norway spruce) sampled at four different sites of differing site quality classes in the area of Värnamo in southern Sweden. The trees were sampled by Nilsson [46], who also made tree and site measurements at the sample plots. The height, type of crown, social class and individual position were determined for each of the standing trees. On every plot, samples were obtained from trees belonging to each of the social classes dominant, co-dominant and dominated, except for one plot where no dominated trees were found. After the trees were felled, the type and distribution of the knots were determined. Two discs were cut at three different heights from each tree, as shown in Figure 3.1. Specimens for mechanical testing were taken from the discs labelled A and specimens for the experiments at the microstructural level from the discs labelled B.

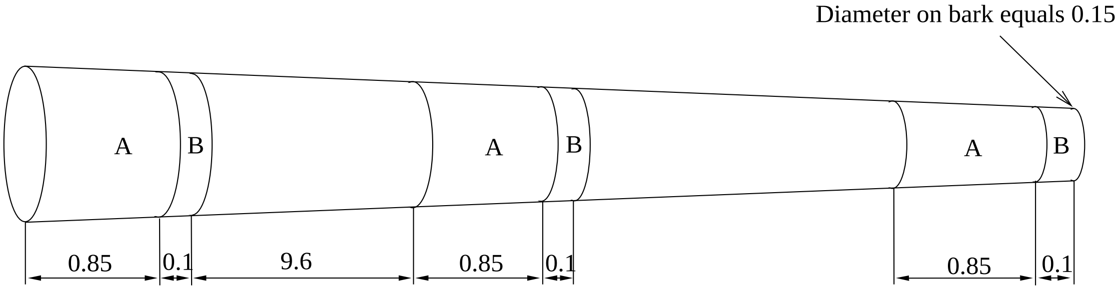

Figure 3.1: *Cutting scheme for the stem. The discs labelled A were used for mechanical testing and the discs labelled B for microstructural measurements.*

3.2. Measurements for Wood Structure Characterization

Measurements at the microstructural level were performed at the Norwegian Forest Research Institute, Kučera [38]. Results and a brief description of the experimental setup are presented here.

An aim of the microstructural measurements was to describe how the microstructure is built up and to attempt to describe it in terms of a few key parameters only. The experimental data will be presented in the way they are to be used later in the microstructural modelling.

In each of the discs labelled B in Figure 3.1, measurements of the growth rings and of the cell properties were made from pith to bark in the north direction. In each growth ring, the following parameters were measured:

- Growth ring width
- Width of the earlywood and latewood regions
- Number of cells in the earlywood and latewood regions
- Width of the cells in the tangential direction
- Ray-cell content

In every third growth ring measurements were also obtained of the following:

- Density and moisture content.
- Cell length

A total of 2300 growth rings were examined. Since no clear definition of transitionwood exists only the widths of the earlywood and the latewood were measured, the definition proposed by Mork [45] being employed. This definition states that the latewood cells are those in which twice the cell wall thickness is greater than the width of the lumen as measured in the radial direction. Specimens were prepared by cutting thin, 35-40μm sheets in the RT-plane by a microtome. The specimens were placed on a slide and were projected onto a screen with a magnification factor of 618. The geometric properties were then measured at a 1 mm resolution by use of a ruler. The precision of the measurements was thus about 1/618 mm. Both the average width of the cells in the tangential direction and the ray cell content were determined by measuring the distance and counting the number of cells between 20 successive rays in each growth ring. The average tangential cell width was determined then by dividing the distance measured by the number of cells between the rays.

Due to the large amount of work involved, the density and the cell length measurements were determined for individual growth ring samples at each third growth ring only. The samples for the density measurements were cut from the discs with a razor-blade knife. The volume was measured by weighing the samples in water at high precision, the weight being determined under both saturated and dry conditions. The density was determined then at dry and saturated conditions and the moisture content at the green condition. The samples for the cell length measurements were also cut from the discs with a razor-blade knife into small pieces of wood about 1x1x10 mm^3 in size. The fibres were disintegrated chemically then by storing the samples in a solution of acetic acid and hydrogen peroxide for 48 hours. The length of 20 separate fibres was determined for each growth ring, using a computer and a digitiser board.

3.2.1. Experimental result of wood structure characterization

In Figures 3.2-3.7 the results of the measurements are shown in relation to the growth ring number from the pith to the bark. The variation in the measured data in the radial direction of the cross section of the stem can be revealed in this way. In Figure 3.2 the variation in growth ring width versus growth ring number is shown. The measurements indicate there to be a larger number of wide growth rings near the pith.

In Figure 3.3 the width of the earlywood region in each growth ring is shown from the pith to the bark. Due to the latewood region being small, the width of the earlywood is close to the width of the whole growth ring.

In Figure 3.4 the width of the latewood region in each growth ring from the pith to the bark is shown. The latewood region is more constant in width than the earlywood, but a slight tendency towards the latewood regions being wider near the pith is discernible.

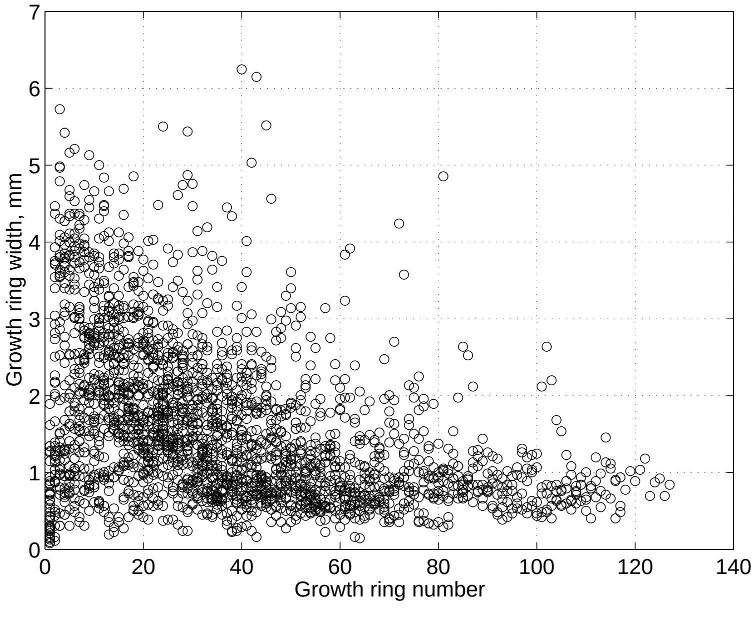

Figure 3.2: *Growth ring widths versus ring number from pith to bark.*

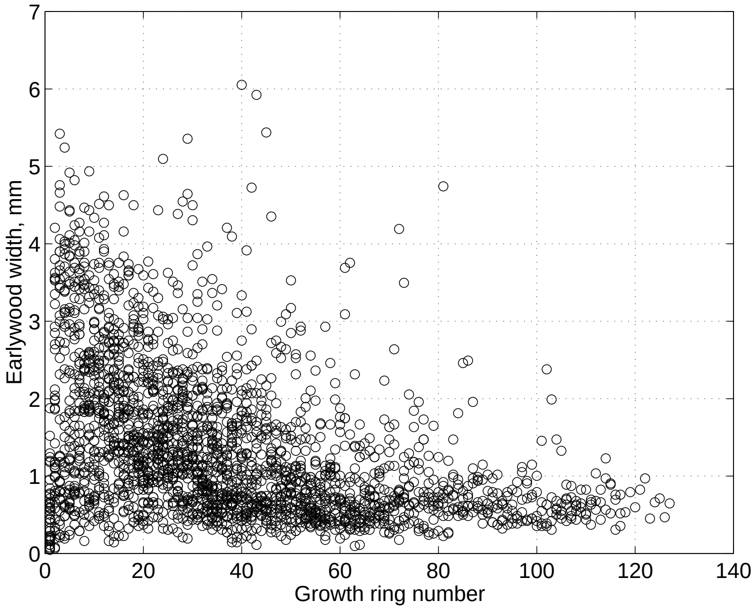

Figure 3.3: *Width of the earlywood region versus ring number from pith to bark.*

In Figure 3.5 the density of each third growth ring from the pith to the bark in all trees at all heights is shown. The density shown is determined from the weight in the dry condition and the volume in a saturated condition. A slight increase in density in the radial direction from the pith to the bark was found.

The width of the cells in the tangential direction at each growth ring is shown in Figure 3.6. The tangential cell width is considerably less in juvenile wood near the pith than in the mature wood.

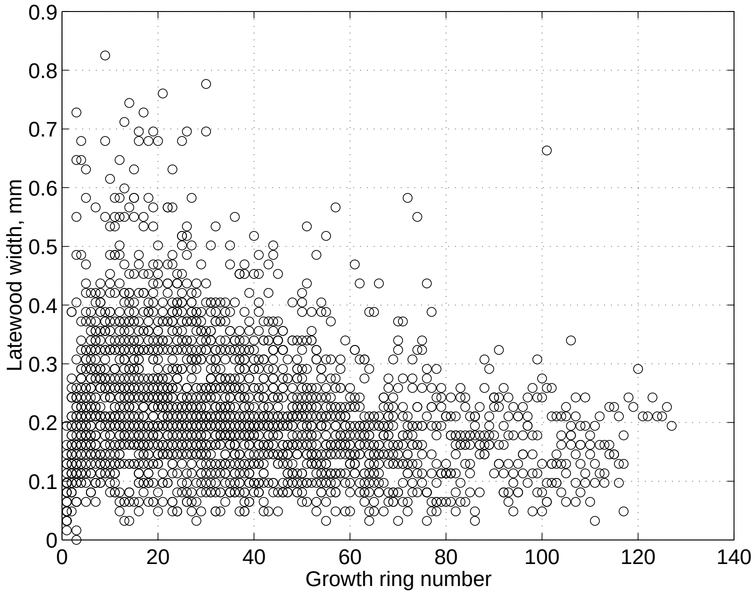

Figure 3.4: *Width of the latewood region versus ring number from pith to bark.*

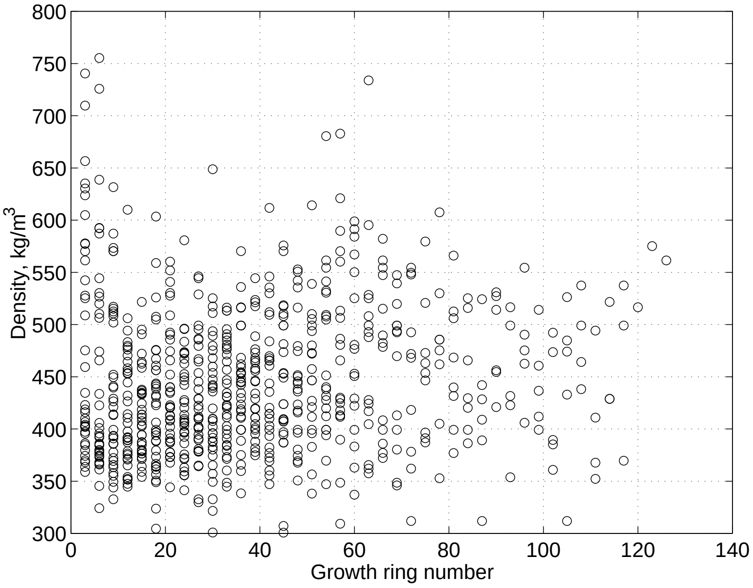

Figure 3.5: *Density of growth rings versus ring number from pith to bark.*

The length of the cells in the longitudinal direction at each third growth ring is shown in Figure 3.7. The measured mean value of the cell length of the samples was 2.9 mm.

3.2.2. Earlywood width and number of earlywood cells in growth ring

The width of the earlywood region in the growth rings was found to correlate very well with the growth ring width, see Figure 3.8. This was expected, since earlywood

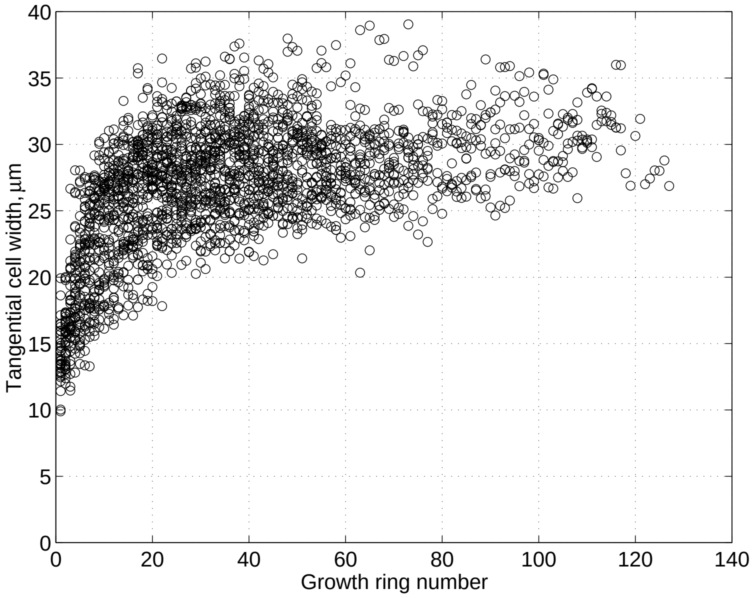

Figure 3.6: *Tangential width of cells versus ring number from pith to bark.*

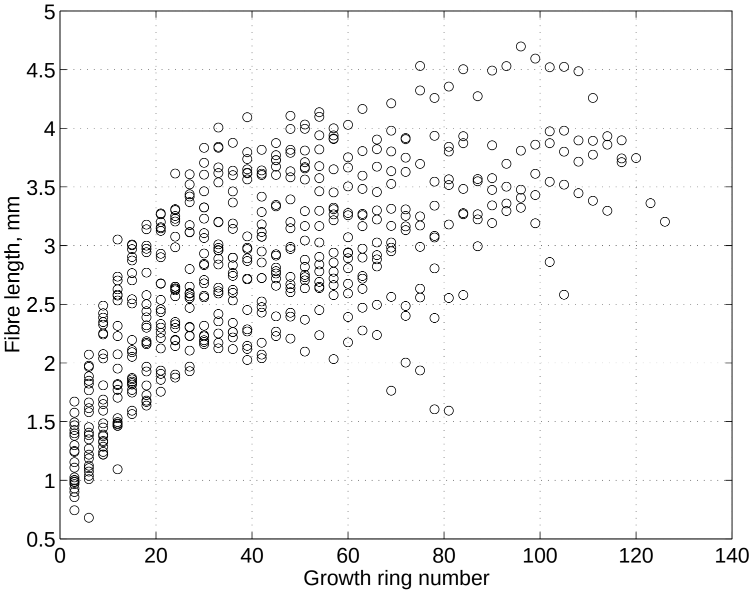

Figure 3.7: *Length of the cells versus ring number from pith to bark.*

makes up the major part of the growth ring. For some growth rings, a one-to-one relationship was found, due to the latewood part being absent.

Figure 3.9 indicates the relationship between the number of earlywood cells and the width of the earlywood. For small growth ring widths, the correlation is better than for larger growth ring widths.

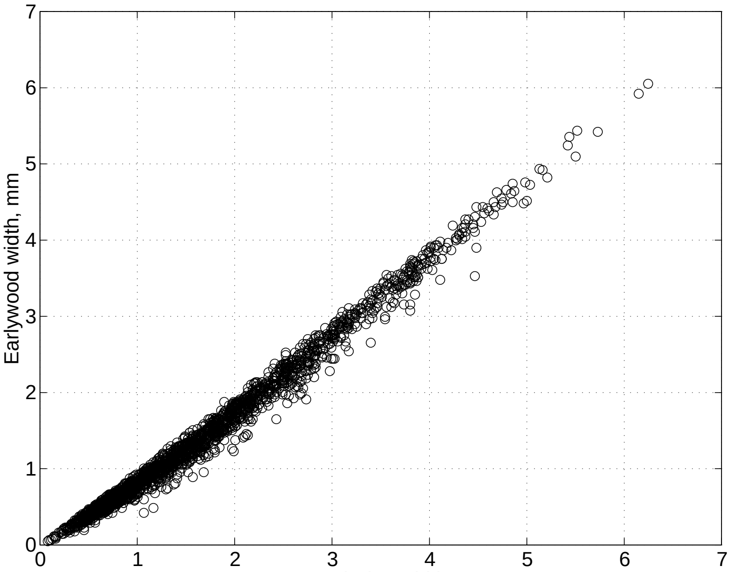

Figure 3.8: *Width of the earlywood region versus the growth ring width.*

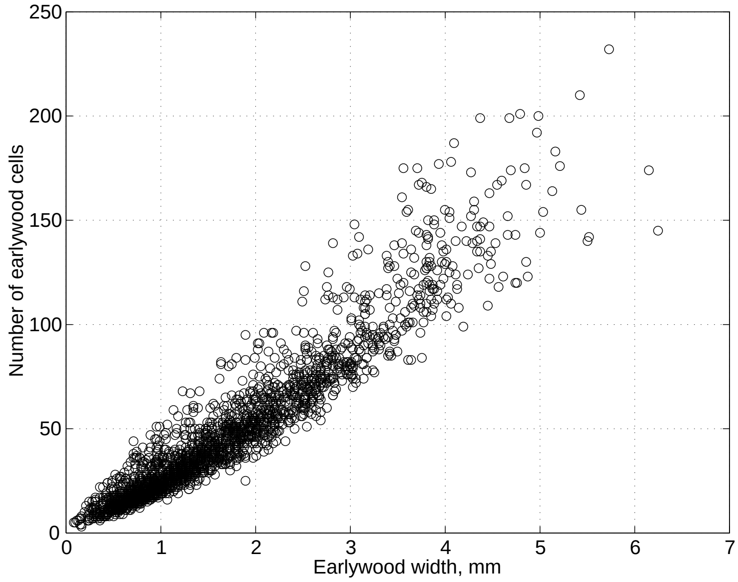

Figure 3.9: *Number of earlywood cells versus width of the earlywood region.*

3.2.3. Latewood width and number of latewood cells in growth ring

The latewood width and the growth ring width showed a low correlation, see Figure 3.10. Since this relationship is weak, the assumption is made that the latewood width can be considered as independent of the growth ring width. The latewood width is thus treated simply as a constant. In Figure 3.11 the distribution of the latewood width is shown, the mean of which was 0.223 mm and the median 0.195 mm. A constant latewood width of 0.20 mm was used in the modelling.

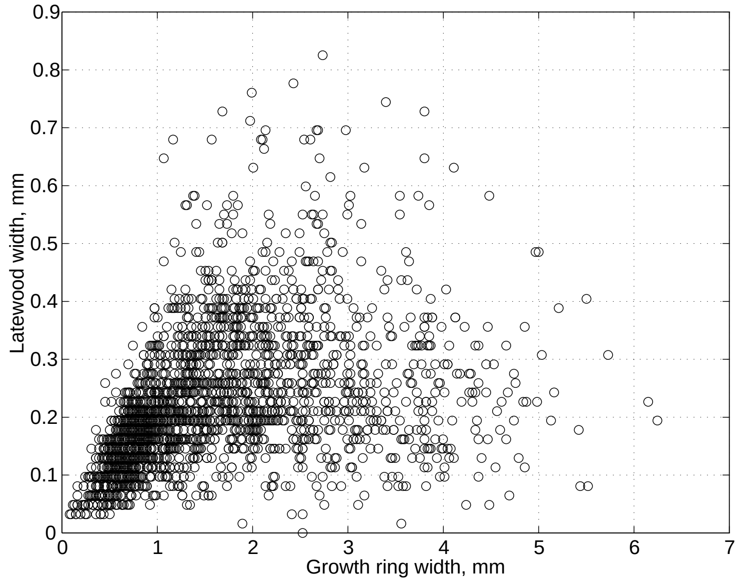

Figure 3.10: *Width of the latewood region versus the growth ring width.*

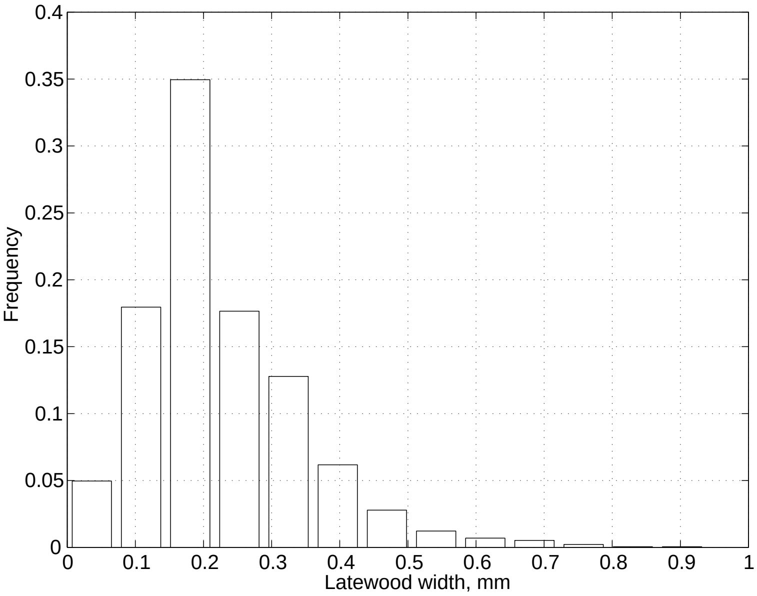

Figure 3.11: *Histogram of the width of the latewood region.*

The number of latewood cells in the growth ring and the growth ring width show a close correlation, see Figure 3.12. In the case of a constant latewood width of 0.20 mm, each growth ring has about 12-13 latewood cells, each with a radial width of about 16 μm.

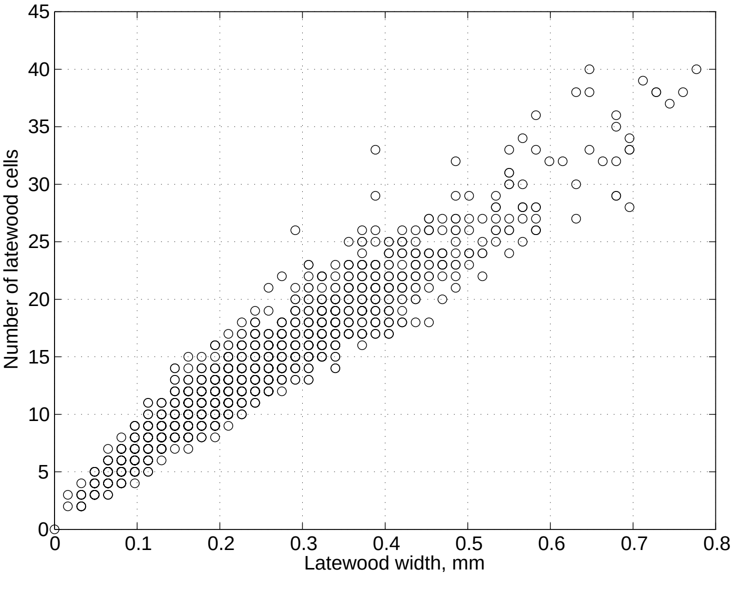

Figure 3.12: *Number of latewood cells versus width of the latewood region.*

3.2.4. Density and growth ring width

The density values presented were determined from the dry weight divided by the volume in a green condition. In Figure 3.13 the relation of density to the growth ring width for all the samples is shown. The correlation between the two is rather poor but is improved if the dominant trees are excluded, yielding a much better correlation, see Figure 3.14.

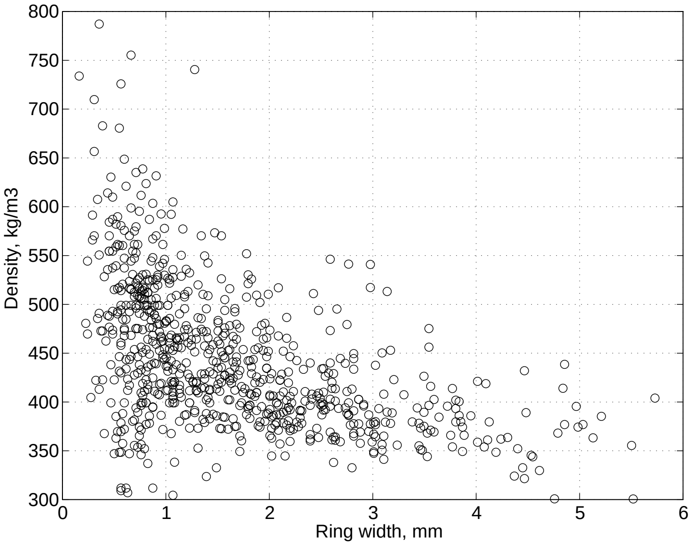

Figure 3.13: *Density versus growth ring width.*

The relation of density to growth ring width for the dominant trees only is shown in Figure 3.15. The results indicate that in the dominant trees the density varies less for different ring widths than in trees with a lower growth rate. However, the number of samples is too few for a more definite conclusion to be drawn.

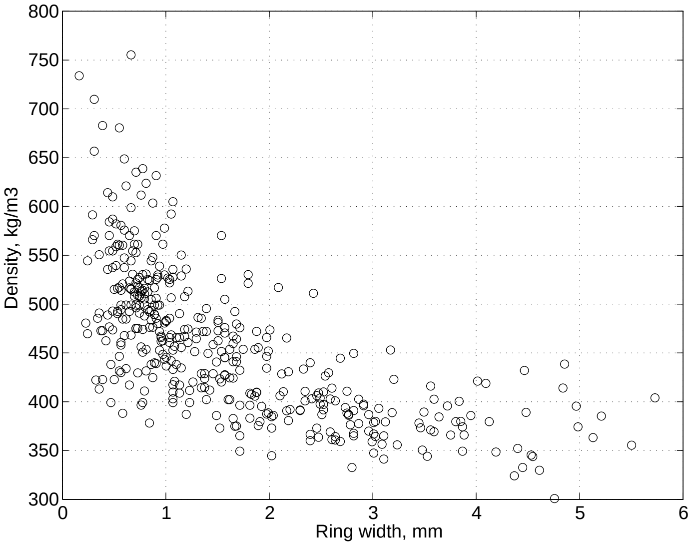

Figure 3.14: *Density versus growth ring width, the dominant trees excluded.*

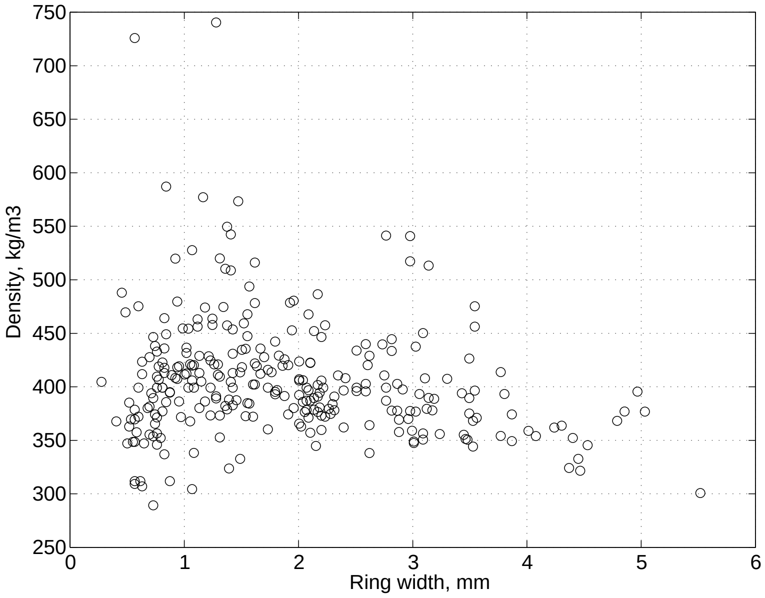

Figure 3.15: *Density versus growth ring width for the dominant trees only.*

3.2.5. Tangential cell width and ray cell fraction

The width of the cells in the tangential direction for the samples is shown in Figure 3.16. The measured mean value of the tangential cell width was 26.9 μm and the median 27.0 μm. For each growth ring, the distances between 20 successive ray cells and the number of cells located between them were determined, Figure 3.17. This indicates the ray cell content, visible on the surface. The mean number of cells contained between two ray cells is 7.1, the median being 6.0.

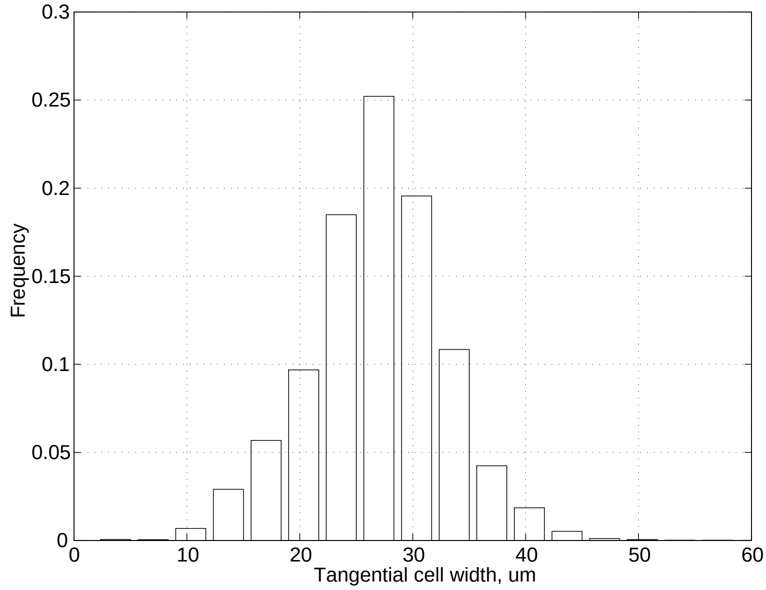

Figure 3.16: *Histogram of cell width in the tangential direction.*

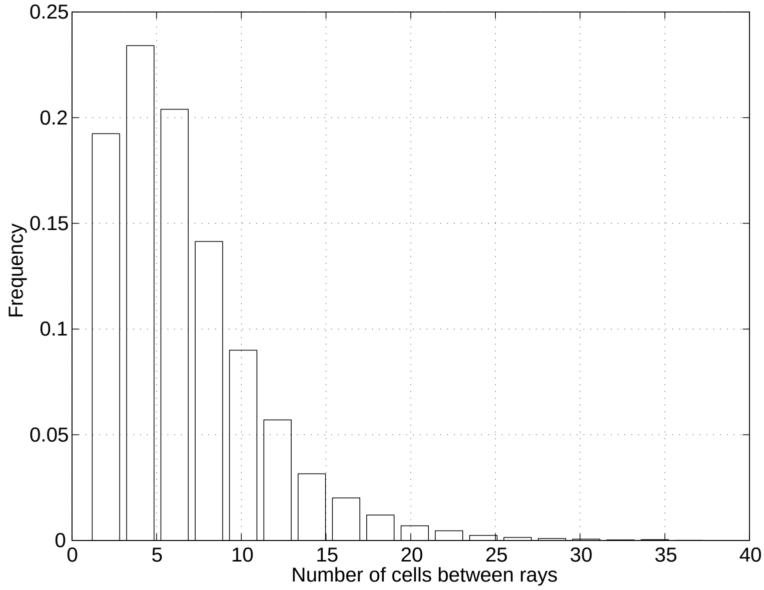

Figure 3.17: *Number of cells between two ray cells in the tangential direction.*

3.3. Characterization of Microstructural Deformations

3.3.1. Microscopic study

The behaviour of the cell structure at the microstructural level during loading has been studied with the aid of a scanning electron microscope (SEM). Some of the experimental that will be discussed here has also been reported by Stefansson [65]. Deformations of the wood specimens under gradually increasing loading were photographed in a SEM for four different load cases. A special loading device for applying either uniaxial or biaxial deformations to wood specimens was employed, see Figure 3.18. The load cases involving a prescribed displacement in one direction at the time only corresponded to pure tension, pure compression and pure shear. By use of prescribed displacements in two directions simultaneously, a loading combination of compression and shear was produced. The study involved loads in the radial direction, the resulting strains that were measured being expressed as the applied displacement divided by the initial length of the specimen. The size of the specimens was 5 mm in the radial and longitudinal directions and 10 mm in the tangential direction. The specimens were glued between metal bars in the loading device, using a fast-hardening glue. Before being placed in the SEM, the specimens were coated with a 25 nm thick gold layer in a coating unit, so as to protect them from being destroyed by being bombarded by electrons in the microscope. In some cases, it proved necessary to coat the specimens before each loading step. To avoid boiling due to the low air pressure in the coating unit and the SEM chamber, the specimens were oven dried prior to testing.

3.3.2. Resulting microstructural deformations

In this subsection some of the results of the microscope study reported by Stefansson [65] will be presented. It was found that in radial compression the cell structure collapsed locally due to instability, already at a relatively small overall deformation, see Figure 3.19. The collapse occurred at an average strain of about $\epsilon \approx -1\%$ and was localised in the first or second cell row of earlywood in the growth ring, Figure 3.19b. This occurred at almost the same time in all of the growth rings of the loaded specimen, with a failure band that extended from the one side to the other. As deformation continued, the cell structure in the earlywood continued to gradually collapse, from the first cell rows in the earlywood towards the latewood, until all the earlywood cells had collapsed, Figure 3.19c. Even for very large applied deformations, however, the deformations of the latewood were small, without any cell wall buckling.

The specimens loaded in tension were provided with notches cut at each side of the specimen, Figure 3.20a. At an applied deformation of about $\epsilon \approx 2\%$ an unstable

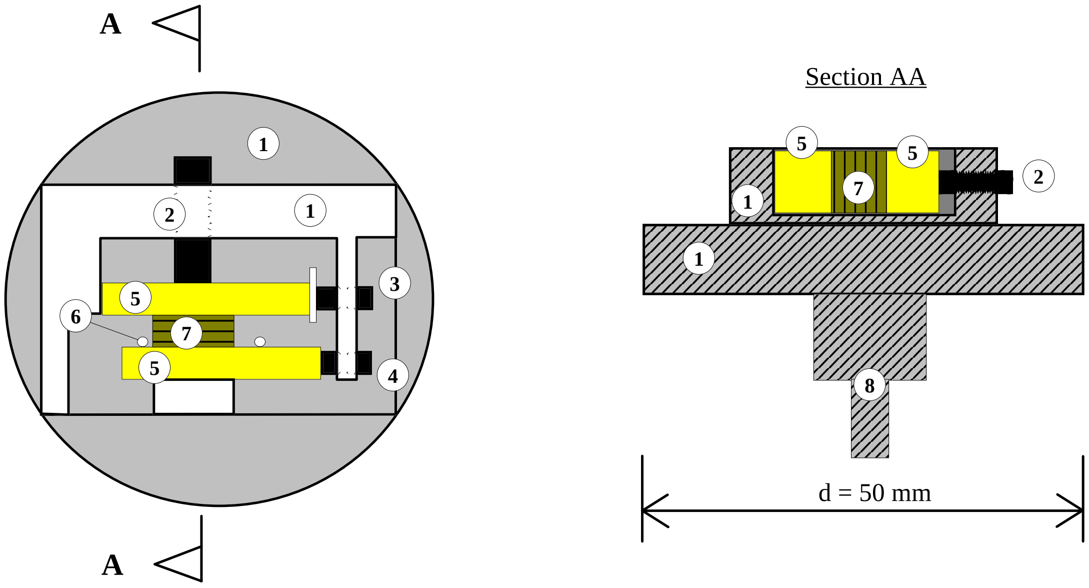

① Circular base plate, supports
② Screw (compression, tension)
③ Screw (support)
④ Screw (support)
⑤ Metal bars
⑥ Supporting pins
⑦ Specimen
⑧ Supporting pin

Figure 3.18: *Device for loading in one or two directions.*

crack propagation began at the ends of these notches, Figure 3.20b. The crack was often found to propagate through the cell walls of the earlywood and to then follow the raycells of the latewood, Figure 3.20c.

The result of shear loading in the RT-plane is shown in Figure 3.21. Again there were large deformations in the first earlywood cell rows but there were no visible deformations in the latewood. At an average shear strain of about $\gamma \approx 10\%$ a shear crack developed in the boundary between the earlywood and the latewood. At moderate shear strain the largest deformations were found in the middle of the earlywood region, Figure 3.21b, but after failure occurred the largest shear deformations were again found in the first-formed cells of the earlywood region, Figure 3.21c.

Combined compression and shear loading is shown in Figure 3.22. The largest localised strains for combined loading were observed in the first cells of the earlywood region, there being no visible deformations in the latewood. The structure collapsed at a combined average strain of about $\epsilon \approx -2.5\%$ and $\gamma \approx 8\%$.

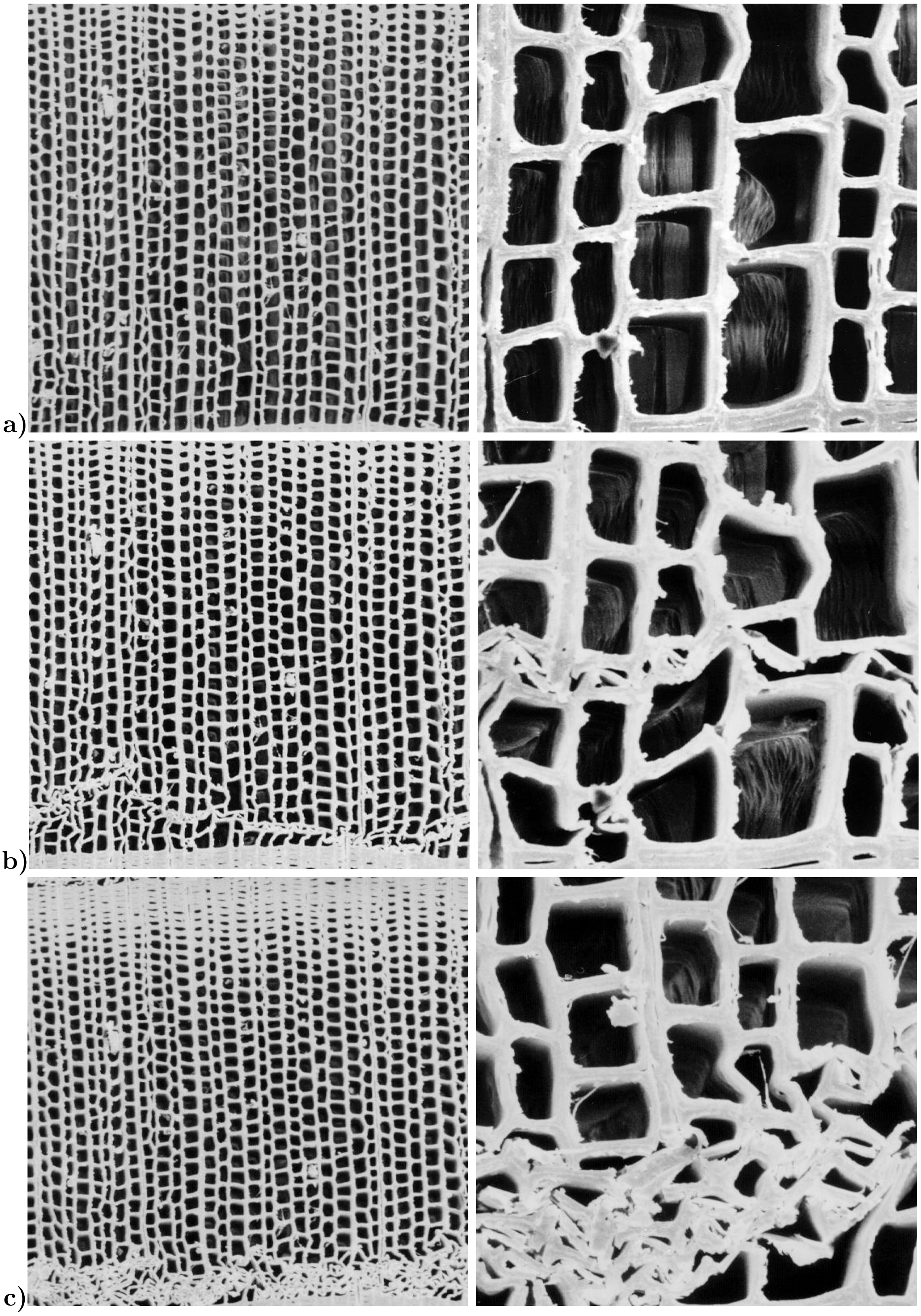

Figure 3.19: *Microstructural deformations for radial compression load.* **a)** *Undeformed.* **b)** *Average strain:* $\epsilon \approx$*-8%.* **c)** *Average strain:* $\epsilon \approx$*-12%.*

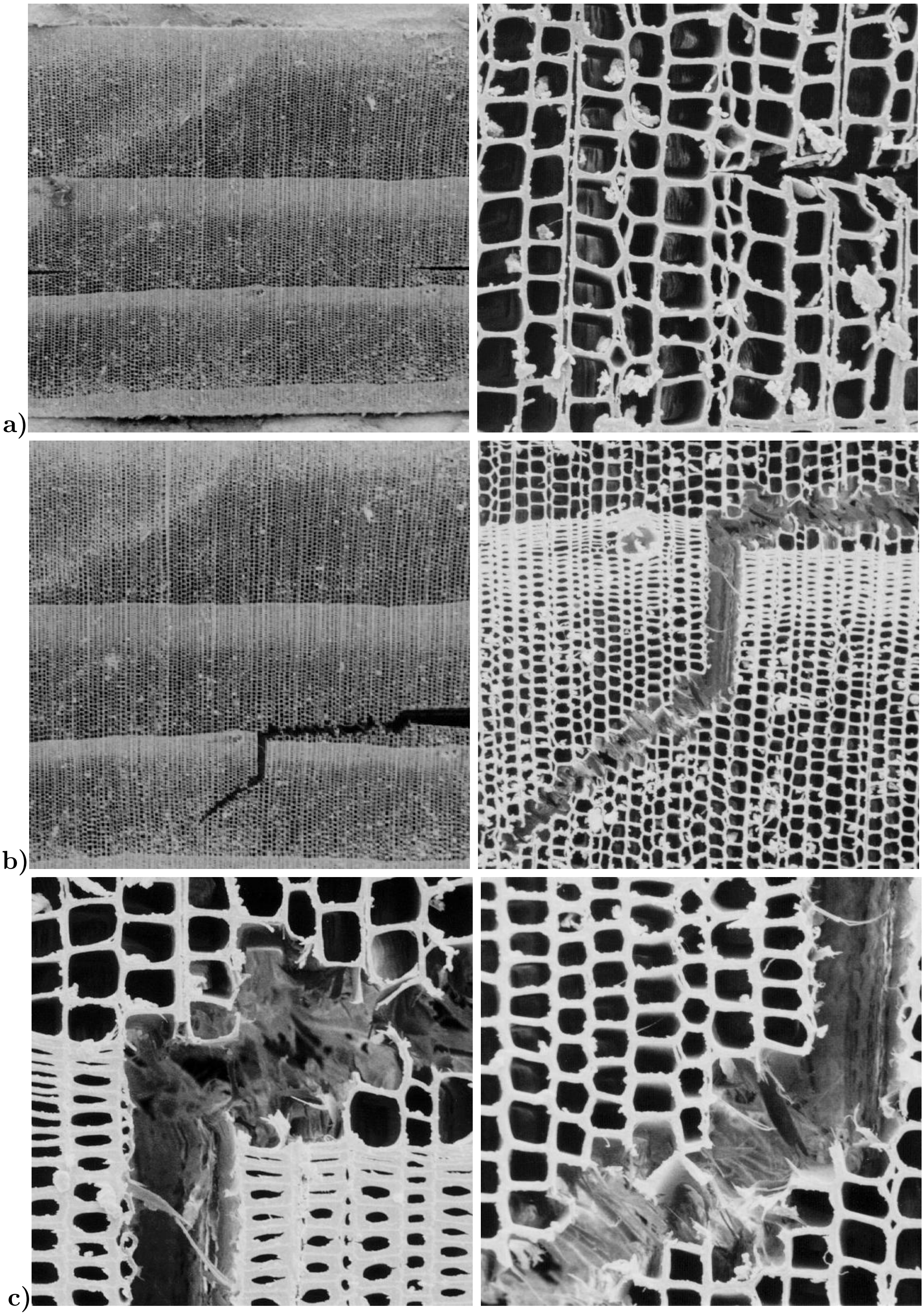

Figure 3.20: *Crack development for radial tension load.* **a)** *Undeformed with initial notch.* **b)** *and* **c)** *average strain at failure:* $\epsilon \approx 2\%$.

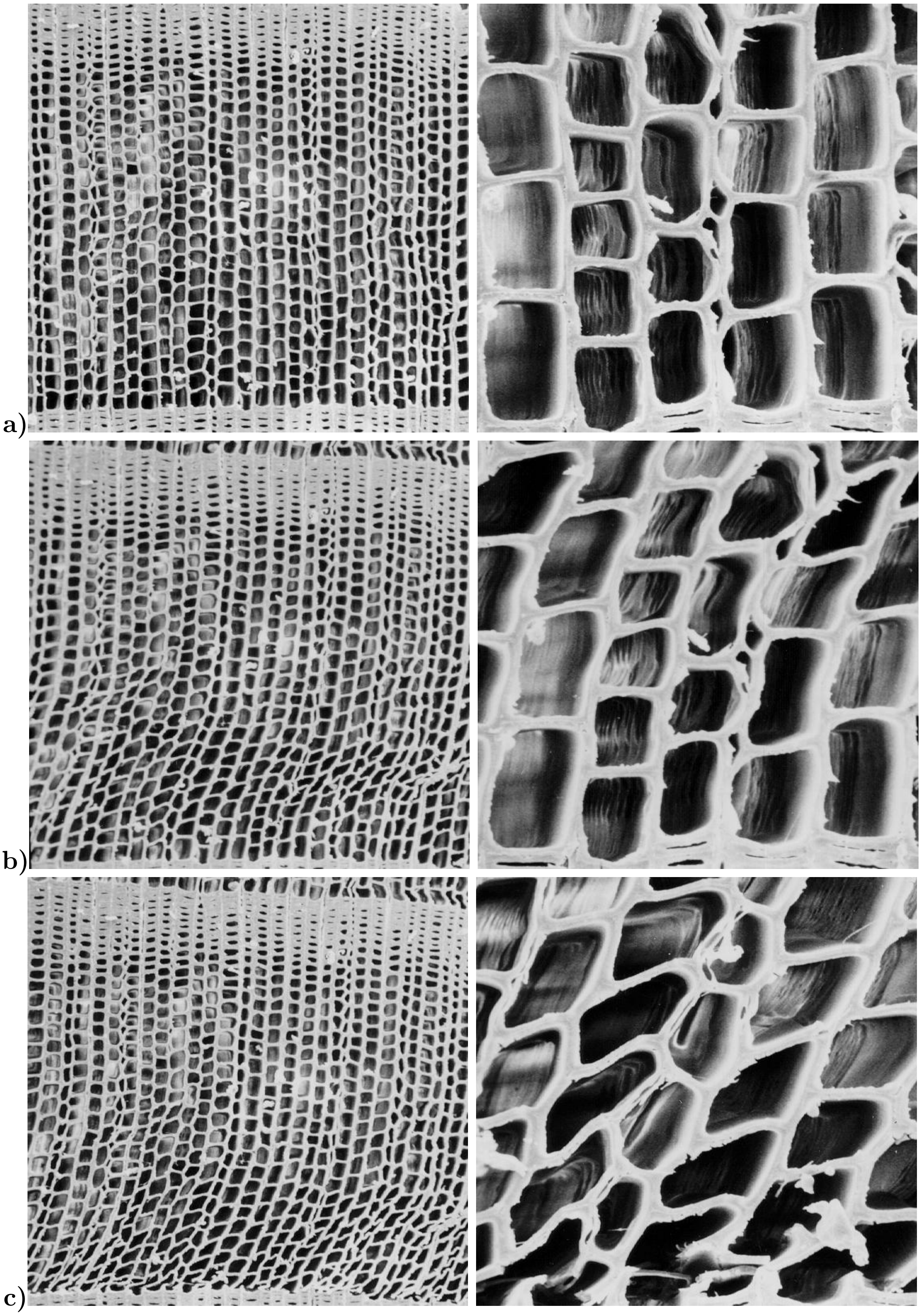

Figure 3.21: *Shear deformation in the RT-plane.* **a)** *Undeformed.* **b)** *Average strain:* $\gamma \approx 7\%$. **c)** *Average strain at failure:* $\gamma \approx 10\%$.

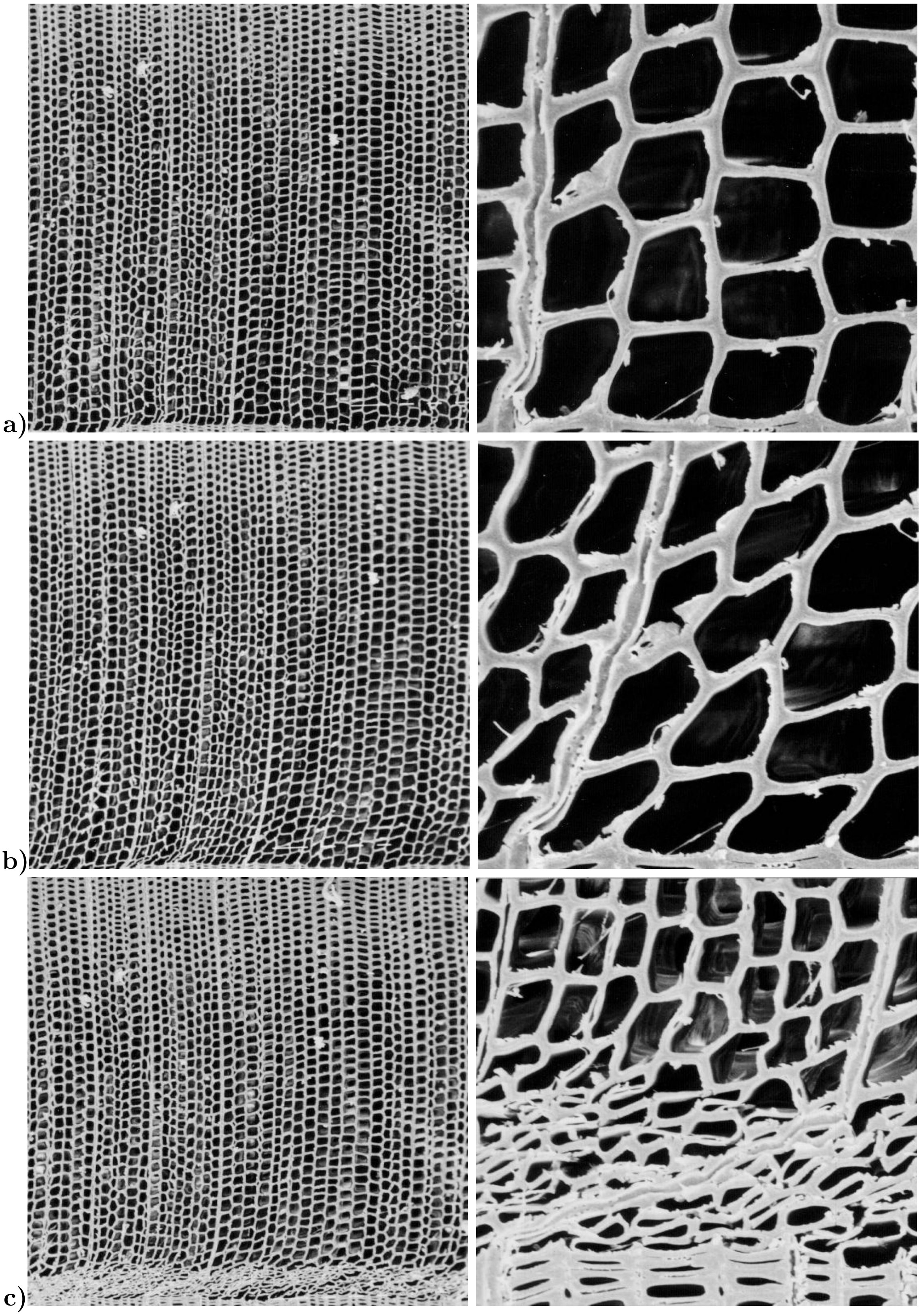

Figure 3.22: *Combined compression and shear deformation in the RT-plane.* **a)** *Undeformed.* **b)** *Average strain:* $\epsilon \approx$*-2% and* $\gamma \approx$*7%.* **c)** *Average strain:* $\epsilon \approx$*-6% and* $\gamma \approx$*15%.*

3.4. Experiments on Clear Wood Specimens

3.4.1. General remarks

The variations in the mechanical properties found within a tree are normally large. To determine how the properties vary, certain basic key parameters were measured. The mechanical properties of spruce are governed by the density and the microfibril angle. However, it is difficult and expensive to determine the microfibril angle. The key parameters that were determined instead were the density and the longitudinal modulus of elasticity. The shrinkage properties represent very important parameters since they strongly influence the shape stability of the final product, Ormarsson [48]. Accordingly, the shrinkage properties were determined in all three directions.

Specimens for clear-wood testing were taken from the discs labelled A in Figure 3.1. Specimens with a length of 300 mm and a cross section area of 10 by 10 mm were cut from north to south from each of the discs, Figure 3.23. Additional specimens were cut from some of the discs in a crossing pattern from east to west. For one of the trees the specimens were taken from eight different diameters that crossed each other at successive angles of 45 degrees. A total of about 700 specimens were used in the testing. The longitudinal modulus of elasticity, the coefficients of moisture induced shrinkage in the three main directions, and the density were determined. For each of the specimens, the angle between the fibre direction and the main longitudinal direction of the specimens was also measured. It was concluded that for most of the specimens this angle was less than 2 degrees and that for only very few was the angle over 5 degrees. Since a fibre direction that deviates 5 degrees from the longitudinal axis affects the longitudinal stiffness less than 5% for normal wood, the fibre deviation has not been considered in the result presentation that follows.

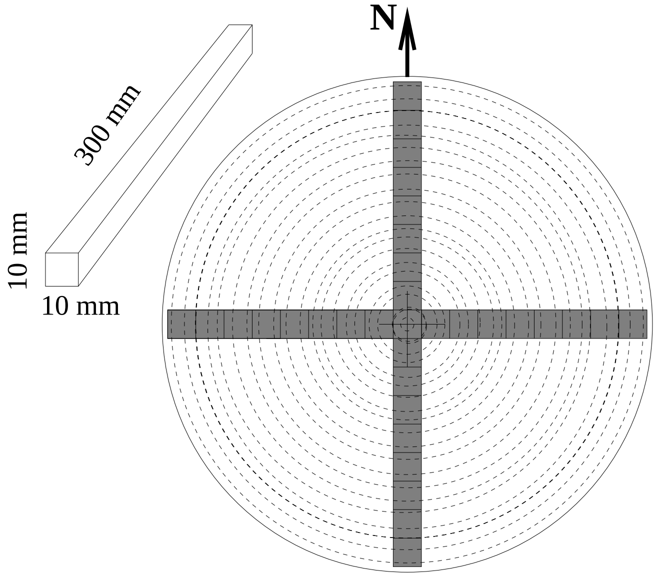

Figure 3.23: *Cutting scheme and specimen used for clear wood testing.*

The experimental setup and the results of the measurements are reported in detail by Dahlblom et al. [15] and [16]. Only results that are of importance in the present context and which are necessary to consider for modelling the mechanical properties of wood are presented here. The measured results dealt with in this section pertain to specimens taken along the south to north diameter.

3.4.2. Density

Density measurements of 40 mm long samples cut from one end of the specimens shown in Figure 3.23 were made. This allows the average density, the longitudinal modulus of elasticity and the shrinkage coefficients to be related to each other directly. The density measurements presented here relate to the dry weight divided by the volume in the dry condition. In the data interpretation, a polynomial third-degree function is fitted to the data in a least square sense. Figure 3.24 shows the densities for all the trees at all the heights studied in the south to north direction in the discs. Since the differences along the north and south directions were very small, it is reasonable to consider only the variation along the radius.

Figure 3.25 shows the density along the radius for all the trees and at all heights studied. In the juvenile wood the density is low, increasing towards the bark. In most of the trees the local density seemed to be higher very close to the pith than in the surrounding wood. Since for many of the discs the density was found to decrease very abruptly just outside the pith, measurements for the pith specimen were excluded in the following from the least square fits of density, resulting in smoother fitting curves.

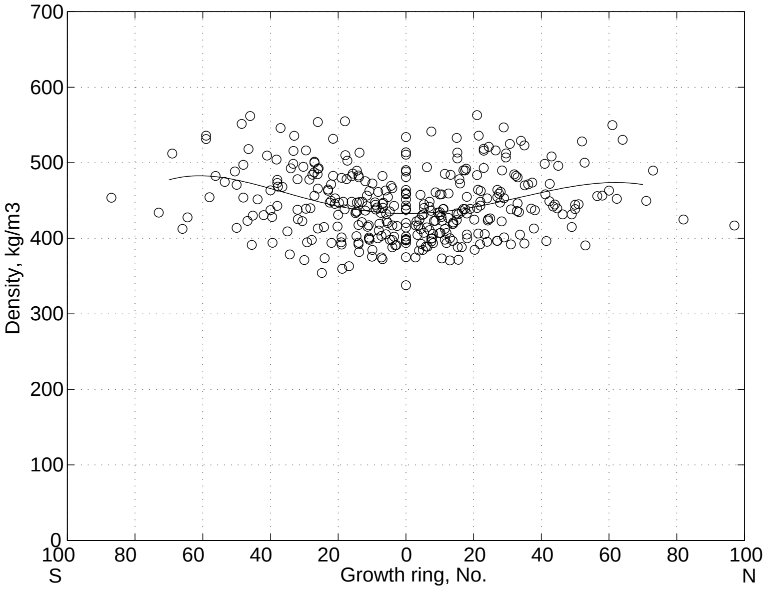

Figure 3.24: *Density versus growth ring number from south to north for all the trees and at all heights studied.*

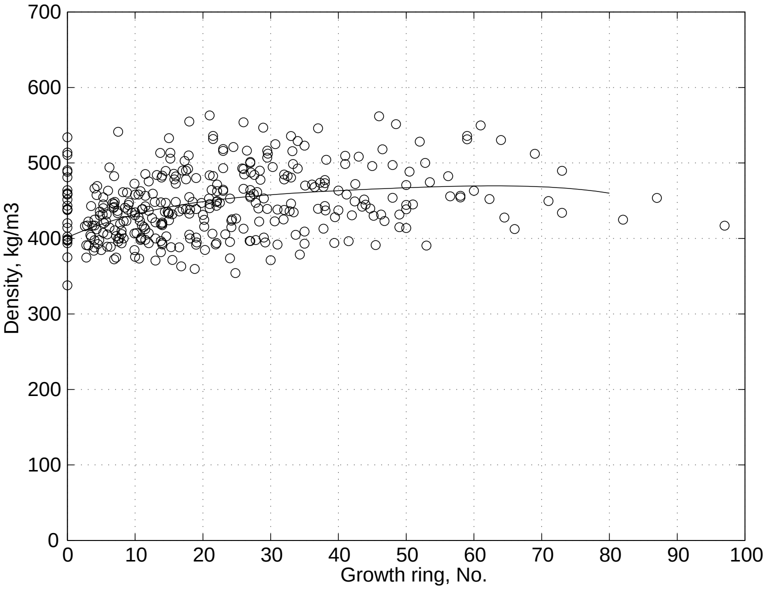

Figure 3.25: *Density versus growth ring number for all the trees at all the three heights studied.*

Figure 3.26 shows the density in relation to the growth ring number for all of the trees and for all of the three social classes, together with fitted curves. The densities of the co-dominant and the dominated trees are similar, but the dominant trees show a lower and less varying density along the radius.

Figure 3.27 shows the density of all the trees at three heights in relation to the growth ring number, together with fitted curves. For each of the heights studied, the density is low near the pith, rising then towards the bark to reach a maximum, decreasing then somewhat closest to the bark. The decrease in the curve is probably due to most of the dominant trees having a lower density and coming from an older stand. The densities for high ring numbers are thus mostly from dominant trees, as can be seen in Figure 3.26.

3.4.3. Stiffness properties

The longitudinal modulus of elasticity was determined for the specimens, see Figure 3.23, by applying a tensional load by use of an MTS testing machine. The force applied was measured by a load cell, whereas the displacements were determined by two 40 mm long strain gauges at the midpoint of the specimens. By using two strain gauges at opposite sides of the specimen, the strains due to curvature of the specimen were eliminated. The strains were determined from the mean elongation of the two strain gauges divided by the initial gauge length. The stresses were calculated as the applied load divided by the initial cross sectional area of the specimens. The moduli of elasticity were determined from the obtained stress-strain curves by determining the slope at the linear part of the curves. Prior to testing, the specimens were conditioned at 65% RH and 20° C for about two weeks.

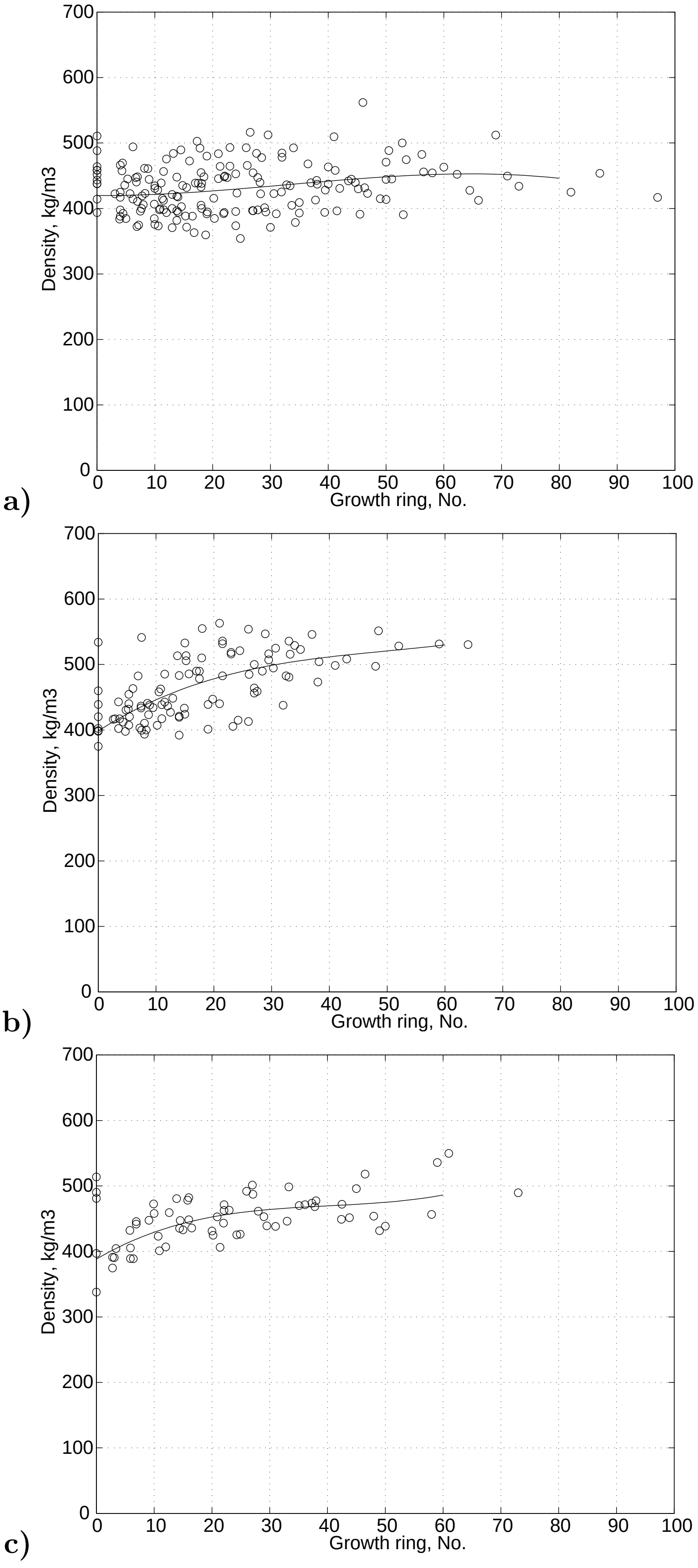

Figure 3.26: *Density versus growth ring number for the three different social classes.* **a)** *Dominant trees.* **b)** *Co-dominant trees.* **c)** *Dominated trees.*

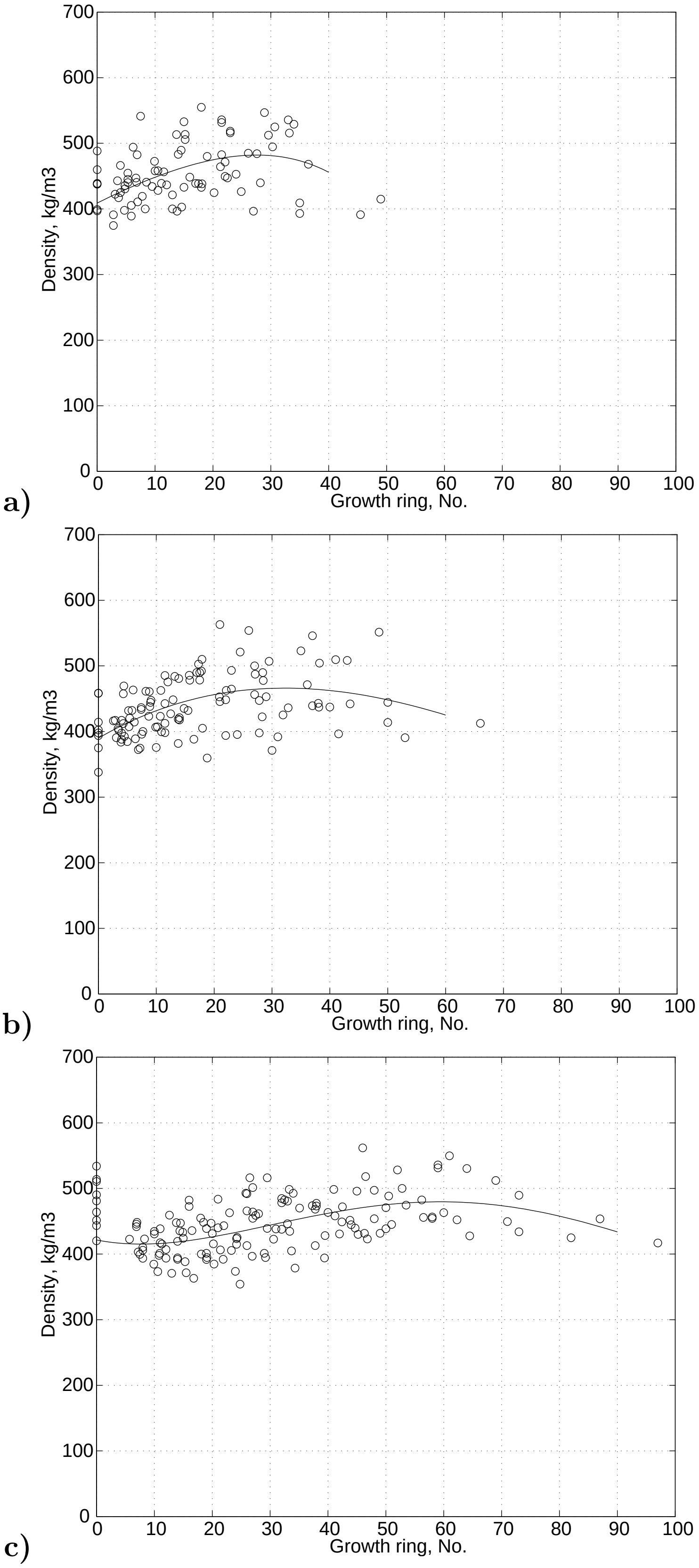

Figure 3.27: *Density versus growth ring number at the three different heights.* **a)** *Top disc.* **b)** *Middle disc.* **c)** *Bottom disc.*

The results of the measurements indicate that the stiffness properties are strongly dependent upon the position in the stem, especially with respect to the radial direction. Figure 3.28 shows the longitudinal modulus of elasticity versus the growth ring number for all trees and at all heights studied for the south to north diameter.

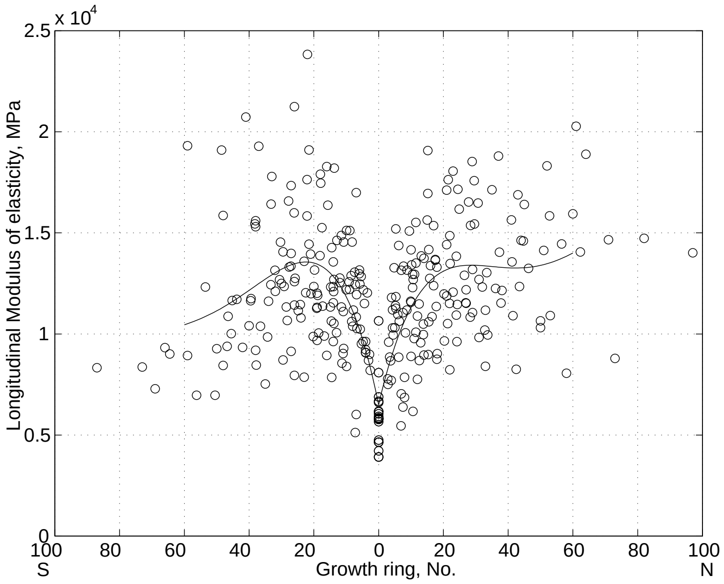

Figure 3.28: *Longitudinal modulus of elasticity versus growth ring number from south to north for all the trees at all three heights.*

The stiffness is low in the juvenile part but increases towards the bark. A stiffness up to four times as great was observed in the mature wood near the bark as compared to the juvenile wood. Since the differences in stiffness between the south and north directions were not found to be significant, the distinction concerning the side of the tree from which the specimens were sampled is neglected in the following and only the variation from pith to bark is considered.

Figure 3.29 shows the longitudinal modulus of elasticity versus the growth ring number for all the trees and for the three different social classes together with fitted curves. For all three social classes, the modulus of elasticity is about 6000 MPa in the pith. The increase along the radius for the co-dominant and dominated trees is similar, but is less in the dominant trees. For the dominated trees there is a decrease of stiffness for higher growth ring numbers, but this result is probably due to the lesser amount of data obtained for this class.

Figure 3.30 shows the longitudinal modulus of elasticity versus the growth ring number for all trees for the three different heights together with fitted curves. For each of the heights, the stiffness is low near the pith and increases then towards the bark. The longitudinal modulus of elasticity is lower for the specimens taken from the bottom disc than for those taken from the middle and upper discs.

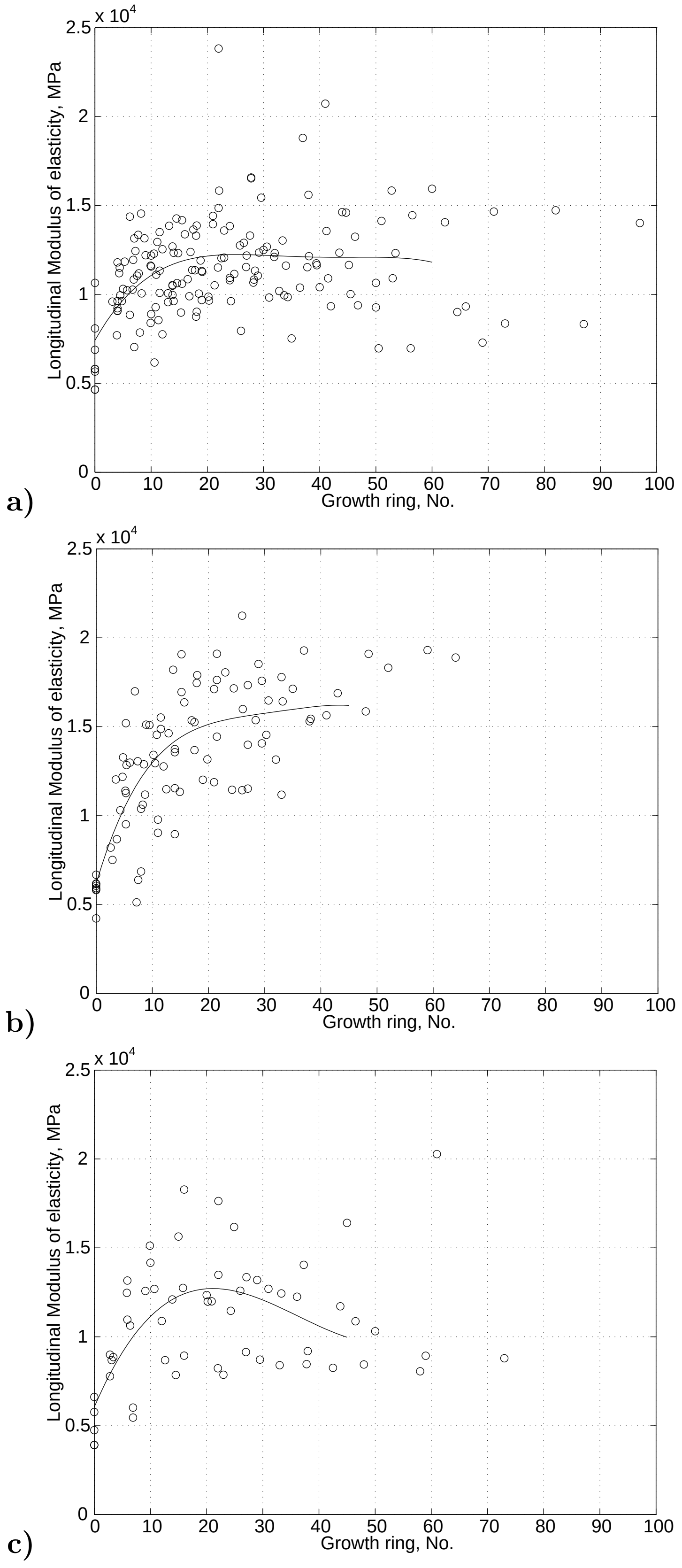

Figure 3.29: *Longitudinal modulus of elasticity versus ring number for the different social classes.* **a)** *Dominant trees.* **b)** *Co-dominant trees.* **c)** *Dominated trees.*

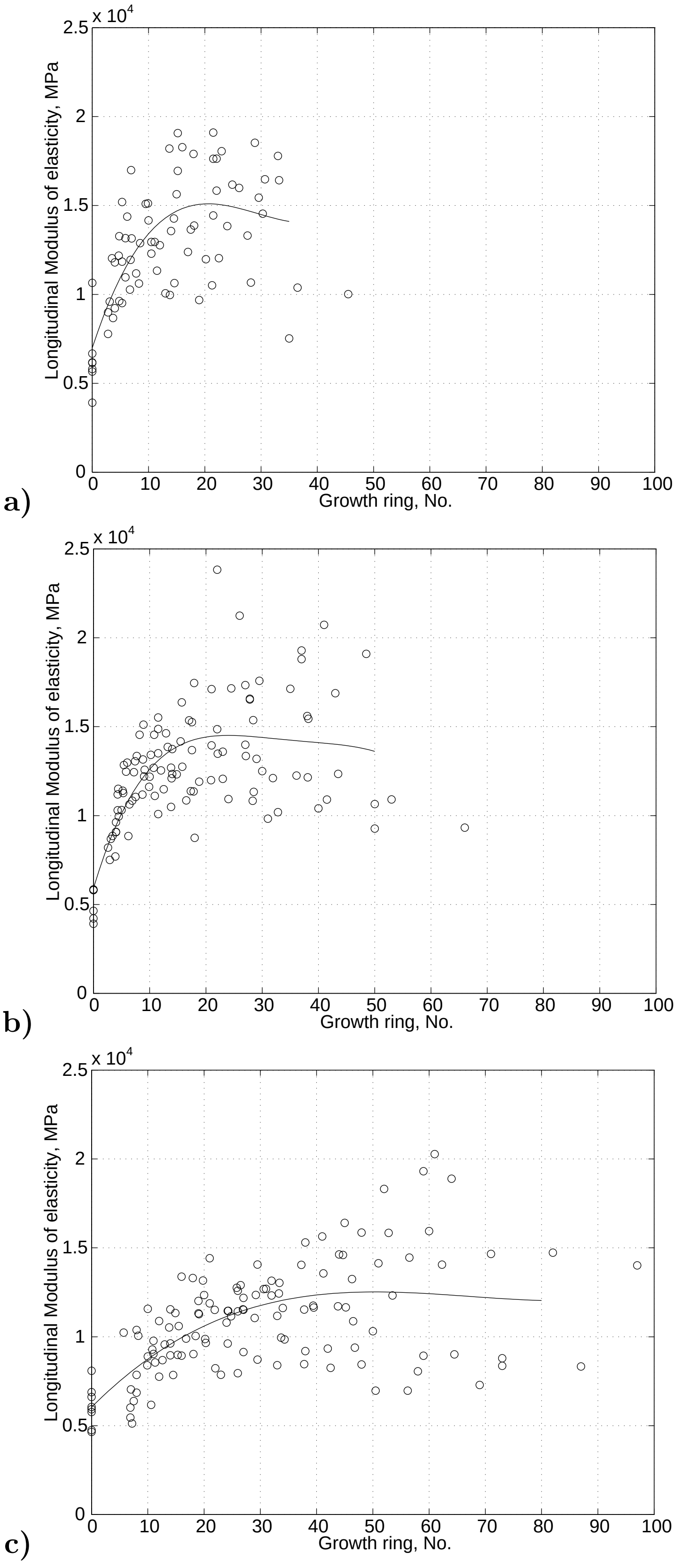

Figure 3.30: *Longitudinal modulus of elasticity versus ring number at the three different heights.* **a)** *Top disc.* **b)** *Middle disc.* **c)** *Bottom disc.*

3.4.4. Shrinkage properties

The shrinkage of the specimens as assessed in terms of four different moisture contents was measured for the three main directions of the wood. The shrinkage strains were determined by measuring the dimensions of conditioned specimens at 95% RH, 65% RH, 50% RH and 35% RH. All conditioning was conducted at 20° C. At each stable moisture content, the dimensions and the weight of the specimens were determined. The shrinkage strains ϵ_i^s were obtained, from the changes in the dimensions between the various stable moisture levels as

$$\epsilon_i^s = \frac{\Delta l_i}{l_i^0}, \qquad i = 1, 2, 3 \tag{3.1}$$

where Δl_i is the change in length in direction i between the two moisture levels involved and l_i^0 is the initial length in green condition. Figure 3.31 shows the mean longitudinal shrinkage obtained from 29 specimens in the intervals of 95-65-50-35% RH at 20° C.

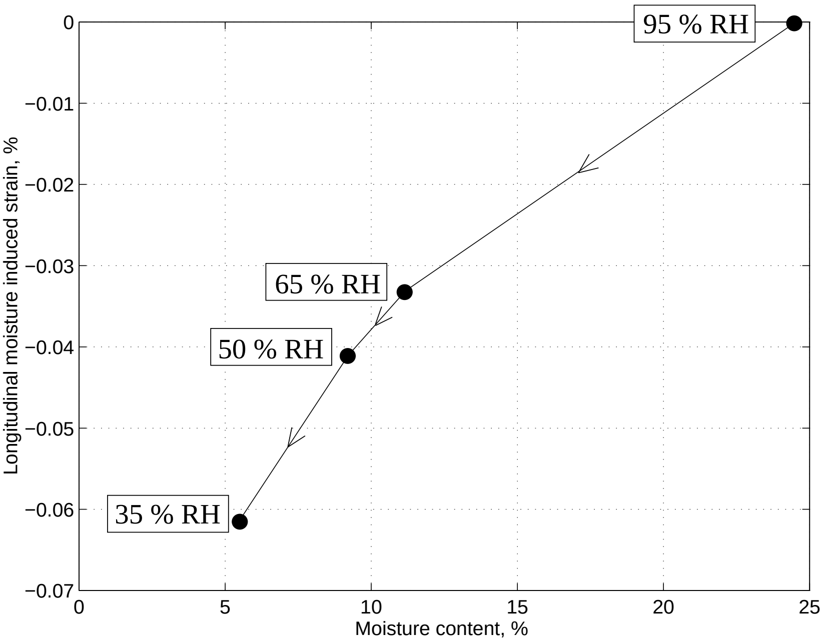

Figure 3.31: *Strain in the longitudinal direction from 95 to 35% RH at 20° C.*

To determine the average shrinkage coefficients between two moisture levels, the shrinkage strains are divided by the change in moisture content Δw

$$\alpha_i = \frac{\epsilon_i^s}{\Delta w}, \qquad i = 1, 2, 3 \tag{3.2}$$

where the moisture content w is determined from Eq.(2.15). The four moisture levels allow three shrinkage coefficients to be determined. Since the shrinkage was found to be non-linear, different coefficients are obtained from each pair of moisture levels.

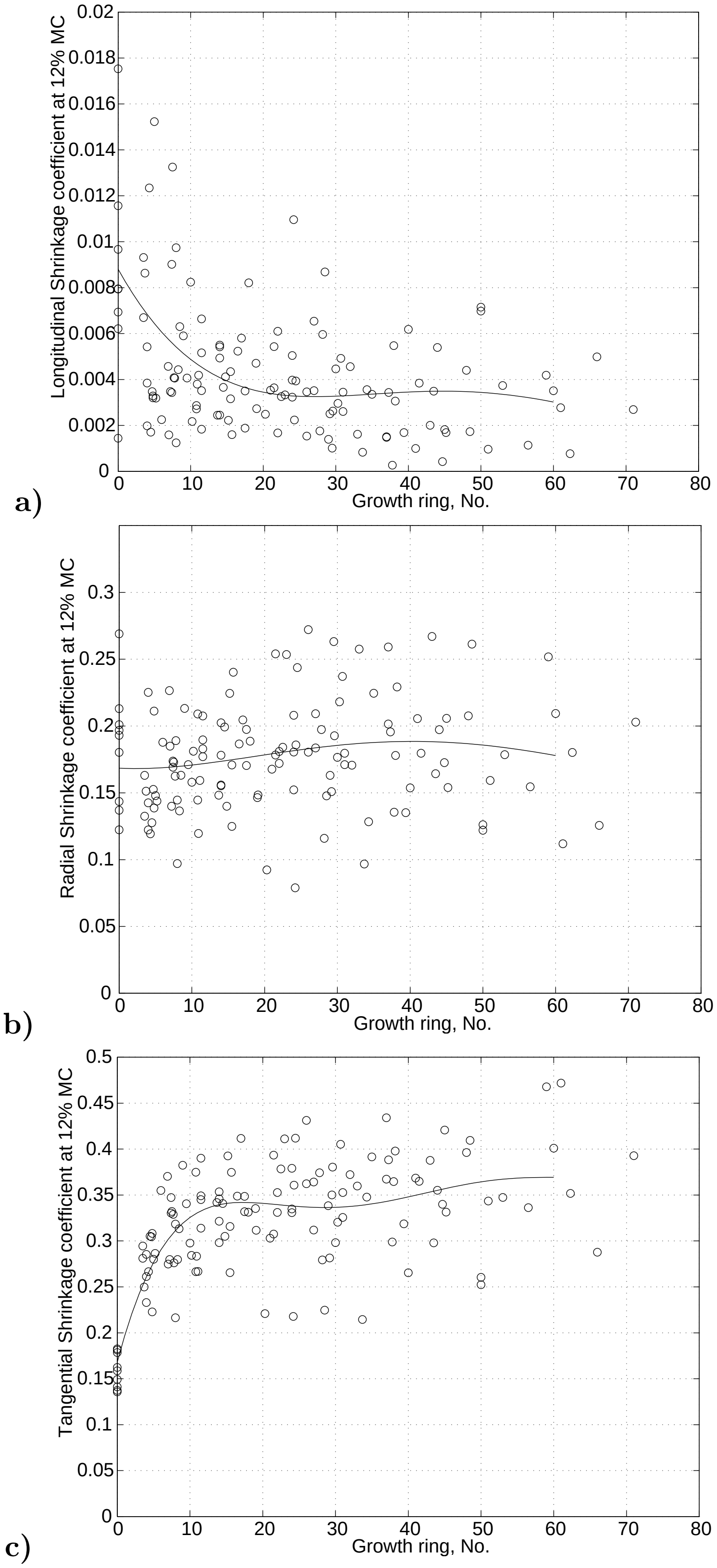

Figure 3.32: *Shrinkage coefficients at 12% moisture content for* **a)** *longitudinal direction,* **b)** *radial direction and* **c)** *tangential direction.*

Shrinkage coefficients of around 12% of moisture content for all trees and at all heights studied are shown in Figure 3.32. The shrinkage coefficients are calculated as the mean of the shrinkages from the intervals 95-65% RH and 65-50% RH. The longitudinal shrinkage is large near the pith and decreases to almost a constant value at about the 20th growth ring. The tangential shrinkage is low near the pith, increasing then to reach an almost constant value. The radial shrinkage is nearly constant along the radius. Note that the specimens sampled from the pith contain the complete first growth rings. The radial and tangential shrinkage measurements are thus mixed in these specimens.

3.5. Discussion on Experimental Results

Several conclusions can be drawn from the experiments performed. The measurements show that the properties of a tree vary strongly in the radial direction. This means that there are large variations in stiffness of timber and that the stiffness depends on the original positions of the boards within the stem. Since the stiffness and the shrinkage parameters vary, in the radial direction particularly, both the strength and the shape stability of the timber is strongly affected.

Through a comparison of measurements obtained by clear-wood testing and those carried out at the microstructural level, valuable information regarding the cellular structure of wood can be obtained. From the measurements presented in this chapter, the microstructure can be determined through knowledge of the density or of the growth ring width. An approximate formula for the relation between the density and the growth ring width was given by Eq.(2.4). This approximation shows good agreement when compared with the experimental data, Figure 3.33.

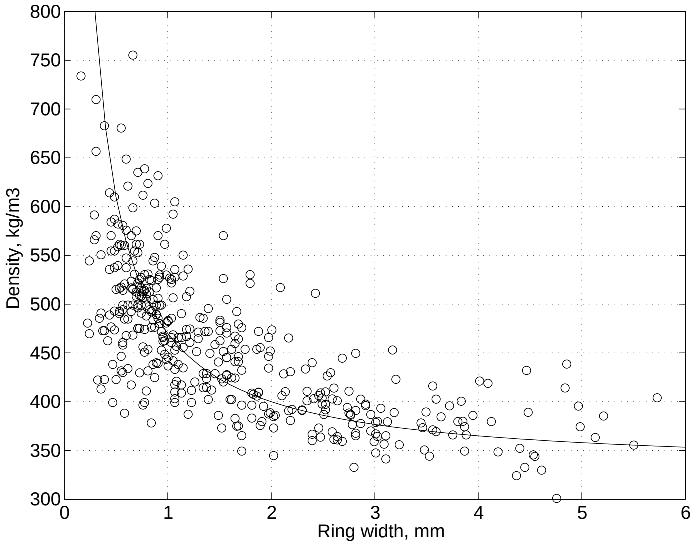

Figure 3.33: *Calculated curve according to Eq.(2.4) and measurements of density versus growth ring width.*

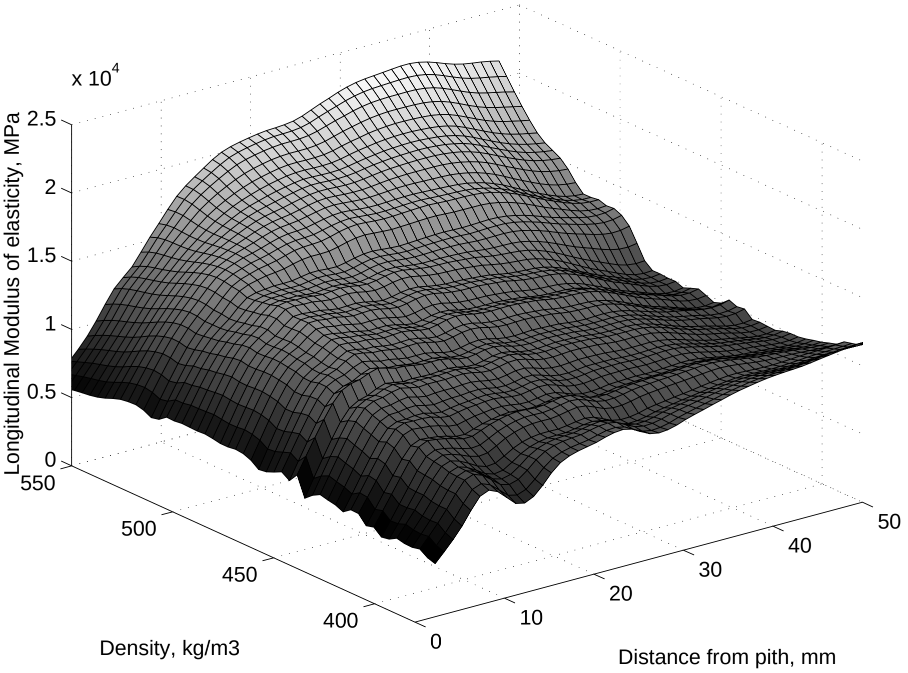

Figure 3.34: *Longitudinal modulus of elasticity versus density and distance from the pith.*

From the measurements obtained from the 11 trees it can be concluded that stiffness properties depend not only on density but also on the position in the stem. Figure 3.34 shows the longitudinal modulus of elasticity versus density and distance from the pith. The relationship shown was obtained by a least-square fit of all the experimental data obtained. The modulus of elasticity increases both with density and with distance from the pith. With the aid of the measurements of density and of the longitudinal modulus of elasticity, it is possible to estimate the average microfibril angle by use of the procedure given in Appendix A. To illustrate this, the average microfibril angles have been calculated for a radius in a tree in which the microfibril angles, the longitudinal modulus of elasticity and the density were measured, Figure 3.35. The microfibril angles have been measured using X-ray diffraction, Sahlberg et al. [59].

The results of the measurements together with the theoretical assumptions made provide a description of the microstructure of spruce. With knowledge of the density or of the growth ring width it is possible to estimate the earlywood, transitionwood and latewood widths by use of Eq.(2.4) and of the results of the microstructural measurements. The longitudinal modulus of elasticity and the density can thus be considered as the prime input parameters for modelling the properties of wood. The microfibril angle is calculated as an intermediate variable in the determining of the parameters characterizing the mechanical properties of wood. The average microfibril angle can be determined approximately from the longitudinal modulus of elasticity and the density by use of Eq (A.10).

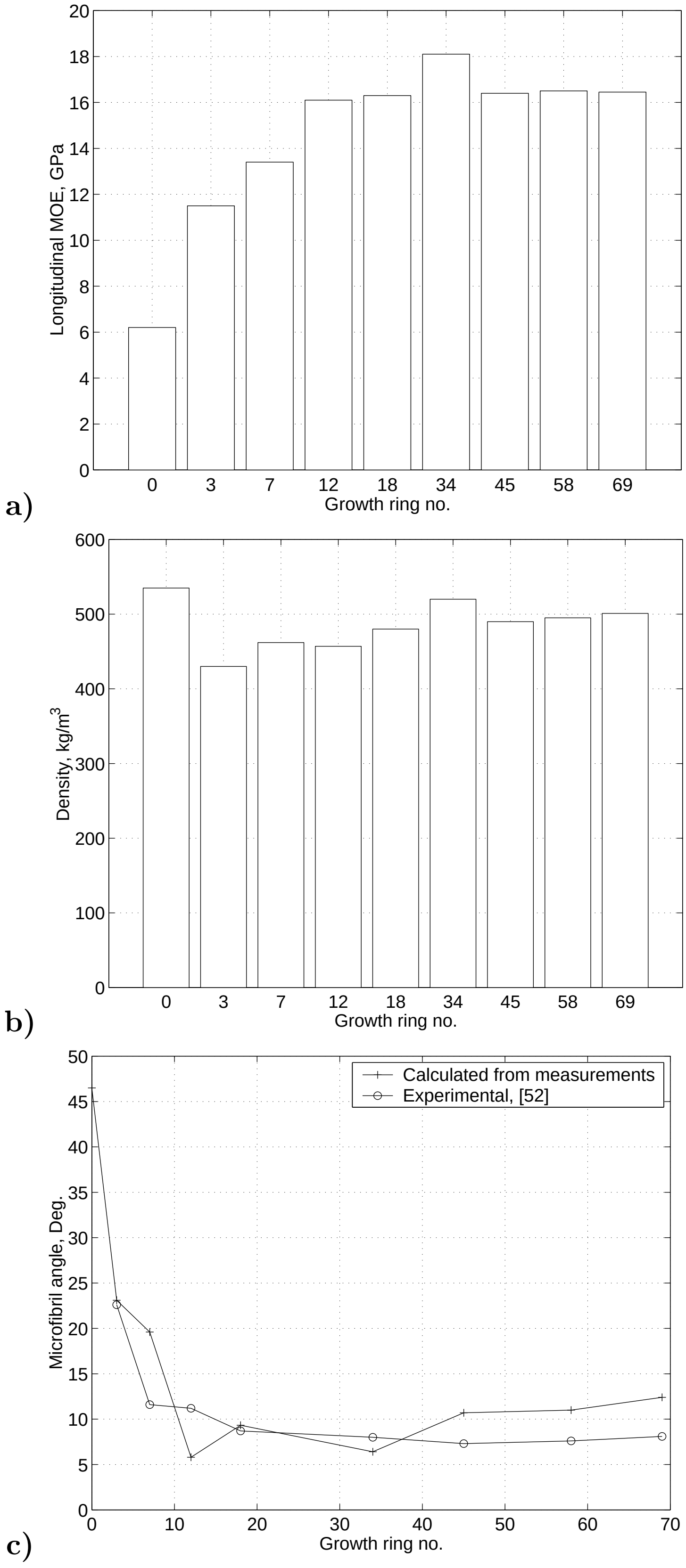

Figure 3.35: *Indirect determination of the microfibril angle.* **a)** *Longitudinal modulus of elasticity.* **b)** *Density.* **c)** *Measured and resulting calculated microfibril angles.*

3.6. Concluding Remarks

The experimental results on the longitudinal modulus of elasticity, density and hygroexpansion presented in this chapter was an initial study, one that has been followed by larger experimental investigations. The specimens that were used were taken from 11 trees in a narrow geographic area. However, after the presented study was carried out a larger study of similar type was performed by Dahlblom et al. [17], [18] and [19]. In that study, the longitudinal modulus of elasticity, the three hygroexpansion coefficients and the spiral grain were measured along the radius in a total of 274 trees at several heights. The trees were selected from different stands in five European countries. The result of that investigation are in close agreement with the results presented in this section.

4. HOMOGENISATION AND THE FINITE ELEMENT METHOD

4.1. General Remarks

The basic idea of homogenisation is to average the behaviour of a material with a complex periodic microstructure through replacing the material by an equivalent homogeneous continuum. With the aid of a homogenisation procedure and the finite element method it is possible to derive the constitutive global behaviour of the corresponding heterogeneous material.

A material with a periodic microstructure has properties which vary in a repetitive pattern throughout the body. In the homogenisation procedure, a representative volume element of the material, which is referred to as the base cell, is defined. The material can be divided into equal substructures if it has a periodic structure, the base cell being chosen as one of the periods of the structure. In wood, periodic structures can be found at several levels. The cell wall layers are constructed of microfibrils that consist of cellulosic chains in a matrix material of hemicellulose and lignin. The microfibrils are of similar size and shape throughout the cell wall and form a periodic structure. At this level the microfibril can be regarded as the base cell. At a higher level of the wood structure, it is evident from the variation in density over the growth rings that the growth ring structure can be regarded as a periodic material, Figure 2.7.

A homogenisation procedure using the finite element method is described in this section and will be used later to derive the equivalent smeared properties of wood from the microstructure. First, a homogenisation procedure is described, the basic equations of the finite element method are then presented, and finally it is shown how the homogenisation problem can be solved by use of the finite element method.

4.2. Governing Continuum Equations

The introduction of the governing continuum equations will be the starting point for describing the finite element method and the homogenisation process used in the numerical simulations. For a further description of the theory of continuum mechanics, see e.g. Malvern [40]. A Cartesian coordinate system x_j, $(j = 1, 2, 3)$ is introduced, that will be used throughout the study. The equilibrium equations for

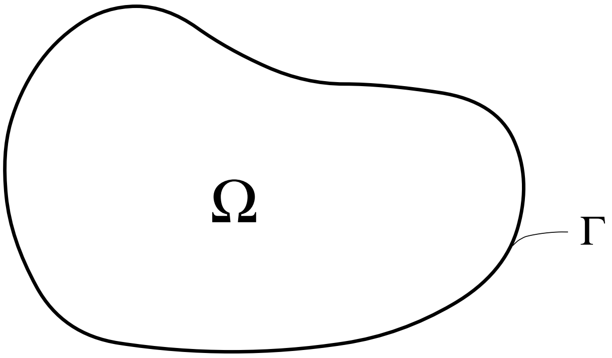

Figure 4.1: *A body* $\mathbf{\Omega}$ *with boundary* $\mathbf{\Gamma}$.

analysis of an elastic body with boundary conditions according to Figure 4.1 are

$$\begin{cases} \dfrac{\partial \sigma_{ji}}{\partial x_j} + b_i = 0 \;\; in \;\; \mathbf{\Omega} \\ \\ \sigma_{ji} n_j = t_i \;\; on \;\; \mathbf{\Gamma} \end{cases} \tag{4.1}$$

where σ_{ji} are components of a symmetric stress tensor that for a general finite deformation case is Cauchy's stress tensor and b_i is a body force vector. The tractions t_i are acting on the boundary $\mathbf{\Gamma}$ surrounding the body, where n_j represents the outward unit vector, normal to the boundary surface. In order to achieve an integral formulation, the basic differential equations are rewritten into an equivalent "weak form", obtained by multiplying the equilibrium equations in Eq.(4.1) by a set of weight functions v_i, $(j = 1, 2, 3)$ and integrating over the volume $\mathbf{\Omega}$ occupied by the body. Taking the scalar product of Eq.(4.1) with respect to the weight functions v_i results in a single scalar equation

$$\int_{\mathbf{\Omega}} v_i \frac{\partial \sigma_{ji}}{\partial x_j} \, d\mathbf{\Omega} + \int_{\mathbf{\Omega}} v_i b_i \, d\mathbf{\Omega} = 0 \tag{4.2}$$

An integration by parts using Green-Gauss's theorem is performed on the first term in Eq.(4.2), resulting in

$$\int_{\mathbf{\Omega}} v_i \frac{\partial \sigma_{ji}}{\partial x_j} \, d\mathbf{\Omega} = \int_{\mathbf{\Gamma}} v_i \sigma_{ji} n_j \, d\mathbf{\Gamma} - \int_{\mathbf{\Omega}} \frac{\partial v_i}{\partial x_j} \sigma_{ji} \, d\mathbf{\Omega} \tag{4.3}$$

Inserting Eq.(4.3) into Eq.(4.2) and using the relation for the tractions on the boundary, $\sigma_{ji} n_j = t_i$, yields the weak form of the equations of equilibrium

$$\int_{\mathbf{\Omega}} \frac{\partial v_i}{\partial x_j} \sigma_{ji} \, d\mathbf{\Omega} = \int_{\mathbf{\Omega}} v_i b_i \, d\mathbf{\Omega} + \int_{\mathbf{\Gamma}} v_i t_i \, d\mathbf{\Gamma} \tag{4.4}$$

The homogenisation procedure and the finite element formulations for a linear and a nonlinear case, described in the following, will be based on this weak formulation of the equilibrium equations. However, in the case of finite displacements, the terms on the left hand side of Eq.(4.4) can be replaced by integrals over the reference volume $\mathbf{\Omega_0}$, giving

$$\int_{\mathbf{\Omega_0}} \frac{\partial v_i}{\partial x_j} \tau_{ji} \, d\mathbf{\Omega_0} = \int_{\mathbf{\Omega}} v_i b_i \, d\mathbf{\Omega} + \int_{\mathbf{\Gamma}} v_i t_i \, d\mathbf{\Gamma} \tag{4.5}$$

where τ_{ij} are components of the Kirchhoff stress tensor defined by

$$\tau_{ij} = \frac{d\mathbf{\Omega}}{d\mathbf{\Omega_0}} \sigma_{ij} \tag{4.6}$$

4.3. Homogenisation

4.3.1. Periodic material

The homogenisation theory will be outlined here for a linear elastic material in which small strains are assumed and geometrical nonlinear effects are neglected. Only basic features of the homogenisation method will be treated in this section. For a more complete treatment of the subject, see for example Bensoussan [6]. It is assumed that the microstructure of the body is periodic and that the material is composed of subcells of equal shape and equal material properties. A subcell can then be chosen as a representative volume element that is repeated throughout the body as illustrated in Figure 4.2.

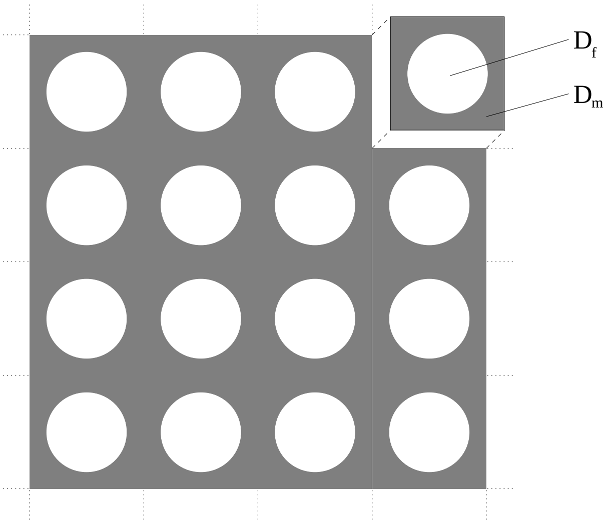

Figure 4.2: *A periodic structure composed of two different materials, D_f and D_m. The representative volume element is shown in the upper right.*

Each representative volume element with the volume $\mathbf{\Omega}$ in the body has the same shape and the same material properties $D_{ijkl} = D_{ijkl}(x, y, z)$ with respect to the local coordinate systems. In the undeformed and deformed configurations, adjacent base cells must always fit together at the boundaries. Moreover, for a homogeneous stress field, cells lying far from the boundaries are subjected to the same loading conditions and will deform in the same manner. The possible shape of the cells in undeformed and deformed configurations are limited in such a way, therefore, that the boundaries of opposing sides of the base cell always have the same shape.

As an introductory example a two-dimensional case is studied in which the base cell consists basically of four corners connected by four curves. Figure 4.3 shows such a rectangular base cell in an undeformed and a deformed state with the material coordinates (x, y), displacements (u, v) and length of the sides (l_x, l_y).

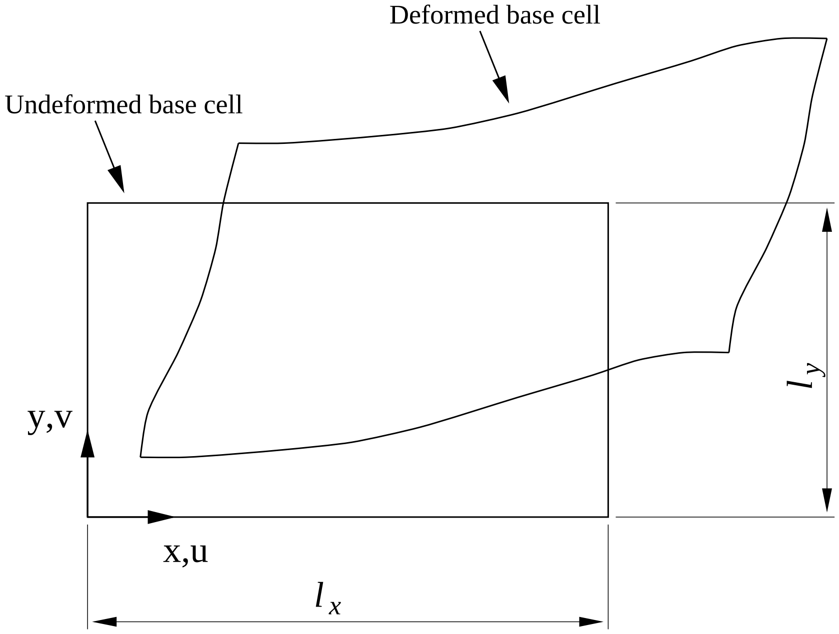

Figure 4.3: *Two-dimensional base cell in undeformed and deformed state.*

The identical shapes and sizes of opposite boundary surfaces of the base cell allow relations between displacements on the boundaries to be established. Although the shape of the base cell can arbitrarily be considered periodic, for simplicity the shape is assumed here to be a right prism in an undeformed state, yielding

$$\begin{aligned} u_i(l_x, y, z) &= u_i(0, y, z) + A_{i1} l_x \\ u_i(x, l_y, z) &= u_i(x, 0, z) + A_{i2} l_y \qquad i = 1, 2, 3 \\ u_i(x, y, l_z) &= u_i(x, y, 0) + A_{i3} l_z \end{aligned} \tag{4.7}$$

where A_{ij} represents nine constants. In Eq.(4.7) the notations $u_1 = u$, $u_2 = v$ and $u_3 = w$ can be used and in the same way $x_1 = x$, $x_2 = y$, $x_3 = z$, $l_1 = l_x$, $l_2 = l_y$ and $l_3 = l_z$ where l_i denotes the base cell length in direction x_i. In accordance with

Eq.(4.7), the elements A_{ij} in the matrix $\mathbf{A}$ are

$$\mathbf{A} = \begin{bmatrix} \dfrac{u(l_x,y,z)-u(0,y,z)}{l_x} & \dfrac{u(x,l_y,z)-u(x,0,z)}{l_y} & \dfrac{u(x,y,l_z)-u(x,y,0)}{l_z} \\ \dfrac{v(l_x,y,z)-v(0,y,z)}{l_x} & \dfrac{v(x,l_y,z)-v(x,0,z)}{l_y} & \dfrac{v(x,y,l_z)-v(x,y,0)}{l_z} \\ \dfrac{w(l_x,y,z)-w(0,y,z)}{l_x} & \dfrac{w(x,l_y,z)-w(x,0,z)}{l_y} & \dfrac{w(x,y,l_z)-w(x,y,0)}{l_z} \end{bmatrix} \tag{4.8}$$

The column j of A refers to the bounding surface normal to the x_j-direction.

Since all the cells are identical and the outward normals n_j to the base cell have opposite signs on opposing sides of the base cell, the tractions $t_i = \sigma_{ji}n_j$ are also opposite on opposing sides of the base cell. Accordingly, the tractions t_i are termed anti-periodic and one can write

$$\begin{aligned} t_i(l_x,y,z) &= -t_i(0,y,z) \\ t_i(x,l_y,z) &= -t_i(x,0,z) \\ t_i(x,y,l_z) &= -t_i(x,y,0) \end{aligned} \tag{4.9}$$

With the periodicity introduced, the equilibrium equation Eq.(4.1) for a linear elastic case involving infinitesimal displacements and no body forces can be written as

$$\begin{cases} \dfrac{\partial \sigma_{ji}}{\partial x_j} = 0 & \text{in } \mathbf{\Omega} \\ t_i = \sigma_{ji}n_j & t_i \text{ anti-periodic on } \mathbf{\Gamma} \\ u_i & \text{periodic on } \mathbf{\Gamma} \end{cases} \tag{4.10}$$

over the base cell volume $\mathbf{\Omega}$, with cyclic boundary conditions on the boundary surface $\mathbf{\Gamma}$. Adopting the Galerkin method, where $v_i = u_i$, and assuming no body forces, the weak formulation of Eq.(4.10) can be written, according to Eq.(4.4) as

$$\int_{\mathbf{\Omega}} \frac{\partial u_i}{\partial x_j}\sigma_{ij}\, d\mathbf{\Omega} = \int_{\mathbf{\Gamma}} u_i t_i \, d\mathbf{\Gamma} \tag{4.11}$$

the boundary constraints for the displacements being in accordance with Eq.(4.7).

The boundary $\mathbf{\Gamma}$ can be split up into three parts $\mathbf{\Gamma} = 2\mathbf{\Gamma}_1 + 2\mathbf{\Gamma}_2 + 2\mathbf{\Gamma}_3$ where $2\mathbf{\Gamma}_j$ contains the two surfaces normal to the x_j-direction. This allows Eq.(4.11) to be written as

$$\int_{\mathbf{\Omega}} \frac{\partial u_i}{\partial x_j}\sigma_{ij}\, d\mathbf{\Omega} = \sum_{j=1}^{3} \Delta u_i \int_{\mathbf{\Gamma}_j} t_i \, d\mathbf{\Gamma} \tag{4.12}$$

where $\mathbf{\Gamma}_j$ is one of the two surfaces normal to the x_j-direction. It should be observed that Δu_i in Eq.(4.12) has different constant values for $j = 1, 2, 3$. According Eq.(4.8), one can write

$$\Delta u_i = A_{ij} l_{<j>} \tag{4.13}$$

where the bracketed index indicates that the summation convention is not applied and where $l_1 = l_x$, $l_2 = l_y$ and $l_3 = l_z$. With use of Eq.(4.13), one can write Eq.(4.12) as

$$\int_{\mathbf{\Omega}} \frac{\partial u_i}{\partial x_j} \sigma_{ij}\, d\mathbf{\Omega} = A_{ij} l_{<j>} \int_{\mathbf{\Gamma}_j} t_i\, d\mathbf{\Gamma} \tag{4.14}$$

Still assuming the base cell to be a right prism in the undeformed state, the average stresses (tractions) on the boundary surfaces can be defined as

$$B_{ij} = \frac{1}{\mathbf{\Gamma}_i} \int_{\mathbf{\Gamma}_{<i>}} t_j\, d\mathbf{\Gamma} \tag{4.15}$$

where $\mathbf{\Gamma}_i$ refers to a surface normal to the x_i-direction. Eq.(4.14) can then be rewritten as

$$\int_{\mathbf{\Omega}} \frac{\partial u_i}{\partial x_j} \sigma_{ij}\, d\mathbf{\Omega} = \mathbf{\Omega} A_{ij} B_{ij} \tag{4.16}$$

where the base cell volume $\mathbf{\Omega} = l_x l_y l_z$. For small macroscale deformations, the average strains can be defined as

$$\bar{\epsilon}_{ij} = \frac{1}{2}(A_{ij} + A_{ji}) \tag{4.17}$$

and, correspondingly, the average stresses as

$$\bar{\sigma}_{ij} = \frac{1}{2}(B_{ij} + B_{ji}) \tag{4.18}$$

The expressions for the average strains and stresses are then substituted into Eq.(4.16) and since B_{ij} is symmetric one obtains

$$\int_{\mathbf{\Omega}} \frac{\partial u_i}{\partial x_j} \sigma_{ij}\, d\mathbf{\Omega} = \mathbf{\Omega}\, \bar{\epsilon}_{ij} \bar{\sigma}_{ij} \tag{4.19}$$

If local cavities appear in the base cell, they are treated as consisting of a material having zero stiffness.

4.3.2. Equivalent stiffness and hygroexpansion properties

A linear elastic material including hygroexpansion is assumed. The constitutive relations for such a material are

$$\sigma_{ij} = D_{ijkl}(\epsilon_{kl} - \epsilon^s_{kl}) \tag{4.20}$$

The hygroexpansion strains ϵ^s_{kl} may be expressed as

$$\epsilon^s_{kl} = \alpha_{kl} \Delta w \tag{4.21}$$

where α_{kl} represents the hygroexpansion coefficients and Δw is the change in moisture content. Due to the inhomogeneous material properties of the base cell, both D_{ijkl} and α_{kl} can vary markedly in space.

The material within the base cell is now assumed to be replaced by an equivalent fictitious material with constant stiffness and hygroexpansion properties denoted by $\bar{D}_{ijkl}$ and $\bar{\alpha}_{kl}$, respectively. With constant moisture content, the constitutive relation becomes

$$\bar{\sigma}_{ij} = \bar{D}_{ijkl}\bar{\epsilon}_{kl} \tag{4.22}$$

having the inverse relationship

$$\bar{\epsilon}_{ij} = \bar{C}_{ijkl}\bar{\sigma}_{kl} \tag{4.23}$$

A simple way of defining the constitutive parameters in Eqs.(4.22) and (4.23) is to choose six elementary cases of either stress or strain states. In the case of stress states chosen, the corresponding stress tensors are

$$\begin{gathered}
\begin{bmatrix} 1 & 0 & 0 \\ 0 & 0 & 0 \\ 0 & 0 & 0 \end{bmatrix} \quad \begin{bmatrix} 0 & 0 & 0 \\ 0 & 1 & 0 \\ 0 & 0 & 0 \end{bmatrix} \quad \begin{bmatrix} 0 & 0 & 0 \\ 0 & 0 & 0 \\ 0 & 0 & 1 \end{bmatrix} \\
\begin{bmatrix} 0 & 1 & 0 \\ 1 & 0 & 0 \\ 0 & 0 & 0 \end{bmatrix} \quad \begin{bmatrix} 0 & 0 & 1 \\ 0 & 0 & 0 \\ 1 & 0 & 0 \end{bmatrix} \quad \begin{bmatrix} 0 & 0 & 0 \\ 0 & 0 & 1 \\ 0 & 1 & 0 \end{bmatrix}
\end{gathered} \tag{4.24}$$

Note that, due to the unit stress value found for each of the six cases in Eq.(4.24), one can identify that

$$\begin{aligned} \bar{C}_{ijkl} &= \bar{\epsilon}_{ij} && \text{for } k = l \\ \bar{C}_{ijkl} = \bar{C}_{ijlk} &= \frac{1}{2}\bar{\epsilon}_{ij} && \text{for } k \neq l \end{aligned} \tag{4.25}$$

For the shrinkage parameters, the averaging can be performed in a similar way. Prescribing for a seventh case that $\bar{\sigma}_{kl} = 0$ for all k and l and that $\Delta w = 1$ yields the relation

$$\bar{\alpha}_{kl} = \bar{\epsilon}_{kl} \tag{4.26}$$

Thus, the constitutive parameters can be identified on the basis of seven elementary cases involving either prescribed average tractions or a change in moisture content.

4.4. Finite Element Method

4.4.1. General

The finite element method is a well established method for solving partial differential equations. A large number of books on the subject have been written, see for example Ottosen and Petersson [50], Zienkiewicz and Taylor [72] and ABAQUS [28]. In this section, a brief presentation of the basic finite element equations will be provided.

4.4.2. Finite element formulation

The finite element formulation is obtained by discretizing the displacement field **u**. This is done by interpolating the displacements between the nodal points according to

$$u_i = N_{ik} a_k \tag{4.27}$$

where N_{ik} are shape functions and a_k are nodal displacements.

Adopting the Galerkin method, the weight functions v_i introduced in Eq.(4.2) are selected as

$$v_i = N_{il} c_l \tag{4.28}$$

where c_l are components of an arbitrary vector. The gradient of the weight functions can now be expressed as

$$\frac{\partial v_i}{\partial x_j} = c_l \frac{\partial N_{il}}{\partial x_j} \tag{4.29}$$

The weak formulation given by Eq.(4.5) can then be written

$$c_l \left(\int_{\mathbf{\Omega_0}} \frac{\partial N_{il}}{\partial x_j} \tau_{ji} \, d\mathbf{\Omega_0} \right) = c_l \left(\int_{\mathbf{\Omega}} N_{il} b_i \, d\mathbf{\Omega} + \int_{\mathbf{\Gamma}} N_{il} t_i \, d\mathbf{\Gamma} \right) \tag{4.30}$$

This equation must be valid for all values of c_l, which means that a system of nonlinear equilibrium equations is obtained

$$\int_{\mathbf{\Omega_0}} \frac{\partial N_{il}}{\partial x_j} \tau_{ji} \, d\mathbf{\Omega_0} = \int_{\mathbf{\Omega}} N_{il} b_i \, d\mathbf{\Omega} + \int_{\mathbf{\Gamma}} N_{il} t_i \, d\mathbf{\Gamma} \tag{4.31}$$

This system can also be written as

$$P_l^{int} - P_l^{ext} = 0 \tag{4.32}$$

where

$$\begin{cases} P_l^{int} = \displaystyle\int_{\mathbf{\Omega_0}} \frac{\partial N_{il}}{\partial x_j} \tau_{ji} \, d\mathbf{\Omega_0} \\ P_l^{ext} = \displaystyle\int_{\mathbf{\Omega}} N_{il} b_i \, d\mathbf{\Omega} + \int_{\mathbf{\Gamma}} N_{il} t_i \, d\mathbf{\Gamma} \end{cases} \tag{4.33}$$

4.4.3. Nonlinear solution method

In the description that follows, it is convenient to use matrix notation. The general nonlinear problem of Eq.(4.32) can be written in terms of the displacement vector **a** as

$$\mathbf{G}(\mathbf{a}_{n+1}) = \mathbf{P}^{ext}(\mathbf{a}_{n+1}) - \mathbf{P}_{n+1}^{int} = 0 \tag{4.34}$$

where **G** is the residual or out-of-balance vector. Due to Eq.(4.34) being a nonlinear system of equations, it is solved in an iterative manner. This is done using the Newton-Raphson method, a solution method that normally provides quadratic convergence for nonlinear equation systems. The principle of this method is to start

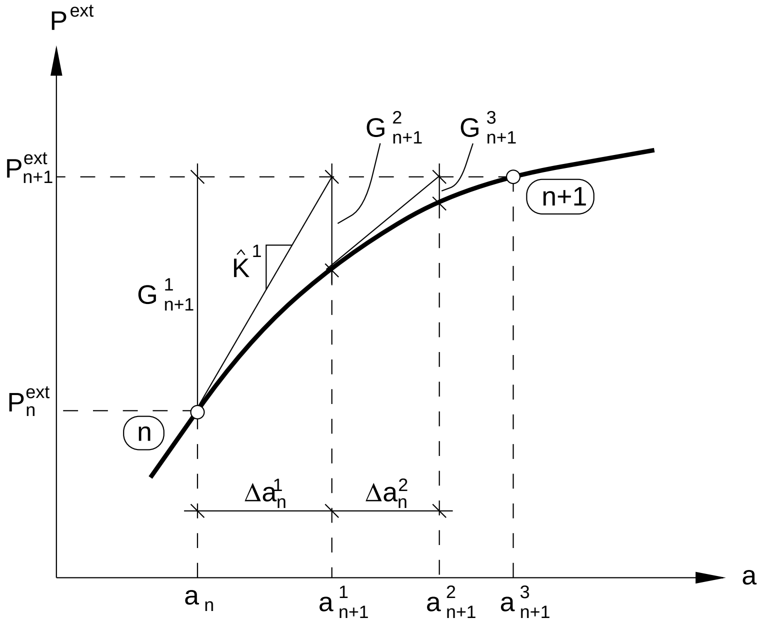

Figure 4.4: *The Newton Raphson method illustrated for a one-degree-of-freedom system.*

with an iteration from an equilibrium state to obtain an approximation to the solution. By successive iterations the approximation to the initial solution is improved until equilibrium is satisfied sufficiently well. In the iteration, Eq.(4.34) can be approximated to the first order as

$$\mathbf{G}(\mathbf{a}^{i+1}_{n+1}) \;\approx\; \mathbf{G}(\mathbf{a}^{i}_{n+1}) \;+\; \left(\frac{\partial \mathbf{G}}{\partial \mathbf{a}}\right)^{i}_{n+1} \Delta\mathbf{a}^{i}_{n} \;=\; 0 \tag{4.35}$$

Here i is the iteration counter starting from

$$\mathbf{a}^{1}_{n+1} = \mathbf{a}_{n} \tag{4.36}$$

and

$$\frac{\partial \mathbf{G}}{\partial \mathbf{a}} = \hat{\mathbf{K}} \tag{4.37}$$

is the Jacobian matrix. Eq.(4.35) gives the iterative correction as

$$\Delta\mathbf{a}^{i}_{n} = -(\hat{\mathbf{K}}^{i})^{-1}\mathbf{G}^{i}_{n+1} \tag{4.38}$$

A series of successive iterations gives

$$\mathbf{a}^{i+1}_{n+1} = \mathbf{a}^{i}_{n+1} + \Delta\mathbf{a}^{i}_{n} \tag{4.39}$$

This process is illustrated in Figure 4.4 for a one-degree-of-freedom system. The criterion to be used for stopping the iteration process is based on all the entries in both $\mathbf{G}$ and $\Delta\mathbf{a}$ being sufficiently small.

The Jacobian matrix $\hat{\mathbf{K}}$ used in the Newton Raphson scheme is derived by differentiating Eq.(4.34) with respect to $\mathbf{a}_{n+1}$ as

$$\frac{\partial \mathbf{G}}{\partial \mathbf{a}_{n+1}} = \hat{\mathbf{K}}_{n+1} = \frac{\partial \mathbf{P}^{ext}}{\partial \mathbf{a}_{n+1}} - \frac{\partial \mathbf{P}^{int}}{\partial \mathbf{a}_{n+1}} \tag{4.40}$$

$\partial \mathbf{P}^{int}/\partial \mathbf{a}_{n+1}$, representing the variation of internal forces with displacement, is generally referred to as the tangent stiffness matrix $\mathbf{K}_T$. It is derived by differentiating the first equation in Eq.(4.33) with respect to $\mathbf{a}$. In component form it becomes

$$K_{lk} = \int_{\mathbf{\Omega_0}} \frac{\partial N_{il}}{\partial x_j} \frac{\partial \tau_{ji}}{\partial a_k} \, d\mathbf{\Omega}_0 + \int_{\mathbf{\Omega_0}} \frac{\partial}{\partial a_k} \left(\frac{\partial N_{il}}{\partial x_j} \right) \tau_{ji} \, d\mathbf{\Omega}_0 \tag{4.41}$$

where the first term corresponds to the usual small displacement stiffness matrix, except that the term $\partial N_{il}/\partial x_j$ is a function of displacement, and where the second term is the initial stress matrix.

$\partial \mathbf{P}^{ext}/\partial \mathbf{a}_{n+1}$, describing the dependence of the external forces upon the geometry, is generally referred to as the load stiffness or load correction matrix $\mathbf{K}_{load}$. It can be derived from the second equation in Eq.(4.33). Using these definitions, the Jacobian matrix can be written as

$$\hat{\mathbf{K}} = \mathbf{K}_T - \mathbf{K}_{load} \tag{4.42}$$

For a review of different techniques of solving nonlinear problems, see e.g. Zienkiewicz and Taylor [72] or Owen and Hinton [52].

4.4.4. Solution method for linear elasticity

For small displacements, a linear strain relation is used, defined in terms of the displacements u_i as

$$\epsilon_{kl} = \frac{1}{2}(\frac{\partial u_k}{\partial x_l} + \frac{\partial u_l}{\partial x_k}) \tag{4.43}$$

Adopting a matrix format and assuming a linear elastic stress-strain relation, Hooke's law with hygroexpansion is written as

$$\boldsymbol{\sigma} = \mathbf{D}(\boldsymbol{\epsilon} - \boldsymbol{\epsilon}^s) \tag{4.44}$$

Using Eq.(4.44) and Eq.(4.43), Eq.(4.32) can be written for a linear elastic case as

$$\mathbf{P}^{int} - \mathbf{P}^{ext} = 0 \tag{4.45}$$

where

$$\begin{cases} \mathbf{P}^{int} = \mathbf{Ka} \\ \\ \mathbf{P}^{ext} = \mathbf{f} + \mathbf{f}^{\mathrm{s}} \end{cases} \tag{4.46}$$

The stresses and the strains are represented by vectors $\boldsymbol{\sigma}$, $\boldsymbol{\epsilon}$ and $\boldsymbol{\epsilon}^s$. Eq.(4.31) can now be written

$$\mathbf{Ka} = \mathbf{f} + \mathbf{f}^{\mathrm{s}} \tag{4.47}$$

where the stiffness matrix $\mathbf{K}$ and the force vector $\mathbf{f}$ can be written as

$$\begin{cases} \mathbf{K} = \int_{\boldsymbol{\Omega}} \mathbf{B}^{\mathbf{T}} \mathbf{D}\, \mathbf{B}\, \mathbf{d}\boldsymbol{\Omega} \\ \mathbf{f} = \int_{\boldsymbol{\Omega}} \mathbf{N}^{\mathbf{T}}\, \mathbf{b}\, \mathbf{d}\boldsymbol{\Omega} + \int_{\boldsymbol{\Gamma}} \mathbf{N}^{\mathbf{T}}\, \mathbf{t}\, \mathbf{d}\boldsymbol{\Gamma} \\ \mathbf{f}^{\mathrm{s}} = \int_{\boldsymbol{\Omega}} \mathbf{B}^{\mathbf{T}}\, \mathbf{D}\boldsymbol{\epsilon}^{\mathrm{s}}\, \mathbf{d}\boldsymbol{\Omega} \end{cases} \tag{4.48}$$

where

$$\mathbf{N} = \begin{bmatrix} N_{1n} \\ N_{2n} \\ N_{3n} \end{bmatrix} \qquad \mathbf{t} = \begin{bmatrix} t_1 \\ t_2 \\ t_3 \end{bmatrix} \qquad \mathbf{b} = \begin{bmatrix} b_1 \\ b_2 \\ b_3 \end{bmatrix} \tag{4.49}$$

n being the number of nodal points and $\mathbf{B} = \tilde{\nabla}\mathbf{N_n}$, where

$$\tilde{\nabla} = \begin{bmatrix} \frac{\partial}{\partial x_1} & 0 & 0 \\ 0 & \frac{\partial}{\partial x_2} & 0 \\ 0 & 0 & \frac{\partial}{\partial x_3} \\ \frac{\partial}{\partial x_2} & \frac{\partial}{\partial x_1} & 0 \\ \frac{\partial}{\partial x_3} & 0 & \frac{\partial}{\partial x_1} \\ 0 & \frac{\partial}{\partial x_3} & \frac{\partial}{\partial x_2} \end{bmatrix} \tag{4.50}$$

The strains, which can be determined from the displacements of the nodal points $\mathbf{a}$ and the matrix $\mathbf{B}$, are given by

$$\boldsymbol{\epsilon} = \mathbf{B}\,\mathbf{a} \tag{4.51}$$

and the stresses by

$$\boldsymbol{\sigma} = \mathbf{D}\mathbf{B}\,\mathbf{a} - \mathbf{D}\boldsymbol{\epsilon}^{s} \tag{4.52}$$

In the application of the finite element method, the body is divided into a large number of finite elements, where the interpolation functions are non-zero over a limited subdomain only. Integration is performed for each element separately, the resulting element equations being assembled into a global system of equations. In the present report, 20-node isoparametric three-dimensional elements with reduced integration and 8-node isoparametric shell elements are employed. These elements, which have quadratic interpolation functions, are described in detail by Zienkiewicz and Taylor [72] and Owen and Hinton [52].

4.4.5. Nonlinear material behaviour

In large-strain analysis of wood cell structures, the material description of the cell wall layers needs to be extended so as to incorporate nonlinear effects. This can be done by adopting an orthotropic elasto-plastic material model such as that proposed by Hill [29]. When the axes of the 123-coordinate system coincide with the axes of orthotropy, the Hill yield criterion is given by

$$\begin{gathered} f(\boldsymbol{\sigma}) = a_1 (\sigma_{22} - \sigma_{33})^2 + a_2 (\sigma_{33} - \sigma_{11})^2 + a_3 (\sigma_{11} - \sigma_{22})^2 \\ + a_4 \sigma_{23}^2 + a_5 \sigma_{13}^2 + a_6 \sigma_{12}^2 - \sigma_{ref}^2 = 0 \end{gathered} \tag{4.53}$$

where $\boldsymbol{\sigma}$ is the stress tensor. The material parameters a_1 to a_6 are expressed as

$$\begin{aligned} a_1 &= \frac{\sigma_{ref}^2}{2}\left(\frac{1}{\sigma_{22y}^2} + \frac{1}{\sigma_{33y}^2} - \frac{1}{\sigma_{11y}^2}\right) & a_4 &= \frac{\sigma_{ref}^2}{\sigma_{23y}^2} \\ a_2 &= \frac{\sigma_{ref}^2}{2}\left(\frac{1}{\sigma_{33y}^2} + \frac{1}{\sigma_{11y}^2} - \frac{1}{\sigma_{22y}^2}\right) & a_5 &= \frac{\sigma_{ref}^2}{\sigma_{13y}^2} \\ a_3 &= \frac{\sigma_{ref}^2}{2}\left(\frac{1}{\sigma_{11y}^2} + \frac{1}{\sigma_{22y}^2} - \frac{1}{\sigma_{33y}^2}\right) & a_6 &= \frac{\sigma_{ref}^2}{\sigma_{12y}^2} \end{aligned} \tag{4.54}$$

where σ_{ijy} are the yield stresses with respect to the orthotropic directions i and j and σ_{ref} is a reference stress. The Hill yield criterion is an extended form of the von Mises criterion for isotropic materials. When the parameters a_1 to a_6 satisfy

$$6a_1 = 6a_2 = 6a_3 = a_4 = a_5 = a_6, \tag{4.55}$$

Eq.(4.53) reduces to the von Mises criterion.

The parameters a_1 to a_6 cannot be chosen arbitrarily. The yield surface must be a closed surface in the deviatoric stress plane. This leads to the following constraint

$$\frac{4}{\sigma_{11y}^2 \sigma_{22y}^2} > \left[\frac{1}{\sigma_{33y}^2} - \left(\frac{1}{\sigma_{11y}^2} + \frac{1}{\sigma_{22y}^2}\right)\right]^2 \tag{4.56}$$

This inequality restricts the degree of orthotropy for which application of Hill's criterion is permissible.

For the various cell wall layers, the yield stresses σ_{ijy} and the reference stress σ_{ref} in Eq.(4.53) need to be determined. The choice of these parameters will be discussed further in the sections that follow. For convenience, six parameters $r_{i,j}$ are introduced as

$$\begin{aligned} r_{11} &= \frac{\sigma_{11y}}{\sigma_{ref}}, & r_{22} &= \frac{\sigma_{22y}}{\sigma_{ref}}, & r_{33} &= \frac{\sigma_{33y}}{\sigma_{ref}}, \\ r_{12} &= \sqrt{3}\frac{\sigma_{12y}}{\sigma_{ref}}, & r_{13} &= \sqrt{3}\frac{\sigma_{13y}}{\sigma_{ref}}, & r_{23} &= \sqrt{3}\frac{\sigma_{23y}}{\sigma_{ref}}, \end{aligned} \tag{4.57}$$

The parameters a_1 to a_6 can now be written in terms of $r_{i,j}$. The integration of the plasticity equations can be found in several references, see for example Ottosen et al. [51].

4.5. Concluding Remarks

In the thesis, a large number of simulations of wood and fibre properties are described, all of which were performed using the general-purpose finite element program ABAQUS [28]. The finite element formulation and solution technique used by the program were outlined in the present chapter.

To determine the average stiffness and shrinkage properties, the equations in the homogenisation procedure were solved using the finite element method. The base cell was then discretized into finite elements and subjected to periodic boundary conditions and to the six elementary cases of mean stress tensors. Periodic boundary conditions were implemented by use of constraint equations through equating the nodal displacements at opposite sides of the base cell in each direction, in accordance with Eq.(4.7). The equivalent average stiffness and shrinkage parameters were then determined according to the procedure outlined in section 4.3.2.

In studies of the behaviour of cell structures subjected to large compressive deformations ABAQUS was used with the nonlinear finite element formulation described in this chapter. In addition to the linear elastic material behaviour of the cell wall layers, nonlinear effects were included through adopting Hill's orthotropic plasticity model. Since the nonlinear effects in the cell walls are of varying nature and only very limited experimental data on this are available, the choice of a material model and of its material parameters is not obvious, matters that will be treated further in a later chapter.

5. MODELLING OF MECHANICAL PROPERTIES OF WOOD

5.1. Introduction

In determining the equivalent average mechanical properties of wood from models of its microstructure, a common task is to determine an equivalent volume element representative of the microstructure. In this chapter a chain of geometrical and mechanical models of the microstructure of wood are presented. The microstructure of wood is divided into a hierarchy consisting of three geometric levels: the microfibril level, the fibre level and the cell structure level. The models chosen are regarded then as being representative elements of the wood microstructure at each structural level. The models developed are utilised in Chapters 6, 7 and 8 with the aim of determining linear and nonlinear homogenised properties of wood and fibres by means of numerical simulations. Since the geometrical models are to be used in numerical simulations involving the finite element method, certain approximations of the microstructure are introduced. However, the aim is to model the microstructure of wood and of wood fibres so as to approximate the real structures in such a way that the impact on the mechanical properties of wood is as small as possible. The geometry of the wood and the fibre microstructure presented is based on the measurements presented in Chapter 3 and on the literature.

Different approaches to deriving the material properties of wood through micromechanical modelling of the wood structure have been adopted earlier. The first reported attempt was made already in 1928 by Price [58], who achieved analytical solutions for the stiffness of wood through modelling the cells as circular tubes. Price demonstrated the high degree of anisotropy of the stiffness in the longitudinal direction as compared with the radial and the tangential directions, but provided no explanation for the differences in stiffness between the radial and the tangential directions.

In more recent approaches, wood cells have been treated as parts of a hexagonal cellular structure. Gibson and Ashby [23] have provided a detailed description of the calculation of the equivalent mechanical properties of cellular solids, of which wood is an example. A drawback of this approach is that it is limited to the study of one cell at a time, so that the properties it provides are those of a material of uniform density. Their study was also limited by its deriving the properties of a regular two-dimensional honeycomb structure, whereas wood has a three-dimensional and more irregular cell structure. An analytical model has also been developed by Thuvander [69]. This model is restricted to the determination of the stiffness and shrinkage properties in the longitudinal and tangential directions of the cell wall only, which is achieved through composite theory. Koponen et al. [36], [37] derived the shrinkage and stiffness properties of wood as a two-dimensional regular honeycomb structure, determining the properties of earlywood and latewood separately through using different densities and cell wall properties for these two wood regions. The average properties for a complete growth ring were not derived. Kahle and Woodhouse [32] determined the stiffness properties of wood by dividing the growth ring into earlywood, transitionwood and latewood. Each of the three regions, seen as being of uniform density, was modelled in terms of irregular hexagonal cell structures. The three regions were combined to form a complete annual ring, the stiffness properties of which were determined by analytical solutions. Modelling of the structure of real wood cells was performed by Stefansson [65], the cell structure being determined on the basis of micrographs and being modelled by use of finite elements. A similar approach has also been employed by Astley et al. [3],[4] and Harrington et al. [24], who also analysed wood properties on the basis of hexagonal structures through use of the finite element method.

In this chapter, the equivalent stiffness and shrinkage properties of wood will be determined by use of a micromechanical approach in which certain of the ideas contained in the earlier studies have been adopted. A homogenisation method is employed in which the partial differential equations are solved by use of the finite element method. The methods to be employed were described briefly in Chapter 4. Figure 5.1 shows a scheme of the basic steps involved in determining the equivalent material properties.

The equivalent properties of wood and of fibres are determined in two major steps. First, the equivalent properties of the different cell walls are calculated from the known properties of cellulose, hemicellulose and lignin as described briefly in Section 2.4. The geometry of the microfibril is simplified to its being seen as composed of repetitive units allowing homogenisation theory to be employed. Microfibril models of different geometries, for which the fractions of the chemical constituents also differ, are created for representing the different layers of the cell wall. The equivalent properties are then determined from these microfibril models by use of the homogenisation method. Transformations of the material stiffness are made so as to express the material properties given in terms of the local microfibril directions in the global directions involved. For each layer of the cell wall, a separate material is applied and transformation computations are performed, corresponding to the structure of each particular layer.

The second major step in modelling here is to determine the equivalent properties of the fibres and of the wood structure. The modelling of the wood cell structures is approached in two different ways. One is to model the real cell structures as selected from micrographs, these cell structures being assumed to be representative of the cell

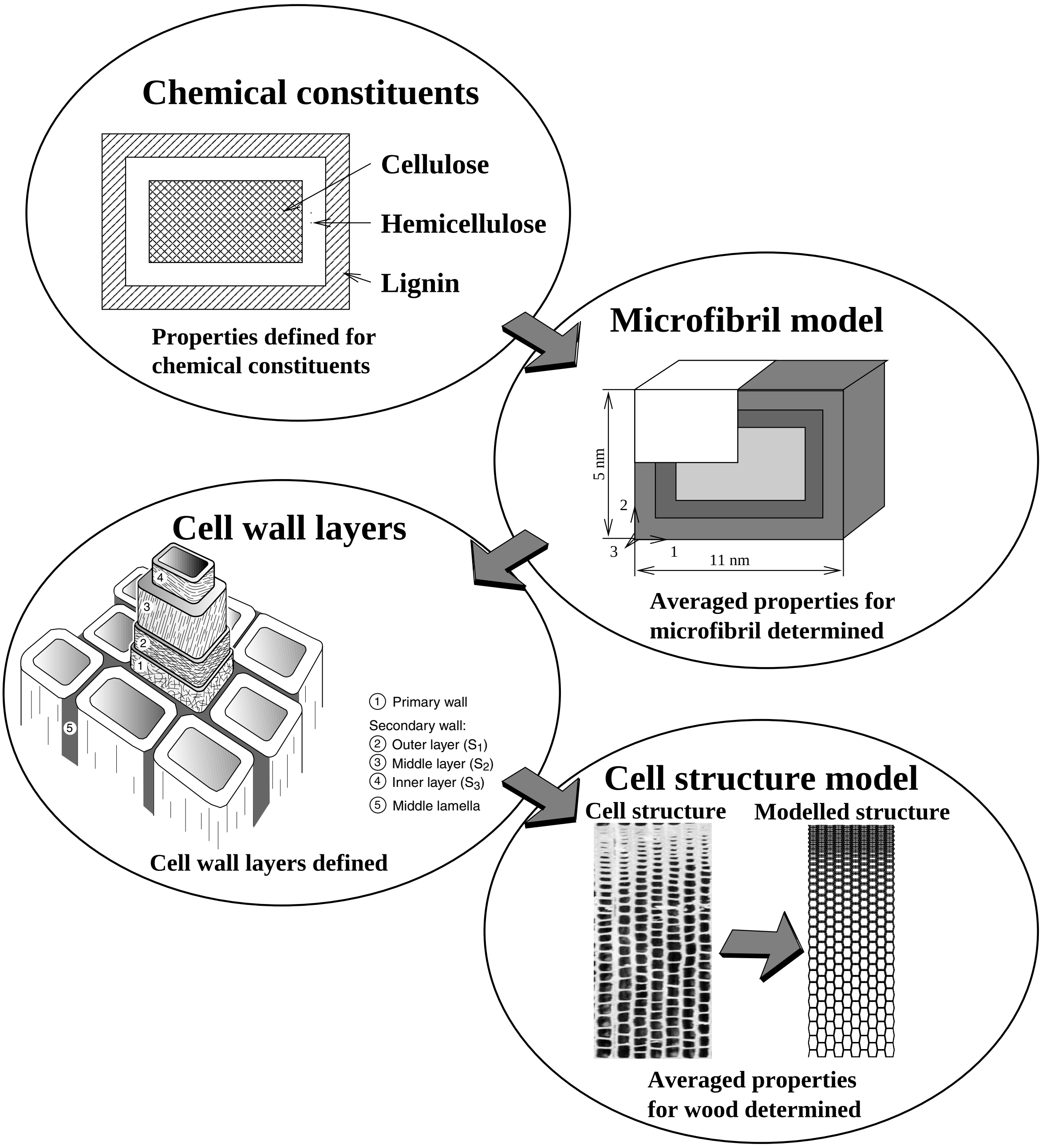

Figure 5.1: *Modelling scheme of the basic steps involved in determining the equivalent material properties.*

structures in the wood generally. Another approach is to model the cell structure on the basis of a fictitious cell structure which has properties representative of those in a real cell structure. Here, a model of a three-dimensional wood cell structure involving irregular hexagonal cells is created, the geometry of the structure being based on micrographs and on the microstructural measurements presented in Sections 3.2 and 3.3.

To calculate all the properties of wood for which the widths and densities and thus the mechanical properties of the growth rings differ, it is necessary that the structural model chosen be able to represent different cell structures. The variation in density over the growth ring is the governing parameter of the cell structure shape in both of the models, allowing complete structures of growth rings to be modelled. The stiffness and shrinkage properties of a growth ring of arbitrary width and average density can be determined then by the combined use of a homogenisation procedure and the finite element method.

5.2. Modelling Properties of the Cell Wall Layers

5.2.1. General remarks

In this section, numerical models aimed at determining the stiffness properties and the hygroexpansion coefficients of the cell walls are presented. The numerical models are based on geometrical models of the microfibrils and the properties of cellulose, hemicellulose and lignin. Geometric models of microfibrils based on models found in the literature are presented first. From the numerical models, the stiffness and the shrinkage properties of the cell wall layers are calculated.

5.2.2. Geometric models of microfibrils and cell wall layers

The basic element in the cell wall is the microfibril, which is chosen as the representative volume element of all of the various layers in the cell wall. A microfibril is assumed to be a repetitive unit of the microstructure, the microfibrils being assumed to be of equal size and shape throughout each cell wall layer. Accordingly, the organisation of the constituents of the microfibril, as shown in Figure 2.5, need to be simplified to that of a repetitive element. Several simplified models of the microfibril organisation formed as repetitive elements have been proposed. The geometrical shapes of the cross section of the various models are similar, however. In the two models studied here, the cellulose chains are assumed to be located in the centre, surrounded by hemicellulose and lignin as the matrix materials, Figure 5.2. The models differ in the coupling of the constituents and differ therefore, in their homogenised properties. Since the microfibrils are very long in comparison to their cross sectional dimensions, the models discussed here are assumed to be infinite in the longitudinal direction. The organisation of the chemical constituents in the ultrastructure is not fully known, although recent studies indicate that the model

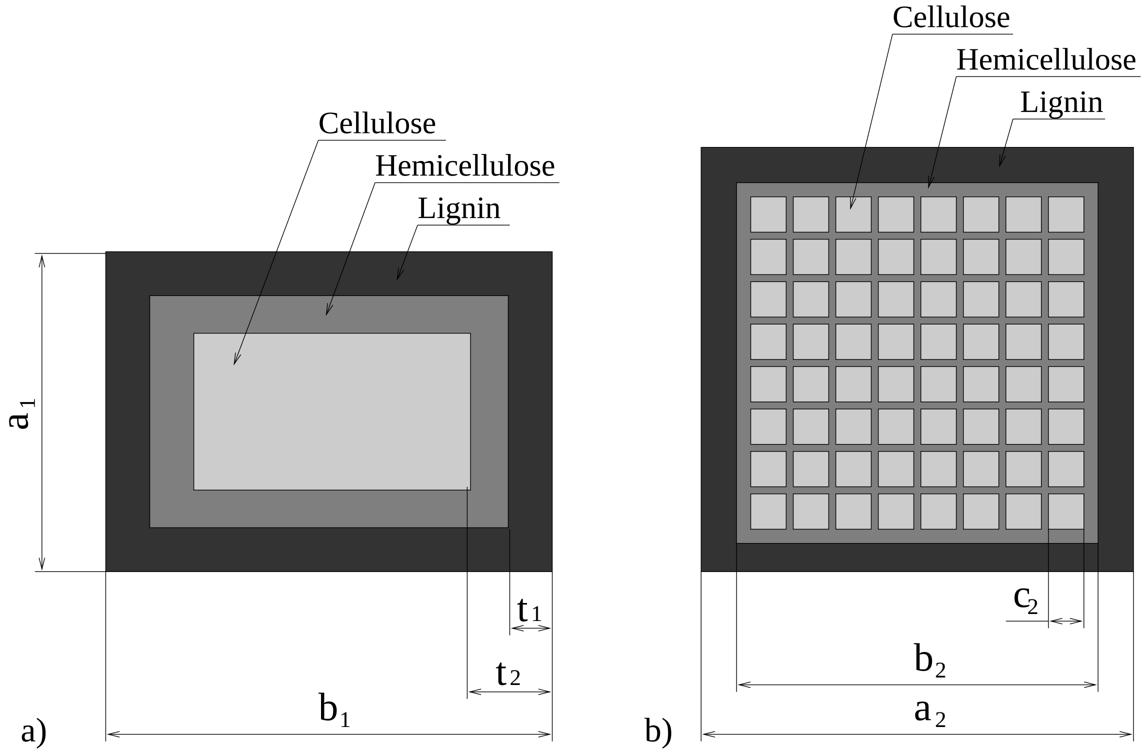

Figure 5.2: *Simplified models of the cross section of the microfibril.* **a***) According to Preston [57].* **b***) According to Fengel [22].*

shown in Figure 5.2.a seems to be more correct than that shown in Figure 5.2.b, Salmén [62].

The fractions of the constituents are not the same in the different layers of the cell wall, the lignin content being high in the middle lamella and decreasing towards the lumen, Figure 2.6. Differences in the volume fractions of the constituents are reflected in the internal geometry of the microfibril model employed. For the microfibril model shown in Figure 5.2.a, different volume fractions of the chemical constituents are assumed to simply change the thickness of the hemicellulose and lignin layers and the size of the cellulose core, Figure 5.2.a. With f_C, f_H and f_L being the volume fractions of the cellulose, hemicellulose and lignin, respectively and a_1, b_1, t_1 and t_2 being defined according to Figure 5.2.a, the volume fractions for this microfibril model are written as

$$\begin{aligned} f_L &= \frac{a_1 b_1 - (a_1 - 2t_1)(b_1 - 2t_1)}{a_1 b_1} \\ f_H &= \frac{(a_1 - 2t_1)(b_1 - 2t_1) - (a_1 - 2t_2)(b_1 - 2t_2)}{a_1 b_1} \\ f_C &= \frac{(a_1 - 2t_2)(b_1 - 2t_2)}{a_1 b_1} \end{aligned} \tag{5.1}$$

Solving the first and last equations above for t_1 and t_2 yields

$$\begin{aligned} t_1 &= \frac{1}{4}\left(a_1 + b_1 - \sqrt{(a_1+b_1)^2 - 4\,a_1 b_1\, f_L}\,\right) \\ t_2 &= \frac{1}{4}\left(a_1 + b_1 - \sqrt{(a_1+b_1)^2 - 4\,a_1 b_1\,(1-f_C)}\,\right) \end{aligned} \tag{5.2}$$

The values of a_1 and b_1 are assumed to be equal for microfibrils that differ in the fractions of their constituents. Preston suggested values of 5 and 10 nm for a_1 and b_1, respectively, whereas Koponen et al. [36] used the model of Preston with values of 5 and 11 nm. Employing the values of a_1=5nm and b_1=11 nm and using f_C+f_H+f_L=1, the internal geometry of this microfibril model can be determined for various fractions of the chemical constituents.

For the microfibril model shown in Figure 5.2.b, different volume fractions of the chemical constituents are assumed to change the lignin layer around the core of cellulose and hemicellulose. The areas of cellulose are assumed to lie at equal spacing in the hemicellulose. With a_2, b_2 and c_2 being defined according to figure 5.2.b, the volume fractions for this microfibril model are written as

$$\begin{aligned} f_L &= \frac{a_2^2 - b_2^2}{a_2^2} \\ f_H &= \frac{b_2^2 - (8\,c_2)^2}{a_2^2} \\ f_C &= \frac{(8c_2)^2}{a_2^2} \end{aligned} \tag{5.3}$$

Solving the first and last equations above for b_2 and c_2 yields

$$\begin{aligned} b_2 &= a_2\sqrt{1-f_L} \\ c_2 &= \frac{a_2}{8}\sqrt{f_C} \end{aligned} \tag{5.4}$$

Assuming in the line with Fengel [21] a side length of a_2=30 nm and using that f_C+f_H+f_L=1, the internal geometry of this microfibril model can be determined for various fractions of the chemical constituents.

The cell walls consist of five main layers that differ in their chemical composition and thus in their mechanical properties. In the present model, the cell wall layers are modelled in an approximate manner. The S$_3$-layer is modelled as a thin inner cell wall layer located next to the lumen. Since the microfibril angle of the S$_3$-layer is large and may contribute significantly to the bending stiffness of the cell wall, it may be important that this layer is included in the model. The dominating S$_2$-layer is modelled as a single layer. The middle lamella, the primary wall and the S$_1$-layer are modelled as a common outer layer because of their being similar in their chemical

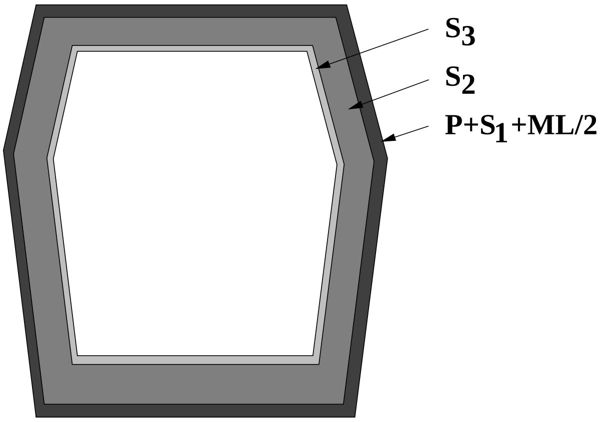

Figure 5.3: *The cell wall modelled as consisting of three layers.*

content and are closely located between two adjacent cells. Their contribution to the bending stiffness of a double cell wall is thus small, Figure 5.3. For the S_2- and S_3-layers, the volumetric fractions of the constituents for the two models shown in Figure 5.2 are assumed to be 49% cellulose, 27% hemicellulose and 24% lignin. By use of Eq.(5.2) and Eq.(5.4) for the respective models, the geometries of the cross section of the microfibrils in the S_2- and S_3-layers can be determined. The geometry of these two layers are indicated in Figures 5.4.a and 5.4.c. Regarding the remaining layers, half the thickness of the middle lamella, together with the primary wall and the S_1-layer, can be regarded as a single layer. The volumetric fractions of the constituents in these three layers are similar, being assumed to be 20% cellulose, 15% hemicellulose and 65% lignin. In Figures 5.4.b and 5.4.d, the geometries of the cross section of two microfibrils having these volume fractions is shown. Since the microfibrils are very long in the longitudinal direction as compared with their cross-sectional dimensions, the geometry of the microfibrils is assumed to be constant in the longitudinal direction.

The cell wall thickness, and thus the thicknesses of the cell wall layers, is variable in the growth ring. The thicknesses of the middle lamella, the primary wall, the S_1-layer and the S_3-layer are nearly constant throughout the growth ring, see Table 2.1. In this study, therefore, only the thickness of the S_2-layer is assumed to be variable, whereas the thicknesses of the middle layer and of the S_3-layer are assumed to be constant.

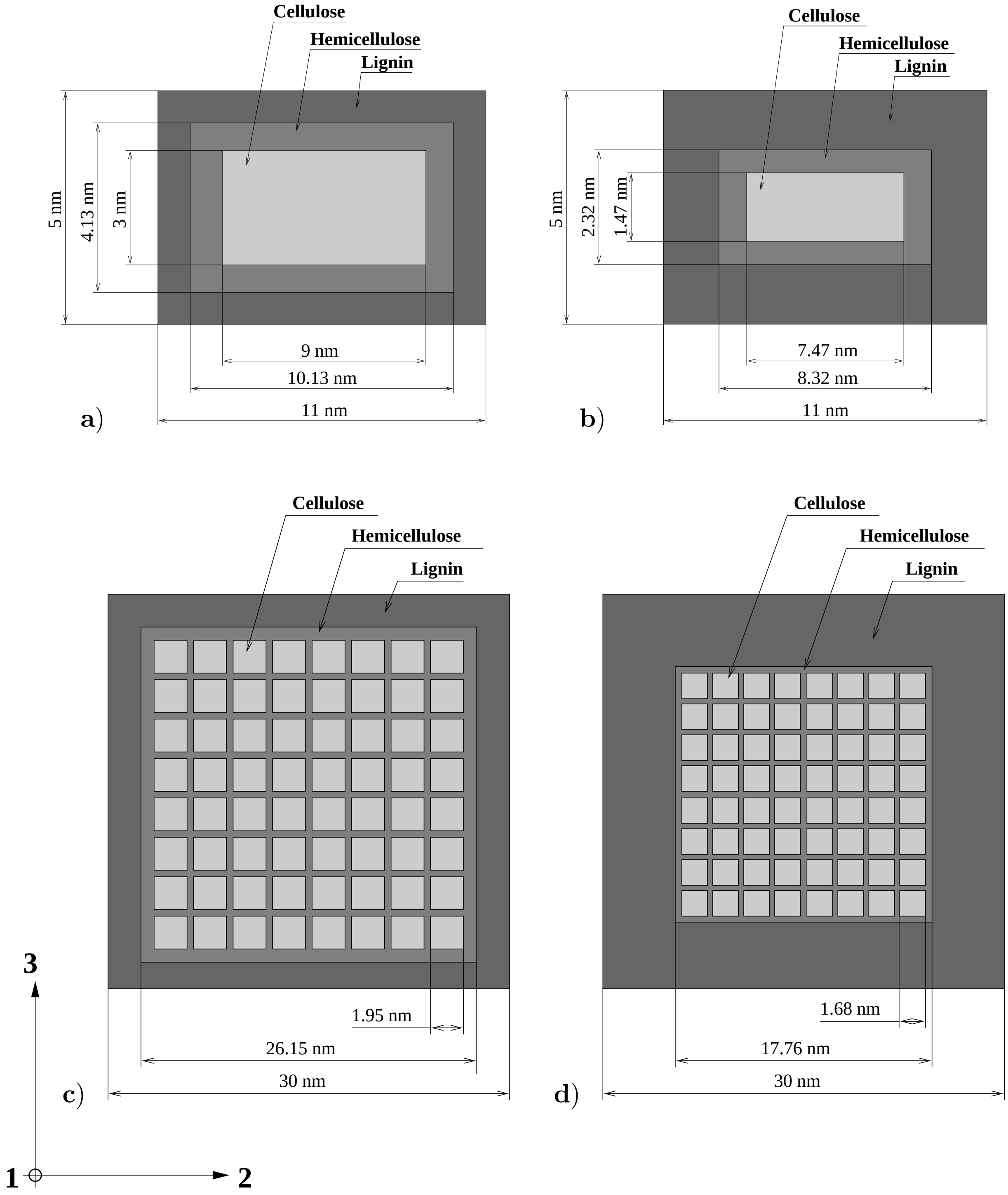

Figure 5.4: *Assumed geometry of the cross section of the base cell.*
a) *Single cellulose string model for the S_2- and S_3-layers.*
b) *Single cellulose string model for the M, P and S_1-layer.*
c) *Multiple cellulose string model for the S_2- and S_3-layers.*
d) *Multiple cellulose string model for the M, P and S_1-layer.*

5.2.3. Equivalent stiffness properties of the cell wall layers

The equivalent stiffness properties of the cell walls were determined by the numerical homogenisation procedure described in Chapter 4. The base cells used in the homogenisation procedures were assumed to have the geometries shown in Figure 5.4. In Chapter 2, the stiffness properties of cellulose, hemicellulose and lignin were discussed. Since several of the values of the stiffness coefficients were found to be uncertain, the properties of the cell wall layers as taken up in the following will be based on three sets of stiffness characterizations of the chemical constituents. These three sets are denoted low, medium and high stiffness values and cover the range of values given in Chapter 2. In Table 5.1 the three sets of stiffness coefficients for the chemical constituents are shown for a moisture content of 12%.

Table 5.1: *Three sets of stiffness coefficients for the chemical constituents employed in this study.*

Constituent	Coefficient	Low	Medium	High
Cellulose	E_{11}, [GPa]	130.0	150.0	170.0
	E_{22}, [GPa]	15.0	17.5	20.0
	G_{12}, [GPa]	3.0	4.5	6.0
	ν_{21}, [-]	0.01	0.01	0.01
	ν_{32}, [-]	0.50	0.50	0.50
Hemicellulose	E_{11}, [GPa]	14.0	16.0	18.0
	E_{22}, [GPa]	3.0	3.5	4.0
	G_{12}, [GPa]	1.0	1.5	2.0
	ν_{21}, [-]	0.10	0.10	0.10
	ν_{32}, [-]	0.40	0.40	0.40
Lignin	E, [GPa]	2.0	2.75	3.5
	ν, [-]	0.33	0.33	0.33

The geometrical models of the microfibrils shown in Figure 5.4 have geometries and fractions of the chemical constituents assuming no water content. The properties of the cell wall layers will be derived assuming a moisture content of 12%. As discussed in Chapter 2, the three chemical constituents differ in their water absorption and thus in the volume changes that occur in response to moisture changes. In a moisture change from 0 to 12%, lignin and hemicellulose increase their volume fractions, whereas cellulose decreases its volume fraction. To take account of the moisture-induced swelling in the modelling, the changes in the geometries of the microfibril models are determined. By subjecting the original models to a moisture change of 12%, the changes of the geometries are calculated by use of the finite element method. In these calculations, periodic boundary conditions are applied, as described in Chapter 4, and the average tractions at the boundaries are set to

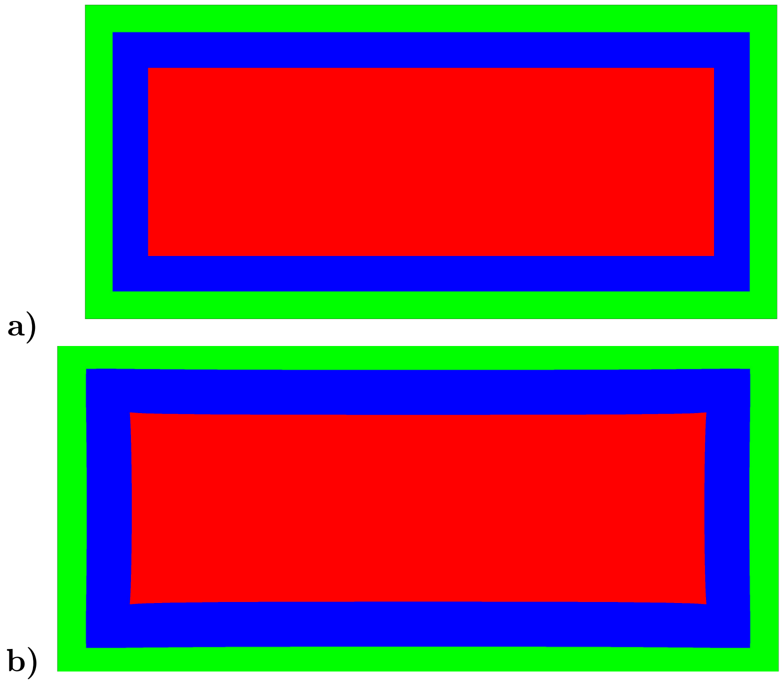

Figure 5.5: *Calculated swelling of a microfibril in the cell wall from 0 to 12% of moisture content.* **a)** *Dry state.* **b)** *State at 12% of moisture content.*

zero. In the simulations, the stiffness properties of the chemical constituents are assumed to be constant for a change in moisture from 0 to 12%. This appears to be reasonable in simulating free hygroexpansion, since the stress levels can be expected to be fairly low. From the geometric changes calculated, the modified geometries of the microfibrils where determined. Since the three chemical constituents differ in their shrinkage properties, the moisture change from 0 to 12% leads to local stress development in the microfibrils. In determining the average mechanical properties, these stresses were neglected.

An example of this, shown in Figure 5.5, is the change in the geometry of the microfibril shown in Figure 5.4.a from a dry state and to a moisture content of 12%. In Table 5.2 the changes in the fractions of the chemical constituents for the models shown in Figure 5.4 can be seen. The results shown in Table 5.2 indicate that, for a moisture change from 0 to 12 %, the volume fraction of the hemicellulose increases, whereas the volume fraction of the lignin remains almost constant and the volume fraction of the cellulose decreases.

In the numerical procedure, the microfibrils were divided into finite elements, 20-node three-dimensional isoparametric solid elements being employed, see Figure 5.6. Periodic boundary conditions were applied and to obtain the equivalent properties the base cell was solved for six elementary load cases.

In Table 5.3, the homogenised stiffness coefficients obtained for the S_2- and S_3-layers by use of the microfibril model shown in Figure 5.4.a are shown for low, medium and high material data sets, respectively.

Table 5.2: *Changes in fractions of the chemical constituents in response to a moisture change from 0 to 12% for the models shown in Figure 5.4.*

Model according to	Fraction at 0% m.c.			Fraction at 12 % m.c.		
	Cellulose [%]	Hemicell. [%]	Lignin [%]	Cellulose [%]	Hemicell. [%]	Lignin [%]
Figure 5.4.a	49	27	24	44.5	31.6	23.9
Figure 5.4.b	20	15	65	18.0	17.6	64.4
Figure 5.4.c	49	27	24	44.3	31.6	24.1
Figure 5.4.d	20	15	65	18.0	17.4	64.6

The stiffness coefficients obtained for the layer representing the middle lamella, the primary wall and the S_1-layer for low, medium, high material data sets are shown in Table 5.4, use being made there of the microfibril model shown in Figure 5.4.b.

Similarly, if the microfibril model shown in Figure 5.4.c is instead employed, the homogenised stiffness coefficients for the S_2- and S_3-layers shown in Table 5.5 are obtained. Finally, by use of the microfibril model in Figure 5.4.d, the stiffness coefficients for the layer representing the middle lamella, the primary wall and the S_1-layer, shown in Table 5.6, are obtained.

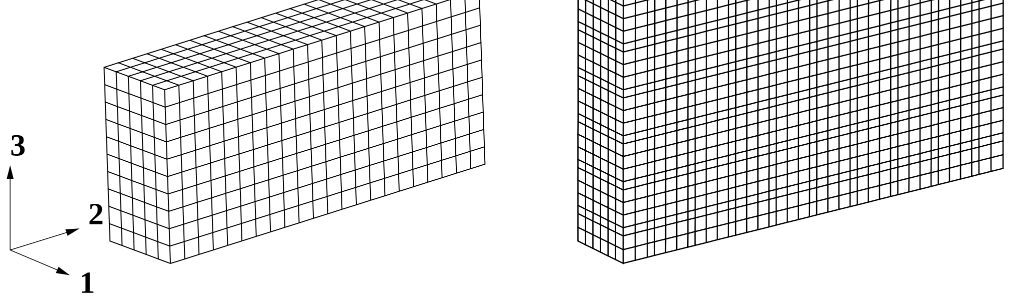

Figure 5.6: *Finite element meshes of microfibril models with cross-sectional dimensions according to Figure 5.2 (the 1-axis being oriented in the longitudinal direction, the 2-axis in the circumferential direction and the 3-axis in the cell wall thickness direction).*

Table 5.3: *Equivalent stiffness coefficients for the S_2- and S_3 layers using the microfibril model shown in Figure 5.4.a.*

Stiffness coefficient	Assumptions regarding stiffness of constituents		
	Low	Medium	High
E_{11}, [GPa]	62.9	72.6	82.3
E_{22}, [GPa]	6.14	7.48	8.23
E_{33}, [GPa]	4.97	6.13	7.24
G_{12}, [GPa]	2.66	3.13	3.60
G_{13}, [GPa]	2.52	2.97	3.41
G_{23}, [GPa]	1.21	1.75	2.27
ν_{21}, [-]	0.0222	0.0234	0.0241
ν_{31}, [-]	0.0199	0.0208	0.0213
ν_{32}, [-]	0.433	0.438	0.441

Table 5.4: *Equivalent stiffness coefficients for middle lamella, primary wall and the S_1-layer using the microfibril model shown in Figure 5.4.b.*

Stiffness coefficient	Assumptions regarding stiffness of constituents		
	Low	Medium	High
E_{11}, [GPa]	27.2	31.7	36.1
E_{22}, [GPa]	3.63	4.69	5.72
E_{33}, [GPa]	3.04	3.17	4.92
G_{12}, [GPa]	1.50	1.85	2.19
G_{13}, [GPa]	1.37	1.68	1.99
G_{23}, [GPa]	0.838	1.18	1.51
ν_{21}, [-]	0.0375	0.0419	0.0450
ν_{31}, [-]	0.0339	0.0377	0.0404
ν_{32}, [-]	0.466	0.467	0.467

The differences in the stiffness properties obtained from the two microfibril models for material arrangement of different types, see Figures 5.2 and 5.4, were small. However, the rectangular-shaped microfibril model shown in Figure 5.2.a results in an orthotropic material, whereas the square-shaped microfibril model in Figure 5.2.b results in a transversely isotropic material. Since large differences in stiffness between the various chemical constituents were assumed, large differences in stiffness properties were obtained when the fractions of the chemical constituents were modified, such as in representing different layers of the cell wall. However, the assumptions made in constructing the models, concerning the geometrical arrangement of the materials at the ultrastructural level and for the stiffness properties of

Table 5.5: *Equivalent stiffness coefficients for the S_2- and S_3 layers using the microfibril model shown in Figure 5.4.c.*

Stiffness coefficient	Assumptions regarding stiffness of constituents		
	Low	Medium	High
E_{11}, [GPa]	62.7	72.4	82.0
E_{22}, [GPa]	5.47	6.70	7.89
E_{33}, [GPa]	5.47	6.70	7.89
G_{12}, [GPa]	2.62	3.10	3.57
G_{13}, [GPa]	2.62	3.10	3.57
G_{23}, [GPa]	0.957	1.36	1.76
ν_{21}, [-]	0.0214	0.0224	0.0230
ν_{31}, [-]	0.0214	0.0224	0.0230
ν_{32}, [-]	0.383	0.391	0.395

Table 5.6: *Equivalent stiffness coefficients for the middle lamella, primary wall and the S_1-layer using the microfibril model shown in Figure 5.4.d.*

Stiffness coefficient	Assumptions regarding stiffness of constituents		
	Low	Medium	High
E_{11}, [GPa]	27.2	31.7	36.1
E_{22}, [GPa]	3.21	4.19	5.16
E_{33}, [GPa]	3.21	4.19	5.16
G_{12}, [GPa]	1.50	1.84	2.19
G_{13}, [GPa]	1.50	1.84	2.19
G_{23}, [GPa]	0.681	0.959	1.23
ν_{21}, [-]	0.0353	0.0395	0.0424
ν_{31}, [-]	0.0353	0.0395	0.0424
ν_{32}, [-]	0.432	0.435	0.437

the constituents, are uncertain. For this reason, the stiffness properties obtained should be considered approximate.

Since, as recent research results indicate, the geometry of the ultrastructure differ in the two directions on the cross sectional plane, as Figure 2.5 indicates, the equivalent material can be expected to be orthotropic. The stiffness coefficients for the different layers of the cell wall to be used later in modelling the fibres and the cell structures are selected from the results shown in Tables 5.3 and 5.4. The stiffness coefficients found in Table 5.3 are used to represent the S_2- and S_3-layers, whereas the stiffness coefficients found in Table 5.4 are used to represent the middle lamella, the primary wall and the S_1-layer.

5.2.4. Equivalent hygroexpansion properties of the cell wall layers

The homogenisation method described in Chapter 4 was used for determining the equivalent hygroexpansion properties. In the numerical procedure, periodic boundary conditions and a load of the base cell a unit moisture change were employed. The hygroexpansion coefficients were obtained using the finite element solution. The four base cells in Figures 5.4.a-d used in determining the stiffness properties of the cell wall layers, as described in the preceding section, were also used for determining the hygroexpansion coefficients.

According to experimental data presented by Kollman et al. [35], the volumetric hygroexpansion of wood is roughly linear in the moisture content range of 0 to 25%. This is also assumed to be valid for the cell wall layers. To determine the linear hygroexpansion coefficients for a moisture content of around 12%, the hygroexpansion properties of lignin and of hemicellulose were evaluated by use of Eq.(2.33) and (2.34), yielding

$$\alpha_L = \begin{bmatrix} 0.351 \\ 0.351 \\ 0.351 \\ 0.0 \\ 0.0 \\ 0.0 \end{bmatrix} \qquad \alpha_H = \begin{bmatrix} 0.0 \\ 1.368 \\ 1.368 \\ 0.0 \\ 0.0 \\ 0.0 \end{bmatrix} \tag{5.5}$$

where α_L and α_H are the hygroexpansion coefficients for lignin and hemicellulose, respectively. Cellulose is assumed to be unaffected by moisture change. The hygroexpansion properties of the cell wall layers were evaluated for the three sets of stiffness properties of the chemical constituents shown in Table 5.1. The equivalent hygroexpansion coefficients are presented in Table 5.7, the numerical procedure for the base cell configuration shown in Figure 5.4.a being used for the S_2- and S_3-layers. Table 5.8 presents the equivalent hygroexpansion coefficients for the middle lamella, the primary wall and the S_1-layer, as obtained by use of the base cell configuration shown in Figure 5.4.b. The equivalent hygroexpansion coefficients obtained by use of the base cell configurations shown in Figures 5.4.c and 5.4.d are shown in Tables 5.9 and 5.10, respectively. The differences between longitudinal hygroexpansion coefficients obtained by use of the two differing geometrical assumptions regarding

Table 5.7: *Equivalent hygroexpansion coefficients for the S_2- and S_3 layers using the microfibril model shown in Figure 5.4.a with the high, medium and low data sets.*

Hygro-expansion coefficient	Assumptions regarding stiffness of constituents		
	Low	Medium	High
α_{11}	0.0087	0.0093	0.0097
α_{22}	0.355	0.353	0.352
α_{33}	0.589	0.587	0.586

Table 5.8: *Equivalent hygroexpansion coefficients for the middle lamella, primary wall and the* S_1*-layer using the microfibril model shown in Figure 5.4.b with the high, medium and low data sets.*

Hygro-expansion coefficient	Assumptions regarding stiffness of constituents		
	Low	Medium	High
α_{11}	0.0244	0.0275	0.0298
α_{22}	0.396	0.395	0.394
α_{33}	0.592	0.589	0.586

Table 5.9: *Equivalent hygroexpansion coefficients for the* S_2*- and* S_3 *layers using the microfibril model shown in Figure 5.4.c with the high, medium and low data sets.*

Hygro-expansion coefficient	Assumptions regarding stiffness of constituents		
	Low	Medium	High
α_{11}	0.0084	0.0089	0.0093
α_{22}	0.479	0.477	0.476
α_{33}	0.479	0.477	0.476

Table 5.10: *Equivalent hygroexpansion coefficients for the middle lamella, primary wall and the* S_1*-layer using the microfibril model shown in Figure 5.4.d with the high, medium and low data sets.*

Hygro-expansion coefficient	Assumptions regarding stiffness of constituents		
	Low	Medium	High
α_{11}	0.0230	0.0261	0.0283
α_{22}	0.505	0.502	0.500
α_{33}	0.505	0.502	0.500

the microfibrils were small. The differences in the hygroexpansion coefficients based on employing the three different stiffness data sets are also found to be small. In the transverse longitudinal plane, the hygroexpansion coefficients determined on the basis of the base cells being square show isotropic properties that probably are not valid for the cell wall. In the following, therefore, the results shown in Table 5.7 and 5.8 have been selected for use. The stress distribution over the base cell for uniaxial loading and the unit moisture change result in complex stress fields. Although, the microfibril is not stress-free after a moisture change that can affect the strength of the material, no account of this is taken in the following.

5.3. Modelling Properties of the Cell Wall

5.3.1. Finite element modelling of the cell wall

In this section the average mechanical properties of the cell wall are studied regarding the cell wall as a continuum. These properties were not used in the development of the chain of properties described earlier. However, measurements for some of these properties are available and a comparison between the measured and the simulated data can be made at the cell wall level.

The equivalent average stiffness and the hygroexpansion properties of a part of the cell wall were determined for two regions of the growth ring. Numerical models of the cell walls were also created for each of the earlywood and latewood regions. The stiffness and hygroexpansion properties were determined by means of the homogenisation method described in Chapter 4. Each model consists of a part of two adjacent cell walls as shown in Figure 5.7. The cell wall portion consists of six layers that from lumen to lumen are the following: S_3-S_2-M-M-S_2-S_3. The compound middle layer (M) is composed of the S_1-layer, the primary wall and half the middle lamella. The six layers are alternately wound around the cells in a left and a right helical pattern which thus differing in their orientation. The stiffness coefficients used for the six layers were taken from the results of the modelling of the cell wall properties, as shown in Tables 5.3 and 5.4. The hygroexpansion properties used for the cell wall layers are shown in Tables 5.7 and 5.8. The thicknesses and the orientation of the material of each layer in the earlywood and the latewood cell wall models are shown in Table 5.11.

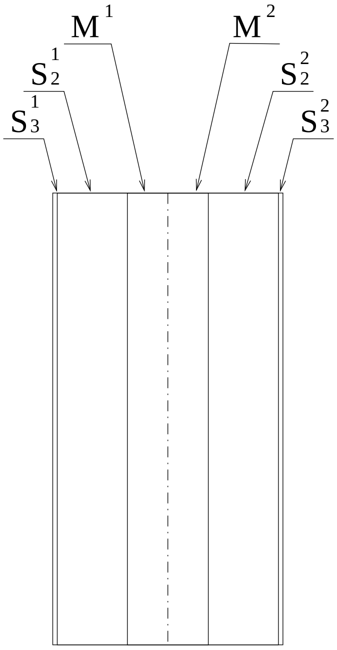

Figure 5.7: *Part of two adjacent cell walls used for determining averaged properties.*

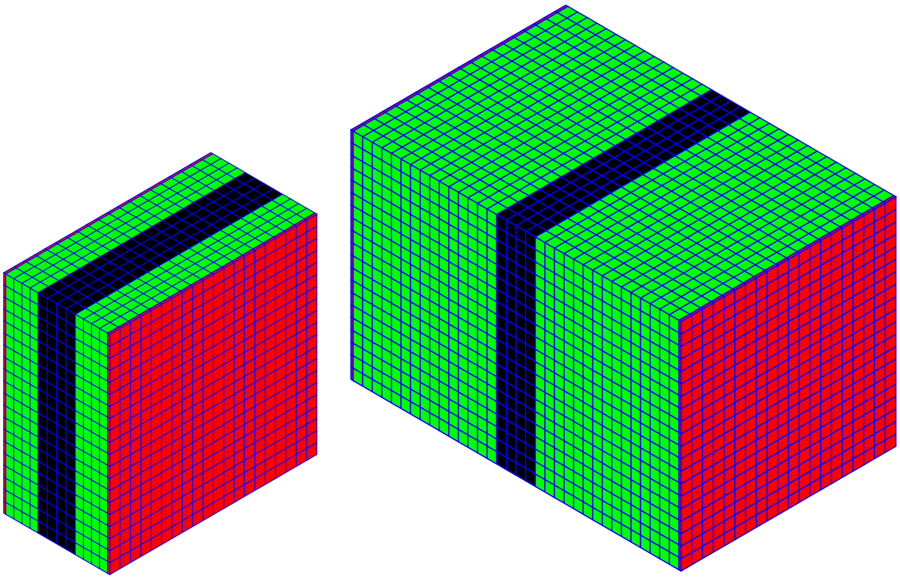

Figure 5.8: *Finite element meshes of the earlywood and latewood cell walls used for determining average stiffness and hygroexpansion properties. The cell wall layers employed in the model are drawn in different shades of grey.*

Three-dimensional eight-node linear solid elements were used in the calculations. The finite element meshes used for determining the average stiffness and the hygroexpansion properties of the earlywood and latewood cell walls are given in Figure 5.8.

The average properties of the earlywood cell wall that were obtained are shown in Figures 5.9-5.12, where the moduli of elasticity, the moduli of shear, Poisson's ratios and the hygroexpansion coefficients are shown for low, medium and high material data sets for the cell wall layers employed. The properties presented are referred

Table 5.11: *Microfibril angles and thicknesses of the earlywood and latewood cell wall layers. The layers are ordered from lumen to lumen according to Figure 5.7.*

Layer	Microfibril angle [degrees]	Thickness of earlywood wall layers, [μm]	Thickness of latewood wall layers [μm]
S_3^1	-75	0.05	0.05
S_2^1	+(0 to 45)	0.78	3.34
M^1	-45	0.45	0.45
M^2	+45	0.45	0.45
S_2^2	-(0 to 45)	0.78	3.34
S_3^2	+75	0.05	0.05
Total	-	2.56	7.68

to a 1,2,3-coordinate system in which the 1-axis is oriented in the longitudinal direction, the 2-axis in the circumferential direction and the 3-axis in the cell wall thickness direction. Figures 5.13-5.16 show the averaged coefficients obtained from the calculations for the latewood cell wall model, the moduli of elasticity, the moduli of shear, Poisson's ratios and the hygroexpansion coefficients being shown for the low, medium and high material data sets of the cell wall layers employed. From the results shown in Figures 5.9-5.16 it is evident that the mechanical properties are highly dependent on the microfibril angle in the S_2-layer. The modulus of elasticity in the longitudinal direction is dependent on both the microfibril angle in the S_2-layer and the thickness of the cell wall. In the radial and tangential directions the modulus of elasticity is affected to only a minor degree by the cell wall thickness. A comparison of the stiffness and the hygroexpansion coefficients for a microfibril angle of the S_2-layer of 10° between the earlywood and latewood is presented in Table 5.12. From these results it can be seen that the modulus of elasticity in the circumferential direction (2-direction) is slightly lower for the latewood cell wall than for the thinner earlywood cell wall. This appears to be due to the microfibril angles in the middle- and S_3-layers being larger than in the S_2-layer. It is assumed here that the S_2-layer is the only layer in the cell wall that is thicker in the latewood region, so that the stiffness of the middle- and the S_3-layers contributes more to the modulus of elasticity in the circumferential direction in the thin earlywood cell walls.

Table 5.12: *Equivalent stiffness parameters determined from cell wall models of earlywood and latewood using low, medium and high material properties of the cell wall layers with the microfibril angle of the S_2-layer set to 10°.*

Coefficient	Assumptions regarding stiffness of constituents					
	For earlywood			For latewood		
	Low	Medium	High	Low	Medium	High
E_{11}, [MPa]	33200	38700	44100	43000	50000	56800
E_{22}, [MPa]	7020	8500	9620	6430	7800	8700
E_{33}, [MPa]	4360	4900	6660	4770	5670	7070
G_{12}, [MPa]	4380	5440	6270	3500	4130	4750
G_{13}, [MPa]	1650	2090	2500	2120	2580	3020
G_{23}, [MPa]	1180	1633	2070	1220	1730	2220
ν_{21}, [-]	0.112	0.115	0.116	0.0671	0.0692	0.0689
ν_{31}, [-]	0.0233	0.0229	0.0264	0.0219	0.0224	0.0242
ν_{32}, [-]	0.403	0.417	0.407	0.416	0.424	0.422
α_{11}, [-]	0.0084	0.0095	0.0105	0079	0.0086	0.0093
α_{22}, [-]	0.243	0.247	0.246	0.308	0.308	0.306
α_{33}, [-]	0.652	0.646	0.646	0.614	0.611	0.611

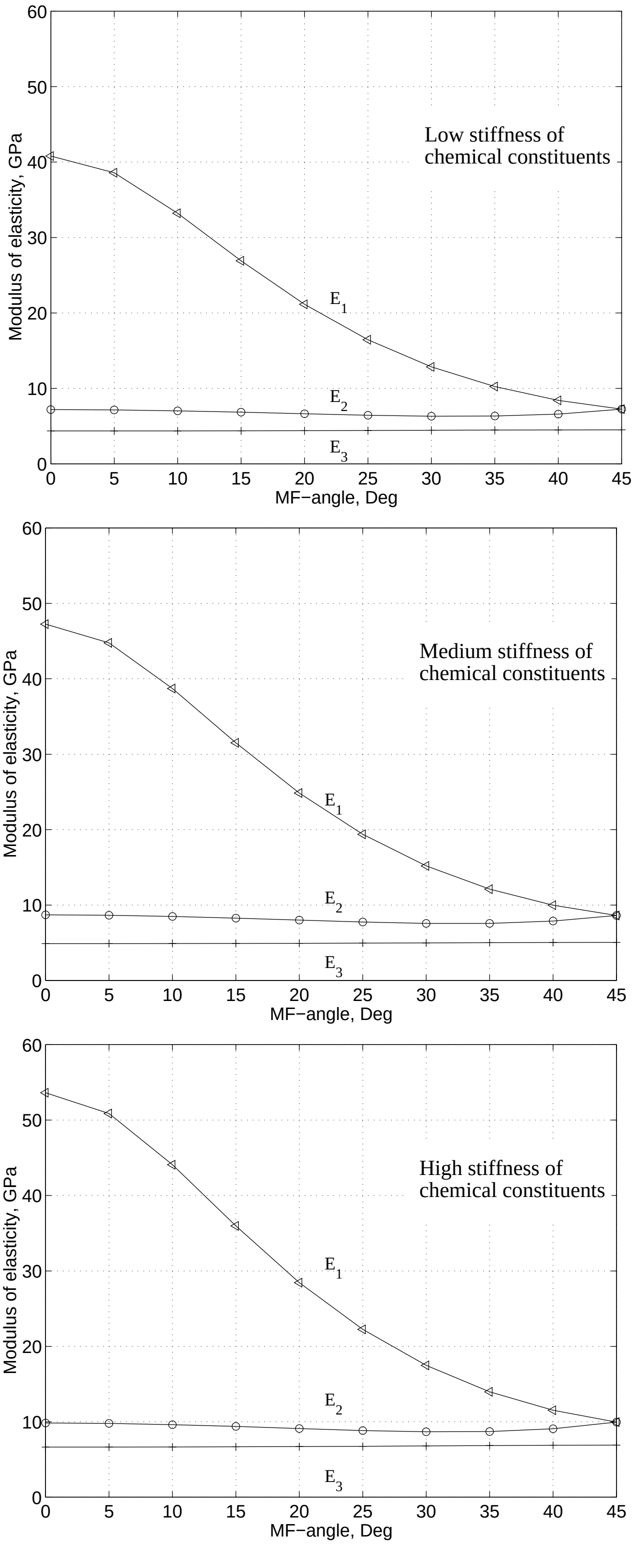

Figure 5.9: *Average modulus of elasticity of the earlywood cell wall versus the microfibril angle of the* S_2*-layer.*

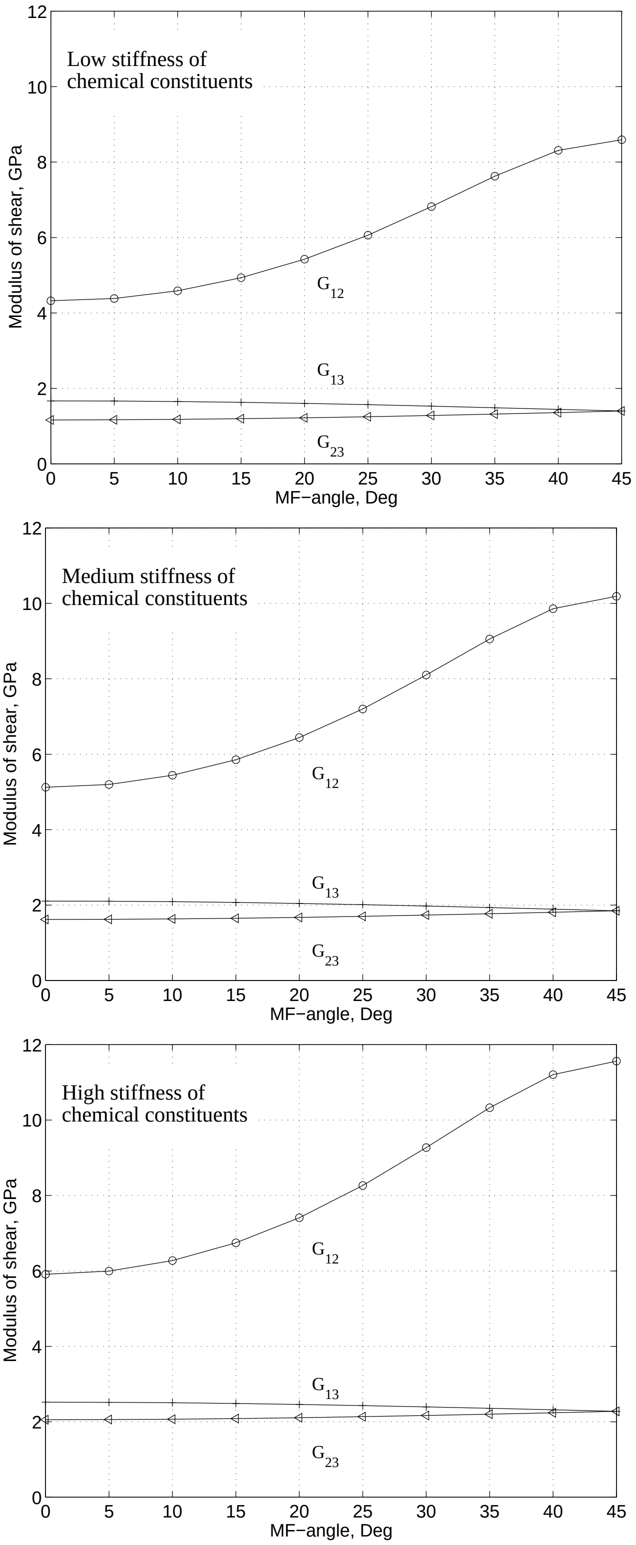

Figure 5.10: *Average modulus of shear of the earlywood cell wall versus the microfibril angle of the* S_2*-layer.*

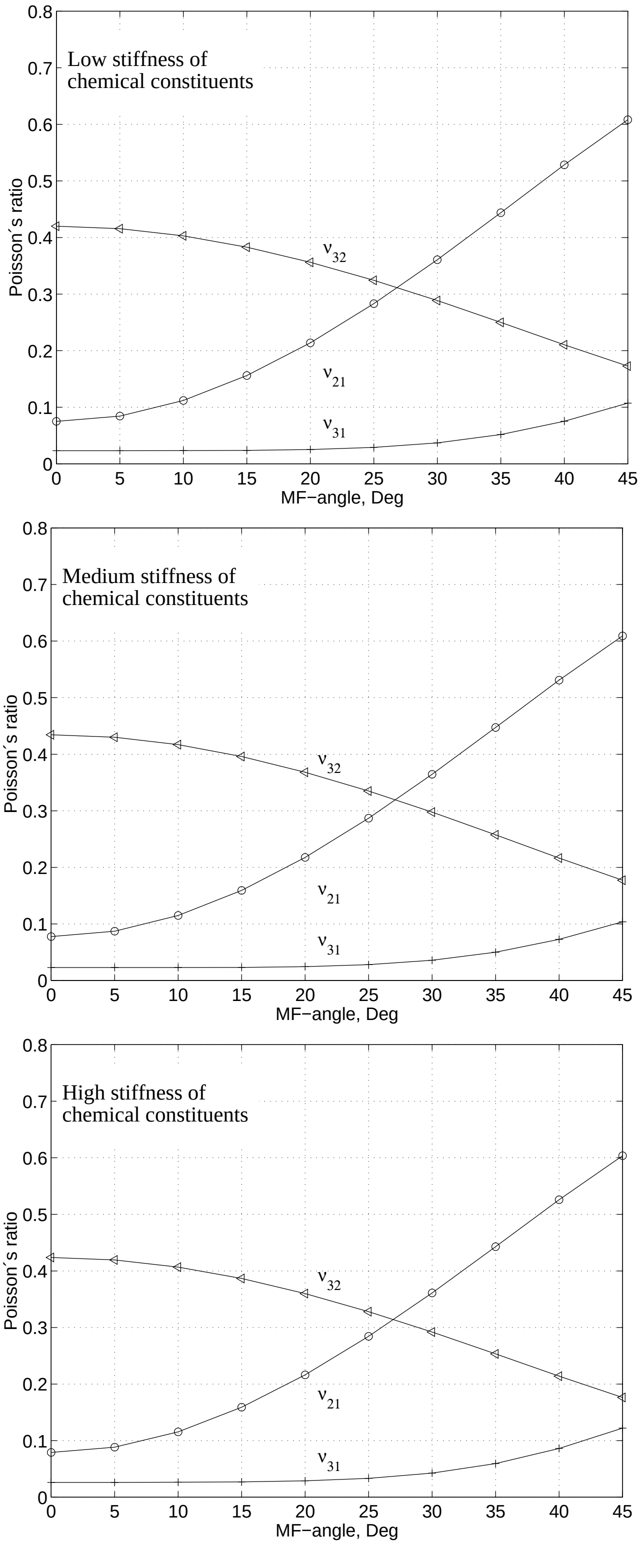

Figure 5.11: *Average Poisson's ratios of the earlywood cell wall versus the microfibril angle of the* S_2*-layer.*

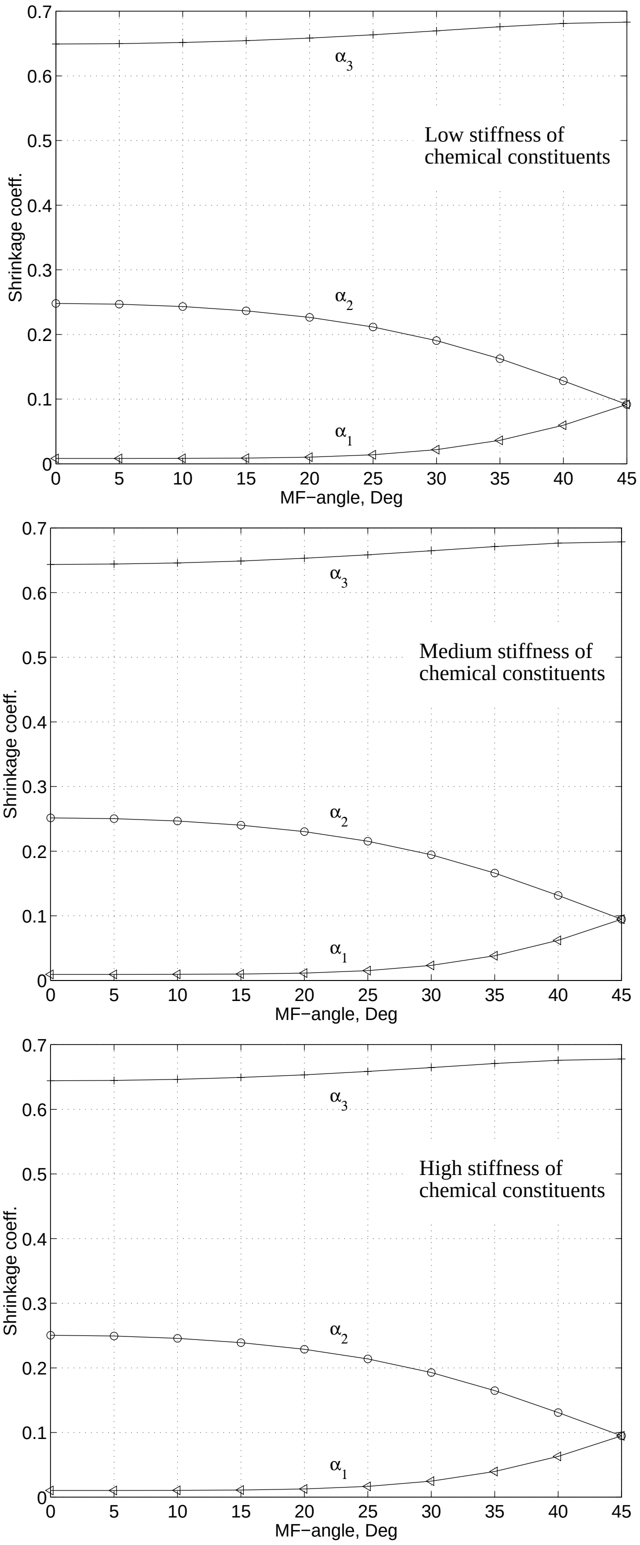

Figure 5.12: *Average shrinkage properties of the earlywood cell wall versus the microfibril angle of the* S_2*-layer.*

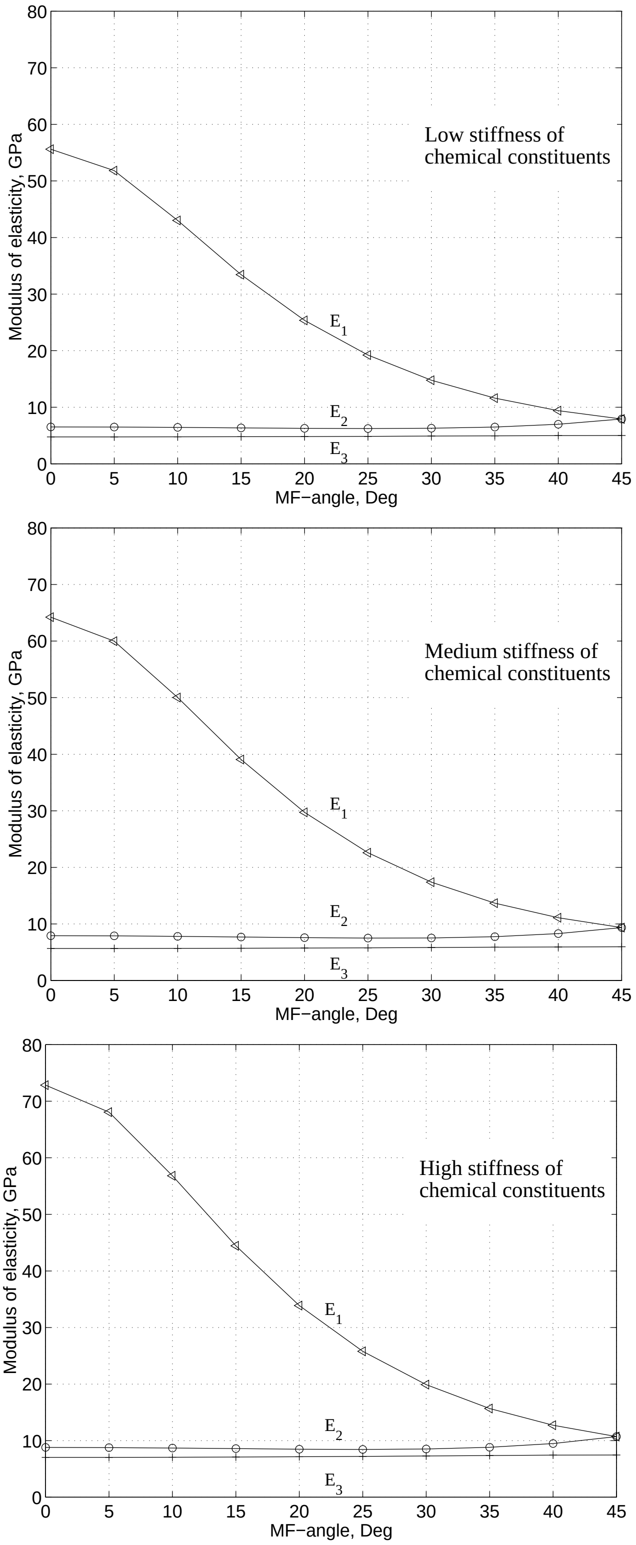

Figure 5.13: *Average modulus of elasticity of the latewood cell wall versus the microfibril angle of the S_2-layer.*

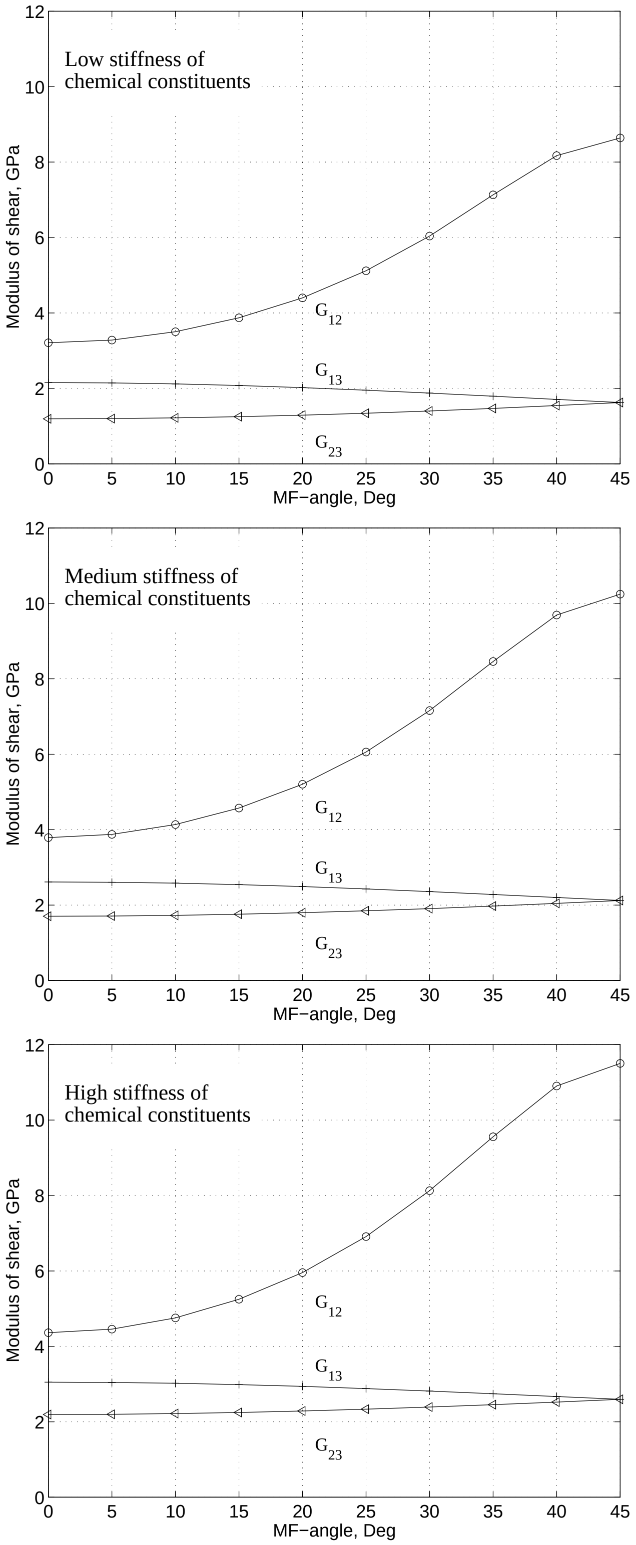

Figure 5.14: *Average modulus of shear of the latewood cell wall versus the microfibril angle of the* S_2*-layer.*

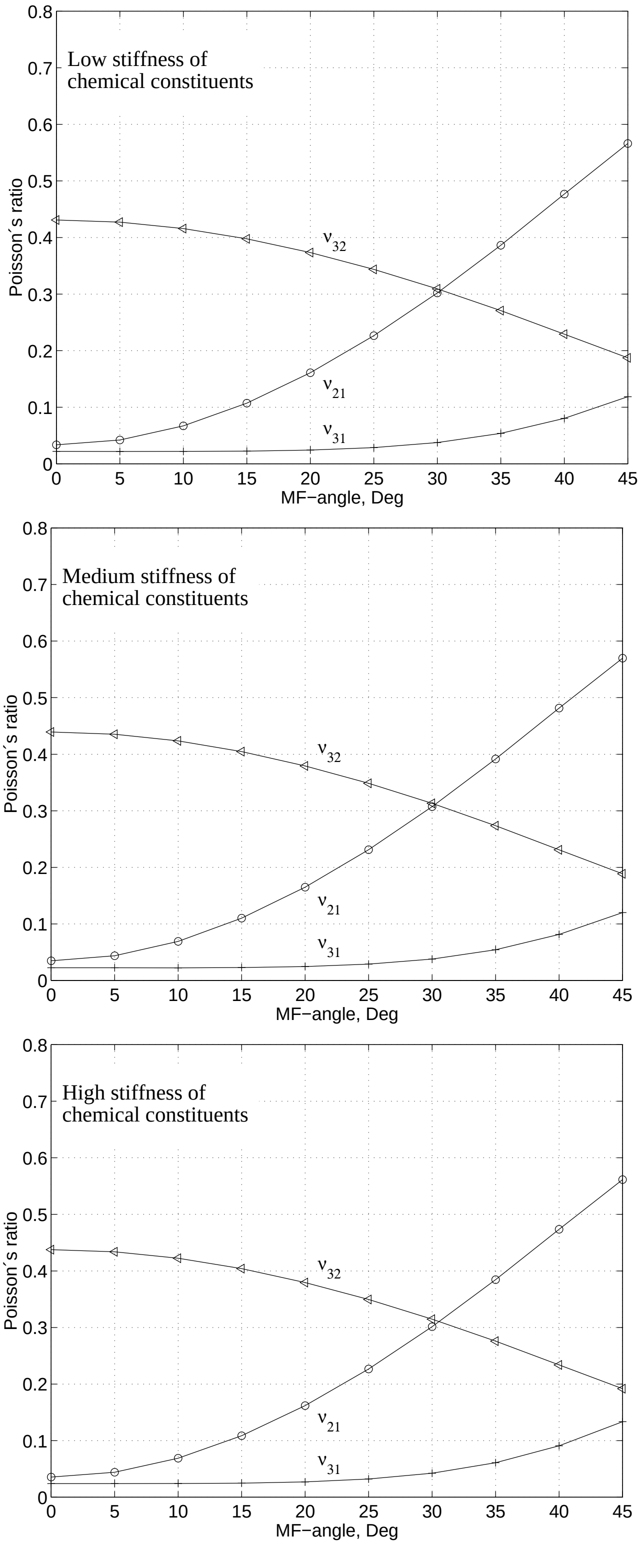

Figure 5.15: *Average Poisson's ratios of the latewood cell wall versus the microfibril angle of the* S_2*-layer.*

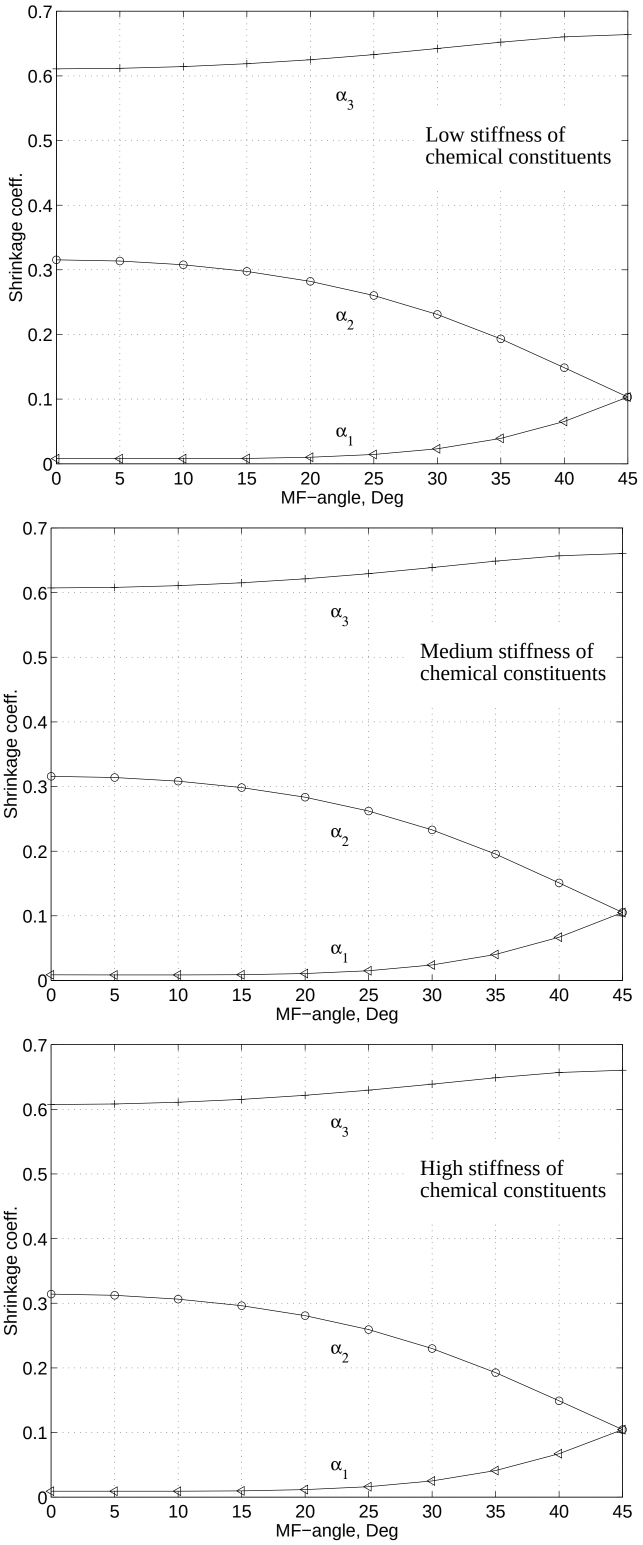

Figure 5.16: *Average shrinkage properties of the latewood cell wall versus the microfibril angle of the S_2-layer.*

As referred to in Chapter 2, Bergander[8] measured the equivalent modulus of elasticity for the radially oriented fibre wall in native wood, the lowest values being obtained for the thick-walled fibres and the highest for the thin-walled earlywood fibres. This finding is in agreement with the results obtained in the present study. The numerical results presented here indicate the average modulus of elasticity in the circumferential direction of the fibre wall to be about 4000 to 7000 MPa, depending on properties of the chemical constituents chosen and the microfibril angle of the S_2-layer. The transverse shrinkage of the fibre wall from fibre saturation at about 30% of moisture content to a dry condition has been measured by Wallström et al. [71]. The shrinkage in the fibre wall thickness direction there was found to be about 20%. Assuming linear shrinkage, this result corresponds to a hygroexpansion coefficient of about 0.66. In the present study the equivalent hygroexopansion coefficient in the fibre wall thickness direction was found to range from 0.61 to 0.67, depending on the properties of the chemical constituents chosen and the microfibril angle of the S_2-layer.

5.4. Modelling Properties of Cellular Structures

5.4.1. General remarks

In this section models are presented for determining properties of cellular structures. The geometry model of a single cell is first described and then the geometry of cellular structures of growth rings is described. The properties of clear wood are determined by use of a geometric model for the growth ring structure together with a finite element model.

5.4.2. Hexagonal cell model

The shape of the cells that makes up the structure of the wood was determined by studying micrographs similar to those found in section 3.3. These revealed a certain regularity in the cell structure. Studying the cell structure of earlywood, one can note that the cell arrangement in the radial and the tangential direction differs. In the radial direction, the cells are stacked in fairly straight lines, whereas in the tangential directions they lie in a more disordered pattern, Figure 5.17. If a uniaxial load is applied in the tangential direction, the cell walls are mainly subjected to bending, whereas if a load is applied in the radial direction the radially well-oriented cell walls are subjected mainly to either compression or tension. The difference in cell arrangement for the two directions makes the tangential stiffness lower than the radial. Moreover, since the ray cells are oriented radially, they contribute to the stiffness in this direction, whereas they have little influence on the stiffness in the tangential direction. The anisotropy between the radial and the tangential directions is also affected by the fact that when loading in the tangential direction occurs the earlywood and the latewood regions are loaded in parallel, whereas when loading is in the radial direction occurs the two regions are loaded in serial. This may indicate

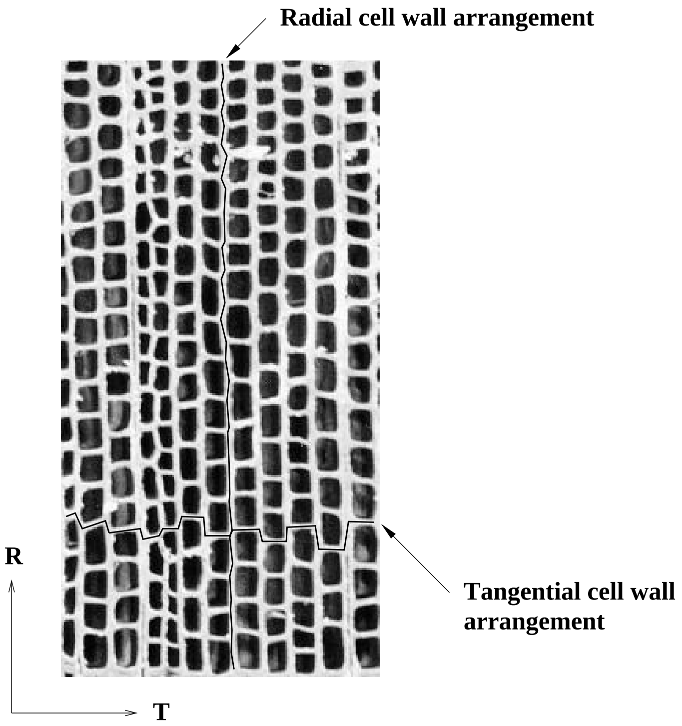

Figure 5.17: *Earlywood cell structure with lines drawn in the radial and tangential cell walls to show the differences in cell arrangement between the two directions.*

that the average stiffness is greater in the tangential than in the radial direction. However, it is well known from measurements that the radial stiffness is about 1.5 to 2 times the tangential stiffness, see for example Bodig and Jayne [9]. The cells are very long in the longitudinal direction as compared with their cross-sectional dimensions. Accordingly, it is assumed in the model that the tracheids are infinitely long in the longitudinal direction, the influence of the end caps of the tracheids being neglected. The pores of the cell walls are also omitted in the modelling.

The cells of Norway spruce are shaped more or less as irregular hexagons, see Figure 5.18. Consequently, in modelling individual cells, these are given a hexagonal shape and an irregularity in structure. Since the cell walls oriented in the radial direction differ in length, the tangential cell wall of an adjacent cell is not connected to the middle of a radially oriented cell wall, cf. Figure 5.17. To account for this, an eccentricity is introduced in modelling the individual cells. The cells are assumed to have a constant geometric shape in the longitudinal direction, as was already indicated. Five parameters are introduced so as to control the geometry of the cell, allowing cells of differing shape, density and individual position in the cell structure to be analysed as adequately as possible. Figure 5.19 shows the hexagonal cell shape that was chosen, its having the radial width w_r, the tangential widths w_{t1} and w_{t2}, the cell wall thickness t and the eccentricity parameter e. The parameter e, defined in Figure 5.19 and valid in the interval $0 < e < 1$, determines the eccentricity of the hexagonal cell. The value of this parameter affects the anisotropy of the stiffness

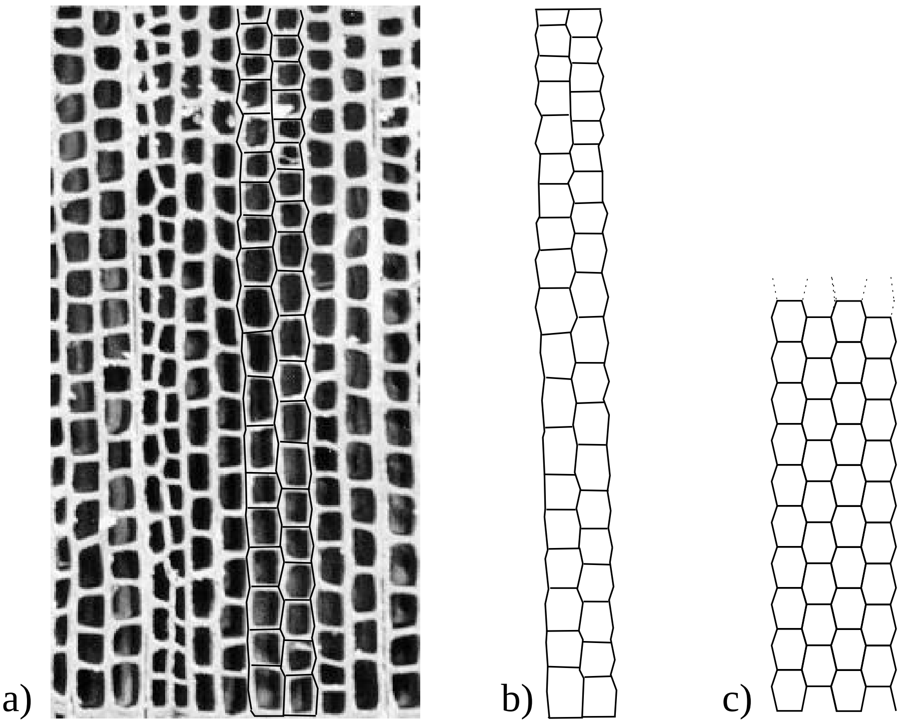

Figure 5.18: *Organisation of the cell structure.* **a)** *Photograph of cell structure with cell wall boundaries outlined.* **b)** *Example of an irregular hexagonal cell structure model.* **c)** *Example of a regular hexagonal cell structure model.*

properties. If $e = 0.5$, the cell structure is regular and the difference between the radial and the tangential stiffness reach a maximum. The ratio of the tangential widths w_{t1} and w_{t2} determines the angle between the adjacent cell walls. This ratio also affects the stiffness anisotropy. If $w_{t1} = w_{t2}$, a quadratic cell shape is obtained, the anisotropy being at a maximum. At a particular ratio of w_{t1} to w_{t2}, the radial and the tangential stiffness are equal. The tangential widths of the cell, the angle between the cell walls and the eccentricity were determined on the basis of microstructural measurements and through studying micrographs. The cell wall thickness t and the radial width w_r of the cell were determined either from the cell density or from the cell wall ratio at the current position within the structure. The average density of a hexagonal cell was obtained by calculating the cell wall ratio of the structure and multiplying this by the bulk density of the cell wall. The ratio, S, of the cell wall area to the total area occupied by the cell is calculated for the cell configuration according to Figure 5.19, using minor simplifications as

$$S = \frac{A_w}{A_t} = \frac{t\left[2w_t + \left(2w_r + \frac{w_{t1} - w_{t2}}{2e}\right)\left(1 - \frac{2t}{w_r}\right)\right]}{w_r w_t} \tag{5.6}$$

where A_w is the cell wall area as seen in cross section, A_t is the total area occupied by the cell, including the lumen, and $w_t = (w_{t1} + w_{t2})/2$. For thin-walled cells, the

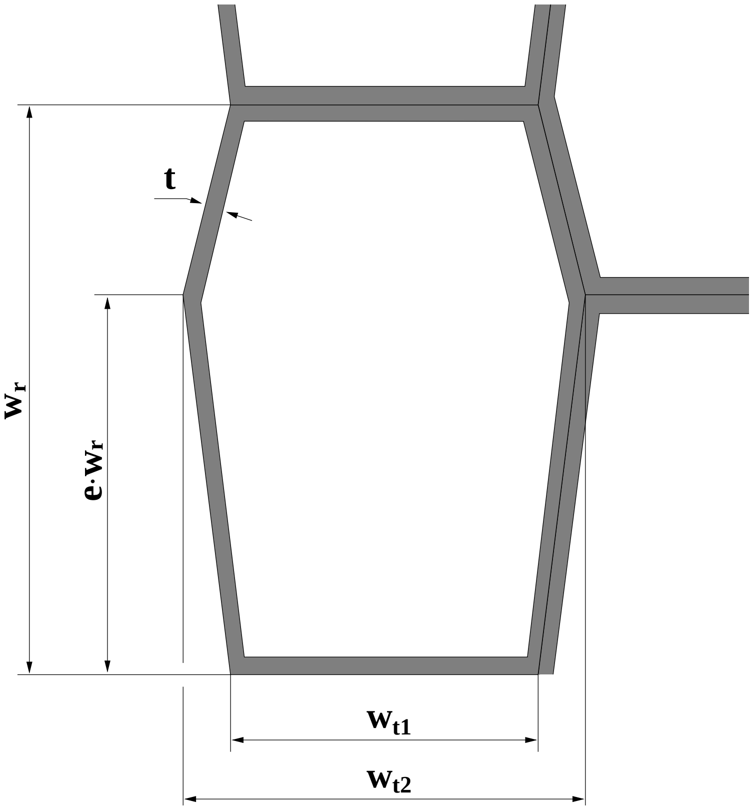

Figure 5.19: *Shape and geometric notation of the cross-section in the hexagonal cell model.*

cell wall area ratio as given in Eq.(5.6) can be simplified to yield

$$S = \frac{A_w}{A_t} = \frac{2t(w_t + w_r - 2t)}{w_r w_t} \tag{5.7}$$

The average density of the cell can be expressed by the cell wall area ratio and the cell wall bulk density as

$$\rho = S\rho_0 \tag{5.8}$$

where the cell wall bulk density ρ_0 is set to 1500 kg/m^3, see Section 2.3.1. If the density is known, the cell wall area ratio can be calculated from the inverse expression as

$$S = \frac{\rho}{\rho_0} \tag{5.9}$$

Through combining Eqs.(5.6) and (5.8), if the variables w_{t1}, w_{t2}, w_r, e and ρ are known, the cell wall thickness t can be determined as

$$t = \frac{1}{2}\frac{C_1}{C_2} - \sqrt{\left(\frac{1}{2}\frac{C_1}{C_2}\right)^2 - \frac{C_3}{C_2}} \tag{5.10}$$

where the constants C_1, C_2 and C_3 are determined by

$$\begin{aligned} C_1 &= w_t + \frac{4ew_r + w_{t1} - w_{t2}}{2e} \\ C_2 &= \frac{4ew_r + w_{t1} - w_{t2}}{ew_r} \\ C_3 &= \frac{\rho}{\rho_0} w_r \frac{w_t}{2} \end{aligned} \tag{5.11}$$

Starting with Eq.(5.7), the cell wall thickness t can be obtained for cells with thin walls as

$$t = \frac{1}{4}\left(w_t + w_r - \sqrt{(w_t + w_r)^2 - 4\frac{\rho}{\rho_0} w_r w_t} \right) \tag{5.12}$$

Thus, if the density, the radial and tangential cell widths and the eccentricity parameter are known, the cell wall thickness of the hexagonal cells can be determined using Eq.(5.10) or (5.12).

5.4.3. Growth ring structures based on hexagonal cells

For the shape of the cells shown in Figure 5.19, the cell structure of a growth ring can be modelled by an appropriate selection of the variables involved, considering the variation over the growth ring. By knowing the variation in density and the radial widths of the cells, a model of a growth ring can be obtained. As was shown earlier, the density varies considerably over the different regions in the growth ring, see Figure 2.7. To model the variation in density, the growth ring is divided into three regions: earlywood, transitionwood and latewood, Figure 5.20. Since in the earlywood region the density is assumed to show only a slight linear increase whereas the radial cell width is assumed to be constant, the cell wall thickness should increase slightly according to Eq.(5.10). In the transitionwood, the density is assumed to increase more rapidly and the radial cell width to decrease, leading to an increase in the cell wall thickness. In the latewood, finally, the density is assumed to increase linearly and the radial cell width to be constant, so that the cell wall thickness increases.

The cell structure is modelled by assuming that the average density ρ_r of the growth ring is known. On the basis of the measurements presented in Section 3.2, it was concluded that the latewood width could be regarded as constant. Measurements indicated the width of the latewood to be 0.20 mm and the average basic density in the latewood was assumed to be 1000 kg/m^3. The width of the earlywood was shown to vary linearly with the growth ring width, Figure 3.8, The average density of the earlywood was assumed to be 300 kg/m^3. The width of the transitionwood was assumed, according to Eq.(2.3), to be a linear function of the growth ring width, the average density being assumed to be 450 kg/m^3. To determine the earlywood width, the growth ring width was calculated from the average density by use of Eq.(2.4). The width of the earlywood was determined then by subtracting

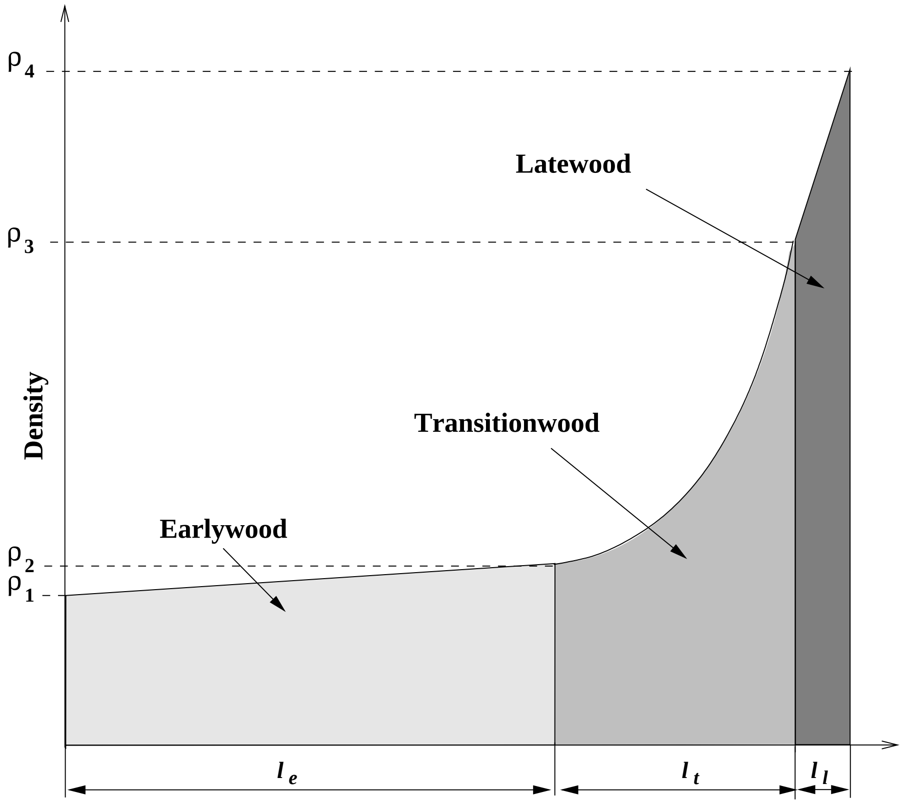

Figure 5.20: *Schematic drawing of growth ring divided into earlywood, transitionwood and latewood.*

the late- and transitionwood widths from the total width of the growth ring

$$l_e = (1 - s)l_r - l_l \tag{5.13}$$

where l_e is the width of the earlywood region, l_l the width of the latewood region, l_r the growth ring width and $s = 0.20$ is the parameter allowing the transitionwood width to be determined in terms of growth ring width according to Eq.(2.3).

The variation in the width of the cells in the radial direction in the three growth ring regions was determined from microstructural measurements and from micrographs. The mean radial cell width in the earlywood region was measured from micrographs as those shown in Section 3.3 to be about 35μm. The radial width of the cells of the latewood region being determined from the measurements presented in Section 3.2 to be 16 μm. In the transitionwood the radial cell width w_{r_t} was assumed to vary linearly varying from the earlywood to the latewood,

$$w_{r_t} = w_{r_e} - \frac{w_{r_l} - w_{r_e}}{l_t} r_t \tag{5.14}$$

where w_{r_e} is the radial width of the cells in the earlywood, w_{r_l} is the radial width of the cells in the latewood and r_t is the radial position in the transitionwood.

The tangential cell widths were determined from measurements shown in Figure 3.16 to be w_{t2}=27 μm. From micrographs, w_{t1} was determined to be 25 μm. The eccentricity parameter e was assumed to be 0.6.

The distribution of the density within the three regions in the growth ring needs to be determined on the basis of functions. The density functions in the radial direction for the earlywood, $\rho_e(r_e)$, and for the latewood, $\rho_l(r_l)$, were assumed to be vary linearly. In the transitionwood the density function, $\rho_t(r_t)$, was assumed to be a quadratic function. The density functions for the three regions in the growth ring then become

$$\begin{aligned} &\text{Earlywood :} && \rho_e(r_e) = \rho_1 + \frac{\rho_2 - \rho_1}{l_e} r_e \\ &\text{Transitionwood :} && \rho_t(r_t) = \rho_2 + \frac{\rho_3 - \rho_2}{l_t^2} r_t^2 \\ &\text{Latewood :} && \rho_l(r_l) = \rho_3 + \frac{\rho_4 - \rho_3}{l_l} r_l \end{aligned} \tag{5.15}$$

where r_e, r_t and r_l are the radial positions in the earlywood, the transitionwood and the latewood, respectively. The densities ρ_1, ρ_2, ρ_3 and ρ_4 as shown in Figure 5.20, were determined for the three regions on the basis of the average densities of 300, 450 and 1000 kg/m^3, respectively. By assuming linear density functions for the earlywood and the latewood and a quadratic density function for the transitionwood, the values of ρ_2, ρ_3 and ρ_4 can be determined, by simply assigning a value to ρ_1 as

$$\begin{aligned} \rho_1 &= 260 && \text{kg/m}^3 \\ \rho_2 &= 2\rho_e^* - \rho_1 && \text{kg/m}^3 \\ \rho_3 &= 3\rho_t^* - 2\rho_2 && \text{kg/m}^3 \\ \rho_4 &= 2\rho_l^* - \rho_3 && \text{kg/m}^3 \end{aligned} \tag{5.16}$$

where the superscript * denotes the average density in the region in question.

Before the thickness of the cells in the model is calculated, the density needs to be reduced due the wood containing extractives and the properties being determined at a moisture content of 12%. According to Eq.(2.20) the volume of wood at a moisture content between 0 and 25% can be written as

$$V = (1 + 0.4w)V_0 \tag{5.17}$$

The weight m of the wood at moisture content w is

$$m = (1 + w)m_0 \tag{5.18}$$

where m_0 is the weight in dry condition. The density measured at different moisture contents is thus

$$\rho = \frac{(1 + w_m)m_0}{(1 + 0.4w_v)V_0} \tag{5.19}$$

where w_m is the moisture content at which the sample was weighed and w_v is the moisture content at which the volume was determined. By use of this equation,

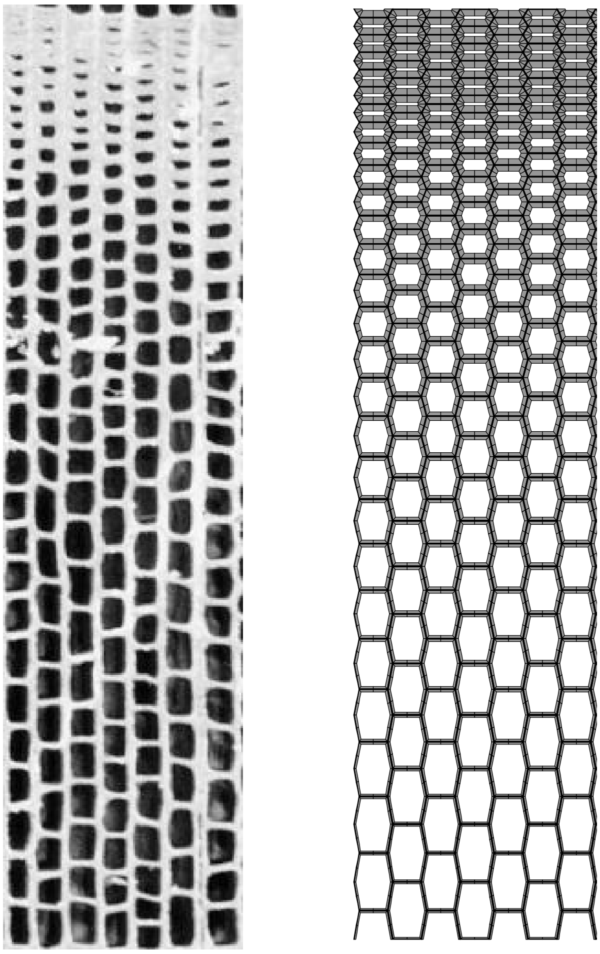

Figure 5.21: *Photographed cell structure and modelled hexagonal cell structure of about the same average density and growth ring width.*

relationships of densities defined with the volume and the weight being determined under differing moisture conditions can be established. In the present study, the properties of the wood are determined at a moisture content of 12%. Using Eq.(5.19), the relationship between the density at 12% moisture content, $\rho_{12\%}$ and the density at a dry condition $\rho_{0\%}$ is written

$$\rho_{12\%} = 1.069\rho_{0\%} \tag{5.20}$$

In addition to this, wood contains about 4% extractives that have an unknown contribution to the stiffness. To account for these facts in the modelling the average density is reduced by 8% before the cell wall thicknesses are determined.

The shape and size of a cell structure in a complete growth ring of average density can be determined then. The steps involved can be summarised as follows:

1. An average density of the wood is selected, the growth ring width being determined from this by use of Eq.(2.4).

2. The width of the earlywood and the transitionwood is determined using Eqs.(5.14) and (2.3).

3. The density functions for the three separate regions are determined and the parameters in Eq.(5.6) of the radial cell width, the tangential cell widths and the eccentricity parameter are selected.

4. The thickness of each cell wall in the growth ring is determined using Eq.(5.10) or (5.12), allowing the number of cells in each region to be determined.

Through following the four steps just described and using the density functions provided by Eqs.(5.15) and (5.16), the cell structure of a complete growth ring can be determined. An example of this is shown in Figure 5.21.

The shape of the cell structure described above is more regular than the cell structure in real wood. A regularly shaped cell structure may show greater stiffness in the radial and tangential directions than a more irregularly shaped one. To account for this in the modelling, an optional random number generated disturbance of the cell structure was introduced. Each of the corner points in the cell structure where the cell walls of adjacent cells meet is translated to a point within a circle in the RT-plane.

A cylindrical local coordinate system at each connection point is assumed. For each connection point i in the cell structure, two random numbers R_i and ϕ_i, with reference to the local cylindrical coordinate system, are generated from uniform distributions, where $0 \leq R_i \leq R_{max}$ and $0 \leq \phi_i \leq 2\pi$. R is the distance at which translation of the connection point in a radial direction occurs in the cross sectional

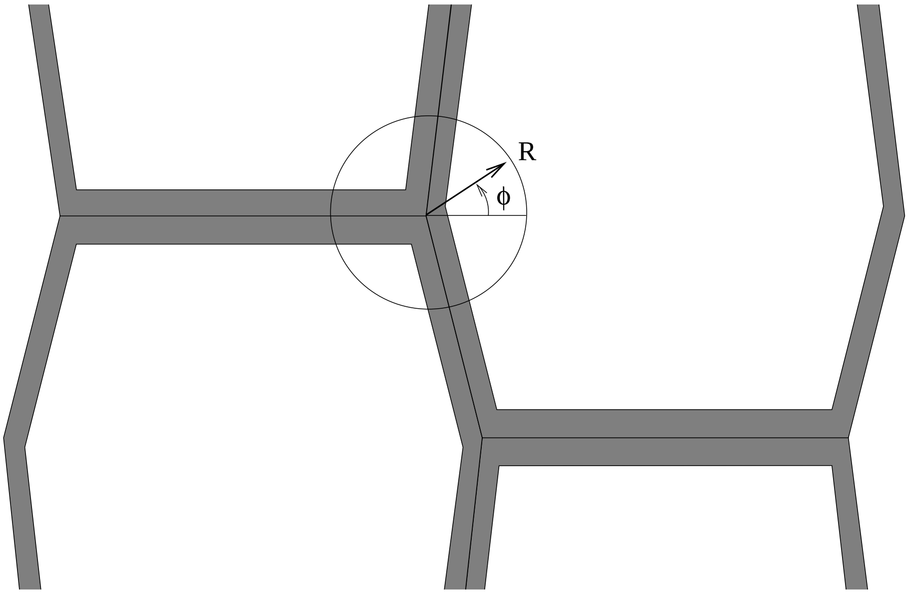

Figure 5.22: *Translation of a connection point by use of R- and ϕ-parameters.*

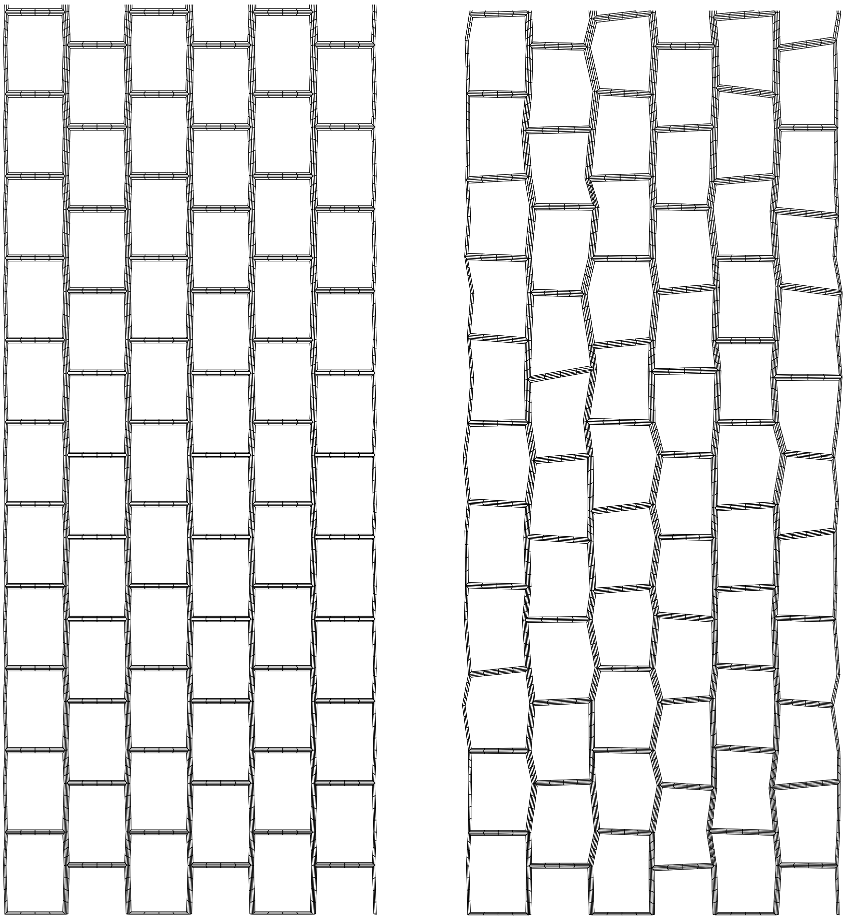

Figure 5.23: *Original cell structure and irregular cell structure with* $R_{max} = 3\mu m$.

plane. ϕ_i is the direction of the translation, measured as the angle from the global T-axis, see Figure 5.22. R_{max} is chosen differently in the different regions of the growth ring. In the earlywood and transitionwood regions, where the cross sectional dimension of the cells is large, a higher value of R_{max} is permitted. In the latewood region, where the cross sectional dimensions of the cells are smaller, R_{max} is reduced to having only one-fourth of the it has value in the earlywood.

Properties of cell structures will later be determined for both regular and irregular cell structures. For irregular cell structures, different values of R_{max} will be employed. In Figure 5.23 an example of a regular structure is shown, together with an irregular cell structure for which R_{max}=3 μm.

5.4.4. Finite element modelling of growth ring structures

To calculate the homogenised stiffness and shrinkage properties using a homogenisation procedure and the finite element method, a representative volume element needs to be chosen. For the structure based on hexagonal cells, the representative element in the radial direction was taken as a whole growth ring having the geometries discussed earlier in this section. In the tangential direction, if the rays are not included in the model, at least two cells must be present for a repetitive pattern to be achieved. However, if ray cells are to be included, the number of cells of the representative element in the tangential direction is set equal to the number of cells that are lying between the rays. In the present model, a ray is included at one side of the representative element. On the basis of measurements it was found that the average number of cells present between adjacent rays in the tangential direction was seven and the corresponding median value six, Figure 3.17. The representative volume element must contain an even number of cells in the tangential direction for a repetitive structure to be obtained. A total of six cells in the tangential direction was used in models in which ray cells were included. The ray cells were modelled by adding to the outer cell wall a layer in which the microfibrils were oriented in the radial direction. Since the density of the ray cells has been reported to be lower than the average density of the growth ring, Kollman and Côté [35], it was assumed in the present model that the stiffness of the ray cell layer was equal to the stiffness of the S_2-layer of an earlywood cell.

The cell walls of each cell in the model were modelled as consisting of three layers, the orthotropic constitutive matrices of which were determined by the stiffness coefficients obtained in Section 5.2. Each of the cell wall layers in the model differs from the others in its microfibril angle, the S_2-layer having a microfibril angle that is variable. The hexagonal cell model contains six walls, each with a different orientation in the RT-plane and thus with a different material direction. Two transformations are thus needed to orient the local coordinate direction of the microfibrils of the different layers to the global coordinate system. The first transformation is made to orient the principal directions of the microfibrils to the coordinate system of the cell walls.

In terms of the notation shown in Figure 5.24, the transformation is performed with respect to a rotation around the m_3-axis as

$$\mathbf{D}_c = \mathbf{L}^T \mathbf{D}_m \mathbf{L} \tag{5.21}$$

where $\mathbf{L}$ is the transformation matrix according to the transformation rule in Eq.(2.14) for rotation around the m_3-axis, $\mathbf{D}_m$ is the stiffness matrix in the microfibril coordinate system and $\mathbf{D}_c$ is the stiffness matrix in the coordinate system of the cell wall layer. Table 2.2 shows the microfibril angles used for the different layers of the cell wall.

The second transformation is made in order to orient the cell wall layers to the directions of the hexagonal cell walls. This is performed by rotation around the c_1-axis, Figure 5.25. This rotation becomes

$$\mathbf{D} = \mathbf{M}^T \mathbf{D}_c \mathbf{M} \tag{5.22}$$

where $\mathbf{M}$ is the transformation matrix for a rotation around the c_1-axis. Each cell in the model contains six walls, each of differing orientation in the global coordinate

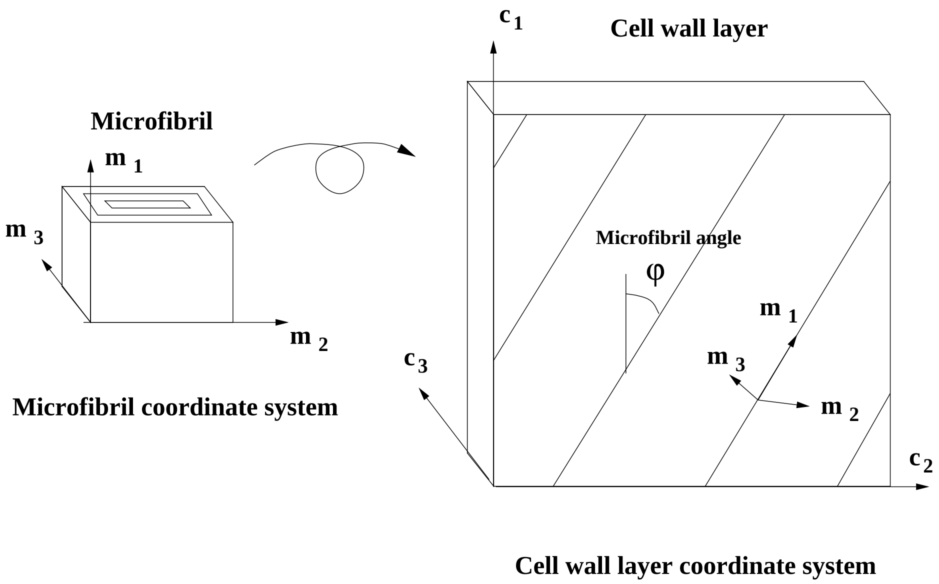

Figure 5.24: *Transformation of the constitutive matrix of the microfibril to the coordinate system of a cell wall layer.*

system. Since the microfibrils are wound around the cell in a helical pattern, the cell wall layers in all six of the walls in the hexagon need to be rotated. This results in the material in almost all of the cell walls in the cell structure having a unique orientation with respect to the global coordinate system.

The transformation from the microfibril coordinate system to the global coordinate system can be performed in a single operation through combining Eqs.(5.21) and (5.22)

$$\mathbf{D} = \mathbf{G}^T \mathbf{D}_m \mathbf{G} \tag{5.23}$$

where

$$\mathbf{G} = \mathbf{LM} \tag{5.24}$$

The equivalent stiffness properties of a cell structure are determined by use of the homogenisation procedure and the finite element method. The hexagonal cell structure is regarded as being a repetitive unit of the wood and is chosen as the base cell in the homogenisation procedure. Using the method described in the previous chapter, the base cell is first divided into 20-node isoparametric three-dimensional solid elements with a composite material formulation. Composite elements are divided into sections in which the different materials can be defined, an integration through the sections resulting then in the element stiffness matrix, see ABAQUS [28]. Each of the six walls of the hexagonal cell is divided into four finite elements in the circumferential cell wall direction, and into two finite elements in the radial cell wall direction and one element in the longitudinal direction. Each of the cell walls consists from the lumen outwards, of the S_3-, S_2- and the middle-layer, the middle layer being a compound of half the thickness of the middle lamella, the primary

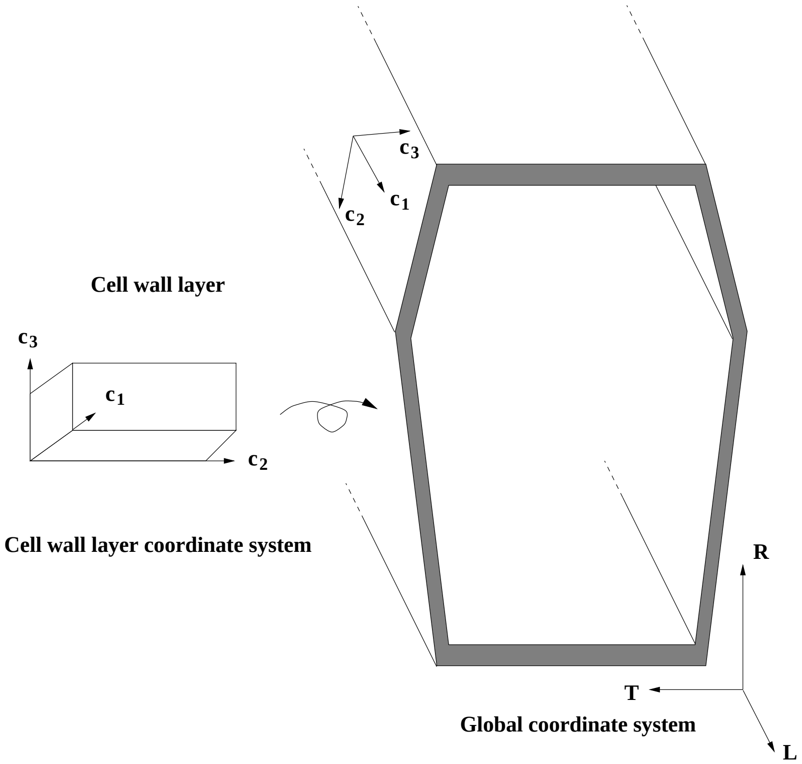

Figure 5.25: *Transformation of the constitutive matrix of a cell wall layer to the global coordinate system.*

wall and the S_1-layer. Since each hexagonal cell consists of 48 finite elements, large growth ring structures contain several thousand elements, see Figure 5.26.

5.4.5. Numerical example of properties of growth ring structures

The equivalent stiffness and the hygroexpansion properties of a representative volume element are determined by means of the homogenisation procedure, as described in Chapter 4. To obtain the equivalent stiffness properties of clear wood, a part of a growth ring is chosen as the representative volume element, which is subjected to periodic boundary conditions and to the six load cases that were described in Chapter 4. The six load cases are solved one by one by means of the finite element method. The equivalent stiffness properties are determined then from the finite element solution. The equivalent hygroexpansion properties of the cell structure are determined by supplementing the hygroexpansion coefficients by the material definition of the cell wall layers and subjecting the base cell to periodic boundary conditions and loading it with a unit moisture change. The stiffness and hygroexpansion properties of a model with hexagonal cells were determined. The wood cell structure was assumed to have an average density of 400 kg/m^3, corresponding, according to Eq.(2.4), to a ring width of 2.01 mm. The stiffness and hygroexpansion properties of the materials in the different cell wall layers employed were determined, as in Section 5.2, for a moisture content of 12%. The microfibril angles employed

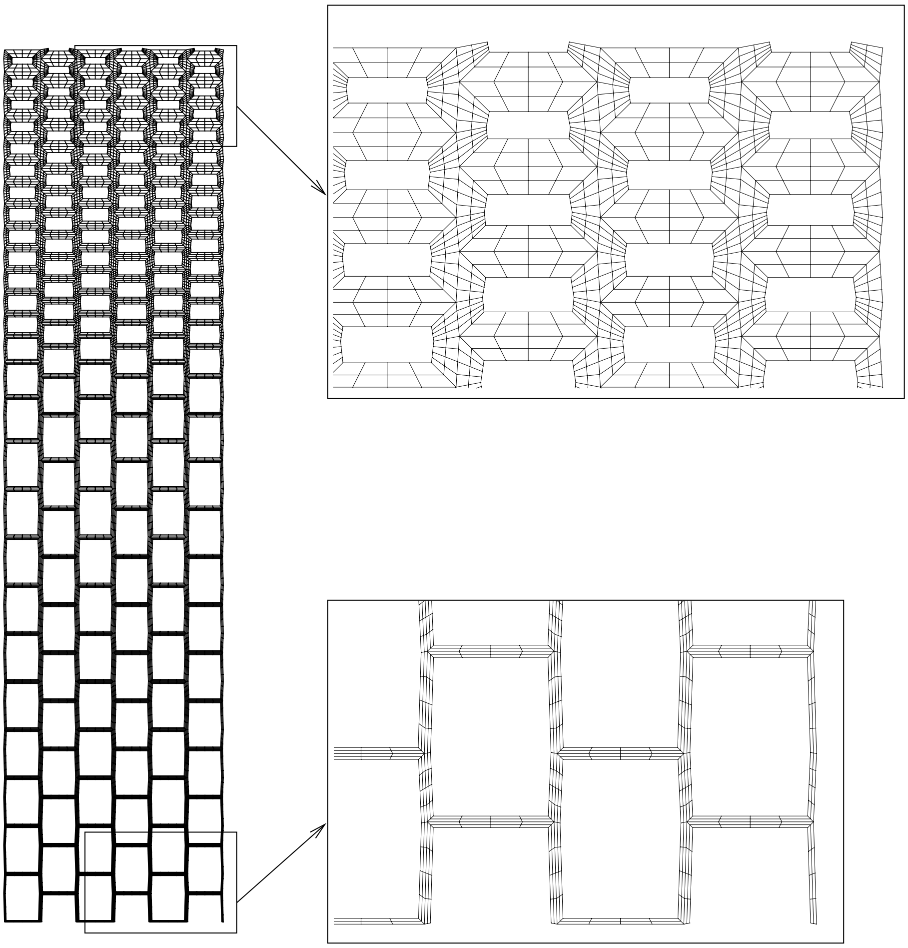

Figure 5.26: *Three-dimensional cell structure with a density of 550 kg/m^3 meshed with finite elements with portions of the earlywood and latewood regions being magnified.*

for the different layers in the model are shown in Table 5.13.

The stiffness and shrinkage properties were determined using two hexagonal models. The models were identical except for the one model involving a regular cell structure and the other an irregular cell structure for which $R_{max} = 3\mu$m. Table 5.14 shows the stiffness properties and the hygroexpansion coefficients obtained for the two models using the low, medium and high material properties for the cell wall layers as given in Tables 5.3 and 5.4. The influence of the stiffness of the cell walls on the average stiffness properties obtained was found to be strong. Irregularity influences primarily the modulus of elasticity in the radial direction. The differences between the hygroexpansion properties obtained that are due to differences in the stiffness properties of the cell wall and the irregularity of the geometry are small. However, the radial hygroexpansion is greater for the cell structure model involving an irregular geometry.

Table 5.13: *Microfibril angles of the cell wall layers.*

Layer	MF angle, φ°
Middle layer	+ 45
S_2	− 10
S_3	+ 75

Table 5.14: *Equivalent stiffness parameters and hygroexpansion coefficients determined from hexagonal cell models with regular and irregular cell structures having a density of 400 kg/m^3 using the low, medium and high material properties of the cell wall layers.*

Coefficient	Regular			Irregular		
	Low	Medium	High	Low	Medium	High
E_L, [MPa]	9576	11180	12744	9554	11160	12730
E_R, [MPa]	1180	1351	1497	835	987	1115
E_T, [MPa]	366	456	530	366	455	528
G_{LR},[MPa]	649	765	880	636	751	863
G_{LT},[MPa]	580	686	789	575	681	783
G_{RT},[MPa]	7.58	9.4	11.0	7.81	9.68	11.3
ν_{RL}	0.049	0.049	0.049	0.039	0.039	0.039
ν_{TL}	0.017	0.018	0.018	0.017	0.018	0.018
ν_{TR}	0.064	0.066	0.07	0.068	0.068	0.072
α_L	0.0053	0.0059	0.0065	0.0042	0.0050	0.0057
α_R	0.202	0.215	0.222	0.224	0.233	0.238
α_T	0.407	0.400	0.400	0.399	0.398	0.397

5.5. Modelling Properties of Real Cell Structures

5.5.1. Models of different regions in the growth ring

The mechanical properties of wood were also determined by modelling real wood cell structures. Three regions of the growth ring were selected from micrographs as being representative of Norway spruce. These included one region with a typical earlywood cell structure, one with a typical transitionwood structure and one with a typical latewood structure. The micrographs of the wood cell structures were scanned into digital images, the geometry of the cell structures being obtained by hand through drawing lines at the boundaries of the cell walls, using a computer drawing program. To create three-dimensional structures, the geometries were extruded in the longitudinal direction and thus assuming that the cell structures are uniform in this direction. The extraction of the geometry and the finite element meshing were carried out by hand. This procedure could also be performed automatically

Table 5.15: *Microfibril angles and thicknesses of the earlywood cell wall layers.*

Layer	Microfibril angle, $\varphi°$	Thickness, μm
Middle layer	+45	0.45
S_2	-10	0.78
S_3	+75	0.05

through determining the geometry by use of an image analysis program, by which the properties being calculated automatically. An automatic procedure should be capable of analysing very large cell structures.

The thickness of the cell walls was determined from the average densities for the respective regions at 300, 450 and 1000 kg/m^3. These thicknesses were assumed to be the same in all the cells in the respective region and were determined by use of Eq.(5.10), the cell wall area ratio of the cell structure being determined on the basis of the cell wall bulk density of 1500 kg/m^3 and the average density of the respective region. The geometrical models obtained from the micrographs were extruded in the longitudinal direction to obtain three-dimensional structures that were meshed with eight-node composite shell elements. Such a composite formulation makes it possible to have several layers of different materials in a given element, ABAQUS [28]. Symmetric boundary conditions were applied, the models being loaded for the six load cases. The equivalent stiffness properties were determined from the reaction forces and the applied deformation at the boundaries.

All pairs of cell walls in the models consist of six layers, except for the cell walls at one of the boundary LR-plane where an additional layer is modelled for representing a ray cell. From lumen to lumen, the six layers in the cell walls are, S_3-S_2-M-M-S_2-S_3, where the middle layer (M) is composed of the S_1-layer, the primary wall and half the middle lamella. The six layers are alternately wound around the cells in a left and a right helical pattern, thus differing in their orientation. As earlier, the rays were modelled using a stiffness equal to that of the S_2-layer of an earlywood cell. The medium set of material parameters used for the six layers was taken from the results of modelling the cell wall properties, as shown in Tables 5.3 and 5.4.

The earlywood cell structure was selected and modelled from a micrograph, as shown in Figure 5.27. It consists of cells of large radial width with thin walls. For the earlywood structure shown in Figure 5.27, the thickness of an M-S_2-S_3-wall was determined as being 1.28 μm on the basis of Eq.(5.10), an average density of 300 kg/m^3 being employed. The thicknesses and the microfibril angles of the individual cell walls used for the earlywood cell structure are shown in Table 5.15.

The cell structure of the transitionwood was selected and modelled as shown in Figure 5.28. The cells of the transitionwood region have slightly thicker walls than those of the earlywood region but the radial width of the cells is considerably smaller. In the transitionwood region, the cells are broader in the tangential than

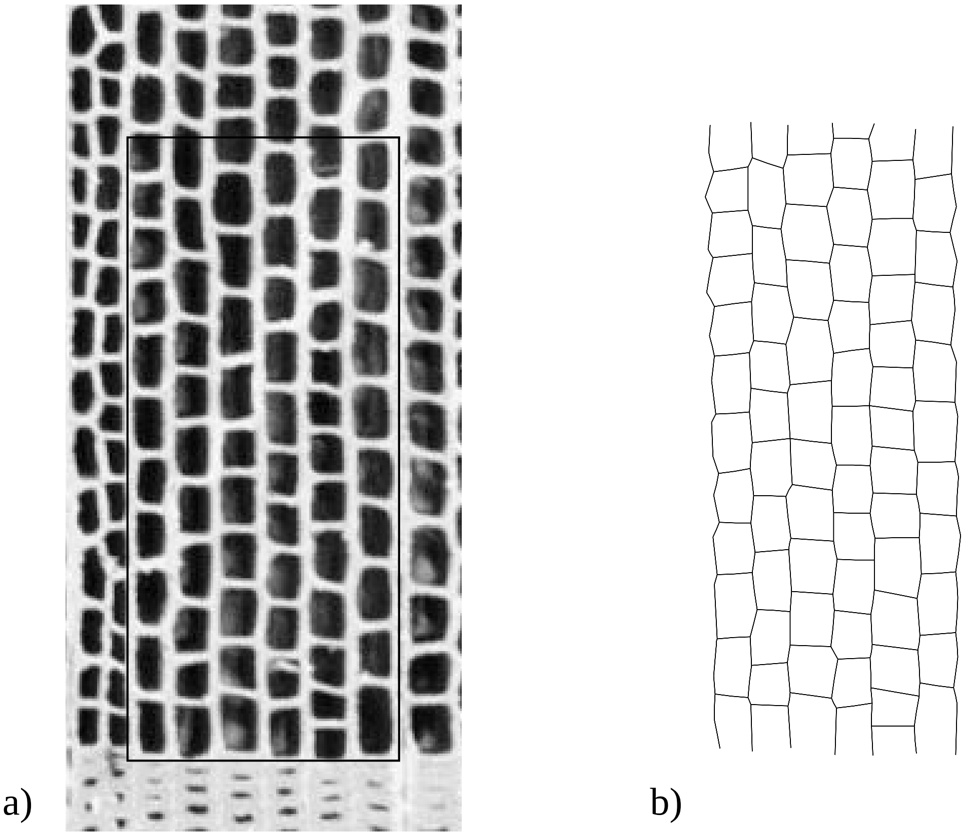

Figure 5.27: *Earlywood cell structure.* **a***) Micrograph of structure.* **b***) Modelled structure.*

Table 5.16: *Microfibril angle and thickness of the transitionwood cell wall layers.*

Layer	Microfibril angle, φ°	Thickness, μm
Middle layer	+45	0.45
S_2	-10	0.87
S_3	+75	0.05

in the radial direction, whereas in the earlywood region the radial width is greater than the tangential. Although the cell wall thickness increases towards the latewood region, the cell wall thickness is assumed in the model to be equal throughout, being determined from the average density of 450 kg/m^3. For the structure shown in Figure 5.28, the cell wall thickness was found to be 1.37 μm. An additional layer representing a ray cell with the stiffness of an earlywood cell is modelled at the left side of the structure. The thickness and the microfibril angles of the different cell wall layers of the transitionwood structure are shown in Table 5.16.

The cell structure of the latewood was selected and modelled as shown in Figure 5.29. In the latewood region, the cell wall thickness increased considerably in com-

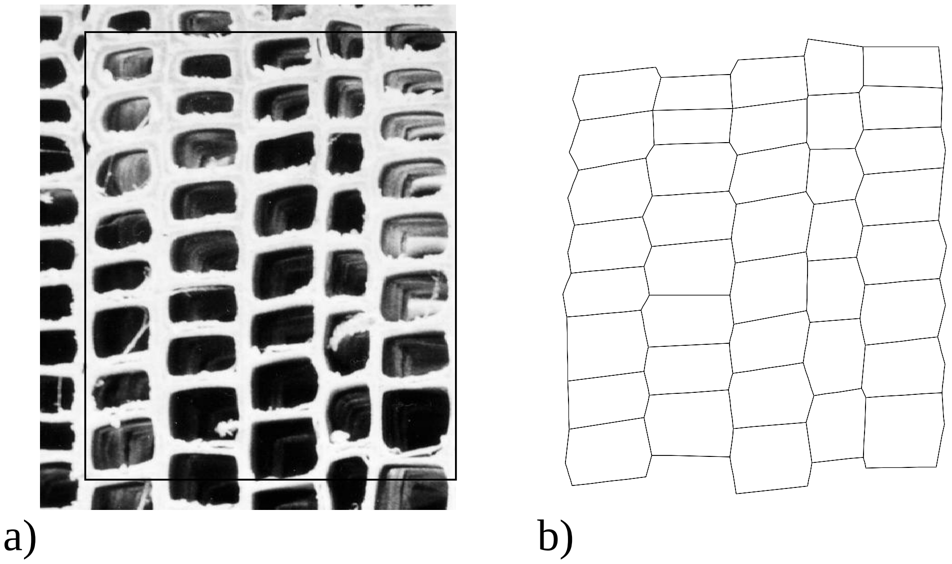

Figure 5.28: *Transitionwood cell structure.* **a**) *Micrograph of structure.* **b**) *Modelled structure.*

parison with the transitionwood region, whereas the width of the cells in the radial direction was similar. The average density of the latewood cell structure was assumed to be 1000 kg/m^3. Using this density, the cell wall thickness was determined as being 3.84 μm. This model also includes ray cells, despite their making only a small contribution to the overall stiffness of the latewood region. The properties of the different cell wall layers of the latewood region are shown in Table 5.17.

5.5.2. Equivalent stiffness and shrinkage of real cell structures

The geometrical models of the three regions, as obtained from micrographs, were extruded in the longitudinal direction and were divided into eight node composite shell elements. In real cell structure models, periodic boundary conditions can often not be applied directly since the cell walls present at opposing boundaries are not exactly alike. For the models of real cell structures, symmetric boundary conditions were instead applied where the displacements at the boundaries have been prescribed in the direction normal to the respective boundary. Each model was then loaded for six cases of prescribed unit displacements at the boundaries and the equivalent stiffness and shrinkage properties were determined from the reaction forces at the boundaries.

The equivalent stiffness parameters and the hygroexpansion coefficients obtained for the earlywood, the transitionwood and the latewood structures shown in Figures 5.27-5.29 are summarised in Table 5.18. It was found that the differences between the radial and tangential stiffnesses were very large in the earlywood region, probably due to the ray cells and to the large width of the cells in the radial direction. The ray cells make a greater contribution to radial stiffness in regions of low density,

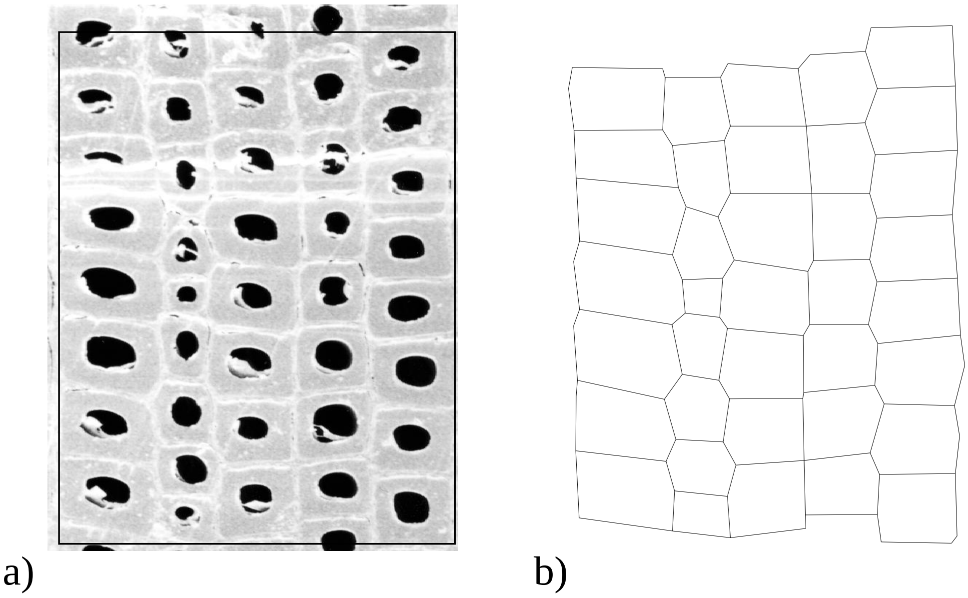

Figure 5.29: *Latewood cell structure.* **a**) *Micrograph of structure.* **b**) *Modelled structure.*

Table 5.17: *Microfibril angle and thickness of the latewood cell wall layers.*

Layer	Microfibril angle, φ°	Thickness, μm
Middle layer	+45	0.45
S_2	-10	3.34
S_3	+75	0.05

the large width of the cells in the radial direction providing only a low tangential stiffness, due to the low bending stiffness of the cell walls. In the transitionwood and latewood regions, the differences between the radial and the tangential stiffness were small and can in the RT-plane be regarded as isotropic. The shrinkage was found to be higher in the latewood region, where the cell walls are thicker. This was expected because of the cell walls being thicker and the shrinkage being greater in the thickness direction of the cell wall.

To determine the equivalent properties of an entire growth ring, a complete structure needs to be analysed. This can be made by determining a complete growth ring structure from micrographs or by averaging the obtained stiffness and shrinkage properties of the three regions directly. To determine the structure of an entire growth ring, use of an image analysis procedure is required as to minimise the amount of work required. Here the obtained stiffness and shrinkage properties shown in Table 5.18 were averaged by modelling a growth ring having three homogeneous regions. By use of the finite element method, the equivalent properties of a com-

Table 5.18: *Equivalent stiffness parameters and hygroexpansion coefficients of the three regions.*

Parameter	Earlywood	Transitionwood	Latewood
E_L, [MPa]	7710	11400	36400
E_R, [MPa]	671	953	1570
E_T, [MPa]	82.9	441	2100
G_{LR},[MPa]	675	780	1760
G_{LT},[MPa]	397	861	1770
G_{RT},[MPa]	9.23	10.0	43.1
ν_{RL}	0.0568	0.00902	0.0184
ν_{TL}	0.00594	0.0541	0.0315
ν_{TR}	0.124	0.241	0.219
α_L	0.00047	0.00282	0.00503
α_R	0.230	0.235	0.335
α_T	0.365	0.386	0.394

plete growth ring were determined. The widths of the three regions were obtained by use of Eqs.(2.4) and (5.13). The widths of the earlywood and transitionwood regions for a growth ring of either arbitrary width or arbitrary average density can then be determined by assuming the latewood width to be a constant of 0.20 mm. The three regions were modelled by means of three-dimensional solid elements and the homogenisation method described in chapter 4. This allows the stiffness and shrinkage properties of an arbitrary growth ring to be obtained.

5.6. Comparison of Cell Structure Models and Discussion

A comparison of the hexagonal cell structure model and the model based on the properties of real cell structures was made. The stiffness and shrinkage properties of a growth ring obtained by use of each of the two models, employing an average density of 400 kg/m^3 and a microfibril angle in the S_2-layer of 10°, were compared. The comparison of the obtained stiffness parameters and hygroexpansion coefficients from the two models is shown in Table 5.19. In that table typical measured values for spruce are also shown, as obtained from the experiments reported in Chapter 3 and from the literature, Carrington [11] and Hearmon [26].

A comparison of the stiffness values obtained shows both models to provide results that are close to the measured data. For both models the values of the stiffness parameters lie in the interval indicated by measurements. However, the radial stiffness was slightly higher than the other stiffness parameters as compared with the measurements. Since this was found for both models, it is probably due to that the same cell wall properties having been used for the tangentially and radially oriented cell walls. First, the two walls may differ in microfibril angle found in the

Table 5.19: *Stiffness parameters and hygroexpansion coefficients obtained from two cell structure models and measurements.*

Coefficient	Irregular hexagonal model	Model based on real structures	Measurements
E_L, [MPa]	11200	11900	6000 - 25000
E_R, [MPa]	987	1022	700 - 1200
E_T, [MPa]	455	384	400 - 900
G_{LR},[MPa]	751	835	600 - 700
G_{LT},[MPa]	681	630	500 - 600
G_{RT},[MPa]	9.68	10.9	20.0 - 70.0
ν_{RL}	0.039	0.042	0.02 - 0.050
ν_{TL}	0.018	0.015	0.01 - 0.025
ν_{TR}	0.068	0.124	0.20 - 0.35
α_L	0.0050	0.0062	0.001 - 0.006
α_R	0.233	0.180	0.13 - 0.25
α_T	0.398	0.352	0.25 - 0.41

S_2-layer. Secondly, the morphology of the radially and tangentially oriented cell walls is not identical as in the model. For example, the pit pores are located in the radially oriented cell wall. These two factors may have a substantial influence on the stiffness properties.

The differences between numerically and experimentally determined hygroexpansion coefficients are small. The hygroexpansion coefficients obtained from the model, as based on real structures, are slightly smaller than the coefficients obtained using the irregular hexagonal model. This is mainly due to the numerical procedure employed for the real cell structure model involving shell elements were used. The shrinkage in the thickness direction of the cell wall is thus underestimated.

6. NUMERICAL STUDIES

6.1. General Remarks

In this chapter numerical studies of cell structures consisting of hexagonal cells are reported. In the first section parametric studies are presented in which the models described in Chapter 5 are utilised to determine the stiffness and hygroexpansion properties for varying geometrical and material input data. In the second section a numerical study concerning how the stiffness and shrinkage properties depend of the location in the tree is reported, use being made of the models developed and the experimental data that were obtained. All the numerical work was carried out using the general purpose finite element program ABAQUS. The homogenisation procedure and the transformations of the material matrices were implemented as FORTRAN subroutines that were linked with ABAQUS.

6.2. Parametric Study

6.2.1. General remarks

The experimental work described in Chapter 3 and the numerical models described in Chapters 4 and 5 make it possible to study the influence of the microstructure on the stiffness and shrinkage properties of clear wood. Two parametric studies were performed. In the first study, how the stiffness and hygroexpansion properties are influenced by some of the basic variables involved in the description of the individual cell and in the determination of the growth ring cell structure geometry was investigated. In the second study, the influence of the microfibril angle of the S_2-layer, the average density and the material parameters of the cell wall layers on the stiffness and the hygroexpansion properties was investigated.

6.2.2. Influence of basic parameters

A number of simulations involving different basic parameters of the cell structure were performed in order to determine how theses influenced the stiffness and hygroexpansion properties. Eleven models were constructed in which the six most uncertain basic parameters were varied. The parameters were the eccentricity parameter e, the irregularity parameter R_{max}, the initial density ρ_1 in the earlywood region, the ray-cell stiffness and the angle between the walls in the hexagonal cell

Table 6.1: *Models with differing basic parameters.*

Model	e [-]	R$_{max}$ [μm]	w$_{t1}$ [μm]	ρ_1 [kg/m^3]	C_{ray} [-]
Reference	0.6	0	25.0	240	1.0
Me$_1$	0.5	0	25.0	240	1.0
Me$_2$	0.7	0	25.0	240	1.0
MR$_1$	0.6	1.5	25.0	240	1.0
MR$_2$	0.6	3.0	25.0	240	1.0
Md$_1$	0.6	0	25.0	220	1.0
Md$_2$	0.6	0	25.0	260	1.0
Mray$_1$	0.6	0	25.0	220	0.5
Mray$_2$	0.6	0	25.0	220	0.0
Mw$_1$	0.6	0	23.0	240	1.0
Mw$_2$	0.6	0	27.0	240	1.0

model. By varying the initial density ρ_1 in the earlywood region, the density profile over the growth ring could be varied. The ray-cell stiffness was varied by multiplying the original choice of the stiffness matrix for the ray cell with a scaling constant C_{ray}. To vary the angle between walls in the hexagonal cell, the tangential width w_{t1} was varied while keeping w_{t2} constant. A reference choice of the parameters was first made with e=0.6, R_{max}=0μm, ρ_1=240kg/m^3, w_{t1}=25μm and the stiffness of the ray-cells as that of the S$_2$-layer of an earlywood cell wall. From this point of reference, each parameter was varied one at a time, resulting in a total of eleven models, from which the average stiffness and hygroexpansion coefficients were determined. The models produced with the different choices of the basic parameters are found in Table 6.1. In models Me$_1$ and Me$_2$ the eccentricity parameter e was varied, in models MR$_1$ and MR$_2$ the irregularity parameter R_{max} was varied, in models Md$_1$ and Md$_2$ the initial density of the earlywood region ρ_1 was varied, in models Mray$_1$ and Mray$_2$ the stiffness of the ray-cells was varied and in models Mw$_1$ and Mw$_2$ the tangential width w_{t1} was varied. The medium set of material parameters of the cell wall layers, as shown in Tables 5.3 and 5.4 was used for all the models. Parameters of the cell structure model not mentioned here were selected in the manner described in Section 5.4. The microfibril angles that were, assumed for the various layers of the cell wall in the models here are shown in Table 6.2. A total

Table 6.2: *Microfibril angles of the cell wall layers.*

Layer	MF angle, φ°
Middle layer	+45
S$_2$	-10
S$_3$	+75

of 77 simulations were performed to determine the stiffness and the hygroexpansion properties of all models. Figures showing the results of the parametric study are presented in Appendix B. The influence of the eccentricity parameter e on each of the stiffness parameters was slight except for the tangential modulus of elasticity, which increases with increasing eccentricity. This was expected since less bending and more normal force loading of the cell walls occur. The irregularity parameter R_{max} was found to have a strong influence on the radial modulus of elasticity, where an increase in irregularity leading to a decrease in the radial stiffness. The hygroexpansion properties in the longitudinal and the radial directions were also affected by an increase in irregularity, the longitudinal hygroexpansion decreasing and the radial hygroexpansion increasing. The influence of the density parameter ρ_1 on all stiffness and hygroexpansion parameters was found to be very slight. As was expected, the stiffness of the ray cells had a strong influence on the stiffness in the radial direction. An increase in ray cell stiffness had a restraining effect on hygroexpansion in the radial direction but an increase in the longitudinal direction. Changing the ratio of the tangential widths of the cell by changing w_{t1} influenced primarily the modulus of shear in the TR-plane and Poisson's ratio ν_{TR}, both of which increased with an increase in the ratio of the tangential widths.

6.2.3. Influence of the microfibril angle, the average density and the basic material parameters on the stiffness and hygroexpansion properties

The influence of the density, the microfibril angle and the material parameters of the cell wall on the mechanical properties of the wood were investigated. A hexagonal cell structure model was used for determining the stiffness and shrinkage properties of 20 different cell structures, each involving three different sets of material parameters. The 20 cell structures were assigned four different average densities, each having five different microfibril angles of the S_2-layer. The cell structures were determined for the average densities shown in Table 6.3, with the corresponding growth ring widths being chosen in accordance with Eq.(2.4). For each average density shown in Table 6.3, models involving five different microfibril angles of the S_2-layer were analysed. The five microfibril angles chosen were 0°, 10°, 20°, 30° and 40°. For each model the average stiffness and hygroexpansion properties were determined for the low, medium and high material data sets of the cell wall layers, as shown in Table 5.3 and 5.4 for the stiffness properties and in Table 5.7 and 5.8 for the shrinkage coefficients. In using these material properties, a moisture content of 12% is assumed. The full six by six stiffness matrix and the hygroexpansion properties were determined for each of the 60 cases described above, resulting in a total of 420 simulations.

In Figures 6.1 - 6.12 the influence of density and microfibril angle on the stiffness and hygroexpansion properties are shown for regular and irregular cell structures, using the low material data sets of the cell wall layers. For microfibril angles larger than about 5°, the longitudinal modulus of elasticity showed a strong dependency

Table 6.3: *Average density and corresponding growth ring width for the analysed growth ring structures.*

Density kg/m^3	Ring width mm
400	2.01
450	1.14
500	0.76
550	0.63

on the microfibril angle, the stiffness decreasing rapidly with an increase in the microfibril angle. For small microfibril angles, the influence was only slight. The influence of the average density on the longitudinal modulus of elasticity was large, especially for small microfibril angles. The influence of the microfibril angle on the tangential modulus of elasticity, in contrast, was found to be small, the stiffness first decreasing slightly and then increasing as the microfibril angle increased. The strong influence of the density on the tangential modulus of elasticity can be explained by the fact that for loading in the tangential direction the cell walls are subjected mostly to bending. For high densities, the growth ring has a high latewood content, leading to an increase in the fraction of cells that are thick-walled and resulting in an increase in tangential stiffness. The radial modulus of elasticity showed a much lesser dependency on average density. This can be explained by the fact that the three regions of the wood structure lie in series with respect to the radial direction. As a result, the radial stiffness of the earlywood region governs the overall radial stiffness. The microfibril angle has a stronger influence, the radial modulus of elasticity first decreasing and then rapidly increasing as the microfibril angles become large.

Density had only a slight influence on the modulus of shear in the RT-plane, whereas the microfibril angle had a strong influence. With an increase in the microfibril angle, the stiffness increased rapidly. The microfibril angle had a strong influence on the modulus of shear in the LT-plane, the shear increasing with an increase in the microfibril angle, whereas the density had a lesser influence. The modulus of shear in the RT-plane was very low for small microfibril angles, increasing slightly as the microfibril angle increased whereas the density had a much greater influence. The low modulus of shear in the RT-plane was expected, due to the low bending stiffness of the earlywood cells walls. The microfibril angle was found to have a strong influence on all the Poisson ratios, whereas the density had little influence. For the parameters of the stiffness properties, it appears that each parameter depends mainly on either the density or the microfibril angle. In terms of the present model, both parameters were shown to be equally important for the stiffness properties.

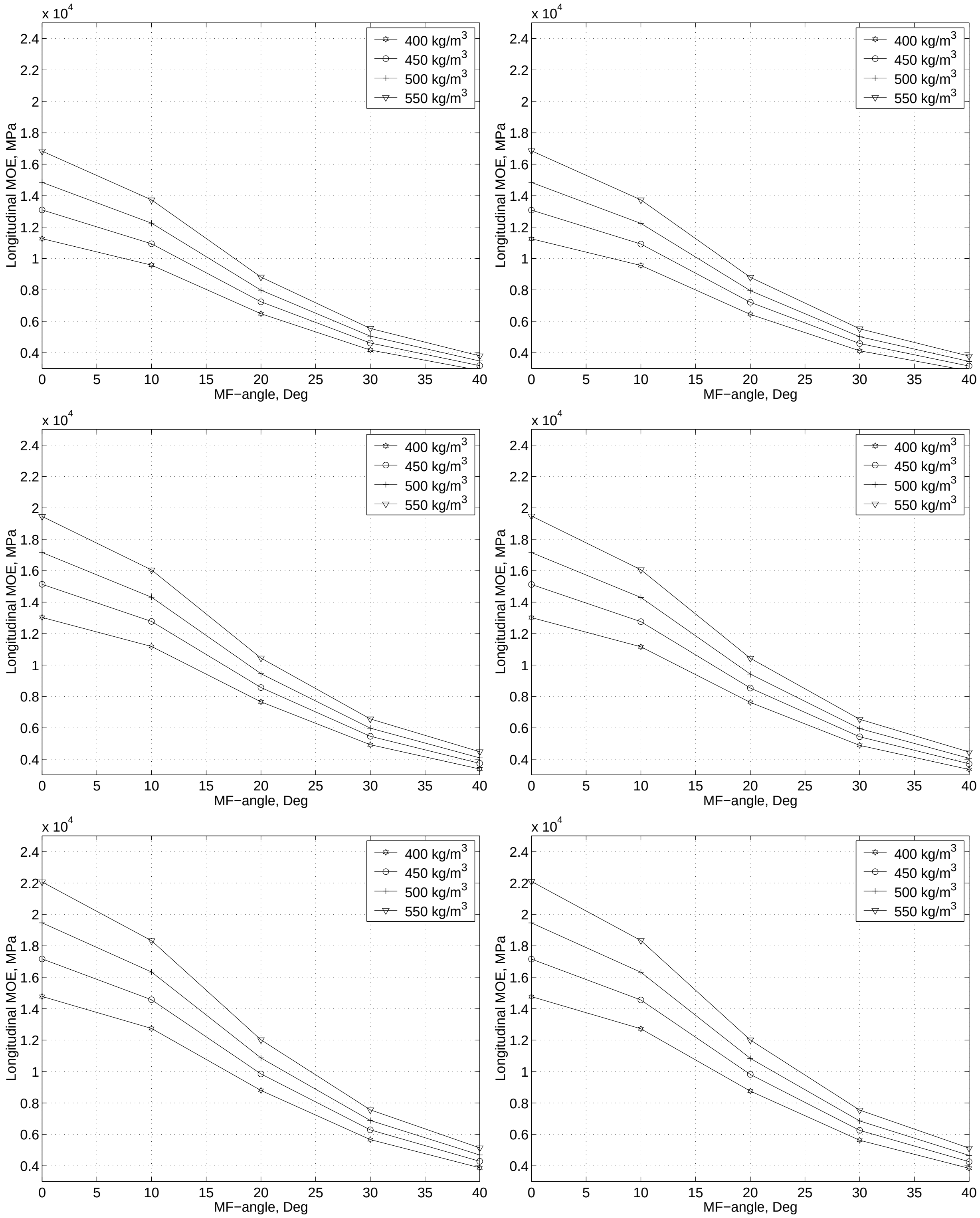

Figure 6.1: *Moduli of elasticity in the longitudinal direction at different average densities versus the microfibril angle for regular cell structures to the left and irregular to the right using from top to bottom the low, medium and high material data sets for the cell wall layers.*

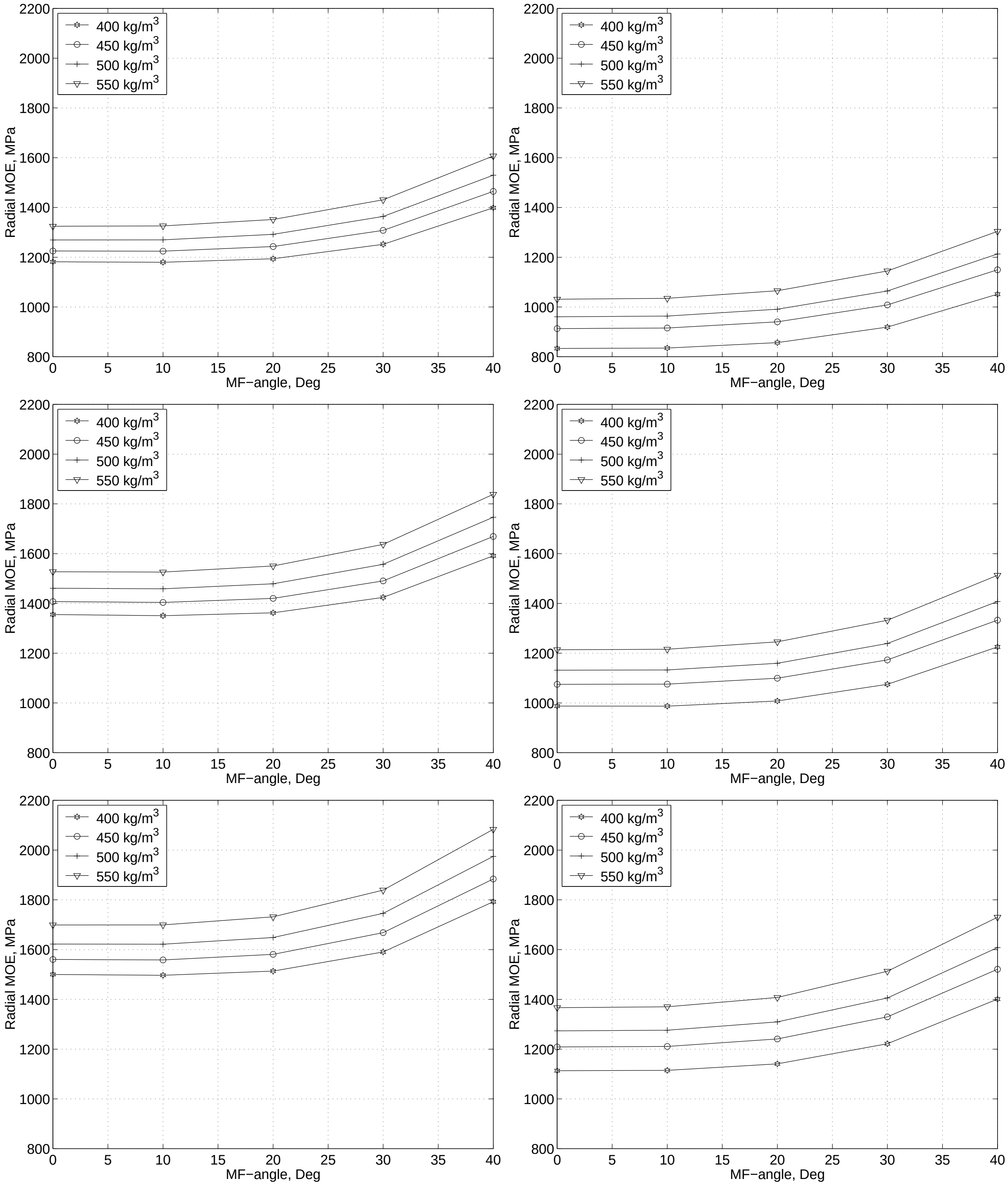

Figure 6.2: *Moduli of elasticity in the radial direction at different average densities versus the microfibril angle for regular cell structures to the left and irregular to the right using from top to bottom the low, medium and high material data sets for the cell wall layers.*

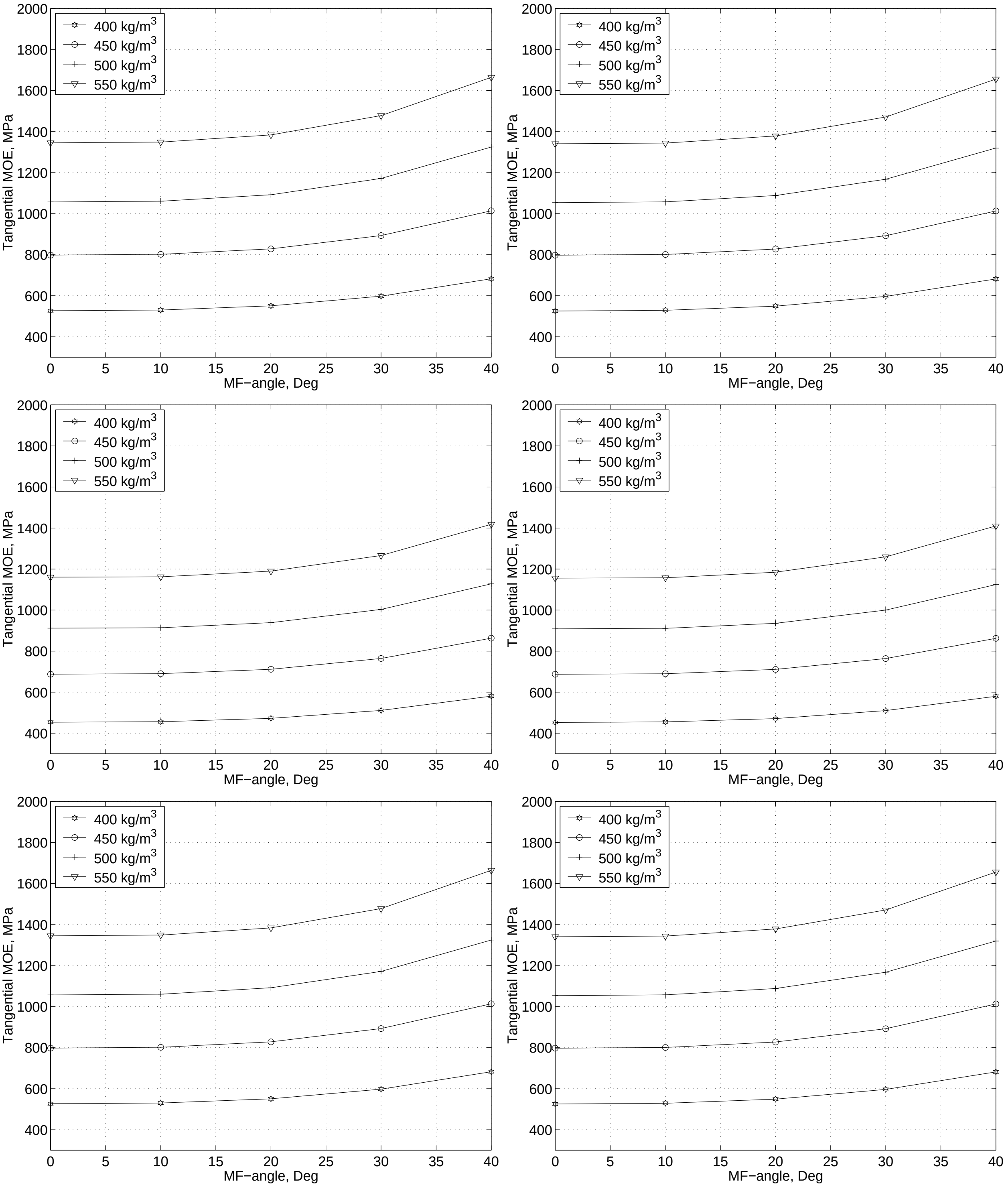

Figure 6.3: *Moduli of elasticity in the tangential direction at different average densities versus the microfibril angle for regular cell structures to the left and irregular to the right using from top to bottom the low, medium and high material data sets for the cell wall layers.*

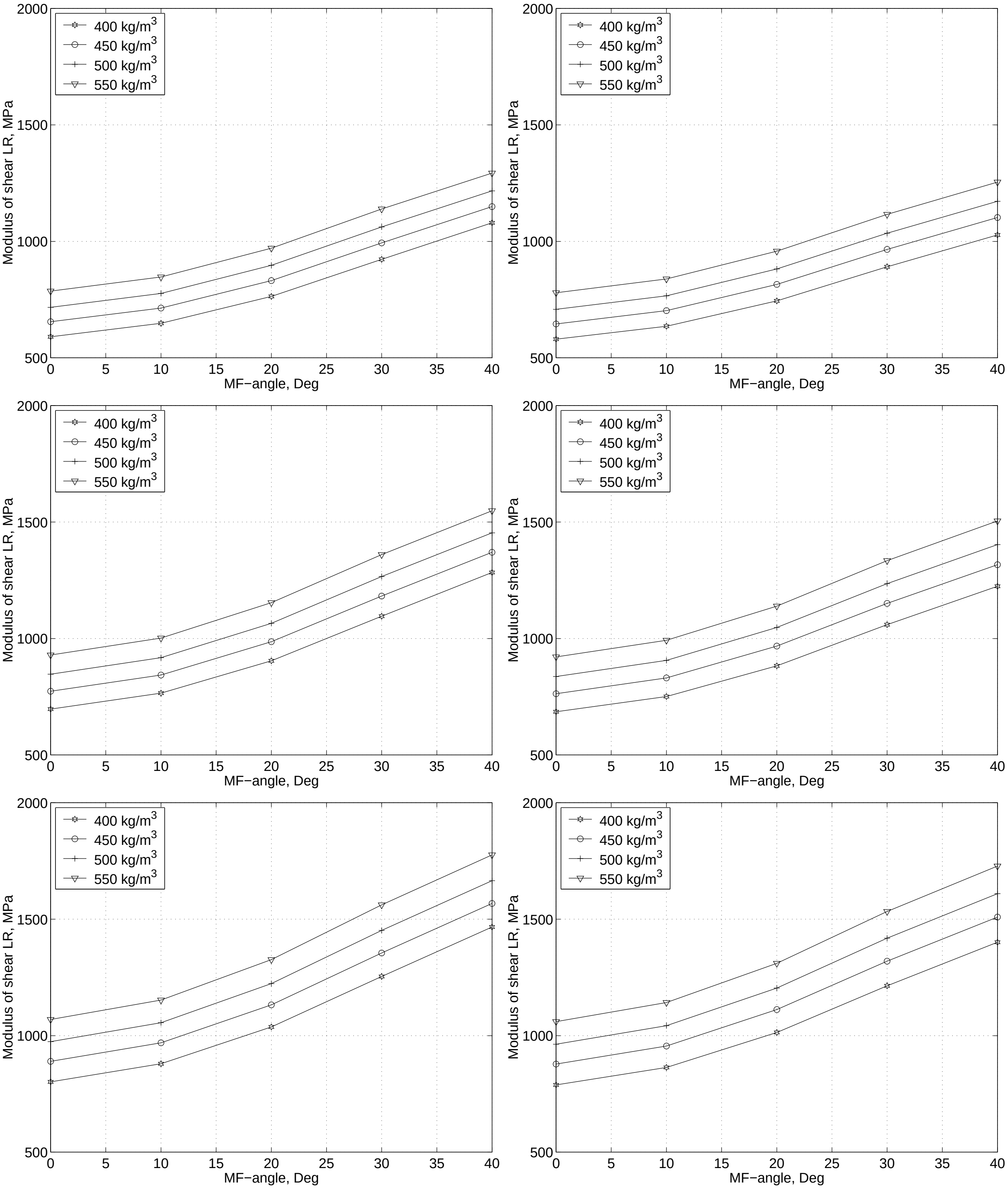

Figure 6.4: *Moduli of shear in the LR-plane at different average densities versus the microfibril angle for regular cell structures to the left and irregular to the right using from top to bottom the low, medium and high material data sets for the cell wall layers.*

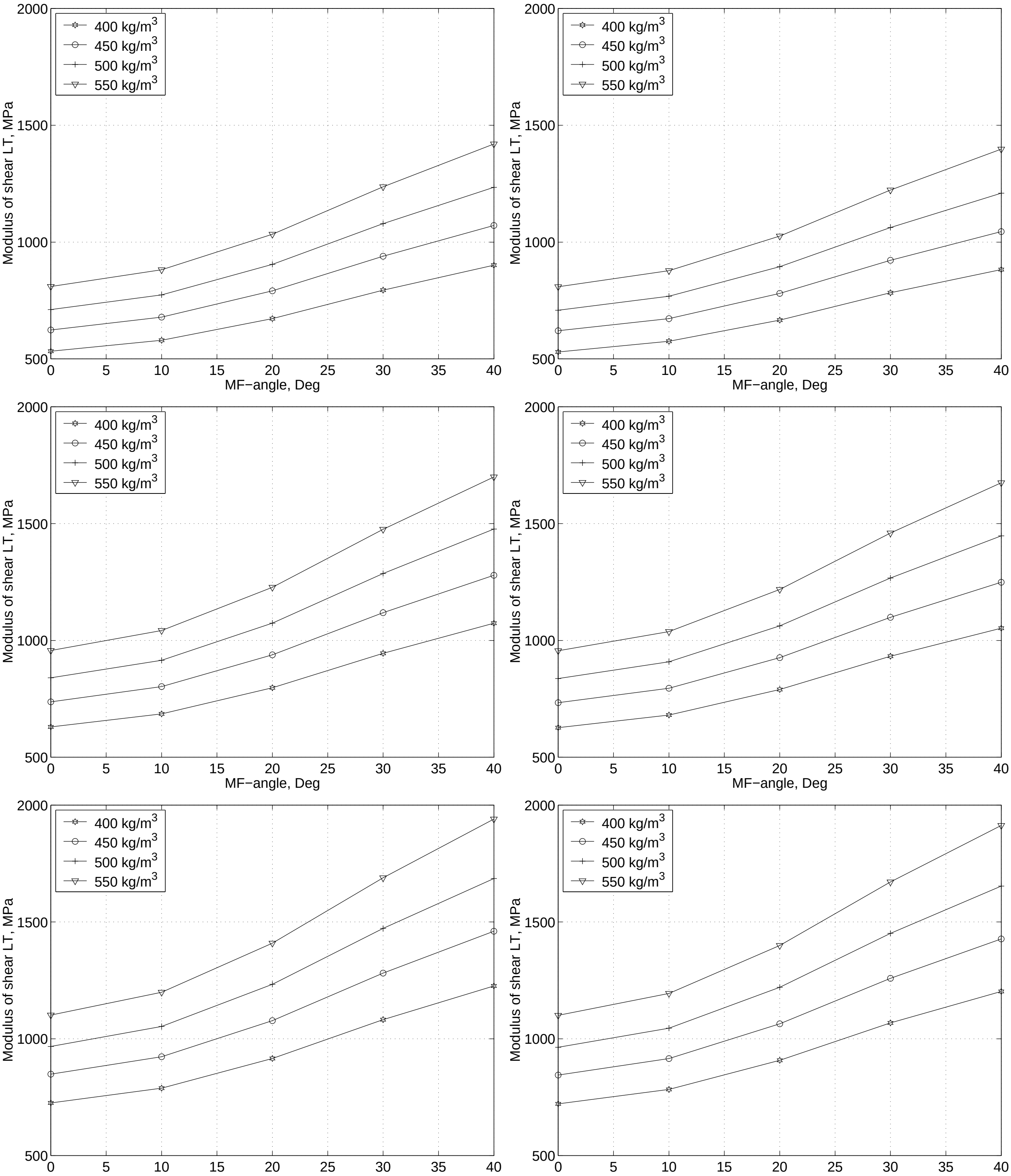

Figure 6.5: *Moduli of shear in the LT-plane at different average densities versus the microfibril angle for regular cell structures to the left and irregular to the right using from top to bottom the low, medium and high material data sets for the cell wall layers.*

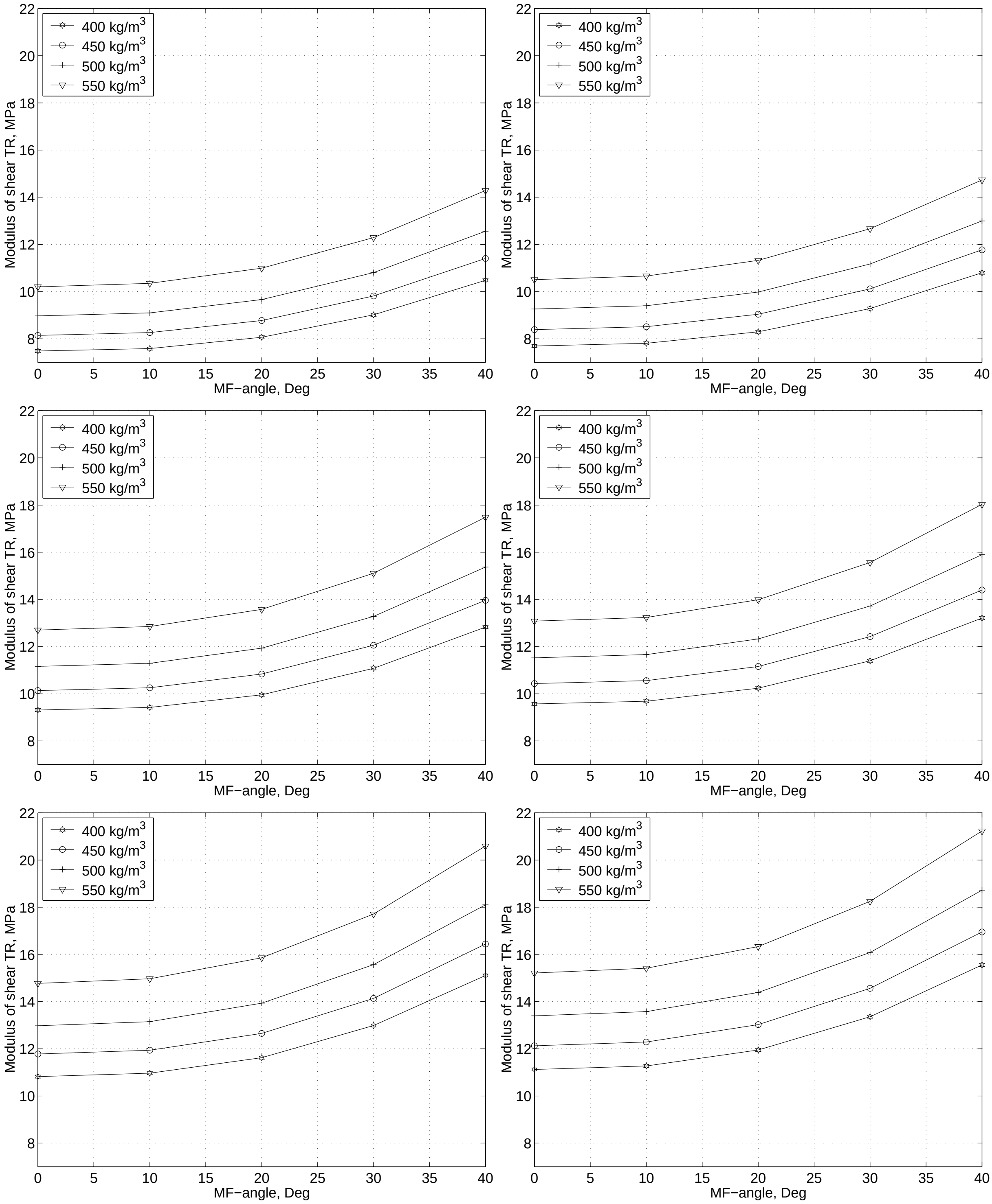

Figure 6.6: *Moduli of shear in the TR-plane at different average densities versus the microfibril angle for regular cell structures to the left and irregular to the right using from top to bottom the low, medium and high material data sets for the cell wall layers.*

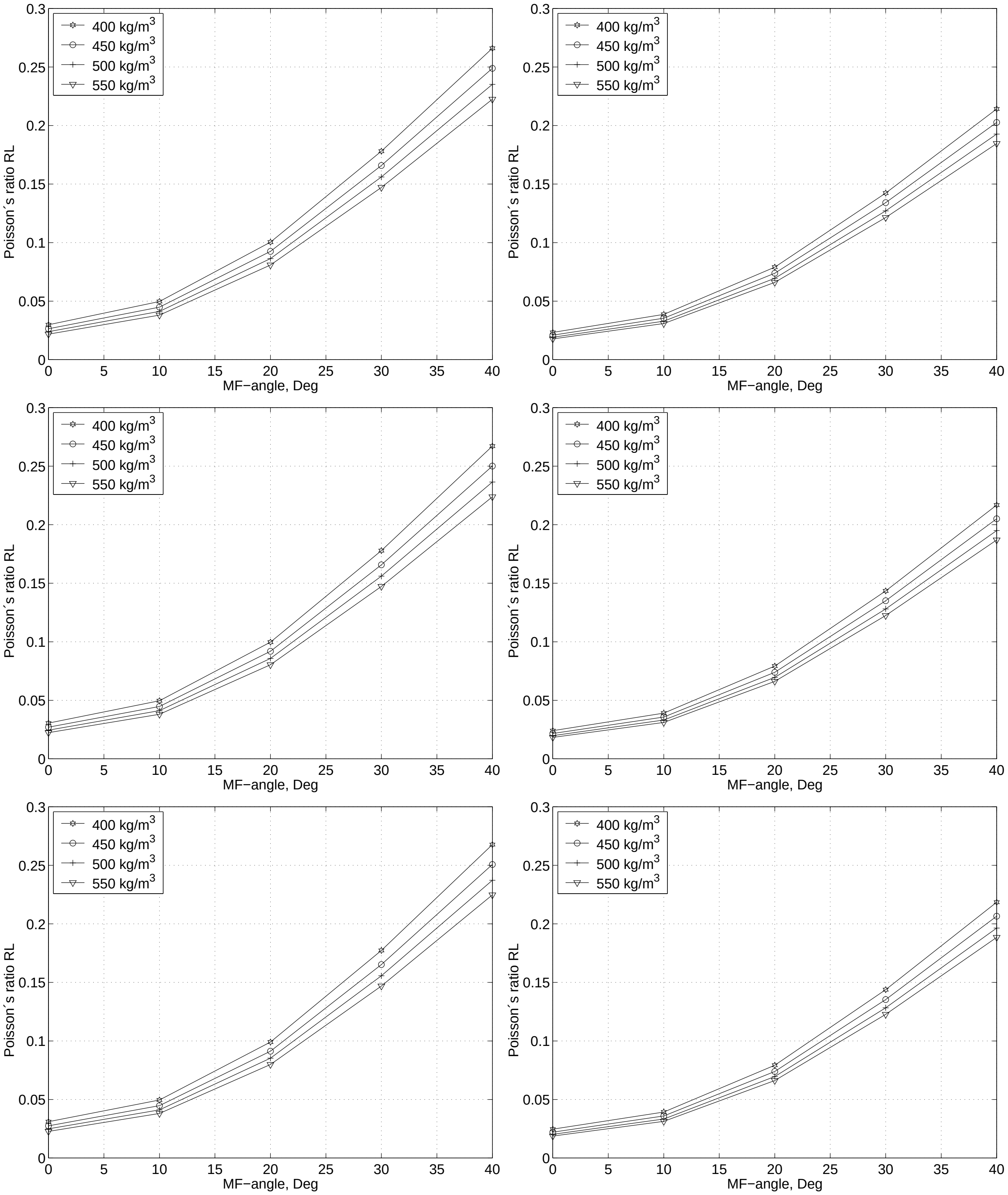

Figure 6.7: *Poisson ratio ν_{RL} at different average densities versus the microfibril angle for regular cell structures to the left and irregular to the right using from top to bottom the low, medium and high material data sets for the cell wall layers.*

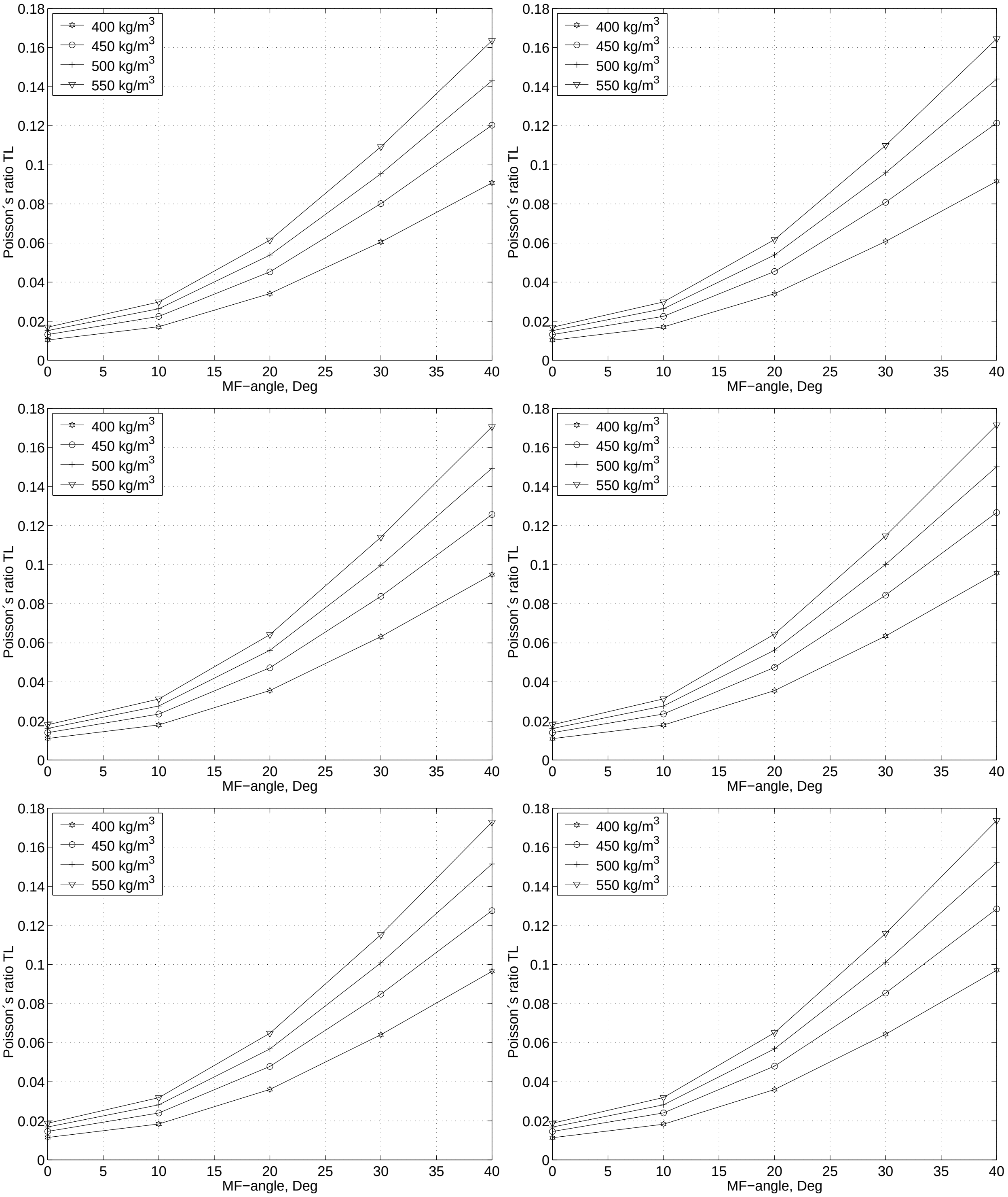

Figure 6.8: *Poisson ratio* ν_{TL} *at different average densities versus the microfibril angle for regular cell structures to the left and irregular to the right using from top to bottom the low, medium and high material data sets for the cell wall layers.*

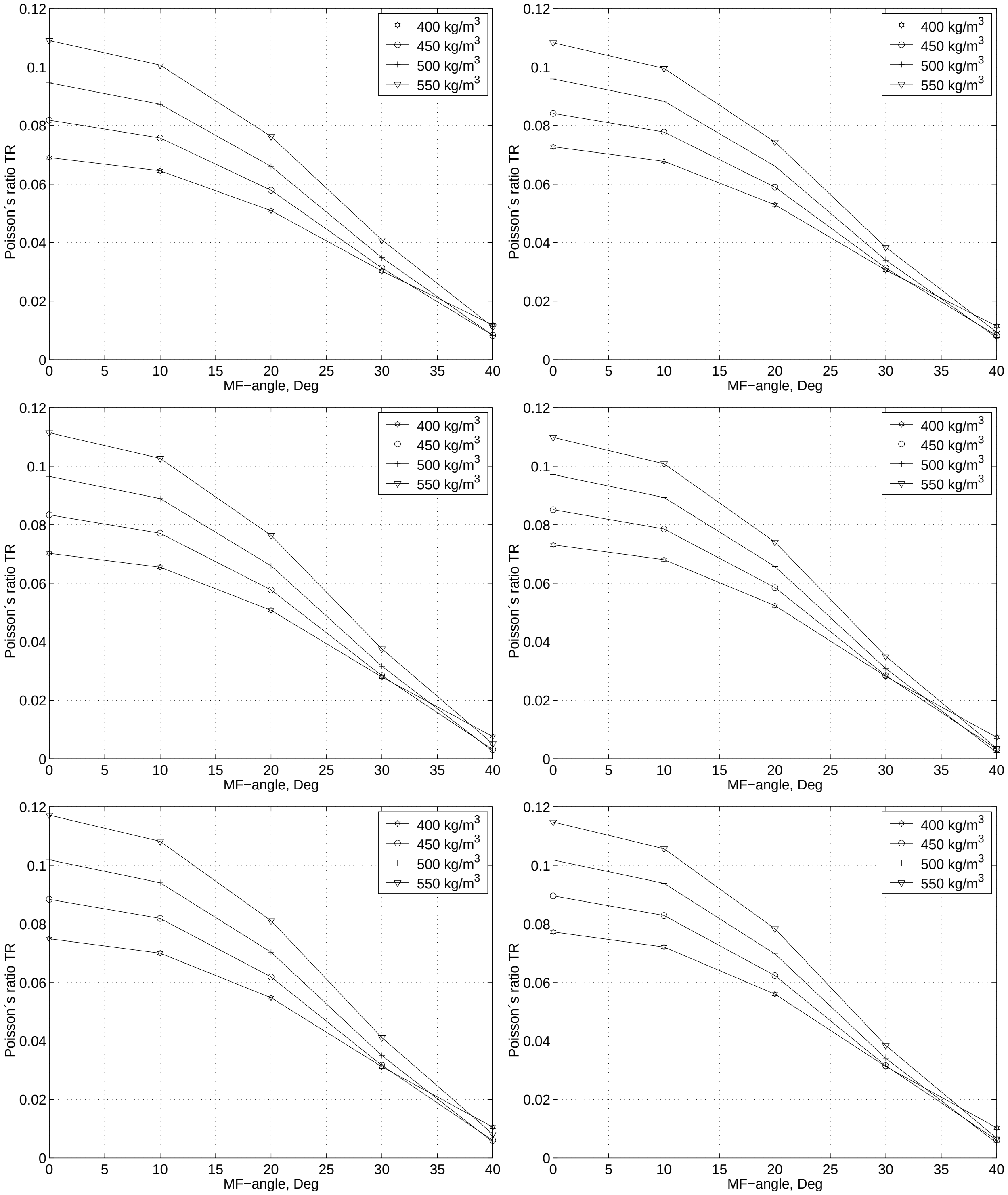

Figure 6.9: *Poisson ratio ν_{TR} at different average densities versus the microfibril angle for regular cell structures to the left and irregular to the right using from top to bottom the low, medium and high material data sets for the cell wall layers.*

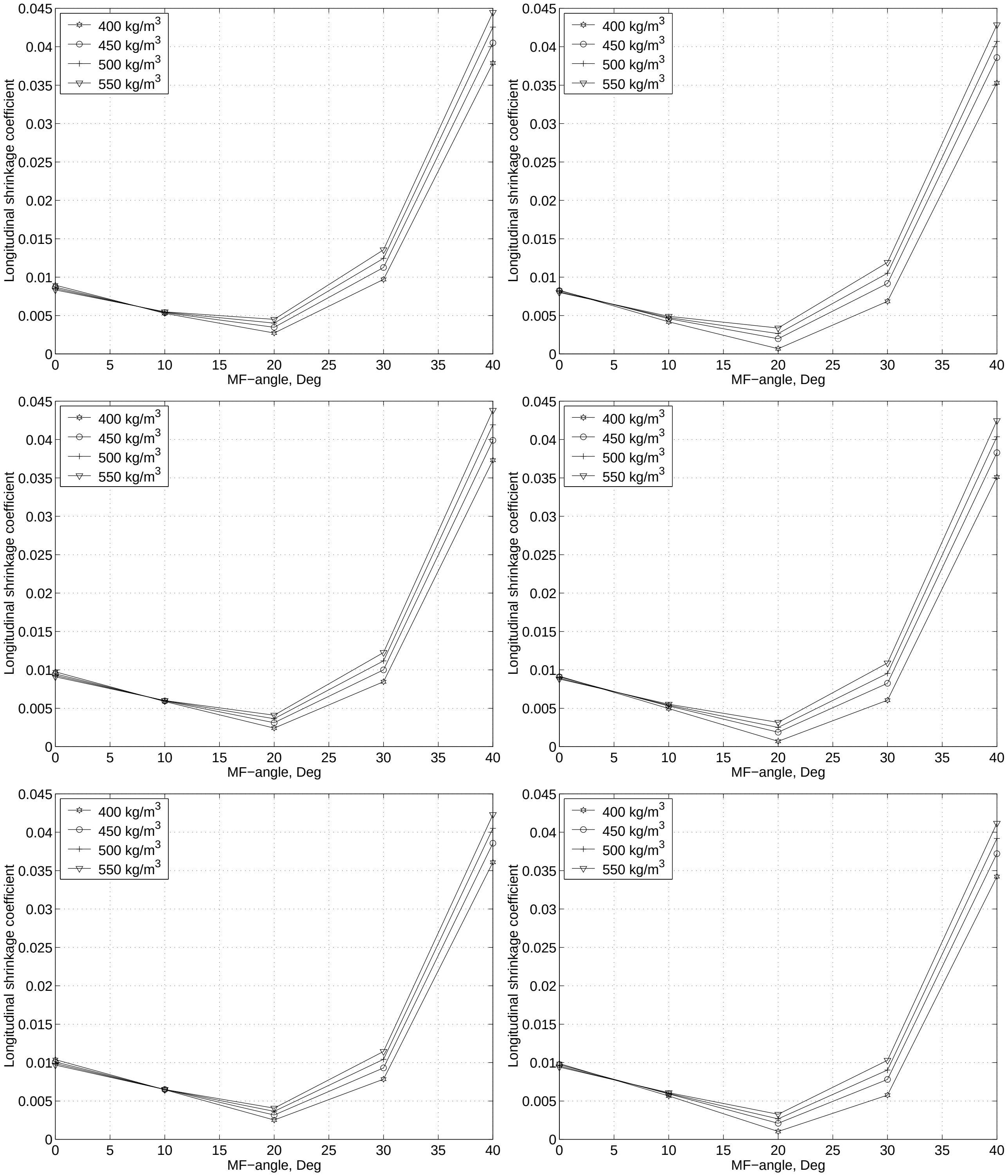

Figure 6.10: *Hygroexpansion coefficient in the longitudinal direction at different average densities versus the microfibril angle for regular cell structures to the left and irregular to the right using from top to bottom the low, medium and high material data sets for the cell wall layers.*

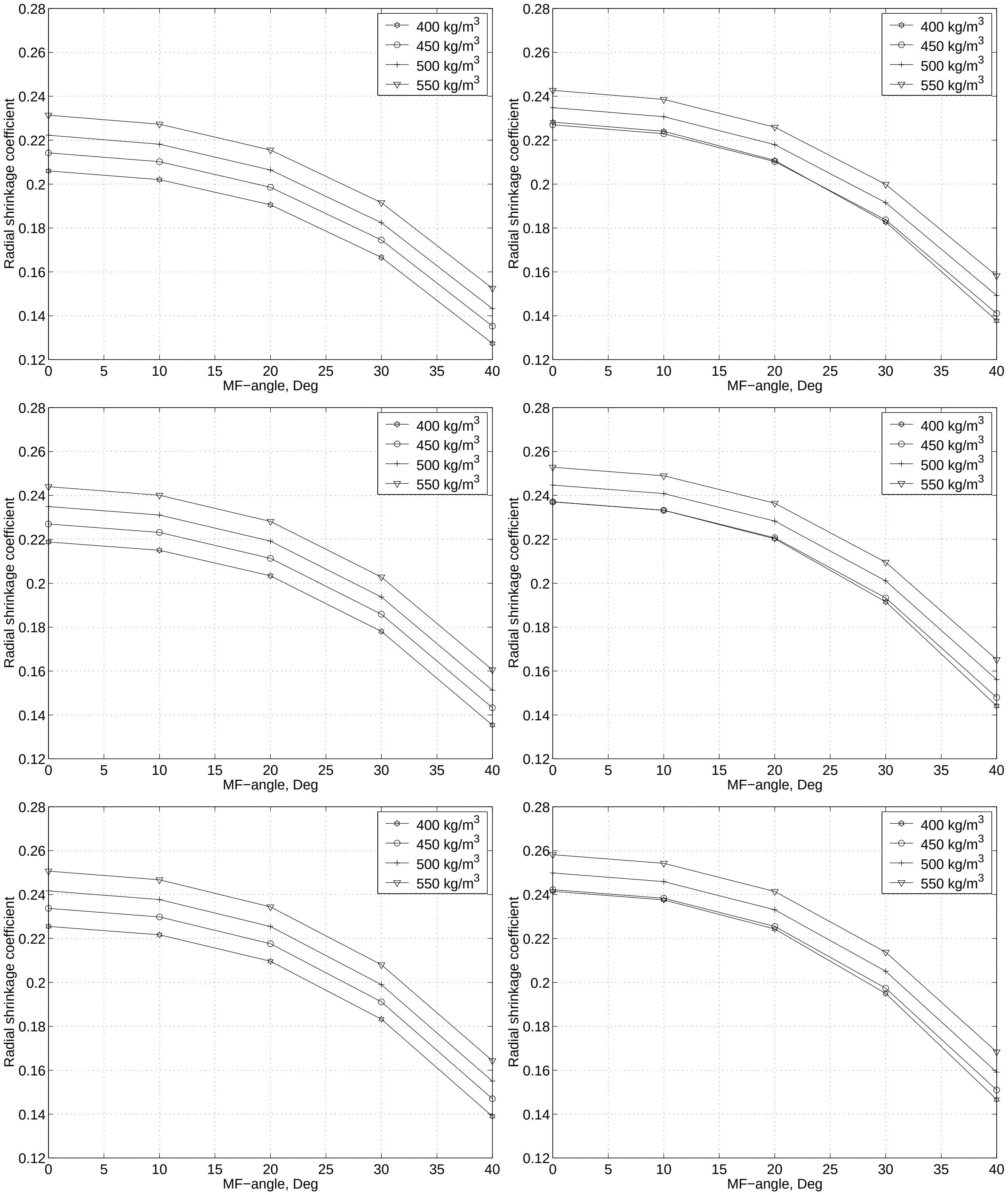

Figure 6.11: *Hygroexpansion coefficient in the radial direction at different average densities versus the microfibril angle for regular cell structures to the left and irregular to the right using from top to bottom the low, medium and high material data sets for the cell wall layers.*

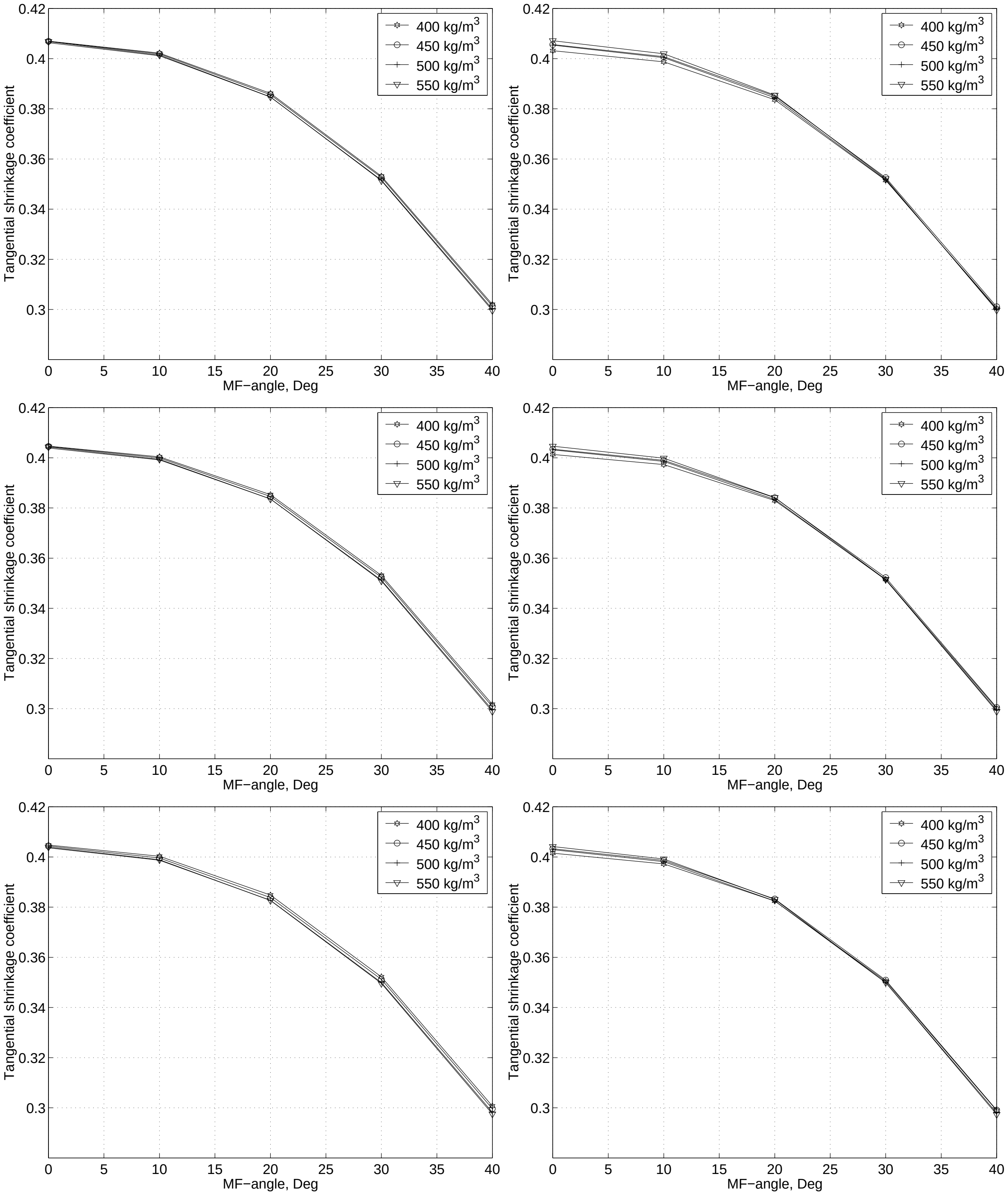

Figure 6.12: *Hygroexpansion coefficient in the tangential direction at different average densities versus the microfibril angle for regular cell structures to the left and irregular to the right using from top to bottom the low, medium and high material data sets for the cell wall layers.*

For small microfibril angles, the hygroexpansion coefficients in the radial and the tangential directions were found to be large, whereas in the longitudinal direction they were found to be small. With an increase in the microfibril angle, the longitudinal hygroexpansion first decreases and then increases. The longitudinal hygroexpansion coefficient was nearly zero for microfibril angles around 20°. The hygroexpansion in the radial and tangential directions decreases with an increase in the microfibril angles. Although it may appears that the influence of the longitudinal hygroexpansion is negligible due to the only very small numerical values of the shrinkage parameters. However, dealing with shape stability of timber, the longitudinal shrinkage is essential in drying processes, see Ormarsson [48].

Employing the three different sets of material parameters of the cell wall layers had a strong influence on each of the stiffness properties. It was shown to be important to have good experimental data concerning the material properties of the chemical constituents. However, studying the results obtained here, together with the experimental data on the stiffness and on the hygroexpansion of wood, can provide guidance in the selection of reasonable values for the material parameters of the chemical constituents.

6.3. Variation of Properties in a Tree

6.3.1. General remarks

On the basis of the measurements presented in Chapter 3, it was concluded that the stiffness and shrinkage properties vary markedly within the tree. These properties were found to differ both along the radius and along the height, although the values for the parameters along the radius showed the largest variation. In Section 3.4.3 measurements of the longitudinal modulus of elasticity along the radius of trees were presented. Here, all the stiffness parameters were calculated, together with the hygroexpansion coefficients. Measurements of the density and the longitudinal modulus of elasticity were used as input to the model.

6.3.2. Influence of location in the tree

Simulations based on the experiments on clear wood specimens were carried out, using the distribution of the longitudinal modulus of elasticity and the density along the radius of the tree shown in Figures 3.24 and 3.28. From these experimental values for the longitudinal modulus of elasticity and the density, average microfibril angles were determined, using the procedure described in Appendix A. A structural wood model using irregular hexagonal cells was employed for determining the stiffness and shrinkage properties along a radius from the pith to the bark of a tree at increments of 10 mm. The mean measured values along the radius for the longitudinal modulus of elasticity and the density, together with the calculated average microfibril angles, are presented in Table 6.4.

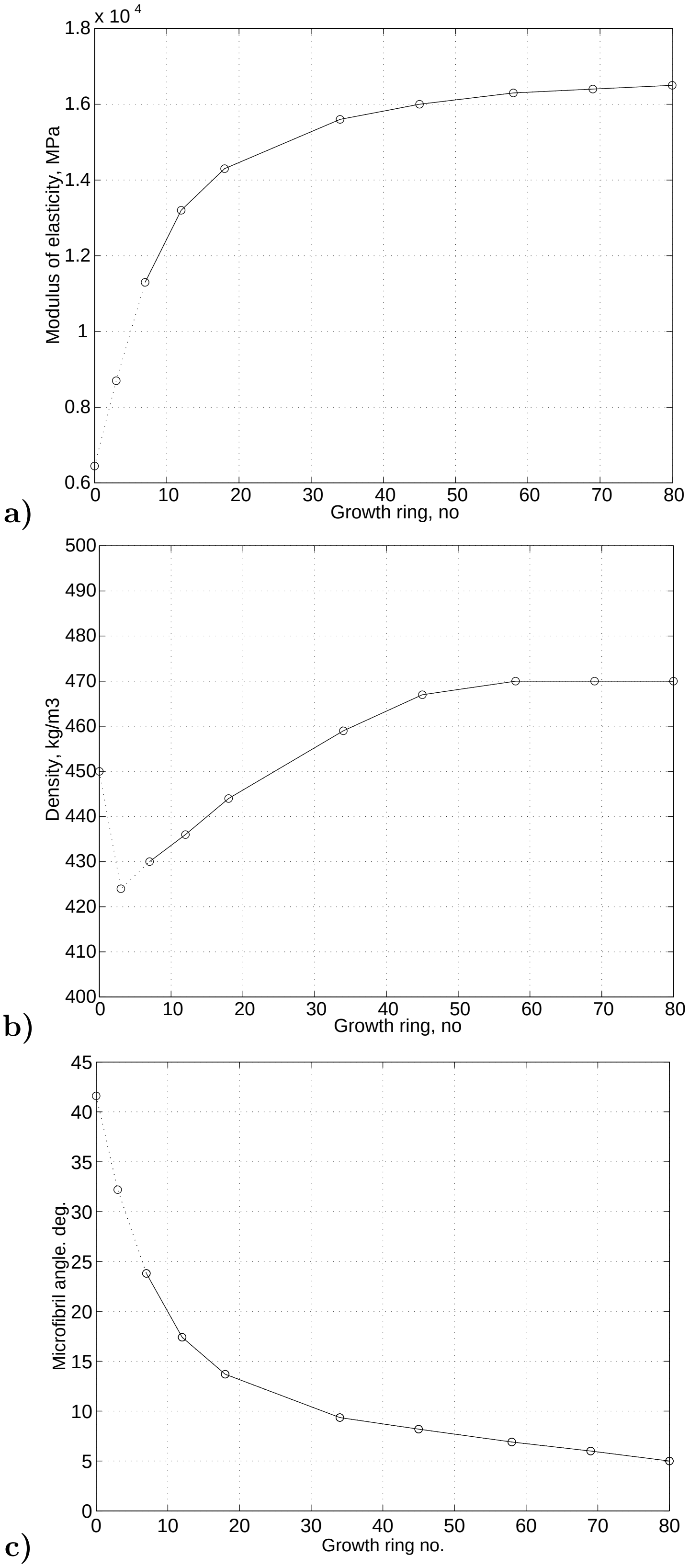

Figure 6.13: *Input data for the model along the radius in a tree.*
a) *Mean of measured longitudinal moduli of elasticity.*
b) *Mean of measured densities.*
c) *Microfibril angles calculated by use of Eq.(2.40) and data in a) and b).*

Table 6.4: *Measured longitudinal moduli of elasticity and densities and the calculated microfibril angles along the radius of a tree.*

Ring No.	Mod. of elast. E_L, MPa	Density, ρ_r, kg/m^3	Microfibril angle, φ°
0	6450	450	41.5
3	8700	424	32.4
7	11300	430	24.2
12	13200	436	17.9
18	14300	444	14.3
34	15600	459	10.1
45	16000	467	9.3
58	16300	470	8.0
69	16400	470	7.2
80	16500	470	6.4

In Figure 6.13 the same values are shown as curves along the radius, the curves near the pith being dotted so as to indicate that the simulation results close to the pith are uncertain, which can be due to various factors, one of which is that differences in chemical composition.

The stiffness and shrinkage properties were calculated using the values for the densities and microfibril angles shown in Table 6.4. Figures 6.14-6.17 show the stiffness and hygroexpansion properties obtained from the simulations. The modulus of elasticity in the longitudinal direction agrees well with the experimental data, see Figure 6.14. Both the radial and tangential moduli of elasticity were found to have high values close to the pith with first a steep decrease and then an increase towards the bark. The high radial and tangential moduli of elasticity in the pith are due to the large microfibril angles and the high density there.

The three moduli of shear also show high values near the pith, Figure 6.15. In the LR- and LT-planes the moduli of shear decrease towards the bark whereas in the RT-plane, outside the pith area, there is an increase in the modulus of shear.

The Poisson ratios in the LR- and LT-planes decrease from the pith towards the bark, whereas those in the RT-plane increase from the pith towards the bark, see Figure 6.16.

The hygroexpansion coefficients obtained from the simulations are shown in Figure 6.17. The longitudinal hygroexpansion is large near the pith and first decreases rapidly and then increases again along the radius towards the bark. The radial and the tangential hygroexpansion are both low near the pith but increase towards the bark. The simulation results agree reasonably well with the experimental observations obtained, cf. Figure 3.32.

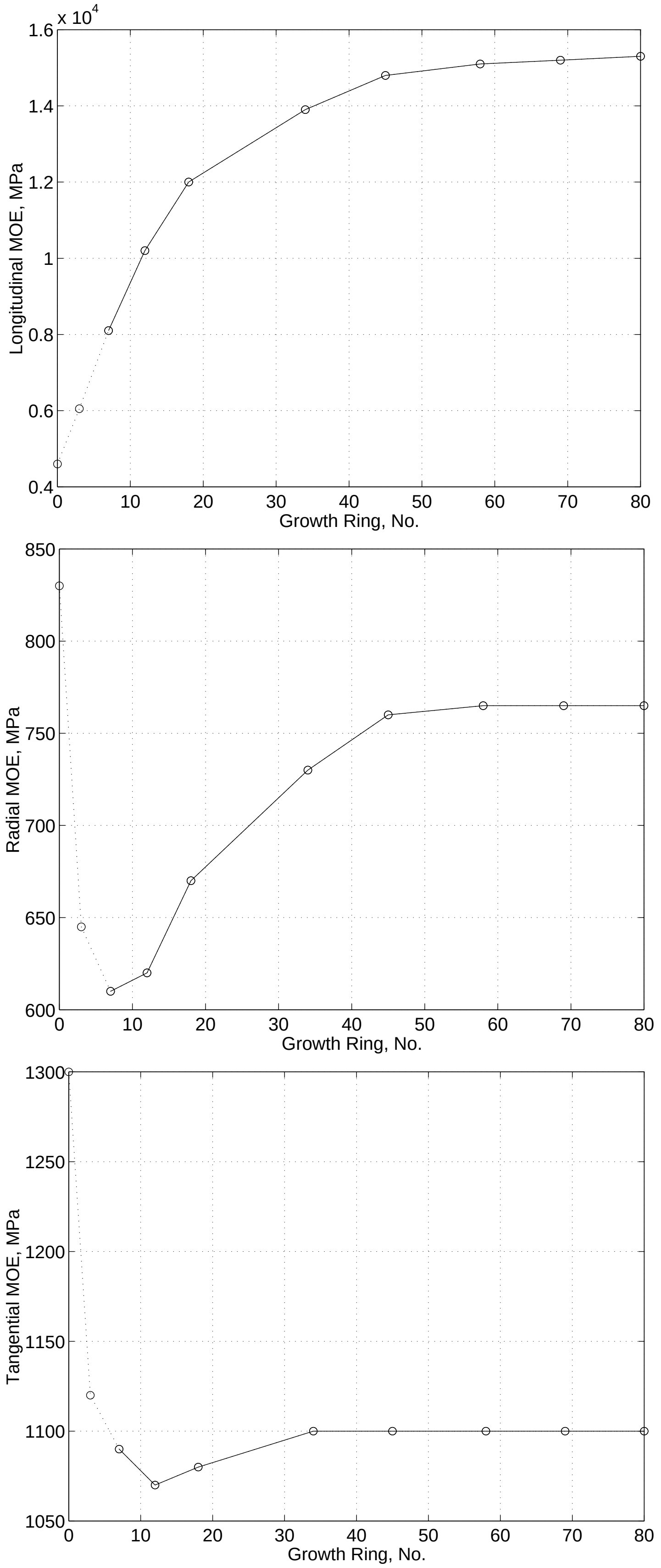

Figure 6.14: *Moduli of elasticity in the longitudinal, radial and tangential directions along the radius of a tree.*

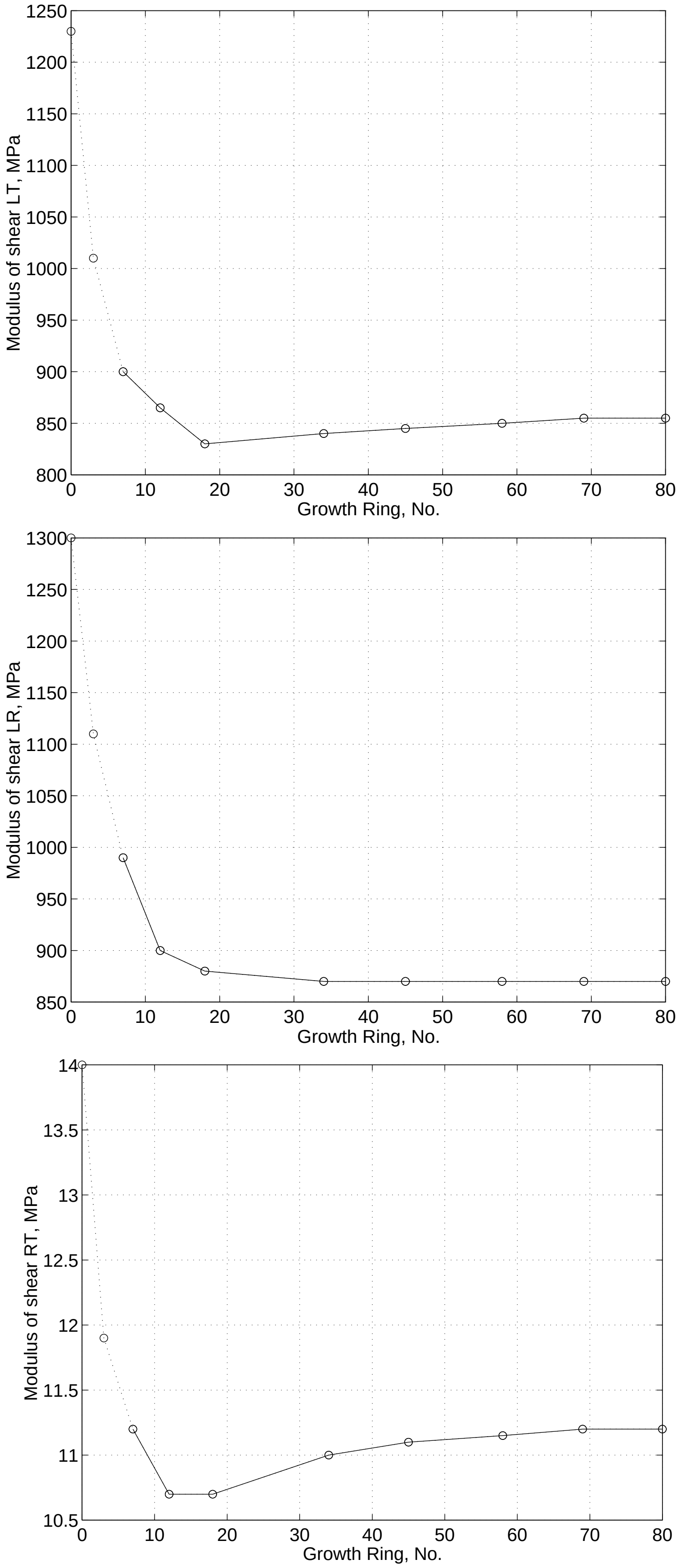

Figure 6.15: *Moduli of shear in the LT-, LR- and RT-planes along the radius of a tree.*

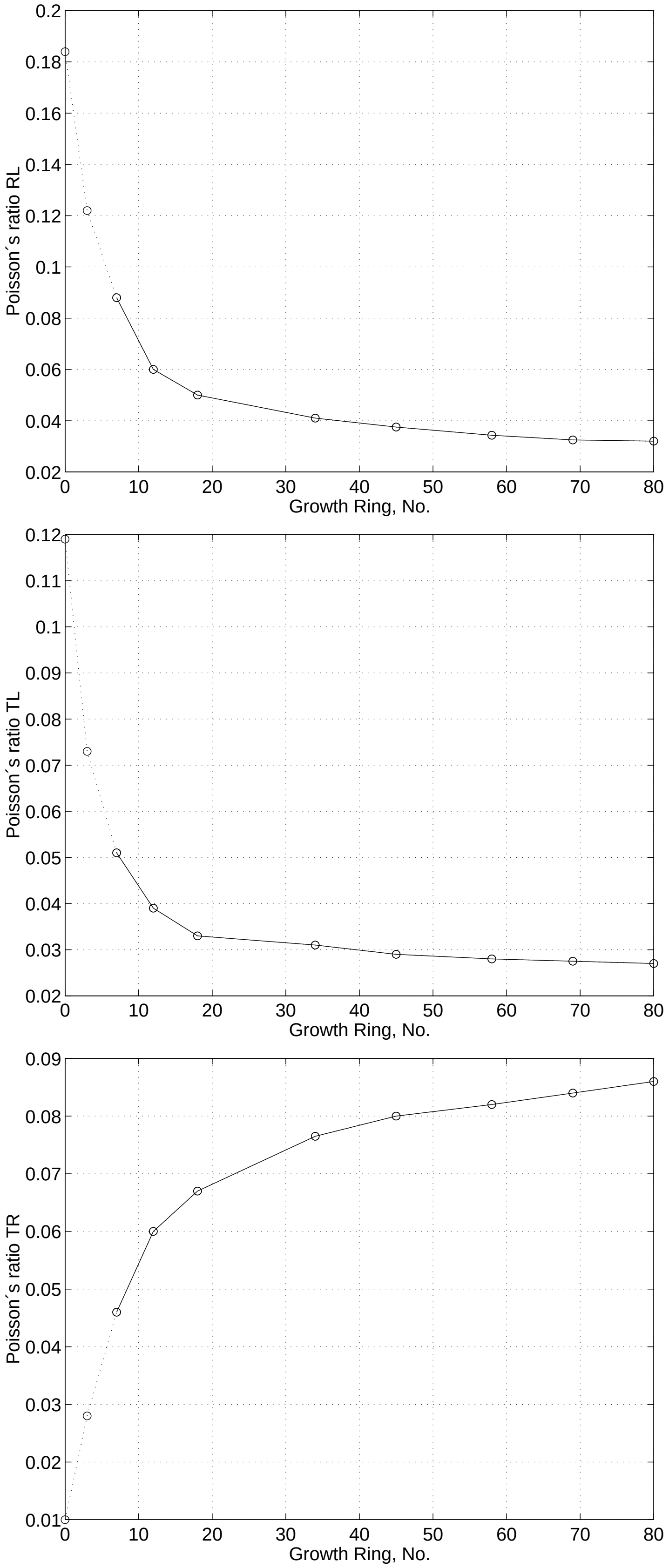

Figure 6.16: *Poisson ratios ν_{RL}, ν_{TL} and ν_{TR} along the radius of a tree.*

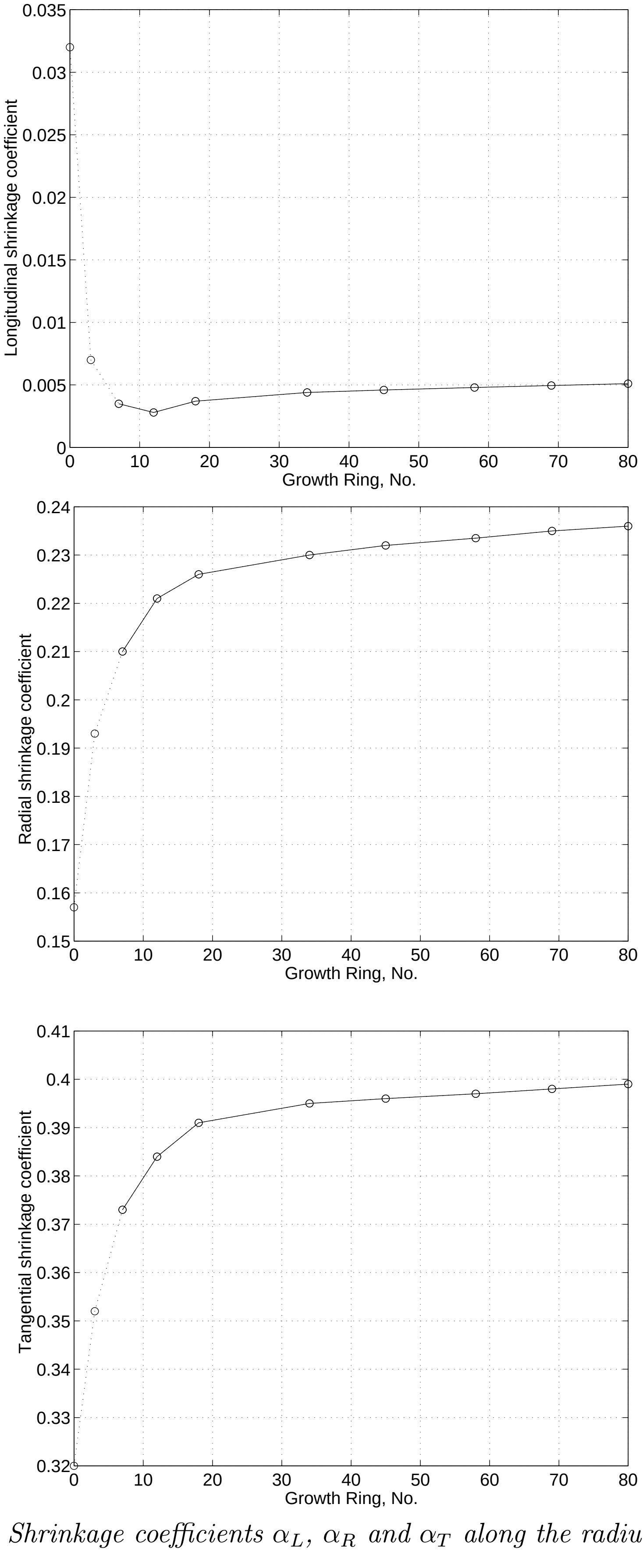

Figure 6.17: *Shrinkage coefficients* α_L*,* α_R *and* α_T *along the radius of a tree.*

6.4. Concluding Remarks

The results of the parametric studies presented show the parameters that governing the stiffness and hygroexpansion properties of wood here to be the microfibril angle of the S_2-layer, the density and the properties of the chemical constituents. The choice of parameters to describe the cell structure geometry did not influence the stiffness and the hygroexpansion properties as much, except in a few cases. The stiffness in the radial direction was strongly influenced by irregularity and by ray cell stiffness. Some parameters were also affected by the ratio of the tangential cell widths that was chosen. To make an accurate prediction of the stiffness and hygroexpansion properties, it is essential that one have reliable material data on the chemical constituents and on the microfibril angle of the S_2-layer. The analyses conducted of the variations in properties within the tree indicate the variations in the stiffness and hygroexpansion properties along the radius of the tree to be large. These variations have a strong influence on shape stability and are important to take into account in analysing of the mechanical behaviour of wood.

7. NONLINEAR PROPERTIES

7.1. Introduction

Wood is a cellular and porous material that exhibits a nonlinear behaviour at loading, especially when loaded in compression perpendicular to the grain and in shear in the radial-tangential plane. Above the limit of proportionality, wood behaves in a highly nonlinear way. The behaviour of wood is influenced by several factors, such as density, moisture content, temperature and duration of loading. For compression loading perpendicular to the grain, three basic failure patterns can be distinguished, depending on the orientation of the growth rings in relation to the direction of loading. For radial compression, local buckling of the cell walls in the earlywood zone occurs. Tangential compression results in a more macroscopic buckling failure where the latewood region buckles into the earlywood. Shear failure often occurs for loading at an angle to the growth rings.

In many applications wood is loaded beyond the elastic limit, where a compressional load perpendicular to the grain often leads to very large deformations. To improve the nonlinear constitutive models for wood, a better understanding of the basic behaviour of wood is needed. To achieve this, micromechanical models from which the nonlinear behaviour of wood can be simulated can be utilised. By use of the numerical models described in Chapters 4 and 5 extended and aided by the experimental work presented in Chapter 3, the behaviour of wood at higher loading was studied. The linear elastic material models for the cell wall layers need to be modified to elastic-plastic material models, since the strains can locally become very large in the cell wall.

7.2. Micromecanical Nonlinear Modelling

7.2.1. General remarks

Nonlinear analysis can be performed with inclusion of the nonlinearities present in both the material and the geometry. In the nonlinear studies here, a three-dimensional hexagonal cell structure model was used for investigating the behaviour of wood in the case of large deformations. The basic parameters defining the geometry of the cell structure were selected in the manner described in Chapter 5. As indicated there, the structure was meshed with 20-node isoparametric three-dimensional elements, using a composite material formulation allowing the various cell wall layers to be defined separately. Cyclic boundary conditions at the model boundaries were employed in the simulations. Three cell wall layers were modelled for each individual cell wall. The orientations chosen for the middle layer were 45°, the S_2-layer -10° and the S_3-layer were 75° for all the models analysed in this chapter.

The elastic material properties of the various cell wall layers were chosen for a moisture content of 12%, as shown in Tables 5.3 and 5.4. To simulate the cell structure when the wood is subjected to large deformations, a finite element formulation with use of large deformation theories, as described in Chapter 4 was employed. This allowed the stability limits of the cell wall in buckling and the post-buckling behaviour of the wood to be simulated. Since no fracture model was applied, the nonlinear simulations were only performed for compression loading. All the simulations presented here were performed using three-dimensional models. Due to the character of this type of analysis, involving large compressive deformations of thin structures, leading to instability and a large degree of contact interaction, together with an anisotropic plastic flow of the material, considerable numerical difficulties and convergence problems occurred in the simulations. The number of different types of cell structures and loading cases that could be analysed without any difficulties of instability was thus limited.

7.2.2. Nonlinear simulations with linear elastic material

The large deformation simulations of wood cell structures presented in this subsection were performed with a linear elastic material behaviour of the cell walls. Simulations for cell structures were carried out using the five different average densities of the growth ring shown in Table 7.1. Since cell structures with a density lower than 400 kg/m^2 result in very large models, the use of which is too time consuming to be practical, simulations of cell structures with an average density of less than 400 kg/m^2 were not performed. In the analyses carried out, the irregularity parameter R_{max} described in Chapter 5, which controls the irregularity of the cell structure was set here to zero, resulting in the cell structures being regular. Analyses were performed for compression loading in the radial and tangential directions only.

Table 7.1: *Average density and corresponding growth ring width for the analysed growth ring structures.*

Density kg/m^3	Ring width mm
400	2.01
425	1.44
450	1.14
475	0.92
500	0.76

In Figure 7.1 the results the analysis provided of compression loading in the radial direction for the five models that differed in average density are shown. Since the five cell structures show almost identical deformations, it can be concluded that, in terms of these models, the buckling of the earlywood cell structure in compressive loading in the radial direction is virtually independent of density. Figure 7.2 shows the compressive stress-strain curve for a cell structure with an average density of 500 kg/m^3. Compressive stress is defined here as the compressive force applied divided by the undeformed area, whereas compressive strain is defined as the negative change of length divided by the original length of the undeformed geometry. The stress-

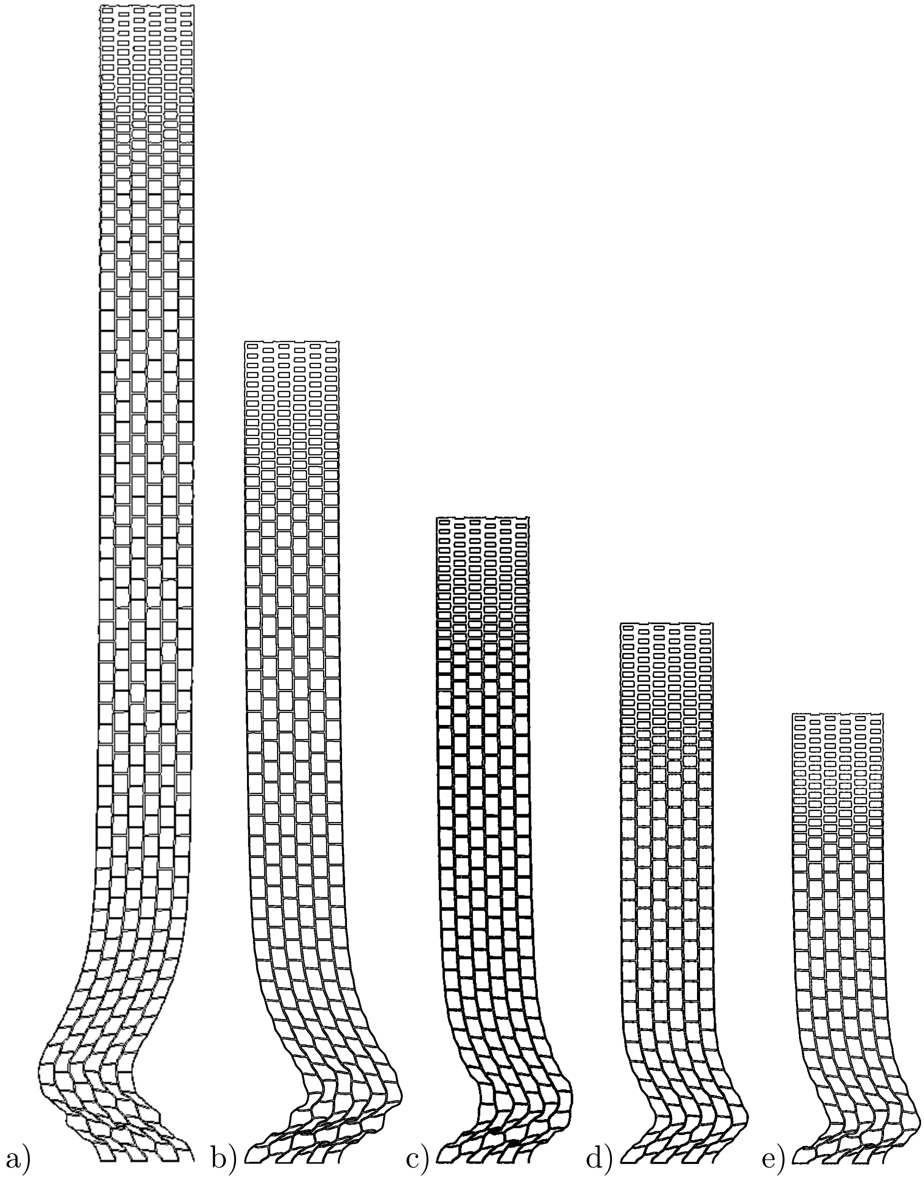

Figure 7.1: *Deformations of wood cell structures assuming elastic material with average densities of a) 400 kg/m^3, b) 425 kg/m^3, c) 450 kg/m^3, d) 475 kg/m^3 and e) 500 kg/m^3.*

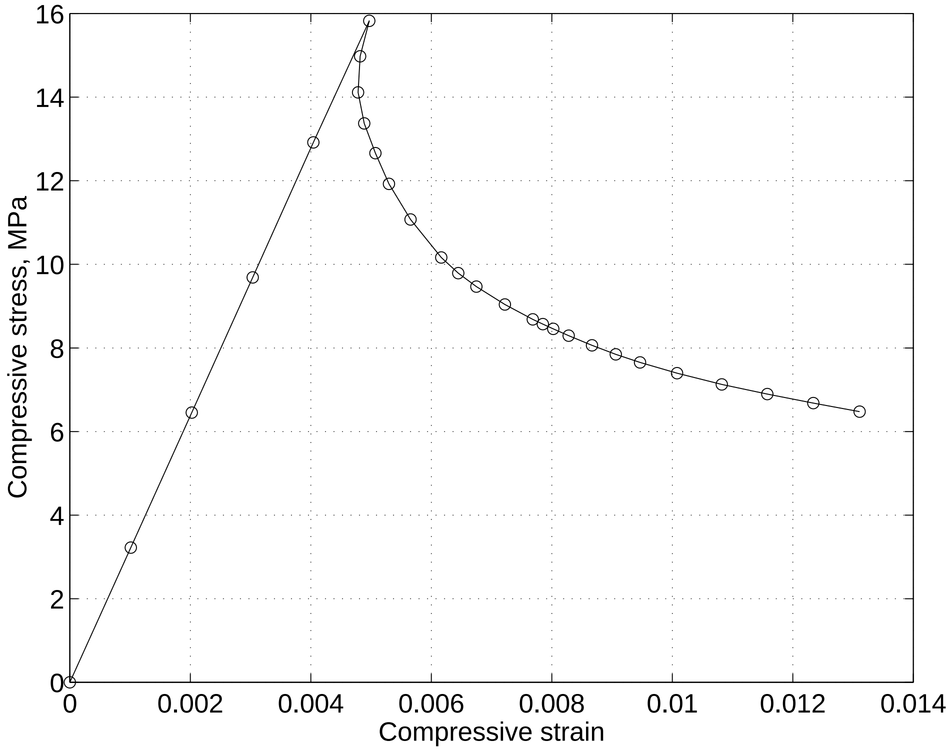

Figure 7.2: *Compressive stress-strain curve for loading of a regular cell structure in the radial direction assuming linear elastic material of the cell wall layers and an average density of 500 kg/m^3.*

strain curve displayed in Figure 7.2 shows linear elastic behaviour initially, followed by a sudden drop in stress with increasing strain. In the experiments on radial compression, a small stress peak can be noted, but the high stress peak shown in Figure 7.2 was not found experimentally, presumably due to the fact that a real cell structure is more irregular.

To investigate the influence of the irregularity parameter R_{max} on the structural response in compressive loading in the radial direction, a model in which R_{max}=3 μm and the average density was 500 kg/m^3 was analysed. The compressive stress-strain curve obtained is shown in Figure 7.3. In the case of an irregular structure, the high initial stress peak completely vanishes and the elastic stiffness is lower, as was shown in Chapter 6. Simulations of an irregular structure in radial compression provide results that are closer to the experimentally observed behaviour, see Holmberg [30]. The buckling mode and strain localisation of the cell structures obtained in simulations involving linear elastic material are not in accordance with the results of experiments on microstructural deformations that was presented in Chapter 3. In the simulations, the cell structures showed a buckling mode caused by shearing of the thin earlywood cells in the RT-plane, whereas in the experiments, collapse occurred completely for one row of cells at a time, resulting in a strain localisation effect.

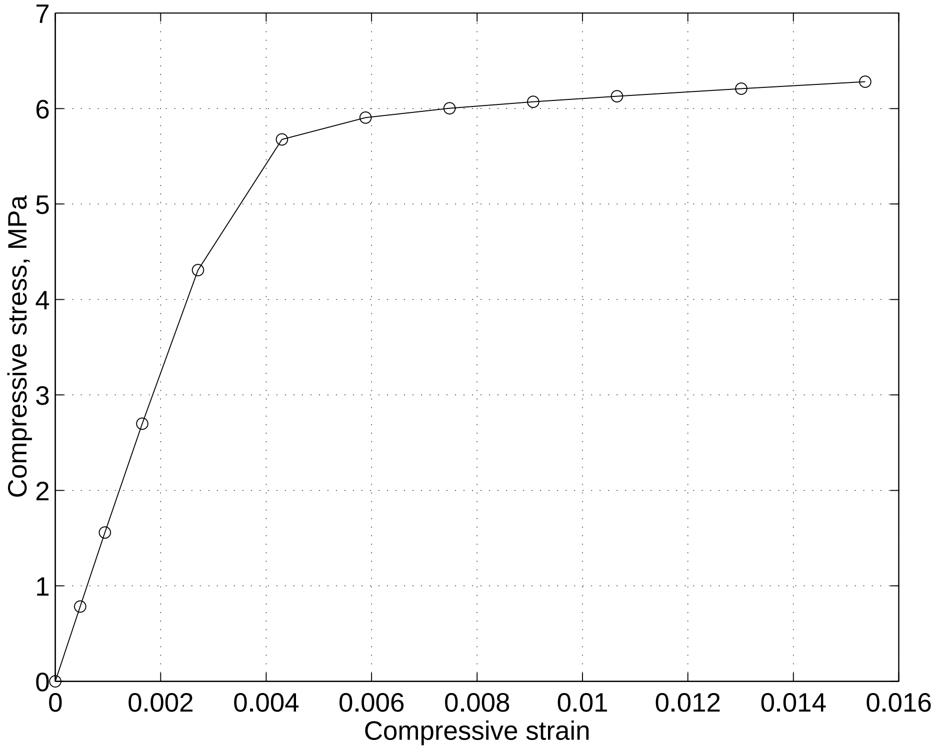

Figure 7.3: *Compressive stress-strain curve for loading of an irregular cell structure in the radial direction assuming linear elastic material of the cell wall layers and an average density of 500 kg/m*^{3}

For compression loading in the tangential direction, the size of the cell structure chosen to be analysed can be expected to be important for the deformation shape obtained. It has been shown in experiments that for tangential loading of cell structures that are very long in the tangential direction, instability occurs, the latewood region buckling into the earlywood in a wavy manner. This is not expected for cell structures that are shorter in length in the tangential direction, for which deformation patterns can be expected to be stable and uniform. Two cell structures of differing length in the tangential direction were modelled for studying the microstructural deformations in loading in the tangential direction. The first cell structure was modelled with six cells in the tangential direction, whereas the second was modelled with 30 cells in the tangential direction. For both models, the average density was 550 kg/m^3, the structure being regular in both cases. The model with 30 cells in the tangential direction was very large, with over a million degrees of freedom. Nonlinear analysis of models as large as this require large computer resources and is very time consuming. For analysing models larger than this, a different modelling approach is needed.

In Figure 7.4 the deformations obtained for the model with six cells in the tangential direction are shown, and in Figure 7.5 the deformations obtained for the model with 30 cells in the tangential direction. It can be seen clearly in studying

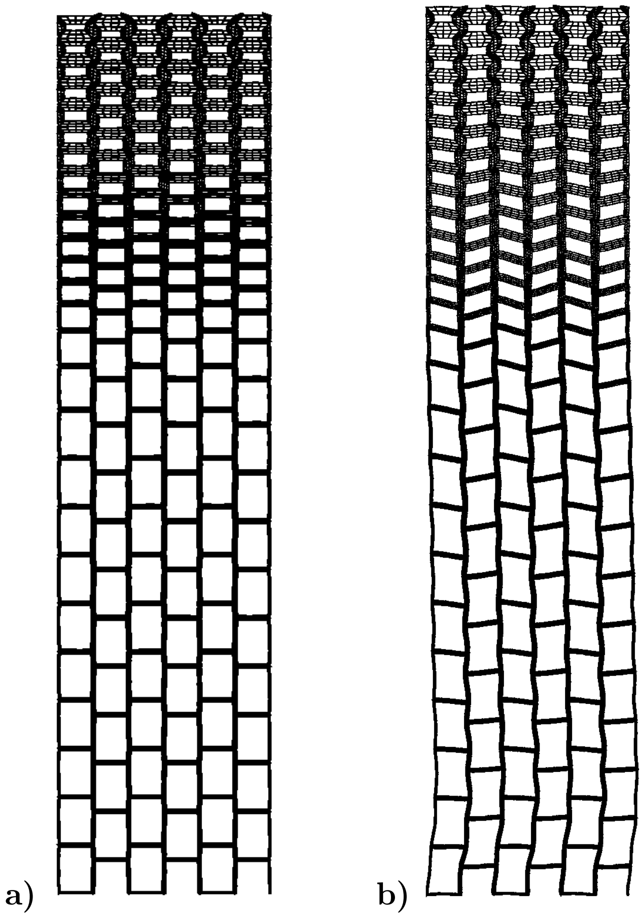

Figure 7.4: *Compressive loading in the tangential direction assuming linear elastic material of the cell wall layers.* **a)** *Undeformed structure.* **b)** *Deformed structure after loading.*

the results obtained that for higher loading in the tangential direction the deformation shape of the structure is strongly dependent on the size of the model. The deformations for the smaller model are distributed throughout the cell structure and no instability occurs, whereas for the larger model the strains are localised to the middle of the cell structure. A clear indication of the buckling of the latewood band can be seen in Figure 7.5.

7.2.3. Nonlinear simulations with elastic-plastic material

The material behaviour of the cell wall layers in large strain simulations is not linear elastic. When the cell walls are subjected to large strains, various nonlinearities occur, such as plastic flow, cracking and other material damage. To obtain better agreement between the results of simulations and the experimentally determined stress-strain curves and deformations presented in Chapter 3, nonlinear material effects were included by adopting the orthotropic elastic-plastic material model proposed by Hill [29]. This model is described briefly in Chapter 4. Although the

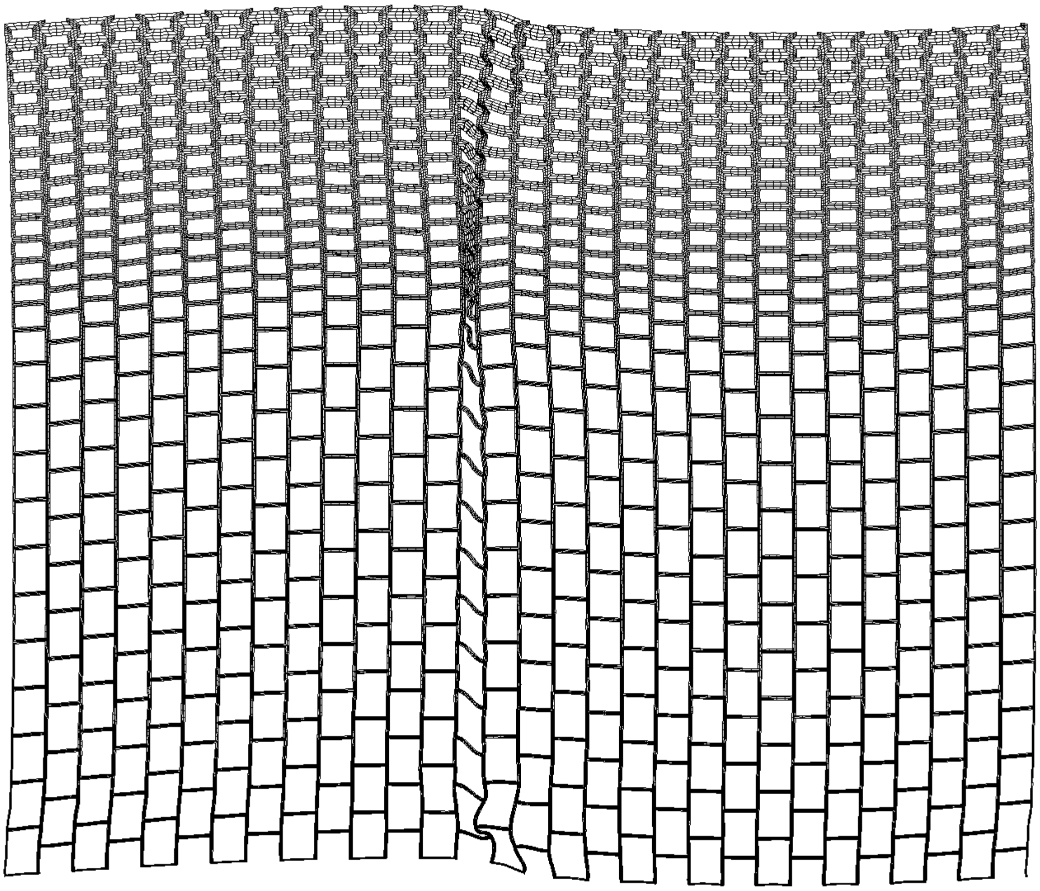

Figure 7.5: *Cell structure deformation for compressive loading in the tangential direction assuming linear elastic material of the cell wall layers.*

nonlinear material effects in the cell walls vary in character, it is assumed that they can be represented in a simple way by use of a plasticity model. For the various cell wall layers the yield stresses σ_{ijy} and the reference stress σ_{ref} in Eq.(4.53) need to be defined. Although the choice of these parameters will be discussed further in the following, as a first choice the parameters are scaled according to the moduli of elasticity. σ_{ref} is set equal to the yield stress for the direction of the cell wall with the highest yield stress, which is in the longitudinal direction of the microfibril, and σ_{ref}=σ_{11y}. Since the moduli of elasticity in the 2- and 3-directions in the cell wall material are only about one-tenth as great as in the 1-direction, the six parameters $r_{i,j}$ that define the yield surface were chosen as

$$r_{11} = 1.0, \quad r_{22} = 0.1, \quad r_{33} = 0.1, \quad r_{12} = 0.25, \quad r_{13} = 0.25, \quad r_{23} = 0.15$$

Since σ_{ref}=σ_{11y}, the yield stress in the longitudinal microfibril direction needs to be specified in order to fully define the yield surface. The value of σ_{11y} not being known, five analyses were performed with a different value of σ_{11y} in each. The values of σ_{ref} employed for the cell walls are shown in Table 7.2. The results obtained for the simulations of the models involving linear elastic material behaviour of the cell wall

Table 7.2: *Microfibril angle and thickness of the latewood cell wall layers.*

Model no.	σ_{ref}, [MPa]	
	Middle layer	S_2 and S_3
1	400	800
2	600	1200
3	800	1600
4	1000	2000
5	1200	2400

indicated the deformations at structural failure of the earlywood cells to be virtually independent of the average density. For this reason, only models with an average density of 500 kg/m^3 were used in simulations with plastic material behaviour.

Figure 7.6 shows the deformations obtained for the five models with differing choices of σ_{ref}. The deformed shape differs depending on the value of σ_{ref} employed. For lower values of σ_{ref}, a crushing of the earlywood cells is obtained. For higher values of σ_{ref}, the deformed shape is more similar to the deformations obtained in the simulations involving elastic material. The results indicate that the lowest value of σ_{ref} that was studied provides deformation results that are close to the experimental results.

Figure 7.7 shows the compressive stress-strain curves obtained for the five models. Since a regular cell structure was used in the simulations, a stress peak in the stress-

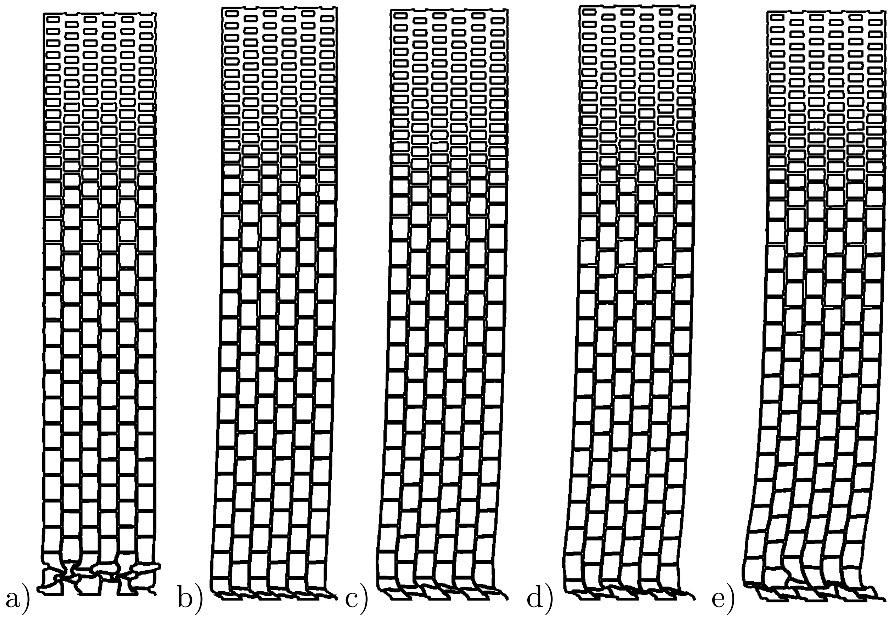

Figure 7.6: *Deformations of wood cell structures assuming elastic-plastic material behaviour with σ_{ref} in the S_2-layer chosen as a) 800 MPa, b) 1200 MPa, c) 1600 MPa, d) 2000 MPa and e) 2400 MPa.*

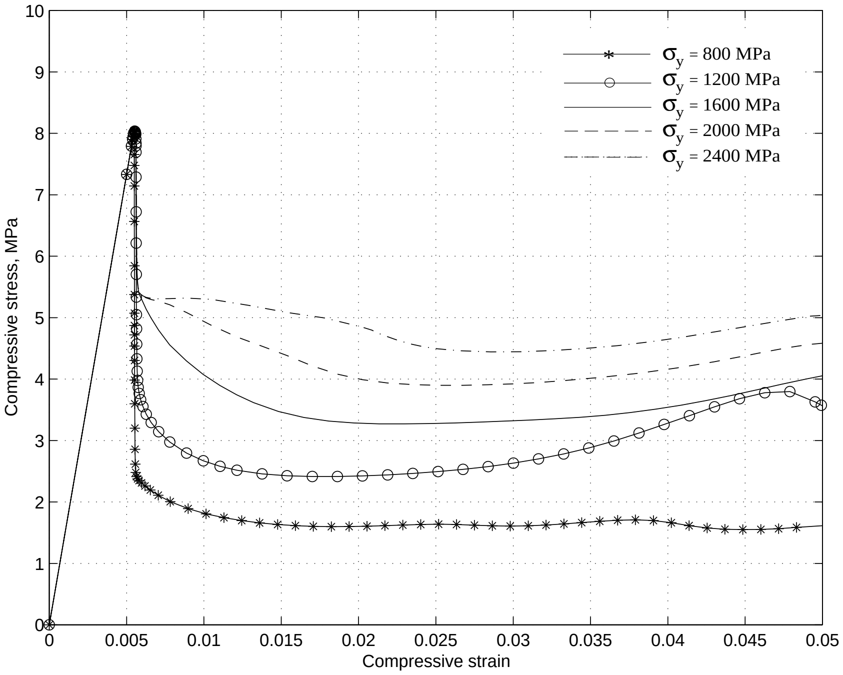

Figure 7.7: *Compressive stress-strain curves for loading in the radial direction assuming a regular cell structure, elastic-plastic material of the cell wall layers with different values of* σ_{ref} *applied and an average density of 500 kg/m*^{3}

strain curve is obtained. However, following this stress peak, as the deformation increases further the stress levels out to a plateau with the stress value for the various values of σ_{ref} differing somewhat. Experimental results indicate that for wood with a 12% moisture content the stress level following collapse is about 4-5 MPa, whereas for wood with a high moisture content it is about 2-3 MPa, Holmberg [30]. The lowest value of σ_{ref} seems to be suitable for analysing wood with a high moisture content and a value of around 1500 MPa seems to be valid for wood with a low moisture content.

7.2.4. Nonlinear simulations with elastic-plastic material and contact

For compressive and shear loading, very large deformations occur locally, resulting in the cell walls coming into contact with each other and interacting as the cells collapse. Due to the strong localisation that occurs for compressive loading that is perpendicular to the grain, this phenomenon occurs already at a rather low average (macroscopic) strain. It is highly important therefore, to take this into account in modelling when large deformations are applied and post-buckling behaviour is to be studied. In each cell lumen, contact conditions were introduced which controlled the contact and prevented the cell walls from penetrating each other. In some of the calculations a Coulomb friction model was employed for the surfaces in contact, so as to study the influence of friction on the results, small differences being found.

For these simulations, σ_{ref}=1600 MPa and the average density=550 kg/m^3.

Figure 7.8 shows deformations obtained from large deformations in the radial direction, contact conditions being applied inside the cell lumen, the average macroscopic strain applied being about 10%. Due to local instabilities, numerical difficulties were encountered, only a limited number of analyses being performed.

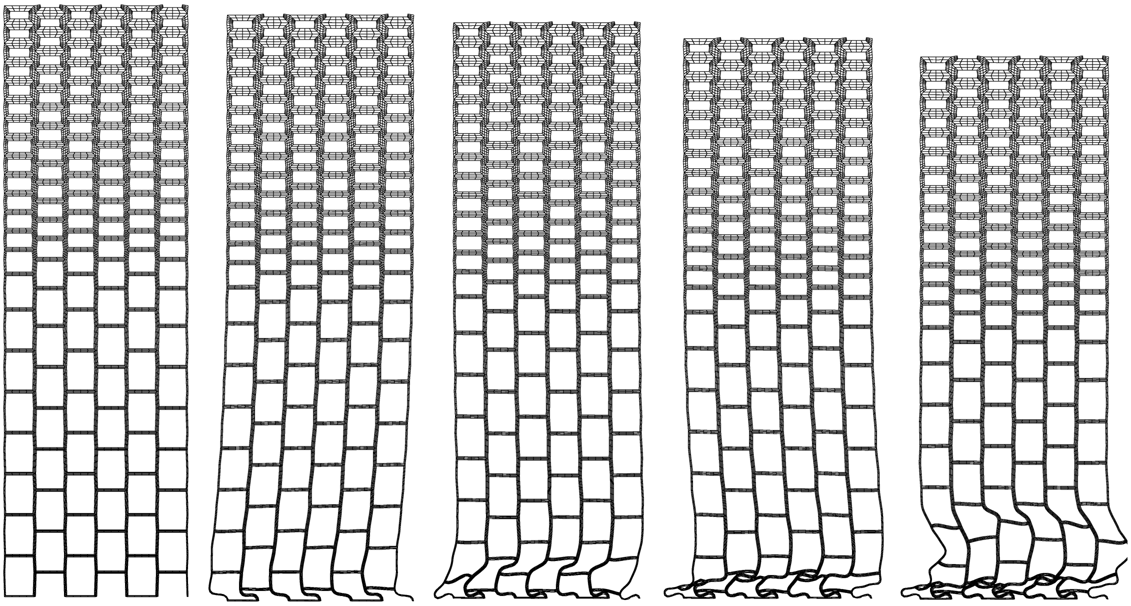

Figure 7.8: *Gradual cell structure deformation for compressive loading in the radial direction.*

7.3. Concluding Remarks

In this chapter, analyses aimed at studying the behaviour of wood under large compression loading perpendicular to the grain were presented. Several assumptions were made regarding the geometry of the cell structure and the constitutive behaviour of the cell wall layers. The nonlinearities occurring in the cell walls were captured by a simple plasticity model which involved making rather crude assumptions. The analyses performed suggest the potential here for studying microstructural deformations by use of numerical modelling rather than to be a complete systematic study. Modelling of this type can be a great help in developing more realistic constitutive models of wood at higher loading and for studying the deformations due to loading at a microstructural level. To be able to achieve results that are closer to experimental results, the constitutive behaviour of the cell wall layers at higher loading need to be studied further. In addition, to overcome the numerical difficulties that were encountered, the numerical procedures need to be developed.

8. MODELLING OF PROPERTIES OF INDIVIDUAL FIBRES

8.1. General Remarks

The purpose of developing models for individual wood fibres is to determine their mechanical properties. These properties are important in numerical simulations of the mechanical behaviour of such wood fibre networks as paper and other wood fibre products. In most sparse fibre network models, see Heyden [27], the fibres are assumed to behave as two- or three-dimensional beam elements that can be either straight or curved.

When single fibres are produced in a refining process, the fibres are exposed to cyclic loading in both compression and shear, see Holmberg [30]. Damage in various forms such as kinks, microcracks and fracture surfaces through the cell walls are very frequent, and mechanical pulp fibres often being broken into shorter pieces. In a chemical pulp, the fibres are more intact than in a mechanical pulp, but the chemical composition of the cell walls is altered due to the lignin and fractions of the hemicelluloses being dissolved. Also, the chemical structure of the hemicelluloses and the cellulose may be altered during the chemical processes. Earlywood fibres with their thin walls are often collapsed in cross section, whereas the thick-walled transitionwood and latewood fibres have a more intact cross sectional geometry. During the pulping process, the complexity of the internal structure of the fibres is increased. Defects are introduced along the length of the fibre, such as, kinks, curl and fibrillation, especially in the case of mechanical pulp fibres.

Due to the defects introduced, large variations in the geometry and in the composition and mechanical properties of the chemical constituents are present. The stiffness and strength properties of the fibres in a paper sheet vary considerably. In this chapter, studies of the properties and the basic mechanical behaviour of chemically unaltered wood fibres of simplified geometric shape will be presented. The composition and properties of the chemical constituents of the fibre wall are assumed to be the same as for native wood fibres. Although several of the assumptions made may be questionable, the results of modelling that are obtained are believed to be very useful in a qualitative discussion, comparing fibres with different morphological characteristics.

8.2. Introductory Fibre Modelling

8.2.1. Fibre cross section modelling

The cross-section of the earlywood fibres is assumed to be collapsed during the pulping and paper manufacturing processes. Different collapse modes can occur. In this study, the shape of the cross section of fibres was determined by means of simulations which imitated the loads applied to fibres in the refining and paper-making processes. The purpose is to determine the final shape of the cross-section of the earlywood fibres found in a paper sheet. In a refiner, wood chips are fed between two discs rotating in opposite directions. The cross section of the fibres is pressed between the two refiner discs and is assumed to be loaded in a state of combined compression and shear. In the paper-making process the cross-sectional deformations that develop in the refining process are further increased when the paper sheet is pressed between the various rollers in the paper machine.

The cross-sectional shape of the thick-walled transition- and latewood fibres is assumed here to not be altered during mechanical and chemical processes that occur. On the other hand, the cross-sectional shape of the earlywood fibres is assumed to be collapsed, which was determined by means of the finite element method for two-dimensional undeformed models of the fibre cross-section. A simplified, undeformed initial cross-sectional shape of the studied fibre was assumed, as shown in Figure 8.1. In that figure, a dashed reference line is drawn in the mid-plane of the thickness direction in the fibre wall. The thickness of the cell wall is different for the earlywood than the latewood. The simplified shape was determined by studying such micrographs as those shown in Chapter 3.

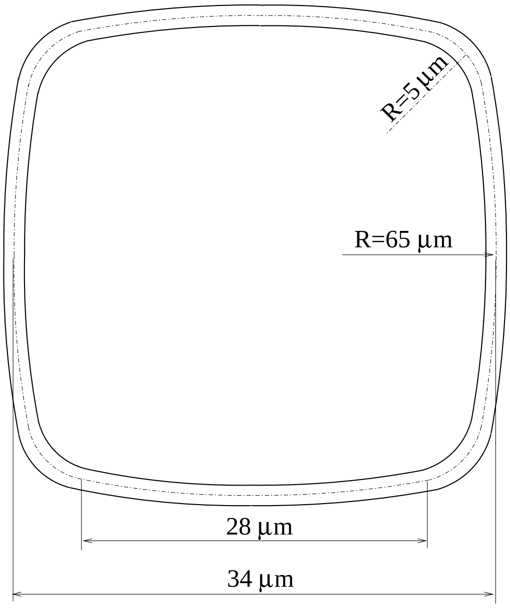

Figure 8.1: *Assumed initial geometry of the cross section of an individual fibre model, the mid-plane of the fibre being the reference of measure.*

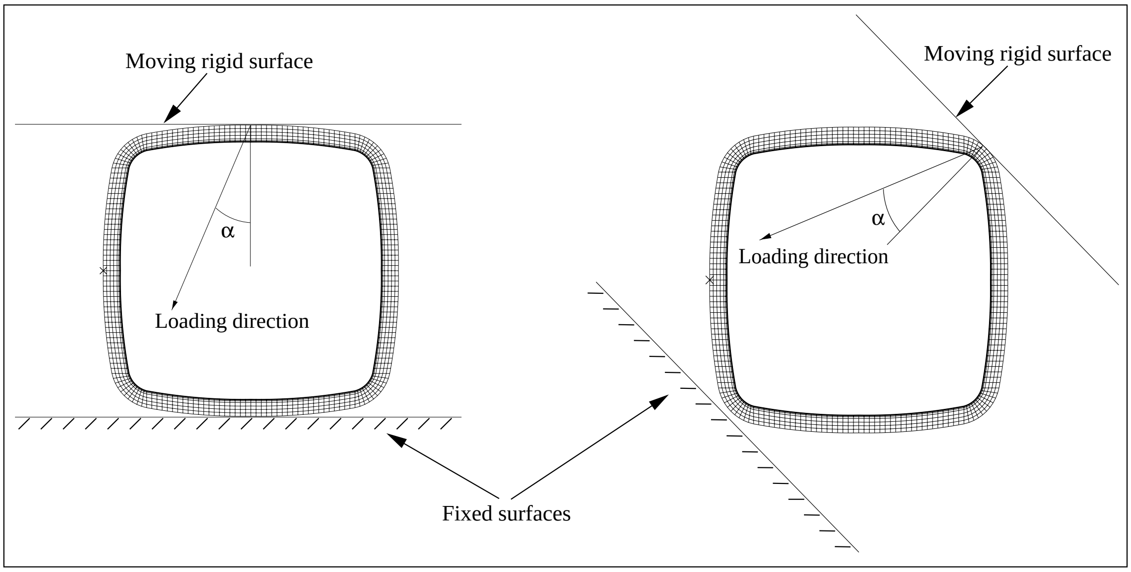

Figure 8.2: *Finite element models of the fibre cross-section with rigid surfaces and with the loading direction defined.*

To determine the shape in collapsed form, the undeformed fibre model was pressed between two rigid surfaces. Four collapsed cross-sectional shapes were determined by applying different loading conditions. The loading cases used for analysing collapse of the fibre are shown in Figure 8.2, in which two major loading cases are shown, one case being modelled with the loading boundary planes oriented horizontally and the other case with the loading planes oriented at a 45° angle in order to simulate the fibre being rotated during collapse. The ratio of the compression to the shear load applied is determined by the angle α, see Figure 8.2. The upper rigid surface in Figure 8.2 was moved along a straight line in the direction determined by the loading angle α, whereas the lower rigid surface was fixed. For each of the two major loading situations, two load cases were constructed where, $\alpha = 0°$ resulting in pure compression, and $\alpha = 45°$ resulting in combined compression and shear. To determine the residual deformations of the fibres after loading, an unloading phase was simulated by moving the upper rigid surface towards its original position.

To simulate the collapse of the fibre cross section, the finite element method was employed, the problem being analysed as a two-dimensional static problem under plane strain conditions. First-order bilinear 4-noded quadrilateral solid elements were employed in the fibre walls. The rigid surfaces were modelled using interface elements on the outward boundary of the fibre to describe the contact forces developed during loading. To describe the contact forces that develop when the fibre is totally collapsed and opposing fibre walls meet, interface elements were also used on the inside boundary, i.e. the boundary facing the lumen. A Coulumb friction model was employed, the coefficient of friction at the contact surfaces being set to

Table 8.1: *Microfibril angles and thicknesses of the earlywood cell wall layers.*

Layer	Microfibril angle, $\varphi°$	Thickness, μm
Middle layer	+45	0.45
S_2	-10	0.78
S_3	+75	0.05

0.25. Three cell wall layers were assumed to be present in the fibre wall, their elastic properties being selected on the basis of the modelling results shown in Tables 5.3 and 5.4, where the medium set of the material parameters was chosen. The assumed thickness and orientation of the material in these layers are given in Table 8.1. Since large strains of the fibre walls develop during loading, nonlinear material behaviour of the layers in the fibre wall is required. Moreover, after the fibres in the refining process are unloaded, permanent deformations remain. The nonlinearities and permanent deformations that develop in the material are due to plastic and viscoelastic deformations, as well as to various types of material degradation such as microcracking and damage. In the simulations, this was accounted for by adopting the elastic-plastic material model proposed by Hill, Eq.(4.53) for the various layers in the fibre wall. The six parameters $r_{i,j}$ and the reference stress σ_{ref} in Eq.(4.53), which defines the yield surface, were chosen as

$$r_{11} = 0.1, \quad r_{22} = 0.1, \quad r_{33} = 1.0, \quad r_{12} = 0.15, \quad r_{13} = 0.25, \quad r_{23} = 0.25$$

and for the middle lamella σ_{ref}=400 MPa and for the S_2- and S_3-layers σ_{ref}=800 MPa. The values chosen for σ_{ref} were low as compared with the values employed in the simulations presented in Chapter 7. They were selected so as to suppress the springback effect after the unloading of the fibre. In the material definition, the 3-axis here is in the longitudinal microfibril direction, the 2-axis in the thickness direction of the fibre and the 1-axis is perpendicular to the other two.

For the model with the horizontally oriented loading planes, successively deformed shapes obtained from the two combinations of compressive loading and shear loading are shown in Figure 8.3. In Figure 8.4, the successively deformed shapes obtained are shown for the model for which the loading planes are oriented at a 45° angle. In each figure, the last subfigure shows the residual deformations after unloading. Since plastic deformations occurred, some stresses remains in the cell walls after unloading. The final deformed shapes after unloading are similar for all the four loading cases. However, the forces required to deform the fibres are different. Figure 8.5 shows the force-displacement curves for the two pure compressional loading cases, i.e. the two cases for which $\alpha = 0°$. The force required to deform the fibre for which the loading planes are oriented at a 45° angle are smaller than for the fibre for which the loading planes are oriented horizontally.

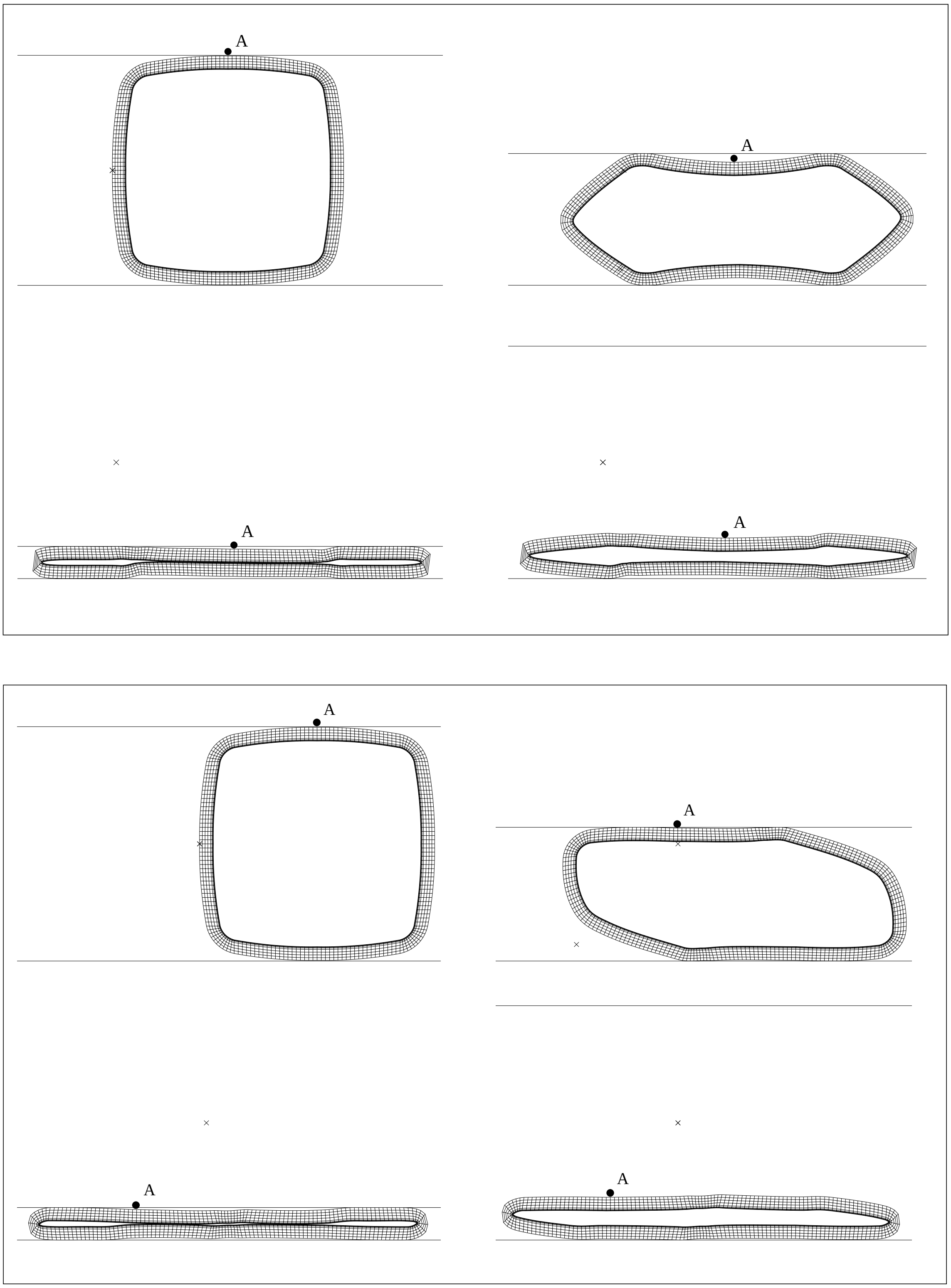

Figure 8.3: *Deformation of the fibre cross-section for loading directions of* α=*0°, top figure and* α=*45°, bottom figure. The last subfigure in each figure shows the residual deformations after unloading of the fibre.*

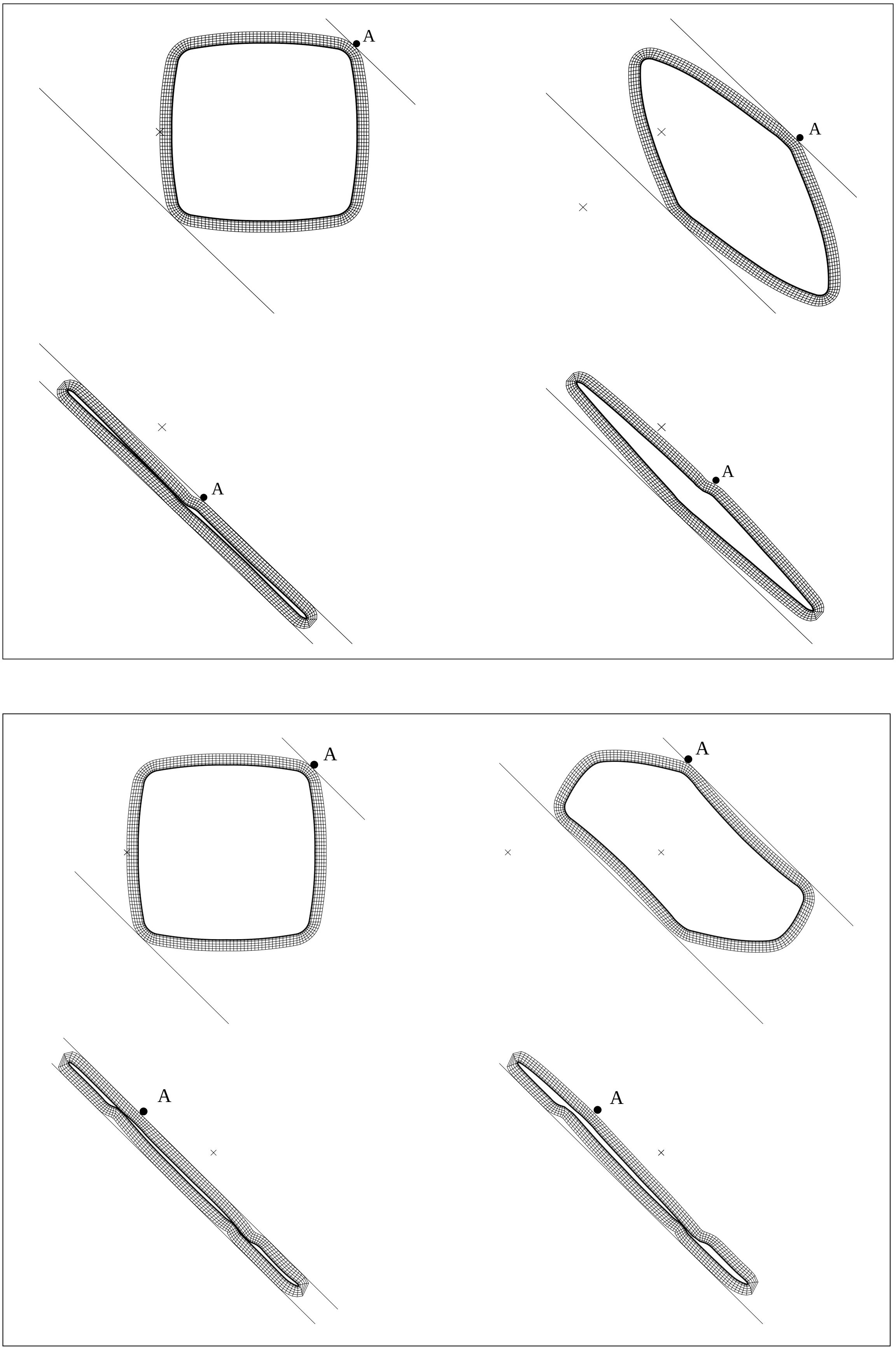

Figure 8.4: *Deformation of the fibre cross-section for loading directions of* α=0°, *top figure and* α=45°, *bottom figure. The last subfigure in each figure shows the residual deformations after unloading of the fibre.*

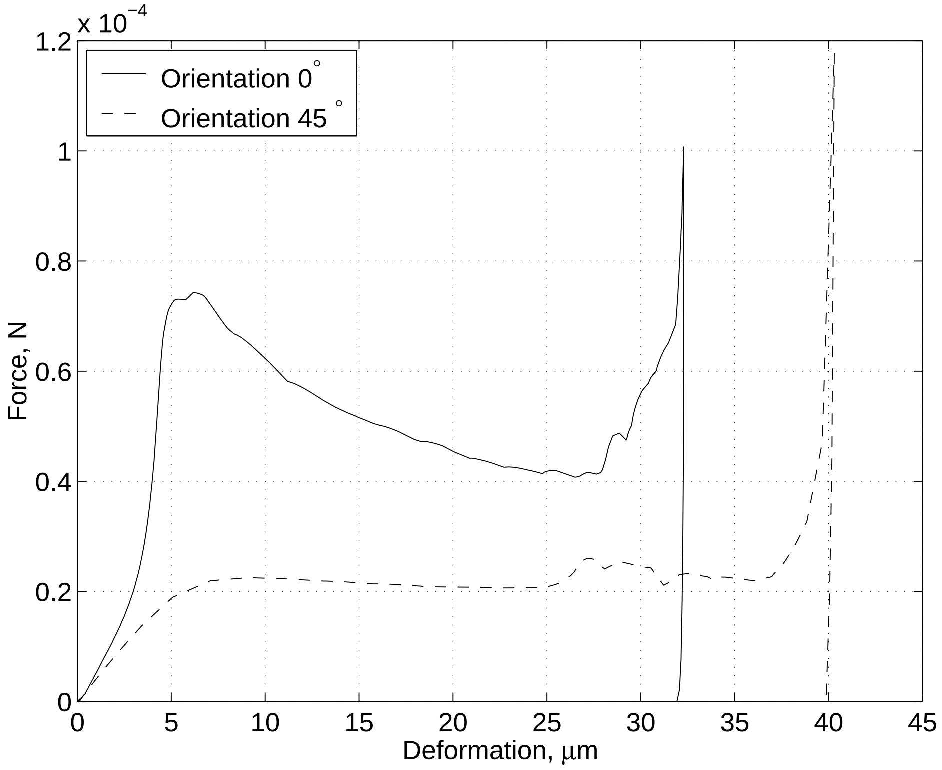

Figure 8.5: *Load-displacement curves obtained from simulations of two loading situations of fibre collapse.*

8.2.2. Stiffness properties of individual fibres

The properties of straight fibres were studied for two geometries of the fibre. Both fibre that were initially undeformed and fibres with collapsed cross-sections were studied. For the undeformed fibres, both thin-walled earlywood fibres and thick-walled latewood fibres were analysed. For the initially undeformed fibre models, a cross section such as shown in Figure 8.1 was assumed, the thickness of the fibre wall being the only difference between the earlywood and the latewood fibre models. A three-dimensional fibre geometry was obtained by extruding the cross section in the longitudinal direction, thus assuming the fibre geometry to be constant along the direction of its length. No damage such as, the presence kinks or fibrillation in the fibre wall was considered in the modelling. For the initially collapsed fibre model, a simplified cross sectional shape was adopted, based on the calculations of the collapse of the cross section carried out in the previous section. The simplified cross section that was assumed for the collapsed fibre model is shown in Figure 8.6. The dashed reference line in the figure is in the mid-plane of the thickness direction of the fibre wall. The cross sectional widths for this model were assumed to be 28 μm and 2.7 μm, respectively, the short sides being half-circular in shape with a radius of 1.35 μm. In the longitudinal direction, the length used in each of the models was 500 μm.

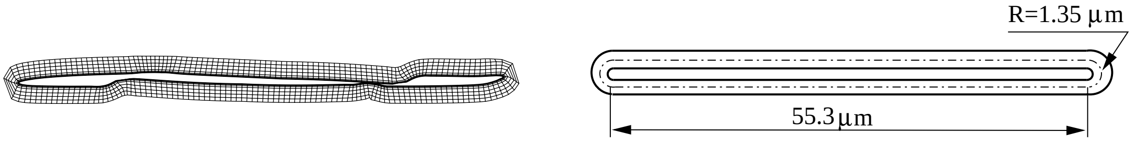

Figure 8.6: *Simulated deformed cross section of an earlywood fibre to the left and the simplified modelled cross section to the right.*

Finite element models of the fibre geometries with undeformed and deformed cross-sections were created. Eight-node isoparametric shell elements with composite material formulation were employed. Figure 8.7 shows the two models meshed with finite elements. The composite material formulation enables one to use materials with different properties and orientations that are stacked in several layers to be defined in an element. At each end of the fibre, an additional node was placed at the centre of mass in the cross-sectional plane. The nodes at each end boundary were then tied, using constraint equations, for the displacements and rotations to the node placed at the centre of the cross section. All loading was applied to these centre nodes, its being assumed that all the loading is referred to the beam centre axis only.

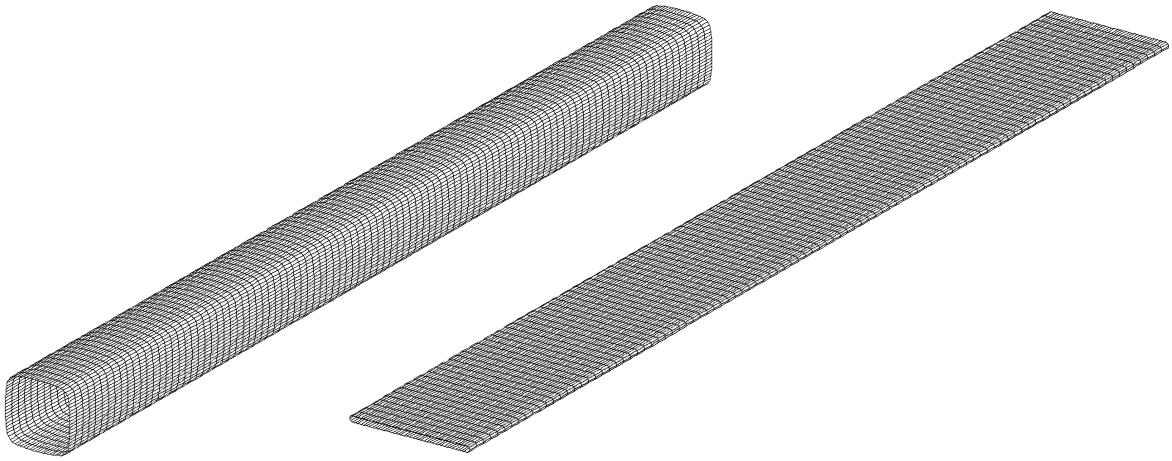

Figure 8.7: *Assumed geometries of segments of undeformed and deformed fibres in three dimensions.*

Figure 8.8: *Beam element in a local coordinate system with the displacement variables defined.*

The force-displacement relationship needed for fibre characterization was determined by assuming that the fibres were modelled as beam elements. The relation between the forces and the displacements for a three-dimensional beam element with two nodes according to Figure 8.8 can be written as

$$\mathbf{K}\mathbf{u} = \mathbf{f} \tag{8.1}$$

where

$$\mathbf{u} = \begin{bmatrix} u_x^1 \\ u_y^1 \\ u_z^1 \\ \phi_x^1 \\ \phi_y^1 \\ \phi_z^1 \\ u_x^2 \\ u_y^2 \\ u_z^2 \\ \phi_x^2 \\ \phi_y^2 \\ \phi_z^2 \end{bmatrix} \quad \mathbf{f} = \begin{bmatrix} N^1 \\ V_y^1 \\ V_z^1 \\ T^1 \\ M_y^1 \\ M_z^1 \\ N^2 \\ V_y^2 \\ V_z^2 \\ T^2 \\ M_y^2 \\ M_z^2 \end{bmatrix} \tag{8.2}$$

where N denotes an axial force, V a transverse force, T a torsional moment and M a bending moment. The superscripts indicate the node number. Further, u denotes displacements in the x-,y- and z-directions and ϕ rotations around the x-, y- and z-axis. The matrix $\mathbf{K}$ is a 12 by 12 symmetric stiffness matrix. The additional nodes that were introduced at each end of the finite element model coincide with the end nodes of the beam element and have equivalent degrees of freedom. The stiffness matrix $\mathbf{K}$ is determined by introducing six load cases in which all the displacement variables are prescribed. For the first load case, where $u_x^1 = 1$ and all the other displacement variables are set to zero, the first column in $\mathbf{K}$ is determined by solving for the unknown reaction forces. The remaining columns in $\mathbf{K}$ are determined in the same manner by prescribing the proper sets of displacement variables.

Table 8.2: *Microfibril angles and thicknesses of the earlywood cell wall layers.*

Layer	Microfibril angle, $\varphi°$	Thickness, μm
Middle layer	+45	0.45
S_2	-(0-30)	0.78
S_3	+75	0.05

Table 8.3: *Microfibril angle and thickness of the latewood cell wall layers.*

Layer	Microfibril angle, $\varphi°$	Thickness, μm
Middle layer	+45	0.45
S_2	-(0-30)	3.34
S_3	+75	0.05

The beam element stiffness matrix **K** was determined for the fibre models using deformed and undeformed cross-sections, respectively. For the undeformed cross-section, **K** was determined for both earlywood and latewood fibres in which three layers were present in the fibre wall. The microfibril angles and the thickness of the layers for these models are shown in Tables 8.2 and 8.3. For the collapsed cross-section, **K** was determined for earlywood fibres only, but with both a three-layer configuration of the fibre wall and a single S_2-layer model. The microfibril angles and thickness of the layers for the model with three layers are shown in Table 8.2. In the single layer model, the microfibril angle and thickness of the layer were selected as the S_2-layer, as shown in Table 8.2. All four models were analysed using three different microfibril angles of the S_2-layer: 0°, 15° and 30°.

As a consequence of having an orthotropic material oriented in a spiral pattern in the walls of the fibre, there are two unique phenomena that occur. The first phenomenon is that a force in the axial direction produces a twist deformation of the fibres and, similar, a twisting load produces a deformation in the axial direction. The second phenomenon is that an in-plane bending moment loading produces an out-of-plane deformation and, conversely, an in-plane shear force loading produces an out-of-plane rotation of the fibre. This behaviour is more pronounced for fibres with larger microfibril angles. These phenomena are shown by the results of the analyses, where coupling terms are found in the matrices **K** between the normal direction and twist and between the in-plane rotation direction and the out-of-plane shear direction. To visualise these deformation modes produced by having a microfibril angle of the S_2-layer of 10 degrees, two loading cases were analysed for the undeformed earlywood fibre model. In the first loading case, an extension of the fibre was applied in the normal direction, producing a twist deformation. Since large rotations occurred, the large-deformation theories described in Chapter 4 were employed. The deformations obtained are shown in Figure 8.9. In the second loading case, an in-plane bending rotation was applied at one end of the fibre, producing an

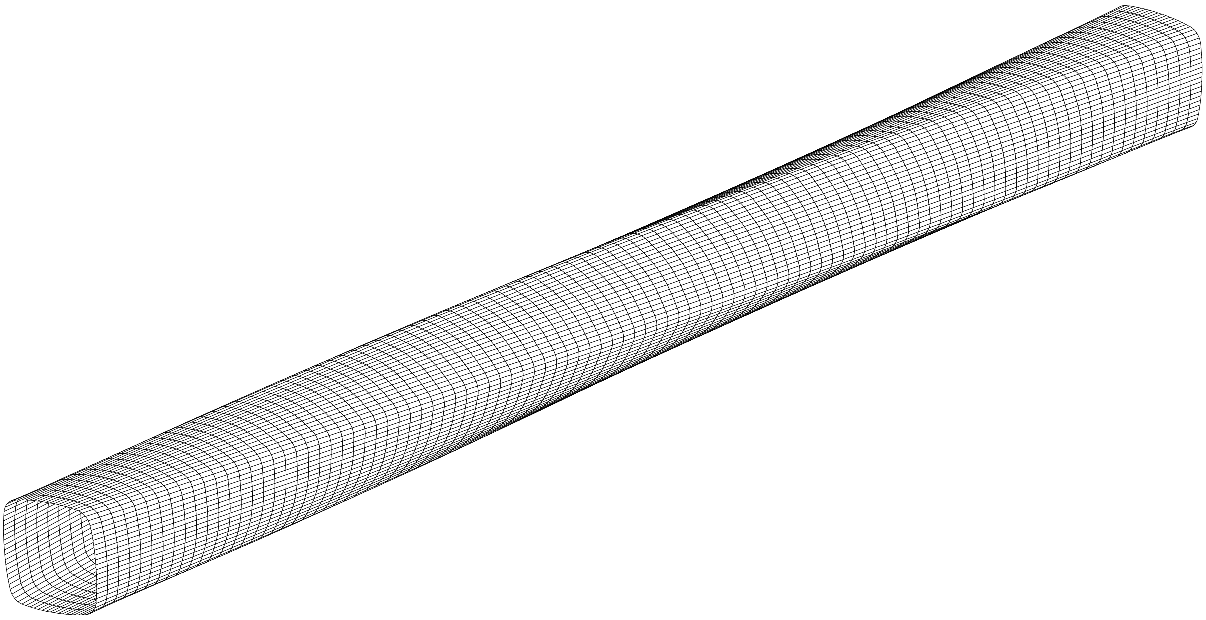

Figure 8.9: *Extension loading of a fibre producing a twist deformation.*

out-of-plane bending deformation, as shown in Figure 8.10. For both of the loading cases shown in Figures 8.9 and 8.10, one end of the fibre was kept fixed in the analysis.

The stiffness matrix **K** was determined for all four models with use of the three alternatives for the microfibril angles of the S_2-layer. For the earlywood fibre model with a collapsed cross section, with three cell-wall layers and with a microfibril angle of 15° in the S_2-layer, the matrix **K** becomes

$$\begin{bmatrix} 13020 & 0.0 & 0.0 & -3572 & 0.0 & 0.0 & -13020 & 0.0 & 0.0 & 3572 & 0.0 & 0.0 \\ 0.0 & 0.8436 & 0.0 & 0.0 & 159.2 & 210.9 & 0.0 & -0.8436 & 0.0 & 0.0 & -159.2 & 210.9 \\ 0.0 & 0.0 & 147.6 & 0.0 & -36900 & 123.4 & 0.0 & 0.0 & -147.6 & 0.0 & -36900 & -123.4 \\ -3572 & 0.0 & 0.0 & 16140 & 253.1 & 0.0 & 3572 & 0.0 & 0.0 & -16140 & 253.1 & 0.0 \\ 0.0 & 159.2 & -36900 & 0.0 & 1.252E7 & 8937 & 0.0 & -159.2 & 36900 & 0.0 & 5.929E6 & 70640 \\ 0.0 & 210.9 & 123.4 & 0.0 & 8937 & 71010 & 0.0 & -210.9 & -123.4 & 0.0 & -70640 & 34450 \\ -13020 & 0.0 & 0.0 & 3572 & 0.0 & 0.0 & 13020 & 0.0 & 0.0 & -3537 & 0.0 & 0.0 \\ 0.0 & -0.8436 & 0.0 & 0.0 & -159.2 & -210.9 & 0.0 & 0.8436 & 0.0 & 0.0 & 159.2 & -210.9 \\ 0.0 & 0.0 & -147.6 & 0.0 & 36900 & -123.4 & 0.0 & 0.0 & 147.6 & 0.0 & 36900 & -123.4 \\ 3572 & 0.0 & 0.0 & -16140 & -253.1 & 0.0 & -3572 & 0.0 & 0.0 & 16140 & 253.1 & 0.0 \\ 0.0 & -159.2 & -36900 & 0.0 & 5.929E6 & -70640 & 0.0 & 159.2 & 36900 & 253.1 & 1.252E7 & 8937 \\ 0.0 & 210.9 & -123.4 & 0.0 & 70640 & 34450 & 0.0 & -210.9 & -123.4 & 0.0 & 8937 & 71010 \end{bmatrix} 10^{-6} \quad (8.3)$$

Since the same loading response is obtained for loading each end of the fibre and since the matrix is symmetric, the number of coefficients needed for describing the equivalent beam element response of the fibre can be reduced. If loading is applied

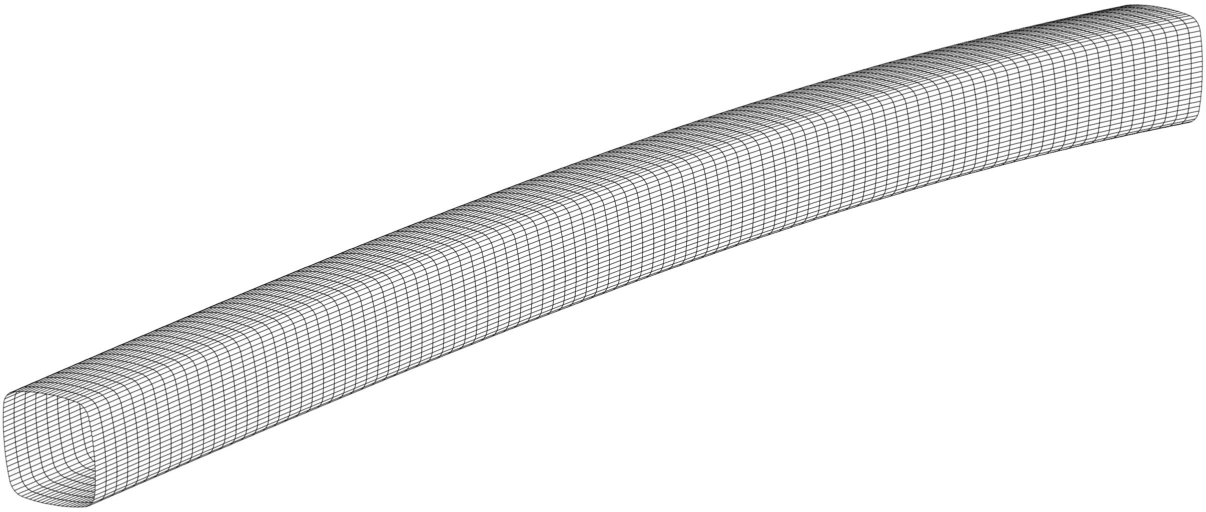

Figure 8.10: *In-plane bending loading of a fibre producing out-of-plane shear deformation.*

to one end of the fibre and the other end is fixed, the reaction forces at the loaded fibre-end are sufficient to describe the stiffness behaviour. This is equivalent to the first six rows and columns of the matrix **K**. For a beam with orthotropic material wound in a spiral pattern around it at a constant inclination, this 6x6 matrix may be written

$$\begin{bmatrix} K_{11} & 0.0 & 0.0 & K_{14} & 0.0 & 0.0 \\ 0.0 & K_{22} & 0.0 & 0.0 & K_{25} & K_{26} \\ 0.0 & 0.0 & K_{33} & 0.0 & K_{35} & K_{36} \\ K_{41} & 0.0 & 0.0 & K_{44} & 0.0 & 0.0 \\ 0.0 & K_{52} & K_{53} & 0.0 & K_{55} & K_{56} \\ 0.0 & K_{62} & K_{63} & 0.0 & K_{65} & K_{66} \end{bmatrix} \tag{8.4}$$

The matrix is symmetric and only 12 nonzero components are required for describing the stiffness behaviour of the fibre, where the remaining components of **K** can be determined by equilibrium equations. The coefficients K_{ii}, $(i = 1..6)$ are the stiffnesses for the six displacement variables and K_{ij}, $(i \neq j)$ are coupling coefficients, where K_{14} describes the coupling between axial deformation and twist. Furthermore, K_{25} and K_{36} describe the coupling between in-plane bending and out-of-plane shear deformation and the coefficient K_{56} describes coupling between the bending rotations. The coefficients K_{26} and K_{35} describe the coupling between in-plane bending and in-plane shear deformation that are found for standard beam element formulations.

Table 8.4: *Coefficients of the beam stiffness matrix* **K** *for the fibre models with an undeformed cross-section.*

Undeformed fibre models						
Stiffness coefficient	Earlywood fibre with three cell wall layers			Latewood fibre with three cell wall layers		
	mfa=0°	mfa=15°	mfa=30°	mfa=0°	mfa=15 °	mfa=30°
K_{11} x 10^6 [N/m]	15550	13140	7324	60410	50540	25120
K_{14} x 10^6 [N]	14780	-35330	-37650	17910	-1.892E5	-1.791E5
K_{22} x 10^6 [N/m]	103.8	85.14	48.61	377.5	251.8	125.5
K_{25} x 10^6 [N]	-1143	1470	535.9	-1912	7627	2195
K_{26} x 10^6 [N]	25950	21280	12150	94380	62950	31370
K_{33} x 10^6 [N/m]	103.8	85.14	48.61	377.5	251.8	125.5
K_{35} x 10^6 [N]	-25950	-21280	-12150	-94380	-62950	-31370
K_{36} x 10^6 [N]	-1143	1470	535.9	-1912	7627	2195
K_{44} x 10^6 [Nm]	4.482E5	7.055E5	1.138E6	-1.118E6	2.135E6	3.405E6
K_{55} x 10^6 [Nm]	9.067E6	7.262E6	4.073E6	3.386E7	2.158E7	1.052E7
K_{56} x 10^6 [Nm]	0.0	0.0	0.0	0.0	0.0	0.0
K_{66} x 10^6 [Nm]	9.067E6	7.262E6	4.073E6	3.386E7	2.158E7	1.052E7

The 12 stiffness coefficients obtained for the undeformed fibre models with the three alternatives for the microfibril angles in the S_2-layer, are shown in Tables 8.4 and 8.5. In Table 8.4 the results obtained for the early- and latewood fibre models with undeformed cross-sections for the three alternatives of microfibril angle in the S_2-layer are shown. Since, in this model, the cross-section is double-symmetric, the force-displacement response in bending around the y- and z-axis is identical and the number of coefficients for describing the beam behaviour can be reduced to 7. In Table 8.5 the results obtained for the collapsed earlywood fibre model both with three layers and with a single layer in the cell wall, and for the three alternatives of microfibril angle for the S_2-layer, are shown. For all of the models, the stiffness coefficients K_{11}, K_{22}, K_{33}, K_{55} and K_{66} were found to decrease with increasing microfibril angle in the S_2-layer, whereas the stiffness coefficient K_{44} increased. The coefficient K_{14} describing the coupling between axial deformation and twist has a positive value for a microfibril angle in the S_2-layer of 0° but a negative value for microfibril angles larger than 15°. This is due to the middle- and S_3-layers being oriented in a reversed spiral as compared with the S_2-layer. This behaviour was found to be similar for the coefficients K_{25} and K_{36} that describe the coupling between in-plane bending and out-of-plane shear deformation, but for a microfibril angle of 0°, these were negative, whereas for larger angles they were positive. For the earlywood fibre model with a single layer and a microfibril angle of 0°, the coupling coefficients K_{14}, K_{25} and K_{36} were zero, as was expected.

Table 8.5: *Coefficients of the beam stiffness matrix* **K** *for the fibre models with a collapsed cross-section.*

Collapsed fibre models						
Stiffness coefficient	Earlywood fibre with three cell wall layers			Earlywood fibre with single cell wall layer		
	mf=0°	mf=15°	mf=30°	mf=0°	mf=15°	mf=30°
K_{11} x 10^6 [N/m]	15380	13020	7308	13490	11270	5368
K_{14} x 10^6 [N]	2724	-3537	-3931	0.0	-6944	-6285
K_{22} x 10^6 [N/m]	0.9364	0.8436	0.5403	0.910	0.4903	0.2260
K_{25} x 10^6 [N]	-110.1	159.1	58.55	0.0	198.7	49.75
K_{26} x 10^6 [N]	234.1	210.9	135.1	227.5	122.6	56.51
K_{33} x 10^6 [N/m]	180.5	147.6	83.36	137.3	86.50	38.18
K_{35} x 10^6 [N]	-45130	-36900	-20840	-34320	-21620	-9545
K_{36} x 10^6 [N]	-178.9	123.4	39.94	0.0	246.8	66.18
K_{44} x 10^6 [Nm]	11820	16140	23410	4503	9420	14610
K_{55} x 10^6 [Nm]	1.570E7	1.252E7	6.957E6	1.255E7	7.270E6	3.154E6
K_{56} x 10^6 [Nm]	17190	8937	4653	0.0	-12020	-4108
K_{66} x 10^6 [Nm]	80650	71010	44760	81240	42080	18950

8.2.3. Hygroexpansion of fibres

Simulations with the aim of studying deformations of fibres subjected to moisture variations were performed. The three-dimensional fibre models with deformed and undeformed cross-sections described in Section 8.2.2 were used to study the deformations produced by subjecting the fibres to a decrease in moisture content from 30 to 0%. For both fibre models, a single S_2-layer with a thickness 0.78 μm and a microfibril angle of 10 degrees was employed. The stiffness and hygroexpansion properties of this layer were taken from the medium set of properties given in Tables 5.3 and 5.7, respectively. Since the material is oriented around the fibre in a spiral pattern, a moisture change is expected to produce a large twisting rotation of the fibre. This is accounted for in the analysis by employing the large-deformation theories described in Chapter 4.

The results of the analysis of the fibre with an undeformed cross-section are shown in Figure 8.11 and those of the fibre with a deformed cross section is shown in Figure 8.12. The results indicate twist along the length axis to be the dominant deformation, and also that the shrinkage of the cross-sections was high. A twist of about 360 degrees/mm was obtained for the fibre with the undeformed cross-section and a twist of about 300 degrees/mm for the fibre with the collapsed cross-section.

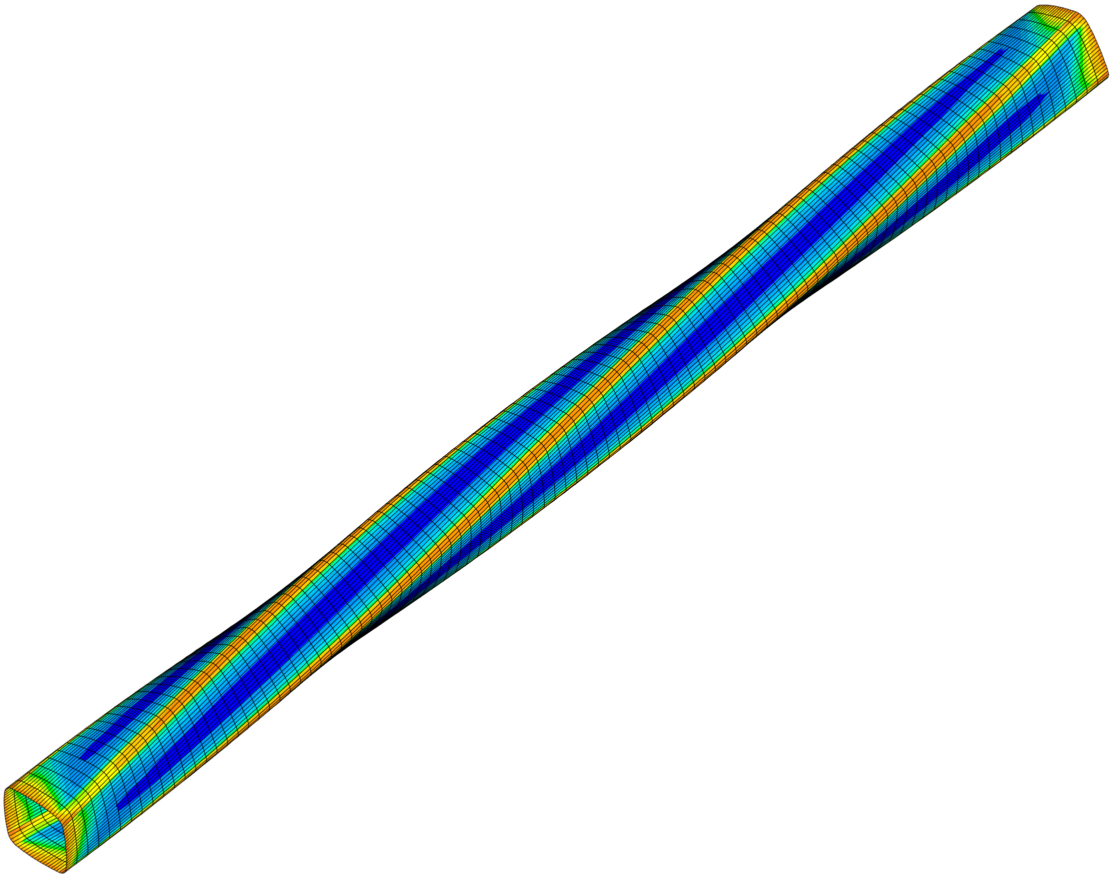

Figure 8.11: *Deformation of an initially undeformed fibre subjected to a moisture change. Lighter and darker areas indicate different stress levels.*

8.2.4. Simplified beam element modelling of individual fibres

Fibre network models can contain several thousand fibres, resulting in very large numerical models. The fibres in a paper network all have different geometries, differing for example in length, curl and cross sectional shape. As a consequence, the model of the individual fibres should be very simple. The fibre models presented in the previous section contains thousands of degrees of freedom, requiring that a separate model be available for each fibre geometry. Thus, models of this type are not suitable for use in large fibre network models. An alternative is to employ a beam theory for the fibres. Beam theories replace the three-dimensional elastic body by a one dimensional formulation. The number of degrees of freedom is thus reduced considerably. In the beam theories, however, the cross-sectional normal stresses are assumed to be zero and if loading response in the cross-sectional directions of the fibres is sought, full three-dimensional analysis needs to be performed. According to the Bernoulli-Euler theory, the stiffness matrix for a three-dimensional beam element with two nodes in a local coordinate system, as shown in Figure 8.8, is given, see

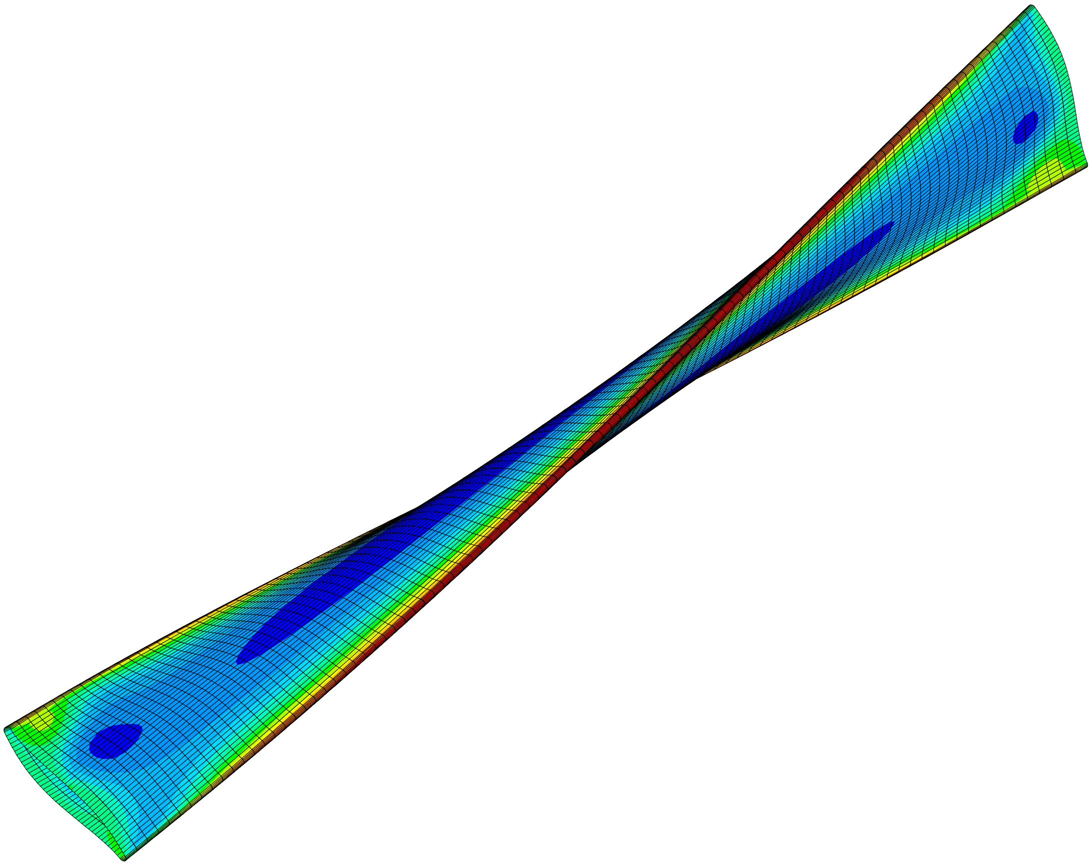

Figure 8.12: *Deformation of a collapsed fibre subjected to a moisture change. Lighter and darker areas indicate different stress levels.*

for example Ottosen et al. [50], by

$$\mathbf{K} = \begin{bmatrix}
k_1 & 0 & 0 & 0 & 0 & 0 & -k_1 & 0 & 0 & 0 & 0 & 0 \\
0 & \frac{12EI_{\bar{z}}}{L^3} & 0 & 0 & 0 & \frac{6EI_{\bar{z}}}{L^2} & 0 & -\frac{12EI_{\bar{z}}}{L^3} & 0 & 0 & 0 & \frac{6EI_{\bar{z}}}{L^2} \\
0 & 0 & \frac{12EI_{\bar{y}}}{L^3} & 0 & -\frac{6EI_{\bar{y}}}{L^2} & 0 & 0 & 0 & -\frac{12EI_{\bar{y}}}{L^3} & 0 & -\frac{6EI_{\bar{y}}}{L^2} & 0 \\
0 & 0 & 0 & k_2 & 0 & 0 & 0 & 0 & 0 & -k_2 & 0 & 0 \\
0 & 0 & -\frac{6EI_{\bar{y}}}{L^2} & 0 & \frac{4EI_{\bar{y}}}{L} & 0 & 0 & 0 & \frac{6EI_{\bar{y}}}{L^2} & 0 & \frac{2EI_{\bar{y}}}{L} & 0 \\
0 & \frac{6EI_{\bar{z}}}{L^2} & 0 & 0 & 0 & \frac{4EI_{\bar{z}}}{L} & 0 & -\frac{6EI_{\bar{z}}}{L^2} & 0 & 0 & 0 & \frac{2EI_{\bar{z}}}{L} \\
-k_1 & 0 & 0 & 0 & 0 & 0 & k_1 & 0 & 0 & 0 & 0 & 0 \\
0 & -\frac{12EI_{\bar{z}}}{L^3} & 0 & 0 & 0 & -\frac{6EI_{\bar{z}}}{L^2} & 0 & \frac{12EI_{\bar{z}}}{L^3} & 0 & 0 & 0 & -\frac{6EI_{\bar{z}}}{L^2} \\
0 & 0 & -\frac{12EI_{\bar{y}}}{L^3} & 0 & \frac{6EI_{\bar{y}}}{L^2} & 0 & 0 & 0 & \frac{12EI_{\bar{y}}}{L^3} & 0 & \frac{6EI_{\bar{y}}}{L^2} & 0 \\
0 & 0 & 0 & -k_2 & 0 & 0 & 0 & 0 & 0 & k_2 & 0 & 0 \\
0 & 0 & -\frac{6EI_{\bar{y}}}{L^2} & 0 & \frac{2EI_{\bar{y}}}{L} & 0 & 0 & 0 & \frac{6EI_{\bar{y}}}{L^2} & 0 & \frac{4EI_{\bar{y}}}{L} & 0 \\
0 & \frac{6EI_{\bar{z}}}{L^2} & 0 & 0 & 0 & \frac{2EI_{\bar{z}}}{L} & 0 & -\frac{6EI_{\bar{z}}}{L^2} & 0 & 0 & 0 & \frac{4EI_{\bar{z}}}{L}
\end{bmatrix} \tag{8.5}$$

In Eq.(8.5) it is evident that a simple Bernoulli-Euler beam theory cannot describe neither the coupling between extension and twist nor the coupling between in-plane bending and out-of-plane shear deformation that were obtained using the finite element models presented in the previous section. The Bernoulli-Euler beam theory is restricted to beams of isotropic or orthotropic materials with one principal direction along the main beam axis.

A beam theory for anisotropic thin-walled beams with closed cross-section have been developed by Berdichevsky et al. [7], a theory which captures the extension twist coupling only. Kim et al. [34] have developed a beam theory for thick composite beams with closed cross-sections, one that captures both the coupling between extension and twist and the coupling between in-plane bending and out-of-plane shear deformation. If the beam to be analysed has fairly thin walls and the coupling between in-plane bending and out-of-plane deformation is of little importance, the theory for thin beams is simpler to utilise. In the following, the theory for thick hollow composite beams according to Kim et al. [34] is outlined briefly. Assuming that each of the composite layers is wound around the fibre in a spiral at a constant angle to the length axis, the constitutive relationship for the cross section of such a beam can be written as

$$\begin{bmatrix} N \\ V_y \\ V_z \\ T \\ M_y \\ M_z \end{bmatrix} = \begin{bmatrix} A_{11} & 0 & 0 & A_{14} & 0 & 0 \\ 0 & A_{22} & 0 & 0 & A_{25} & 0 \\ 0 & 0 & A_{33} & 0 & 0 & A_{36} \\ A_{41} & 0 & 0 & A_{44} & 0 & 0 \\ 0 & A_{52} & 0 & 0 & A_{55} & 0 \\ 0 & 0 & A_{63} & 0 & 0 & A_{66} \end{bmatrix} \begin{bmatrix} \dfrac{du_x}{dx} \\ \dfrac{du_y}{dx} - \phi_y \\ \dfrac{du_z}{dx} - \phi_z \\ \dfrac{d\theta}{dx} \\ \dfrac{d\phi_z}{dx} \\ \dfrac{d\phi_y}{dx} \end{bmatrix} \tag{8.6}$$

where N is the axial force, V are the transverse forces, T is the torsional moment and M are the bending moments. The stiffness coefficients of the cross section A_{ij} $(i, j = 1, 6)$ are written in terms of integrals of the material property of the fibre wall and the cross sectional geometry, see [34]. In global coordinates, the stress-strain relation for the layers in the fibre wall can be written as

$$\begin{bmatrix} \sigma_{ll} \\ \sigma_{tt} \\ \sigma_{nn} \\ \tau_{lt} \\ \tau_{ln} \\ \tau_{tn} \end{bmatrix} = \begin{bmatrix} \hat{D}_{11} & \hat{D}_{12} & \hat{D}_{13} & \hat{D}_{14} & 0 & 0 \\ \hat{D}_{21} & \hat{D}_{22} & \hat{D}_{23} & \hat{D}_{24} & 0 & 0 \\ \hat{D}_{31} & \hat{D}_{32} & \hat{D}_{33} & \hat{D}_{34} & 0 & 0 \\ \hat{D}_{41} & \hat{D}_{42} & \hat{D}_{43} & \hat{D}_{44} & 0 & 0 \\ 0 & 0 & 0 & 0 & \hat{D}_{55} & \hat{D}_{56} \\ 0 & 0 & 0 & 0 & \hat{D}_{65} & \hat{D}_{66} \end{bmatrix} \begin{bmatrix} \epsilon_{ll} \\ \epsilon_{tt} \\ \epsilon_{nn} \\ \gamma_{lt} \\ \gamma_{ln} \\ \gamma_{tn} \end{bmatrix} \tag{8.7}$$

where $\hat{D}_{ij}$ $(i{,}j{=}1..6)$ are components of an orthotropic material stiffness matrix subjected to a rotational transformation around the 3-axis, using the transformation rule given in Eq.(2.14). The indices l, t and n denote the longitudinal, tangential and normal directions, respectively, in the beam wall. In this beam theory it is assumed that $\sigma_{tt} = \sigma_{nn} = \tau_{tn} = 0$, a reduced stress-strain relation being found by inversion of the matrix $\hat{D}_{ij}$ in Eq.(8.7) and introduction of these constraints.

The relation in Eq.(8.6) can be split up into two systems of equations, one system describing coupled extension-twist and the other describing coupled three-dimensional bending. The equilibrium equations for a straight beam segment are given by

$$\begin{aligned} \frac{dN}{dx} + q_x = 0 \\ \frac{dV_y}{dx} + q_y = 0 \\ \frac{dV_z}{dx} + q_z = 0 \\ \frac{dT}{dx} + q_w = 0 \\ \frac{dM_y}{dx} + V_z = 0 \\ \frac{dM_z}{dx} + V_y = 0 \end{aligned} \tag{8.8}$$

where q_x, q_y, q_z, and q_w are distributed loads along the beam. The two coupled systems of equations in Eq.(8.6) are solved by use of the equilibrium equations in Eq.(8.8). Omitting the distributed loads and adopting a two node beam element with 12 degrees of freedom as shown in Figure 8.8 allows a beam element equation to be written. The beam theory was implemented as a two noded three-dimensional finite element in the Matlab toolbox CALFEM [10].

Analyses using this beam theory were carried out for the two simplified fibre models shown in Figure 8.13, one model with a square cross-section and the other with a rectangular cross-section. For the two simplified fibre geometries shown in Figure 8.13, a comparison was also made with three-dimensional FE-models. The FE-model were modelled in the same manner as described in Section 8.2.2 but with the simplified square and rectangular cross-sections that is shown in Figure 8.13.

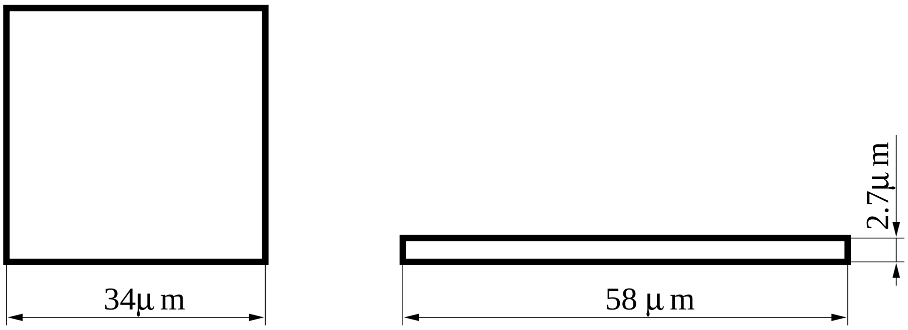

Figure 8.13: *Simplified geometries of fibres with square and with rectangular cross-sections.*

Table 8.6: *Coefficients of the beam stiffness matrix* **K** *for the fibre model with a square cross-section as determined by the simplified beam theory and the finite element method (FE).*

Square cross-section fibre model						
Stiffness coefficient	Simplified beam model			FE-model		
	mf=0°	mf=15°	mf=30°	mf=0°	mf=15°	mf=30°
K_{11} x 10^6 [N/m]	15410	12840	6026	15410	12860	6098
K_{14} x 10^6 [N]	0.0	-51860	-46300	0.0	-51950	-46910
K_{22} x 10^6 [N/m]	92.73	58.22	27.20	94.73	57.41	26.28
K_{25} x 10^6 [N]	0.0	2536	678.2	0.0	2472	654.2
K_{26} x 10^6 [N]	23180	14560	6800	23680	14350	6551
K_{33} x 10^6 [N/m]	92.73	58.22	27.20	94.73	57.41	26.28
K_{35} x 10^6 [N]	-23180	-14560	-6800	-23680	-14350	-6551
K_{36} x 10^6 [N]	0.0	2536	678.2	0.0	2472	654.2
K_{44} x 10^6 [Nm]	1.919E5	4.306E5	6.708E5	1.923E5	4.310E5	6.771E5
K_{55} x 10^6 [Nm]	8.764E6	5.094E6	2.300E6	8.889E6	4.980E6	2.204E6
K_{56} x 10^6 [Nm]	0.0	0.0	0.0	0.0	0.0	0.0
K_{66} x 10^6 [Nm]	8.764E6	5.094E6	2.300E6	8.889E6	4.980E6	2.204E6

The fibres were analysed for a single S_2-layer only. The models were analysed for three alternatives of microfibril angles of the S_2-layer: 0, 15 and 30 degrees. The thickness and orientations of the cell wall layers employed for the S_2-layer are shown in Table 8.2.

As was discussed earlier, only 12 nonzero components of the beam stiffness matrix **K** are required for describing the stiffness behaviour of a simplified fibre. For the fibre with a square cross-section, a comparison between the results obtained for the simplified beam model and for the FE-model is shown in Table 8.6 and for the fibre with rectangular cross-section a similar comparison is shown in Table 8.7.

The results indicate that for the fibres of square cross-section the differences between the simplified beam model and the finite element model are small for all microfibril angles chosen. For the fibres with a rectangular cross-section, certain differences in the matrices were found, especially for large microfibril angles. The simplified beam theory shows a reasonably close agreement with the finite element models and, for modelling sparse fibre network structures, the simplified approach should provide a proper behaviour of the wood fibre.

Table 8.7: *Coefficients of the beam stiffness matrix* **K** *for the fibre model with a rectangular cross-section as determined by the simplified beam theory and the finite element method (FE).*

Rectangular cross-section fibre model						
Stiffness coefficient	Simplified beam model			FE-model		
	mf=0°	mf=15°	mf=30°	mf=0°	mf=15°	mf=30°
K_{11} x 10^6 [N/m]	13750	11460	5377	13750	11490	5476
K_{14} x 10^6 [N]	0.0	-7024	-6270	0.0	-7016	-6352
K_{22} x 10^6 [N/m]	1.106	0.3864	0.158	0.9274	0.5016	0.2313
K_{25} x 10^6 [N]	0.0	28.70	6.725	0.0	209.6	52.59
K_{26} x 10^6 [N]	276.4	96.58	39.53	231.8	125.4	57.82
K_{33} x 10^6 [N/m]	139.4	134.7	69.18	143.5	91.52	40.43
K_{35} x 10^6 [N]	-34840	-33670	-17290	-35880	-22880	-10100
K_{36} x 10^6 [N]	0.0	465.8	137.0	0.0	261.8	70.27
K_{44} x 10^6 [Nm]	3944	8840	13790	4526	9451	14650
K_{55} x 10^6 [Nm]	1.290E7	1.165E7	5.831E6	1.3169E7	7.696E6	3.338E6
K_{56} x 10^6 [Nm]	0.0	-1.093E5	-32570	0.0	-13040	-4419
K_{66} x 10^6 [Nm]	93420	33880	13460	82950	43090	19400

8.3. Concluding Remarks

In this chapter an introductory study of the mechanical properties of cellulose fibres was presented. Several of the assumptions made regarding fibre morphology and the properties of the chemical constituents are not valid for the fibres in a paper sheet. However, some of the results for the fibre behaviour due to loading and moisture changes are presumably valid and can serve as a basis for discussion and as a starting point for future studies. The fibre collapse simulations show that the shapes of the collapse that can occur depend in part on the loading situation. The energy required to collapse a fibre was also found to be dependent on the loading situation, a fact that is interesting in analysing defibration processes in which a low energy consumption is of importance, see Höglund [31] and Holmberg [30]. The three-dimensional analyses of fibres performed demonstrate the basic behaviour of a cellulose fibre due to loading and during shrinkage. The deformation modes obtained were shown to be dependent on the value of the microfibril angle of the S_2-layer. The analyses made of deformations due to moisture change revealed that twist along the length axis was the dominating deformation for both undeformed fibres and fibres with a collapsed cross-section. The mechanical behaviour of fibres as determined by use of a beam theory was compared with the behaviour as determined by use of the FE-method. Close agreement was achieved and the beam theory investigated was found to be sufficient for representing the fibres in a sparse fibre network.

9. CONCLUDING REMARKS

9.1. Summary and Conclusions

In the present study both experimental and numerical work concerning the mechanical properties of wood and fibres has been presented. The experimental work involves both experiments at the microstructural level and the testing of clear-wood specimens of spruce. Models of the microfibrils in the cell wall, models of the cellular structure of wood and models of fibres were developed, with the aim of determining the stiffness and hygroexpansion properties of wood on different scales. Results of numerical studies that were performed using the models that were developed are also presented.

The trees used in the experimental investigation were sampled from four sites of differing soil conditions. At each site, trees belonging to each of the social classes, dominant, co-dominant and dominated, were selected. The specimens used in the testing were sampled along the diameter from north to south at three heights in each tree. The experiments performed at the microstructural level provide valuable information on the cellular structure of wood, information that is needed when wood is to be modelled from the microstructure. The relationships between the earlywood width and the growth ring width, as well as the number of cells in the earlywood region and the earlywood width were found to correlate well, whereas the latewood width in relation to the growth ring width showed only a weak correlation. The results suggest that the latewood width can be assumed as basically constant in the growth rings. Nevertheless, it would also be consistent with the results to choose a latewood width that varied linearly with growth ring width.

The average density of individual growth rings was measured and was found to correlate well with growth ring width when the dominant trees were excluded. The dominant trees in the present study had an average density that varied to a lesser degree in relation to the growth ring width. A theoretical relation between average density and growth ring width was derived through the growth ring width being divided into three regions: earlywood, transitionwood and latewood. With average densities in the three regions being assumed, the theoretical relationship was found to agree well with the corresponding relationship as determined by measurements. A subdivision of the growth ring into three regions when the structure of wood is to be modelled is thus suggested.

Deformations of the microstructure due to loading were characterized by use of SEM. These tests showed the earlywood and latewood regions to differ much in behaviour when subjected to compression loading in the radial direction. The deformations in the earlywood region were very large, the earlywood cells collapsing when even rather moderate deformations were applied. In the latewood region, no visible deformations occurred, even for large deformations in the earlywood. This behaviour was also found with shearing tests in the RT-plane and with biaxial tests of shear and compression. The tests showed there to be a large difference between the two regions in equivalent stiffness and that a non-linear material model may be needed for the earlywood region. In many stress analysis applications of wood where load is applied in the cross-grain direction, separate types of material models for the two regions may be called for. It was found, in addition, that the bending stiffness of the earlywood cell-walls was important for the overall average stiffness.

The longitudinal modulus of elasticity, shrinkage coefficients and density were determined by the testing of clear wood specimens. The longitudinal modulus of elasticity and the shrinkage coefficients were found to be highly variable along the radius of the trees. The longitudinal modulus of elasticity was found to be very low in the juvenile wood but to increase rapidly towards the mature wood. The density also varied along the radius, but the variation was not as great as for the longitudinal modulus of elasticity. A conclusion can be drawn that the mechanical properties of wood are dependent not only on density but also on the microfibril angle. Based on this conclusion, a relation between the stiffness in the longitudinal direction and the stiffness of the S_2-layer in the microfibril direction was established. By use of this relation, an average microfibril angle can be obtained on the basis of measurements of the longitudinal modulus of elasticity and density. Since the mechanical properties are strongly dependent on the microfibril angle, it is important to know its value. The microfibril angle is difficult to measure, but the relationship found makes it possible to obtain an approximate value that may be sufficient.

Models for determining the mechanical properties of wood and wood fibres based on consideration of the microstructure were proposed. The models involved include the chain from the mechanical properties of the chemical constituents of the cell wall to the average mechanical properties of a growth ring and of a single fibre. The parameters describing the geometry of the models are based mainly on the results of the experiments that were performed. Models of the microfibril were developed to determine the properties of the various cell wall layers. The models are based on the geometry and the properties of the chemical constituents of the microfibril. The equivalent stiffness and shrinkage properties of two different models of the microfibril were determined both by use of a numerical homogenisation method and by use of the finite element method. There were small differences between the two models in the stiffness and hygroexpansion properties that were obtained. The equivalent average properties of the cell wall were determined based on the basis of the results of analysing the microfibril models. The average properties of the fibre wall obtained agreed fairly well with the small amount of experimental data available in the literature.

Two models of the cellular structure of wood were proposed, the structure of wood in one model being composed of hexagonal cells and in the other model obtained from micrographs. The geometry of the cellular structure of a growth ring composed of hexagonal cells was modelled on the basis of the results of the microstructural measurements that were obtained. The stiffness properties the two models yielded agreed well with experimentally derived properties. The modulus of elasticity in the radial direction was an exception, being found to be slightly too high. A considerably lower radial stiffness was obtained, however, by introducing irregularity into the cell structure. The shrinkage properties determined by the two models also agreed well with experimentally determined values.

Three numerical studies were performed by use of the hexagonal cell model. First, a parametric study of the influence of some of the basic parameters in determining the cell structure on the stiffness and hygroexpansion properties was presented. Secondly, the results of a parametric study of the influence of the average density and of the microfibril angle on the stiffness and the hygroexpansion properties were considered. The results of the parametric studies showed that the parameters governing the stiffness and the hygroexpansion properties of wood are the microfibril angle of the S_2-layer, the density and the properties of the chemical constituents. Finally, a study was presented concerning how the stiffness and the hygroexpansion properties vary in a tree from pith to bark. The results of this study revealed these properties to vary considerably along the radius of a tree.

An introductory study of the nonlinear behaviour of cell structures was carried out. Analyses of deformations in cell structures caused by compression loading in the radial and tangential directions were performed. For loading in the radial direction, the influence of density on the resulting collapse of the earlywood was founf to be small. From this, it can be concluded that small high-density models are sufficient for studying the behaviour of loading in radial compression. A simple plasticity model was employed for representing the nonlinearities occurring in the cell wall layers. The influence of making different assumptions regarding the parameters that describe the plasticity model was studied. For compression loading of cell structures in the tangential direction, it was concluded that very large cell structure models are required in order to achieve simulation results that accord with the experimental results. The numerical difficulties that were encountered indicate that the numerical procedure employed here needs to be developed further. A possible solution is to employ an explicit dynamic finite element formulation.

The mechanical behaviour of chemically unaltered fibres was studied using simplified geometric shapes. The mechanical properties of fibres are important parameters in numerical simulations of the mechanical behaviour of such wood fibre networks as paper and other wood fibre products. The study presented here are intended was an introduction to the determination of the mechanical properties of fibres by means of micromechanical modelling. Straight fibres both with undeformed and with collapsed cross-sectional shapes were studied, both the composition and the properties of the chemical constituents being assumed to be the same as for native wood fibres. Collapse of the fibre cross-section was analysed by numerical simulations, its being found that the force required for collapsing a fibre is highly dependent on the fibre orientation. The results of the simulations of the stiffness behaviour of fibres revealed two unique coupled deformation modes. These were coupling between extension and twist and coupling between in-plane bending and out-of-plane shear deformation. The deformation modes obtained were shown to be dependent on the value of the microfibril angle of the S_2-layer. The analyses of deformations due to moisture change revealed that twist along the length axis was the dominating deformation both for undeformed fibres and for fibres with a collapsed cross-section. In sparse fibre networks, such as in fibre fluff materials, a simplified beam model is commonly used for representing the fibre. A comparison of the mechanical behaviour of fibres as determined by a beam theory and by the FE-method that was performed showed them to agree well. The beam theory investigated was found to be sufficient for representing the fibres in a sparse fibre network. For paper materials in which the fibres are densely packed, a different modelling approach needs to be developed. In such modelling, the properties of the cell wall layers need to be determined, allowing the procedures presented in Chapter 5 to be employed.

9.2. Future Work

The experimental and modelling work presented in this study can be developed further in many ways. From results of the parametric studies it was concluded that the average properties obtained through modelling cell structures are highly dependent on the values chosen for the properties of the chemical constituents and the microfibril angle of the S_2-layer. To improve the modelling results further, better knowledge of the properties of the chemical constituents is required. Also, a better description of the cell wall morphology is nedeed. In modelling the cell structures, several assumptions were made that can influence the quality of the properties obtained. The stiffness and hygroexpansion properties were determined at a moisture content of 12% but it is highly important to know as well the values for these properties in the moisture content interval of 0% to 30%. The present investigation dealt mainly with the linear stiffness and shrinkage properties, plastic properties being studied only briefly. There are many other important properties of wood, related to fracture, mechano-sorption, time-dependency and other types of nonlinear behaviour. Further development of the present models could include studies of such properties as well.

The properties of fibres were studied with the intention that these be used in simulations of the mechanical behaviour of wood fibre networks as found in paper and other wood fibre products. Since the study was of an introductory character, several tentative assumptions needed to be made. The investigation was limited to study the basic mechanical behaviour of chemically unaltered wood fibres of simplified geometrical shape. The composition and properties of the chemical constituents of the fibre wall were assumed to be the same as for native wood fibres. Since these assumptions are not valid for fibres used in paper products, the models need to be developed further so as to be able to represent the fibres in such products. In order to study paper during drying, the properties of fibres as a function of moisture content need to be determined. Moreover, in drying simulations, knowledge of the mechano-sorptive and the load-rate dependency of the fibres may be required. It is important to bear in mind that all numerical simulations require validation by adequate experimental tests. In the case of the fibre and cell wall properties of mechanical and chemical pulp fibres, there is a strong need of experimental data.

It would be of great interest in the long run to study the complete chain of properties from those of the microstructure to those of boards and paper products, as shown in Figure 1.1. The models of wood must also include imperfections, such as knots and fibre deviations, whereas models of paper, require adequate descriptions of the fibre network and of the connections between the fibres. The present study is hopefully a valuable step forward toward a more complete micro-macro modelling approach.

BIBLIOGRAPHY

[1] Aboudi J. (1991), *Mechanics of Composite Materials: A unified micromechanical approach.* Elsevier, Amsterdam, Netherlands.

[2] Van den Akker J.A., *Some theoretical considerations on the mechanical properties of fibrous structures.* In The Fundamentals of Papermaking, ed. F. Bolam, British Paper and Board Makers Assoc., London, pp. 205-241, 1962

[3] Astley R.J., Harrington J.J., Tang S. and Neumann J. *Modelling the influence of microfibril angle on stiffness and shrinkage in radiata pine.* In: Microfibril Angle in Wood, ed: Butterfield B.G., Proceeding of the IAWA/IUFRO Int. Workshop on the Significance of Microfibril Angle in Wood. Westport, New Zealand, Nov. 1997.

[4] Astley R.J., Stol K.A. and Harrington J.J. *Modelling the elastic properties of softwood - Part II: The cellular microstructure:* , holz roh werkst 56: (1) 43-50 Jan 1998.

[5] Atmer B. and Thörnqvist T. (1982), *Fiber properties in spruce and pine. (In Swedish)*, Rapport nr. 134, Inst. för virkeslära, SLU, Uppsala, Sweden.

[6] Bensoussan A., Lions J.L. and Papanicolaou G. (1978), *Asymptotic Analysis for Periodic Structures.* North-Holland, Amsterdam.

[7] Berdichevsky V., Armanios E. and Badir A., *Theory of anisotropic thin-walled closed cross-section beams.* Composites Engineering, vol 2, pp 411-432, 1992.

[8] Bergander A., (1999), *The transverse elastic modulus of the native wood fibre wall.* Licentiate thesis, Report 1999:6, Royal Institute of Techn., Dep. of Pulp and Paper Chem. and Techn., Stockholm, Sweden.

[9] Bodig J. and Jayne B.A. (1982), *Mechanics of Wood and Wood Composites.* Van Nostrand Reinhold, New York, NY, USA.

[10] *CALFEM - A finite element toolbox to MATLAB.* Lund University, Lund, Sweden, 1995.

[11] Carrington H. *The elastic constants of spruce.* Phil. Mag. vol 45, pp 1055-1057, 1923.

[12] Cave I.D., *Modelling moisture-related mechanical properties of wood. Part I: Properties of the wood constituents.* Wood Science and Technology. vol 12, pp 75-86, 1978.

[13] Cousins W.J., *Elastic modulus of lignin as related to moisture content.* Wood Science and Technology. vol 10, pp 9-17, 1976.

[14] Cousins W.J., *Youngs modulus of hemicellulose as related to moisture content.* Wood Science and Technology. vol 12, pp 161-167, 1978.

[15] Dahlblom O., Persson K, Petersson H. and Ormarsson S. *Investigation of variation of engineering properties of spruce.* In Wood Drying Research & Techn. for Sustainable Forestry Beyond 2000, pp 253-262. Proc. of the 6th International IUFRO Wood Drying Conference, Dept of Wood Science, University of Stellenbosch, South Africa, January 25-28, 1999.

[16] Dahlblom O., Persson K, Ormarsson S. and Petersson H. *Stiffness and shape stability analysis of sawn timber based on experimentally found variations of wood properties.* In Connection between Silviculture and Wood Quality through Modelling Approaches and Simulation Softwares, IUFRO WP S5.01-04. La Londe-Les-Maures, France, September 5-12, 1999.

[17] Dahlblom, O., Petersson, H. and Ormarsson, S.: *Characterization of shrinkage properties*, Improved Spruce Timber Utilisation, FAIR CT 96-1915, Final Report Subtask AB1.5, Report TVSM-3042, Lund University, Division of Structural Mechanics, Lund 2000.

[18] Dahlblom, O., Petersson, H. and Ormarsson, S.: *Characterization of spiral grain*, Improved Spruce Timber Utilisation, FAIR CT 96-1915, Final Report Subtask AB1.6, Report TVSM-3043, Lund University, Division of Structural Mechanics, Lund 2000.

[19] Dahlblom, O., Petersson, H. and Ormarsson, S.: *Characterization of modulus of elasticity*, Improved Spruce Timber Utilisation, FAIR CT 96-1915, Final Report Subtask AB1.7, Report TVSM-3044, Lund University, Division of Structural Mechanics, Lund 2000.

[20] Dinwoodie J.M. (1981), *TIMBER - its nature and behaviour.* Van Nostrand Reinhold, New York, NY, USA.

[21] Fengel D., *The Ultrastructure of Cellulose from Wood. Part 1: Wood as the basic material for the isolation of cellulose*, Wood Science and Technology. vol 3, pp 203-217, 1969.

[22] Fengel D. (1970), *The Physics and Chemistry of Wood Pulp Fibres.* TAPPI.

[23] Gibson L.J. and Ashby M.F. (1988), *Cellular solids. Structure and properties.* Pergamon press, U.K.

[24] Harrington J.J., Booker R. and Astley R.J. *Modelling the elastic properties of softwood - Part I: The cell-wall lamellae*, holz roh werkst 56: (1) 37-41 Jan 1998.

[25] Hartler N. and Nyrén J., *Transverse compressibility of pulp fibers II. Influence of cooking method, yield, beating and drying.* Tappi, vol. 53, no 3, pp 820-823, 1970.

[26] Hearmon R.F.S. (1948), *The elasticity of wood and plywood.* For. Prod. Res. Special Report, No 7, HMSO London.

[27] Heyden S. (2000), *Network modelling for the Evaluation of Mechanical Properties of Cellulose Fibre Fluff.* Doctoral thesis, Report TVSM-1011, Lund University, Div. of Struct. Mech., Lund, Sweden.

[28] Hibbitt, Karlsson & Sorensson Inc, ABAQUS Theory manual, Version 5.4, Pawtucket, Ri. 1994.

[29] Hill R. *The mathematical theory of plasticity.*, Oxford University Press, London, 1950.

[30] Holmberg S. (1998), *A numerical and experimental study of initial defibration of wood.* PhD thesis, Report TVSM-1010, Lund University, Div. of Struct. Mech., Lund, Sweden.

[31] Höglund, H., Bäck, R., Falk, B. and Jackson, M. *Thermopulp - a new energy efficient mechanical pulping system.* Proc. International Mechanical Pulping Conference in Canada, pp. 213-225, 1995.

[32] Kahle E. and Woodhouse J. *The influence of cell geometry on the elastic constants of softwood.* J. of Materials Sci., vol 29, pp 1250-1259, 1994.

[33] Kerr A.J. and Goring D.A.I., *The ultrastructural arrangement of the wood cell wall.* Cellul. Chem. Technol. vol 9, pp 563-573, 1975.

[34] Kim C. and White S.R., *Thick hollow composite beams under general loadings* Composite Structures, vol 34, pp 263-277, 1996.

[35] Kollman F.F.P. and Côte W.A. (1968), *Principles of Wood Science and Technology, 1. Solid Wood.* Springer-Verlag, Berlin, Germany.

[36] Koponen S., Toratti T. and Kanerva P. *Modelling longitudinal elastic and shrinkage properties of wood.* Wood Science and Technology. vol 23, pp 55-63, 1989.

[37] Koponen S., Toratti T. and Kanerva P. *Modelling elastic and shrinkage properties of wood based on cell structure.* Wood Science and Technology. vol 25, pp 25-32, 1989.

[38] Kučera B., *Experimental data results.* Norwegian Forest Research Institute, Wood Technology Section, Ås, Norway, 1996.

[39] Kyrkjeeide P.A. (1990), *A wood quality study of suppressed, intermediate and dominant trees of plantation grown Picea Abies.* Forest Products Laboratory, Madison, WI, USA.

[40] Malvern L.E. (1969), *Introduction to the Mechanics of a Continuous Medium.* Prentice-Hall, Englewood Cliffs, N.J., USA.

[41] Mark R.E. (1967), *Cell Wall Mechanics of Tracheids.* Yale Univ. Press, New Haven, USA.

[42] Mark R.E. (1972), *Mechanical behavior of the molecular components of fibers.* In Jayne, B.A. (ed.), Theory and Design of Wood and Fiber Composite Materials, Syracuse University Press, Syracuse, N.Y., pp 49-82.

[43] Matsuo M., Sawatari C., Imai Y. *Effect of orientation distribution distribution and crystallinity on the measurement by x-ray-diffraction of the crystal-lattice moduli of cellulose-I and cellulose-II.* Macromolecules, vol 23, no 13, pp 3266-3275, 1990.

[44] Mohlin,U-B. *Fibre development during mechanical pulp refining.* J. Pulp and paper science, vol. 23, no. 1, pp. 28-33, 1997.

[45] Mork E., *Die Qualität des Fichtenholz unter bezondere Rucksichtnahme auf Schleif- und Papierholz.*, Der Papierfabrikant vol. 26, pp 741-747, 1928.

[46] Nilsson M. (1995), *Measaurements of Growth Stresses.* Report TVBK-7049, Lund University, Dept. of Struct. Eng., Lund, Sweden.

[47] Nishino T., Takano K., Nakamae K., *Elastic modulus of the crystalline regions of cellulose polymorphs.* J. of Polymer Science Part B-Polymer Physics. vol 33, no 11, pp 1647-1651, 1995.

[48] Ormarsson S. (1999), *Numerical Analysis of Moisture-Related Distortions in Sawn Timber.* Doctoral thesis, Report 1531, Chalmers University of Technology, Dept of Struct. Mech., Göteborg, Sweden.

[49] O'Sullivan A.C., *Cellulose: the structure slowly unravels.* Cellulose, vol. 4, pp. 173-207, 1997.

[50] Ottosen N.S. and Petersson H. (1992), *Introduction to the finite element method.* Prentice Hall, U.K.

[51] Ottosen N.S. and Ristinmaa M. (1996), *The Mechanics of Constitutive Modelling.* Report LUTFD2/TFHF-3076, Dept. of Solid Mechanics, University of Lund, Sweden.

[52] Owen D.R.J. and Hinton E. (1980), *Finite elements in plasticity: theory and practice.* Pineridge Press Limited, Swansea, U.K.

[53] Page D.H., El-Hosseiny F., Winkler K. and Lancaster A.P.S. *Elastic modulus of single wood pulp fibres. Part V. Elastic modulus.* Tappi vol 60, no 4, pp 114-117, 1977.

[54] Panshin A.J. and deZeeuw C. (1970), *Textbook of Wood Technology, Vol1.* 3rd ed., McGraw-Hill, U.K.

[55] Paavilainen,L. *Effect of sulphate cooking parameters on the paper making potential of pulp fibres.* Paperi ja Puu, vol. 71, no. 4, pp. 356-363, 1989.

[56] Perilä O. and Seppa T., *The chemical composition of wood cells. II. Carbohydrates of spruce cells.* Suomen Kemistilethi, B33, pp 114-116, 1960.

[57] Preston R.D. (1974), *The Physical Biology of Plant Cell Walls.* Chapman and Hall.

[58] Price A.T. *A mathematical discussion on the structure of wood in relation to its elastic properties.* Philos. Transact. Royal Soc., London, vol 228, pp 1-62, 1928

[59] Sahlberg U., Salmén L. and Oscarsson A., In press, *The fibrillar orientation of the* S_2*-layer of wood fibres as determined by X-ray.*

[60] Sakurada I. and Nukushina Y.,Ito T., *Experimental determination of the elastic modulus of the crystalline region of oriented polymers.* J. Polym. Sci, vol 57, pp 651-660, 1962.

[61] Salmén L. (1991), *Properties of ionic polymers; natural and synthetic.* Swedish Pulp and Paper Research Inst., Stockholm, Sweden, pp. 285-294.

[62] Salmén L. (1998), *Interaction between hemicelluloses, lignin and cellulose: Structure-property relationships.* J. Pulp and Paper Sci, vol. 24, no. 3, pp. 285-294.

[63] Shallhorn P. and Karnis A., *Tear and Tensile Strength of Mechanical Pulps.* Transactions of the Technical Section - CPPA, vol 5, pp. TR92-TR99, 1979.

[64] Srinivasan P.S., *The elastic and thermal properties of timber.* Quart. J. Indian Inst. Sci., 1941, vol 4, no 2, pp. 222-314.

[65] Stefansson F. (1995), *Mechanical properties of wood at microstructural level.* Masters thesis, Report TVSM-5057, Lund University, Div. of Struct. Mech., Lund, Sweden.

[66] Säll and Dahlblom O., *Silviculture influence on spiral grain in Norway Spruce*, In Connection between Silviculture and Wood Quality through Modelling Approaches and Simulation Softwares, IUFRO WP S5.01-04., page 181-186, La Londe-Les-Maures, France, September 5-12, 1999.

[67] Tashiro K., Kobayashi M., *Molecular theoretical study of the intimate relationships between structure and mechanical properties of polymer crystals.* Polymer. vol 37, No 10, pp 1775-1786, 1996.

[68] Tashiro K., Kobayashi M., *Theoretical evaluation of three-dimensional elastic constants of native and regenerated celluloses: role of hydrogen bonds.* Polymer. vol 32, No 8, pp 1516-1526, 1991.

[69] Thuvander F. (1996), *Wood-Cell Wall Damage: A Composite Materials Approach.* Licentiate thesis, 1996:27 L, Luleå University of Technology, Div. of Polymer Engineering, Luleå, Sweden.

[70] Wigge B., *Unpublished experimental data.* Inst. f skogsproduktion, SLU, Garpenberg, Sweden, 1996.

[71] Wallström L. Lindberg K.A.H, Johansson I., *Wood surface stabilization.* Holz als Roh und Werkstoff, vol 53, pp 87-92, 1995.

[72] Zienkiewicz O.C. and Taylor R.L. (1988), *The finite element method, fourth edition. Volume 1 and 2.* McGraw-Hill, U.K.

Appendices

A. SIMPLIFIED RELATION FOR THE MICROFIBRIL ANGLE

A formula for determining the average microfibril angle from the average density and the longitudinal modulus of elasticity is derived here, based on the assumption that the longitudinal stiffness depends on the density and the microfibril angle only. The microfibril angle that is derived is an average value, here considered to be the same throughout the growth ring. The stiffness matrix for the S_2-layer in the cell wall, denoted as $\mathbf{D}^{S_2}$, is assumed to be known. The bulk density of the cell wall ρ_0 is set to 1500 kg/m^3 as mentioned earlier. The parameters that determine the microfibril angle in the procedure are the density ρ and the longitudinal modulus of elasticity E_L as measured over a few annual rings.

The transformation of the stiffness between the local directions in the microfibrils of the S_2-layer and the global directions is performed according to Eq.(2.14) by use of the transformation relation

$$\hat{\mathbf{D}}^{S_2} = \mathbf{G}^T \mathbf{D}^{S_2} \mathbf{G} \tag{A.1}$$

$\mathbf{D}^{S_2}$ is the stiffness of the S_2-layer in the principal orthotropic directions, $\hat{\mathbf{D}}^{S_2}$ is the stiffness in the global cell wall directions and $\mathbf{G}$ is the transformation matrix according to Eq.(2.13).

By only considering the stiffness in the global longitudinal direction $\hat{D}^{S_2}_{LL}$ the only transformation that is to be considered is a rotation around the local 3-axis. The direction cosines in Eq.(2.10) for this transformation are

$$\mathbf{A} = \begin{bmatrix} a^x_L & a^x_R & a^x_T \\ a^y_L & a^y_R & a^y_T \\ a^z_L & a^z_R & a^z_T \end{bmatrix} = \begin{bmatrix} cos(\varphi) & sin(\varphi) & 0 \\ -sin(\varphi) & cos(\varphi) & 0 \\ 0 & 0 & 1 \end{bmatrix} \tag{A.2}$$

where φ is the microfibril angle of the S_2-layer. The stiffness of the S_2-layer in the global longitudinal direction in terms of the stiffness of the S_2-layer for this transformation yields

$$\hat{D}^{S_2}_{LL} = [D^{S_2}_{11} - 2D^{S_2}_{12} + D^{S_2}_{22} - 4D^{S_2}_{44}]\cos^4\varphi + [2D^{S_2}_{12} - 2D^{S_2}_{22} + 4D^{S_2}_{44}]\cos^2\varphi + D^{S_2}_{22} \tag{A.3}$$

The S_2-layer makes up about 80 % of the volume of the cell wall and the stiffness of the S_2-layer in the longitudinal direction is assumed to be five times the average stiffness of the other layers. Assuming a parallel coupling of the layers in the cell wall, the equivalent stiffness in the longitudinal direction of the cell wall can be expressed as

$$D_{LL}^{cw} = 0.8\hat{D}_{LL}^{S_2} + 0.2\frac{\hat{D}_{LL}^{S_2}}{5} = 0.84\hat{D}_{LL}^{S_2} \tag{A.4}$$

where D_{LL}^{cw} is the stiffness in the longitudinal direction of the cell wall. This can be written as

$$D_{LL}^{cw} = \beta_1 \hat{D}_{LL}^{S_2} \tag{A.5}$$

where β_1=0.84 according to the assumptions made above.

The global stiffness in the longitudinal direction can be expressed, through multiplying the longitudinal cell-wall stiffness by the cell wall area ratio S of the cell structure, as

$$D_{LL} = SD_{LL}^{cw} \tag{A.6}$$

where the cell wall area ratio can be written as

$$S = \frac{\rho_a}{\rho_0} \tag{A.7}$$

ρ_0=1500 kg/m^3 being the bulk density of the cell wall and ρ_a that part of the average density of the growth ring ρ_r that is structural active, which means that part of the density that contributes to the stiffness. This may be written as

$$\rho_a = \beta_2 \rho_r \tag{A.8}$$

where the average ring density has been multiplied by the factor β_2=0.92 so as to compensate for the amount of extractives present, which is about 4 %, and the amount of ray cells of about 4 % that has negligible contribution to the stiffness in the longitudinal direction.

Although, if a specimen containing a few growth rings is subjected to a uniaxial load in the global longitudinal direction the cell wall may be subjected to a three-dimensional stress state if the deformations in the R- and T-directions of the cell wall mostly are constrained in the cell structure. For this case, the S$_2$-layer of the cell wall is assumed to be subjected to a plane strain state. The stiffness in the longitudinal direction of the S$_2$-layer of the cell wall can then be set equal to the longitudinal modulus of elasticity. By use of Eqs.(A.5) to (A.8), the relation between the longitudinal stiffness of the S$_2$-layer and the average density and stiffness in the longitudinal direction can be established

$$\hat{D}_{LL}^{S_2} = \frac{E_L}{\beta}\frac{\rho_0}{\rho_r} \tag{A.9}$$

where $\beta = \beta_1\beta_2 = 0.84 \times 0.92 \approx 0.77$. The average density ρ_r and the average longitudinal stiffness E_L are assumed to be known from measurements.

An estimate of the average microfibril angle can then be calculated by solving Eq.(A.3), together with Eq.(A.9), for $\cos\varphi$, which provides an explicit expression of the average microfibril angle

$$cos(\varphi) = \sqrt{\sqrt{\frac{B^2}{4A^2} + \frac{C}{A}} - \frac{B}{2A}} \tag{A.10}$$

where the parameters A, B and C are

$$\begin{aligned} A &= D_{11}^{S_2} - 2D_{12}^{S_2} + D_{22}^{S_2} - 4D_{44}^{S_2} \\ B &= 2D_{12}^{S_2} - 2D_{22}^{S_2} + 4D_{44}^{S_2} \\ C &= \hat{D}_{LL}^{S_2} - D_{22}^{S_2} \end{aligned} \tag{A.11}$$

The unbarred stiffness parameters are obtained from the stiffness matrix D_{S_2} of the S_2-layer, the determination of which is taken up Chapter 5. With the values given in Table 5.3 for the medium set of stiffness parameters of the chemical constituents, together with Eq.(A.9) with inserted values for β and ρ_0, the parameters A, B and C in Eq.(A.10) become

$$\begin{aligned} A &= 65.1014 \cdot 10^9 \\ B &= -0.6078 \cdot 10^9 \\ C &= 1950\frac{E_L}{\rho_r} - 9.9173 \cdot 10^9 \end{aligned} \tag{A.12}$$

Since the parameter B is small compared with the parameter A, the first and last terms on the right hand side of Eq.(A.10) can be neglected. Further, by introducing

$$c_1 = \frac{D_{12}^{S_2}}{D_{11}^{S_2}} \approx 0.045; \quad c_2 = \frac{D_{22}^{S_2}}{D_{11}^{S_2}} \approx 0.13; \quad c_3 = \frac{D_{44}^{S_2}}{D_{11}^{S_2}} \approx 0.042 \tag{A.13}$$

Eq.(A.10) can be written

$$cos(\varphi) = \left(\frac{\dfrac{\rho_o}{\beta\rho_r}\dfrac{E_L}{D_{11}^{S_2}} - c_2}{1 - 2c_1 + c_2 - 4c_3} \right)^{1/4} \approx \left(\frac{\dfrac{\rho_o}{\beta\rho_r}\dfrac{E_L}{D_{11}^{S_2}} - 0.13}{0.872} \right)^{1/4} \tag{A.14}$$

This equation provides a simple approximate relation between the longitudinal stiffness, the average density and the microfibril angle of the S_2-layer.

B. Results of parametric study of basic properties

In Figures B.1 to B.12 the results of a parametric study with the aim of determining the influence on stiffness and hygroexpansion properties of some of the basic variables involved in the description of the individual cell and in the determination of the growth ring cell structure are shown. A reference choice of the parameters was first made with e=0.6, R_{max}=0μm, ρ_1=240kg/m^3 and w_{t1}=25μm. From this reference choice each parameter was varied one at a time which resulted in a total of nine models with different geometry from which the average stiffness and hygroexpansion coefficients were determined. The models with the different choices of the geometry parameters are found in Table 6.1. In models Me$_1$ and Me$_2$ the eccentricity parameter e was varied, in models MR$_1$ and MR$_2$ the irregularity parameter R_{max} was varied, in models Md$_1$ and Md$_2$ the initial density of the earlywood region ρ_1 was varied, in models Mray$_1$ and Mray$_2$ the stiffness of the ray-cells was varied and in models Mw$_1$ and Mw$_2$ the tangential width w_{t1} was varied.

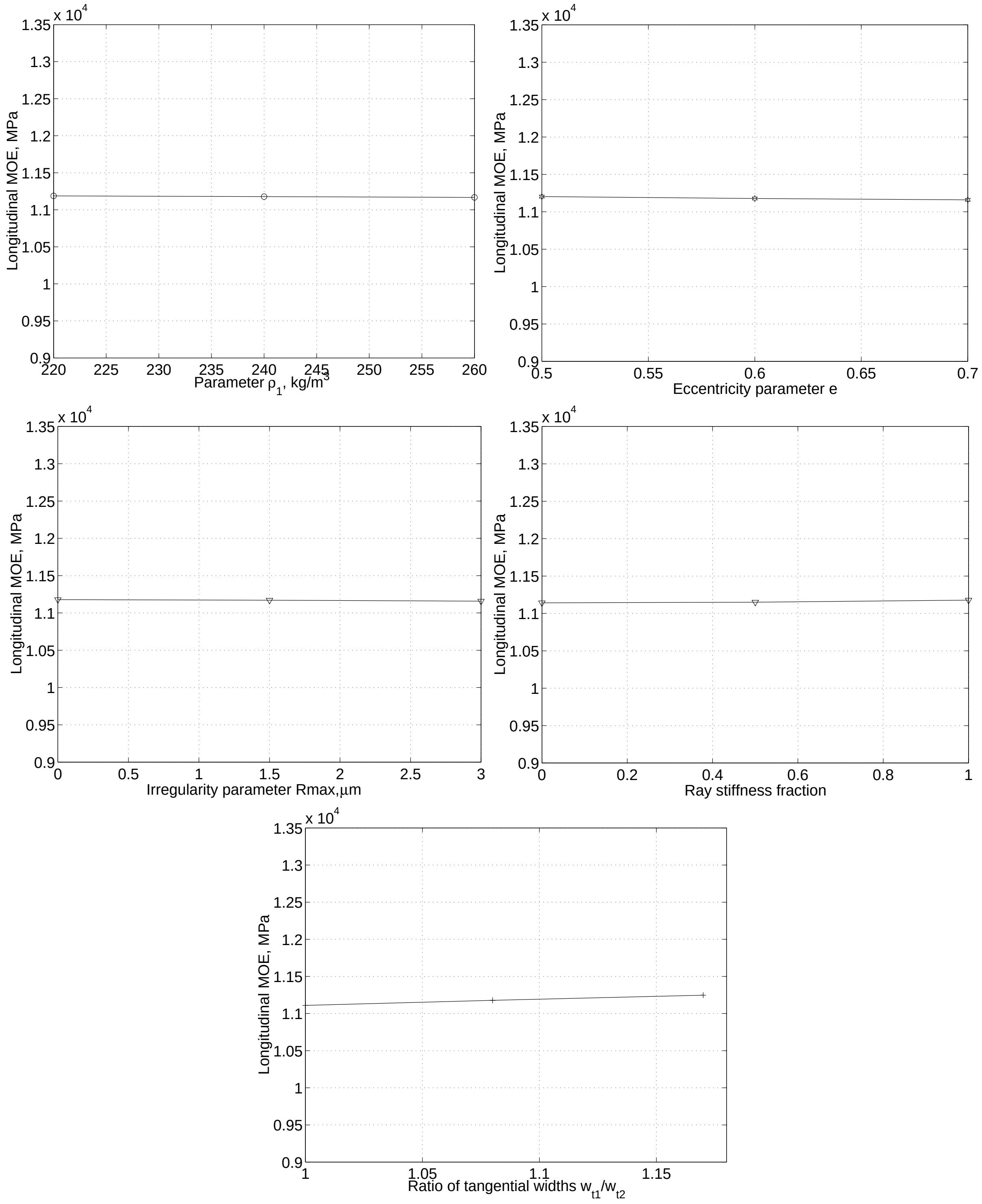

Figure B.1: *Moduli of elasticity in the longitudinal direction obtained from cell structures with varying geometry according to Table 6.1.*

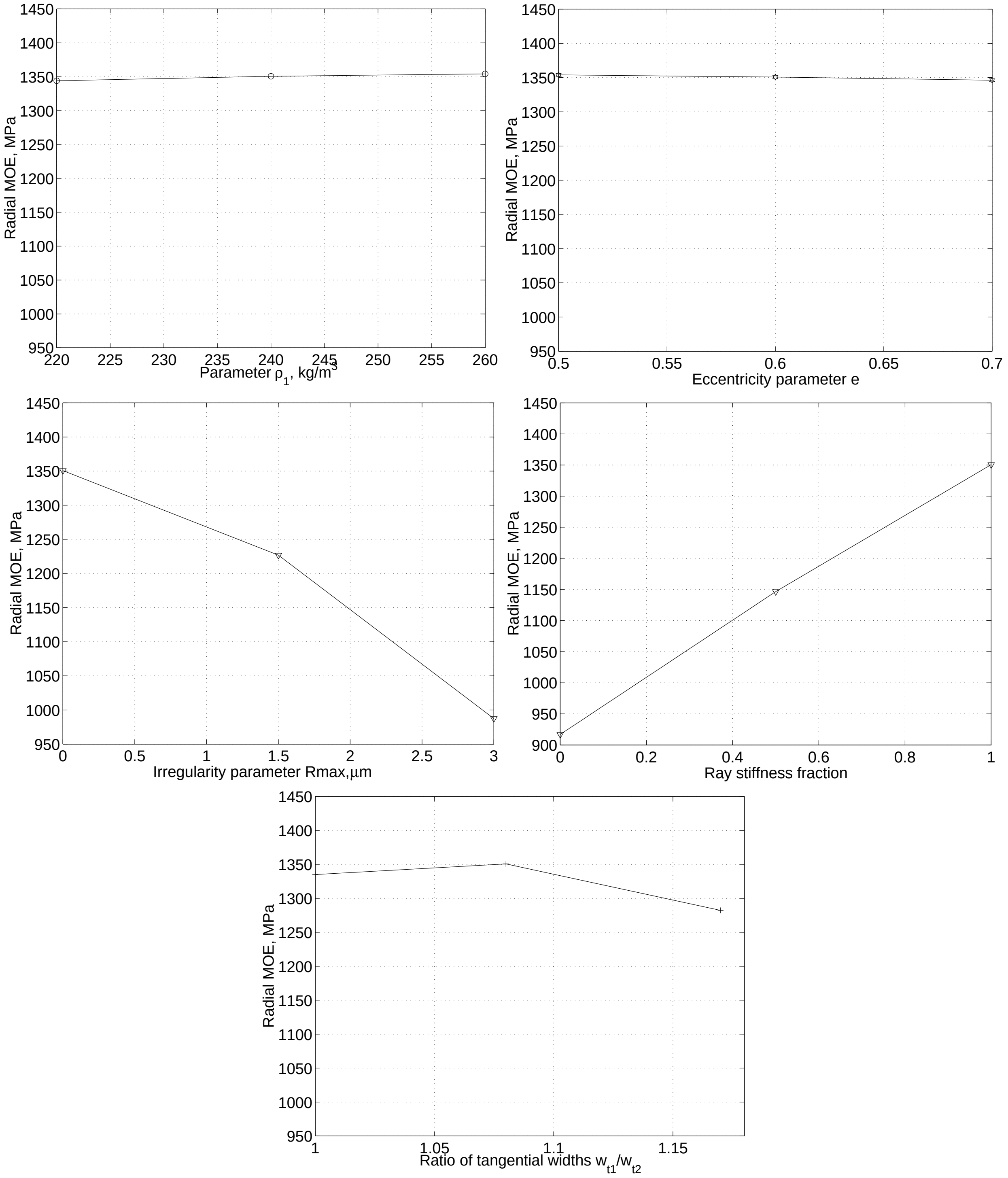

Figure B.2: *Moduli of elasticity in the radial direction obtained from cell structures with varying geometry according to Table 6.1.*

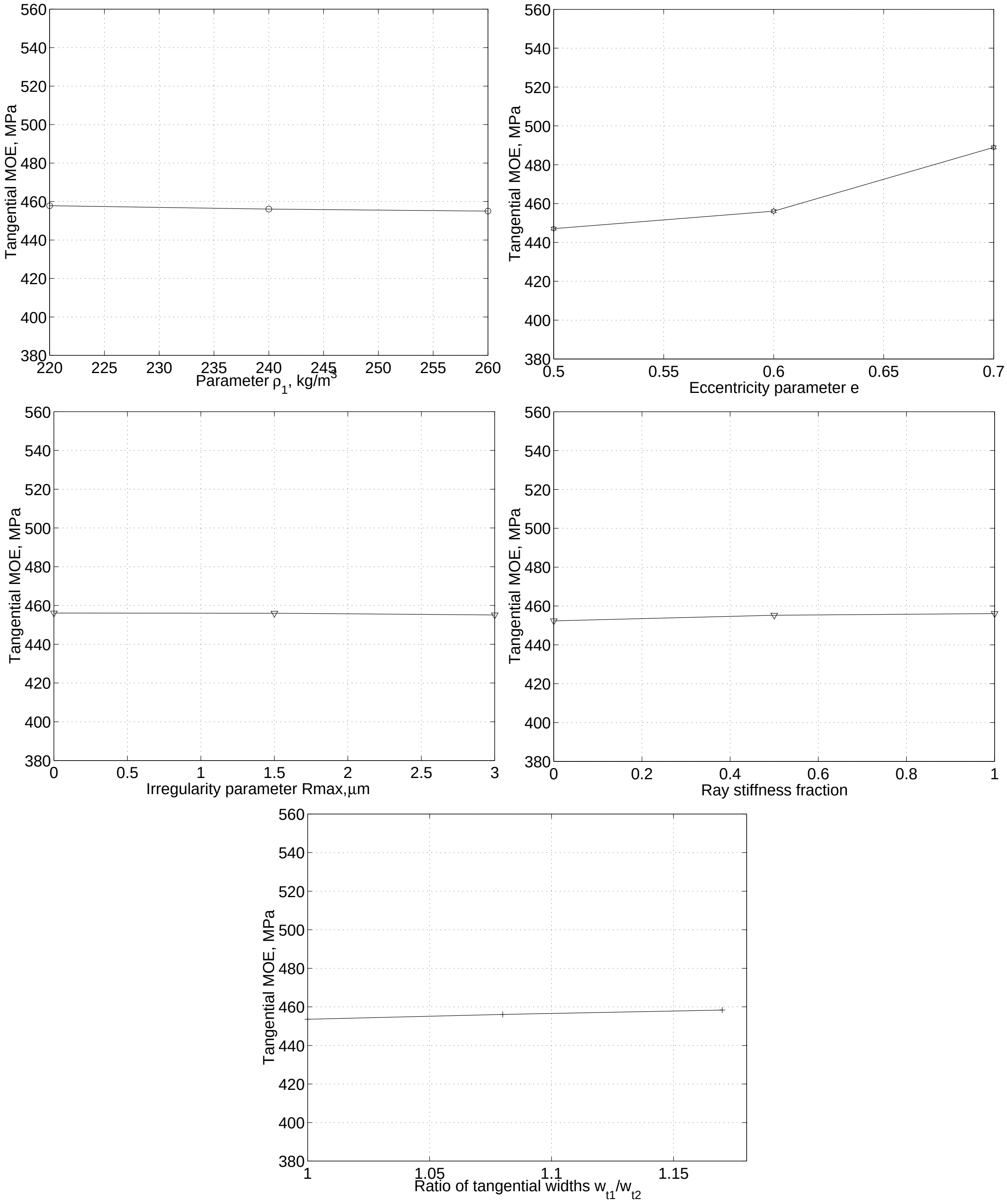

Figure B.3: *Moduli of elasticity in the tangential direction obtained from cell structures with varying geometry according to Table 6.1.*

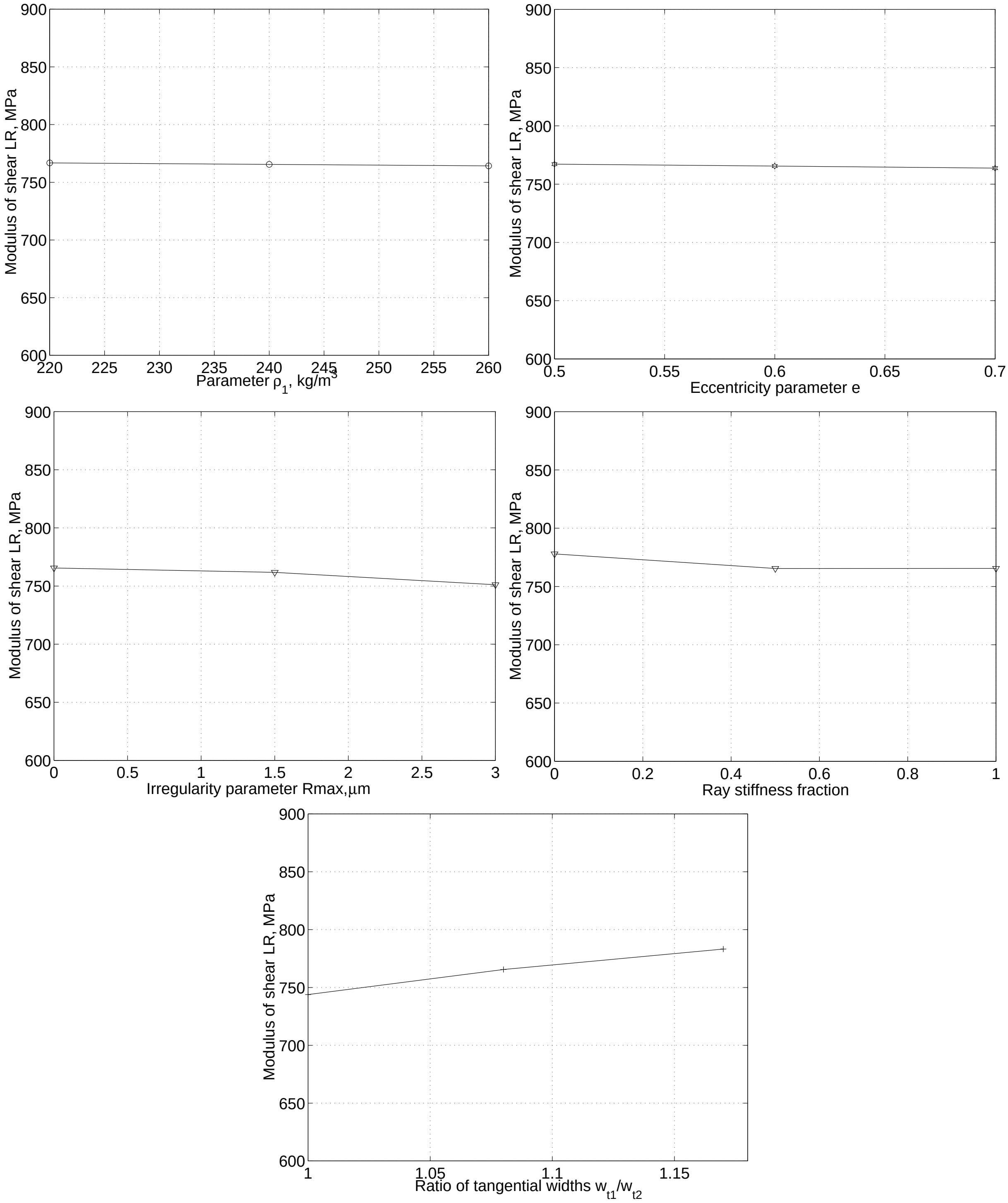

Figure B.4: *Moduli of shear in the LR-plane obtained from cell structures with varying geometry according to Table 6.1.*

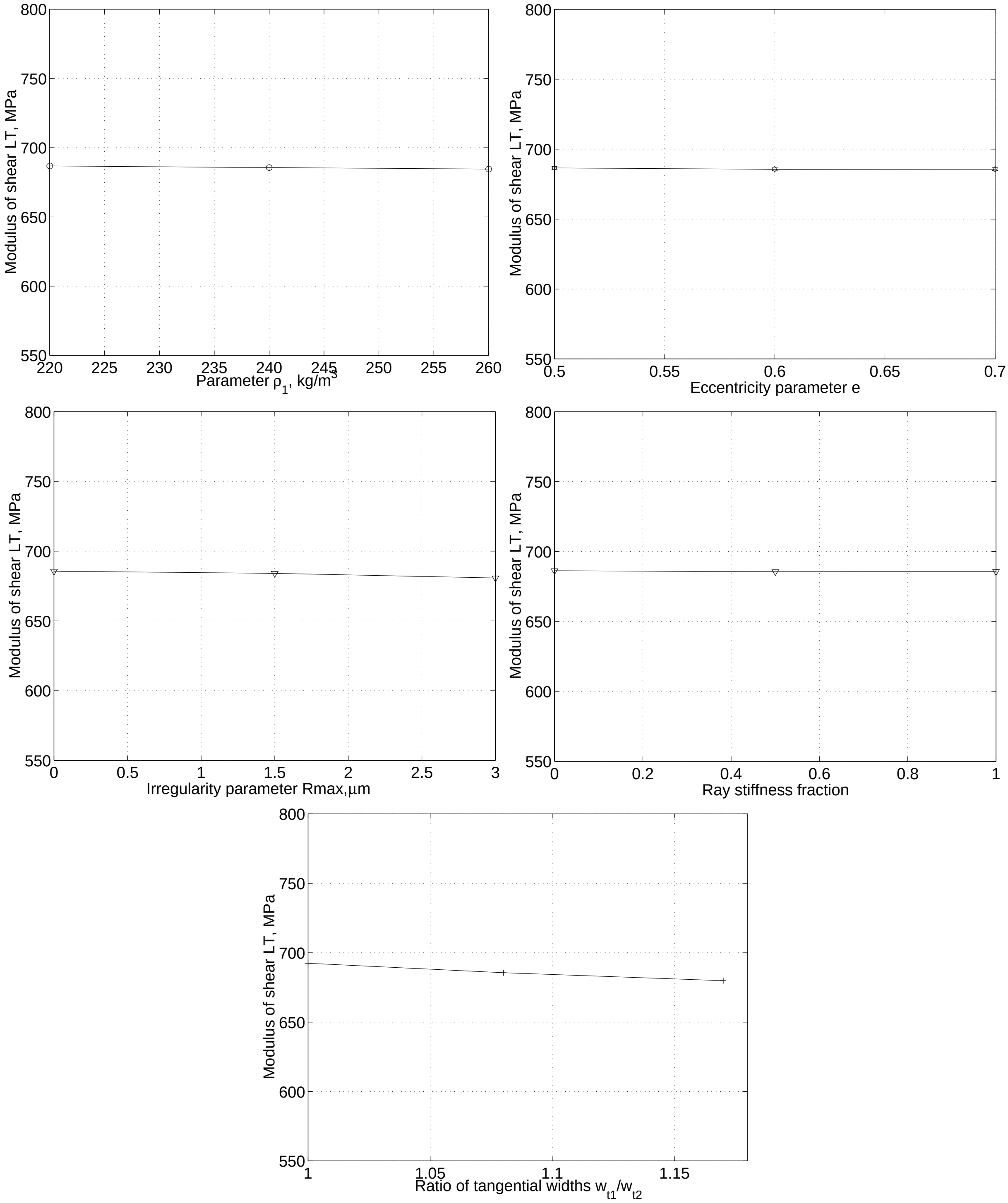

Figure B.5: *Moduli of shear in the LT-plane obtained from cell structures with varying geometry according to Table 6.1.*

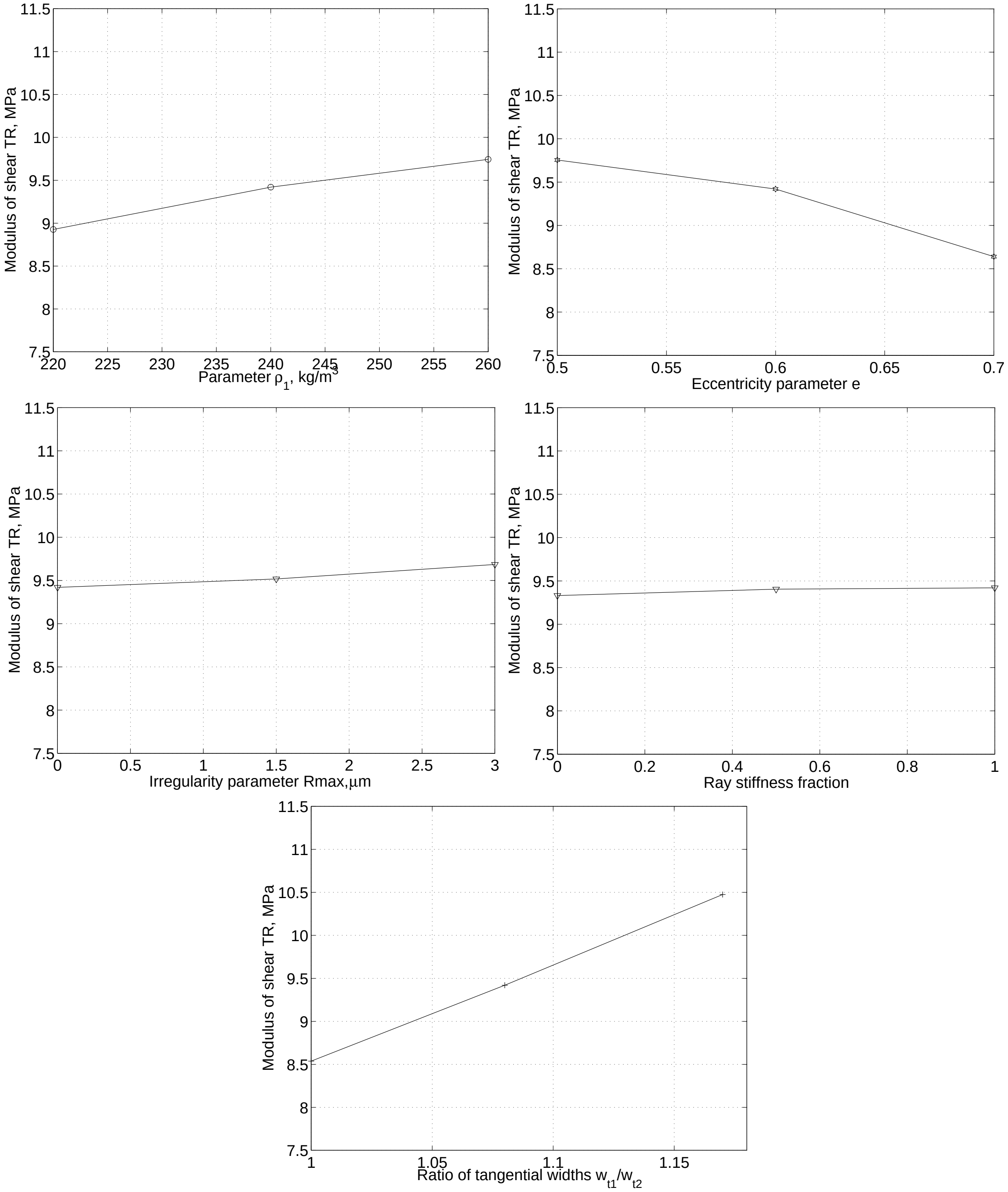

Figure B.6: *Moduli of shear in the TR-plane obtained from cell structures with varying geometry according to Table 6.1.*

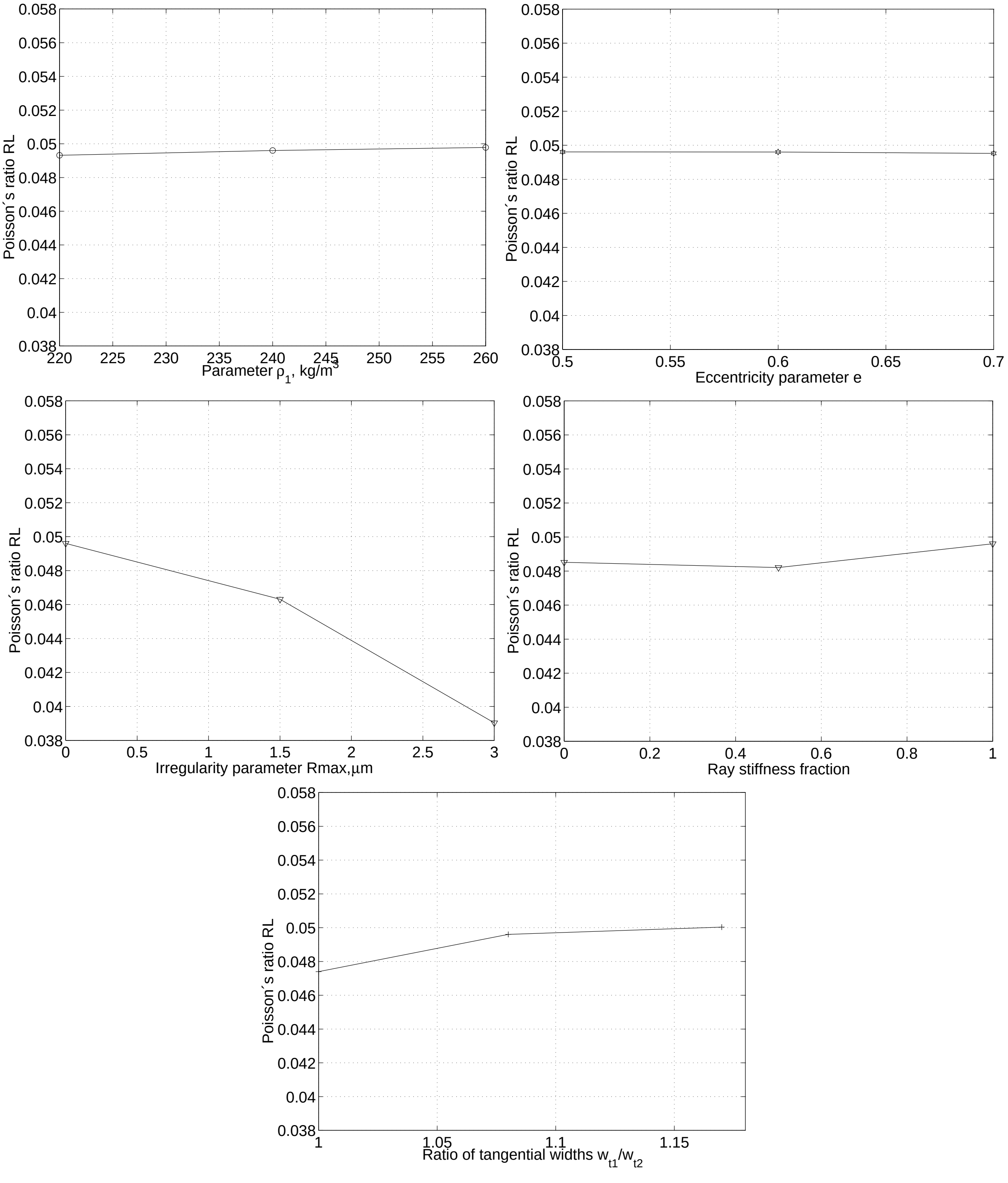

Figure B.7: *Poisson ratio ν_{RL} obtained from cell structures with varying geometry according to Table 6.1.*

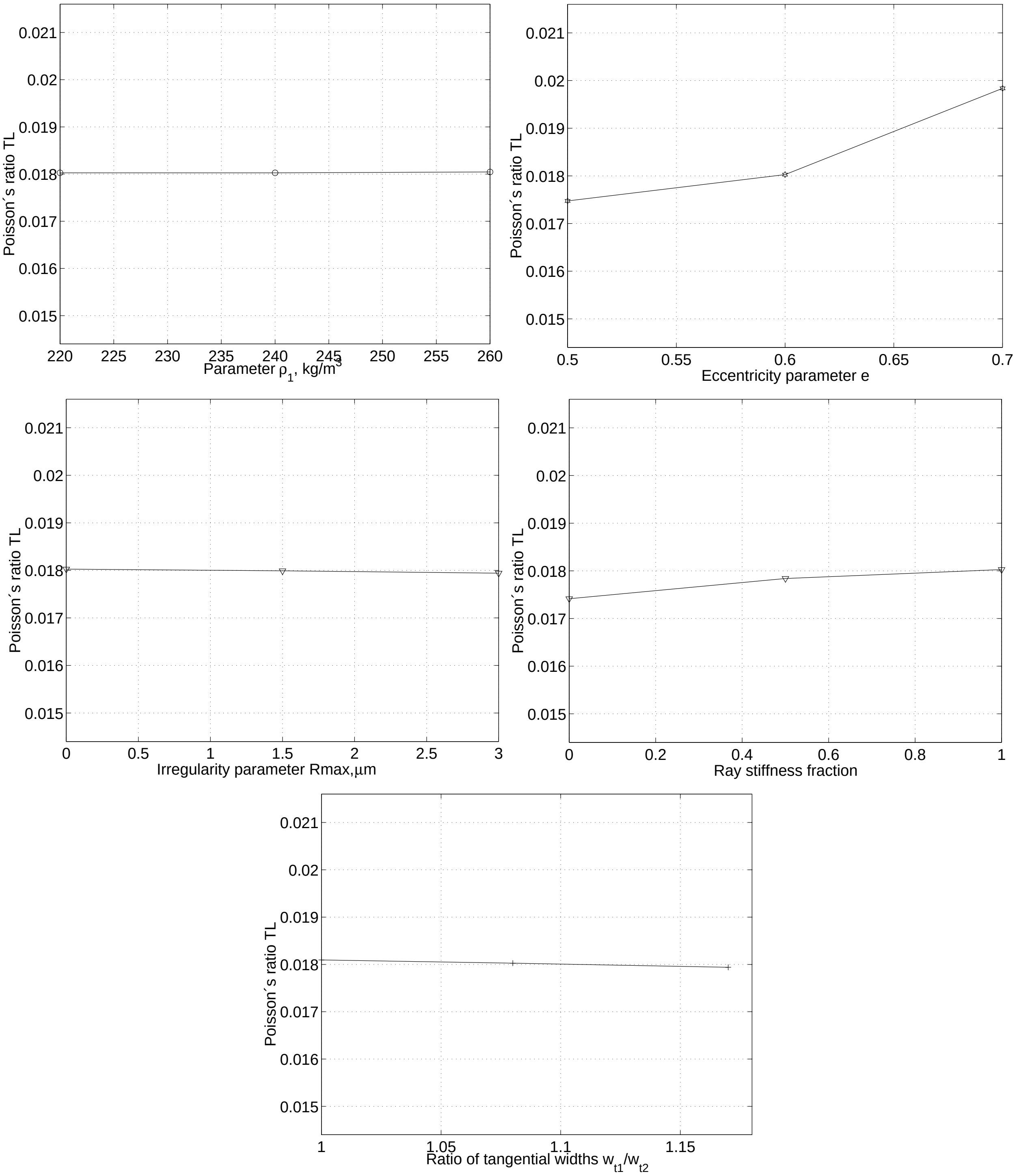

Figure B.8: *Poisson ratio* ν_{TL} *obtained from cell structures with varying geometry according to Table 6.1.*

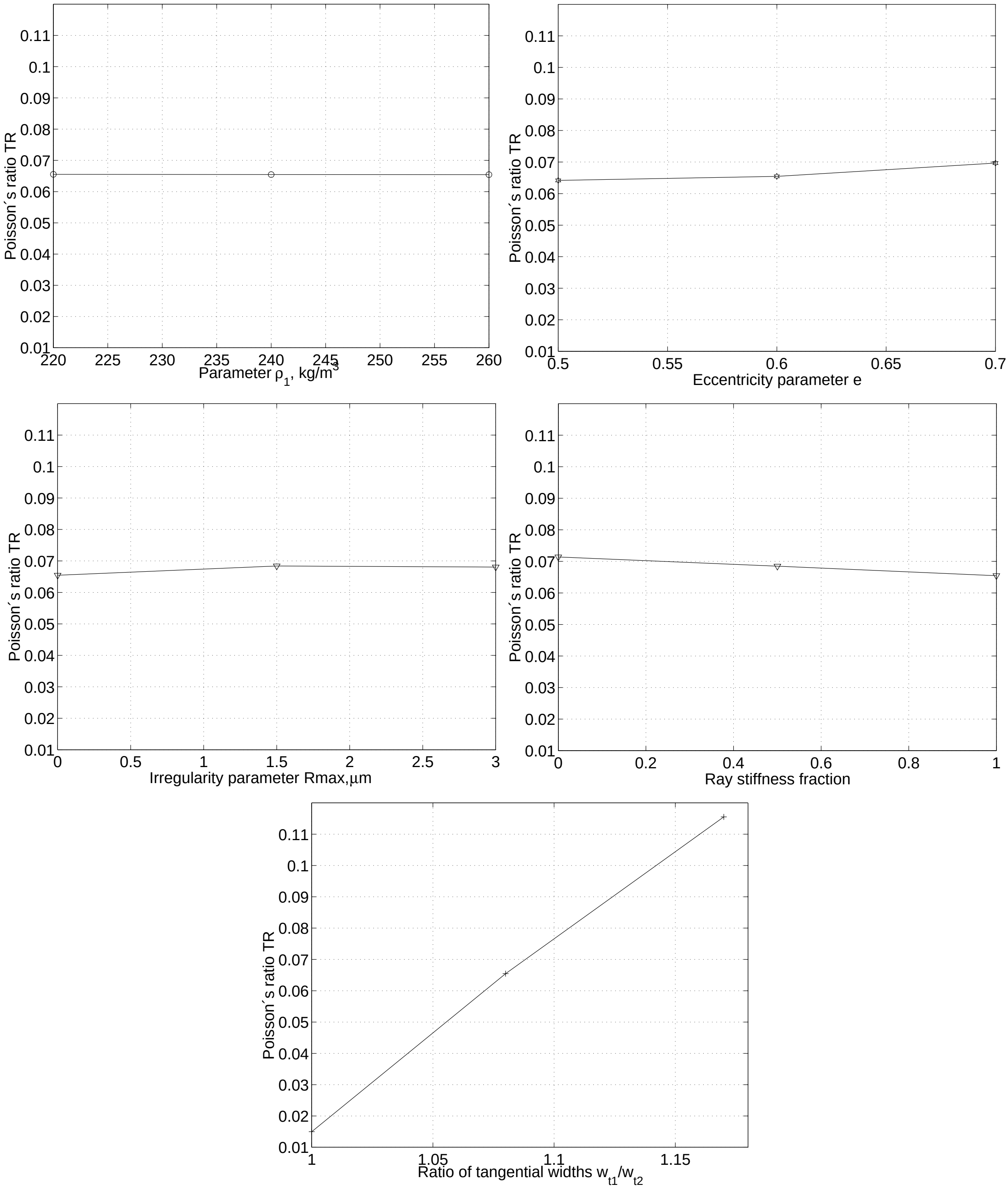

Figure B.9: *Poisson ratio* ν_{TR} *obtained from cell structures with varying geometry according to Table 6.1.*

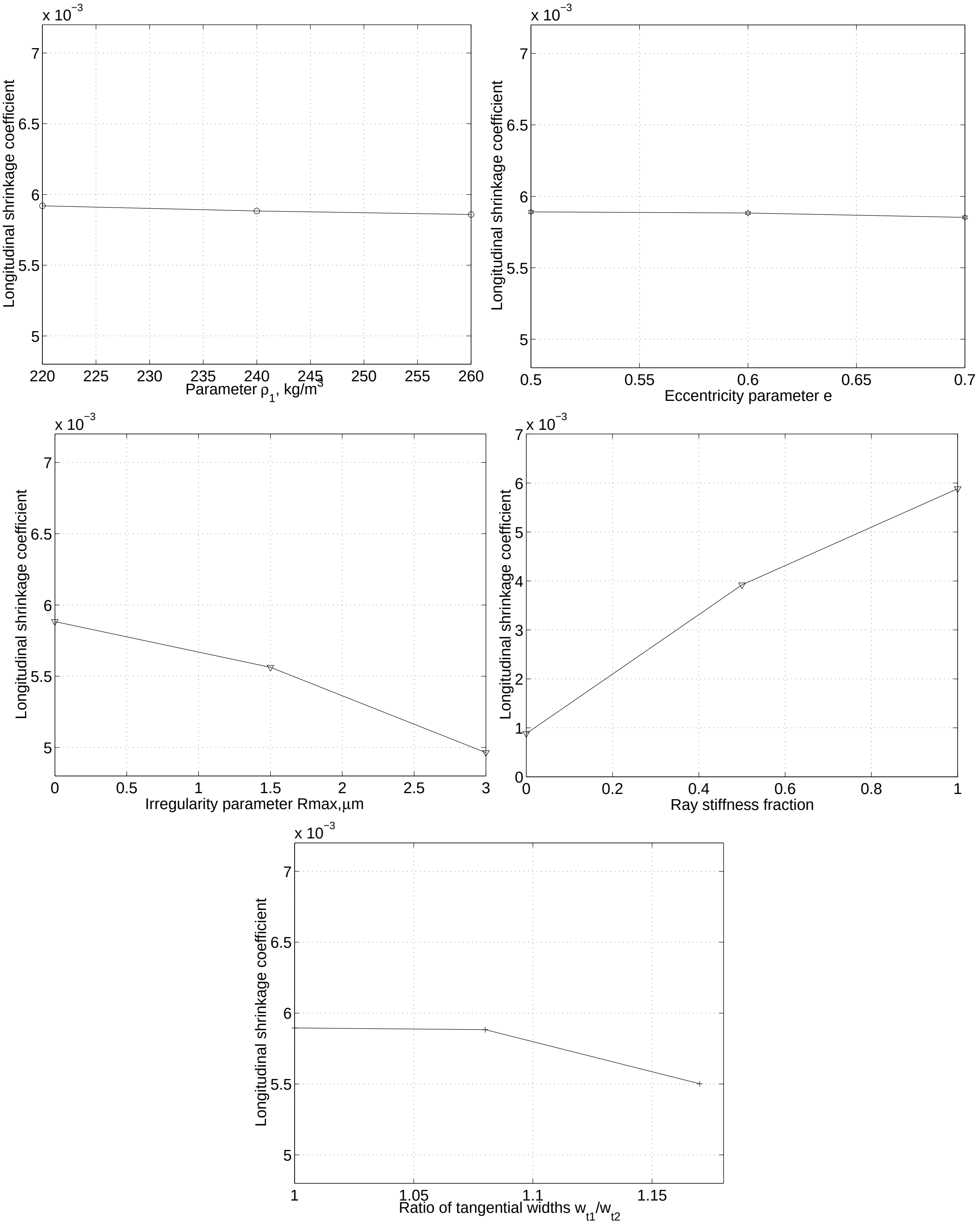

Figure B.10: *Hygroexpansion coefficient in the longitudinal direction obtained from cell structures with varying geometry according to Table 6.1.*

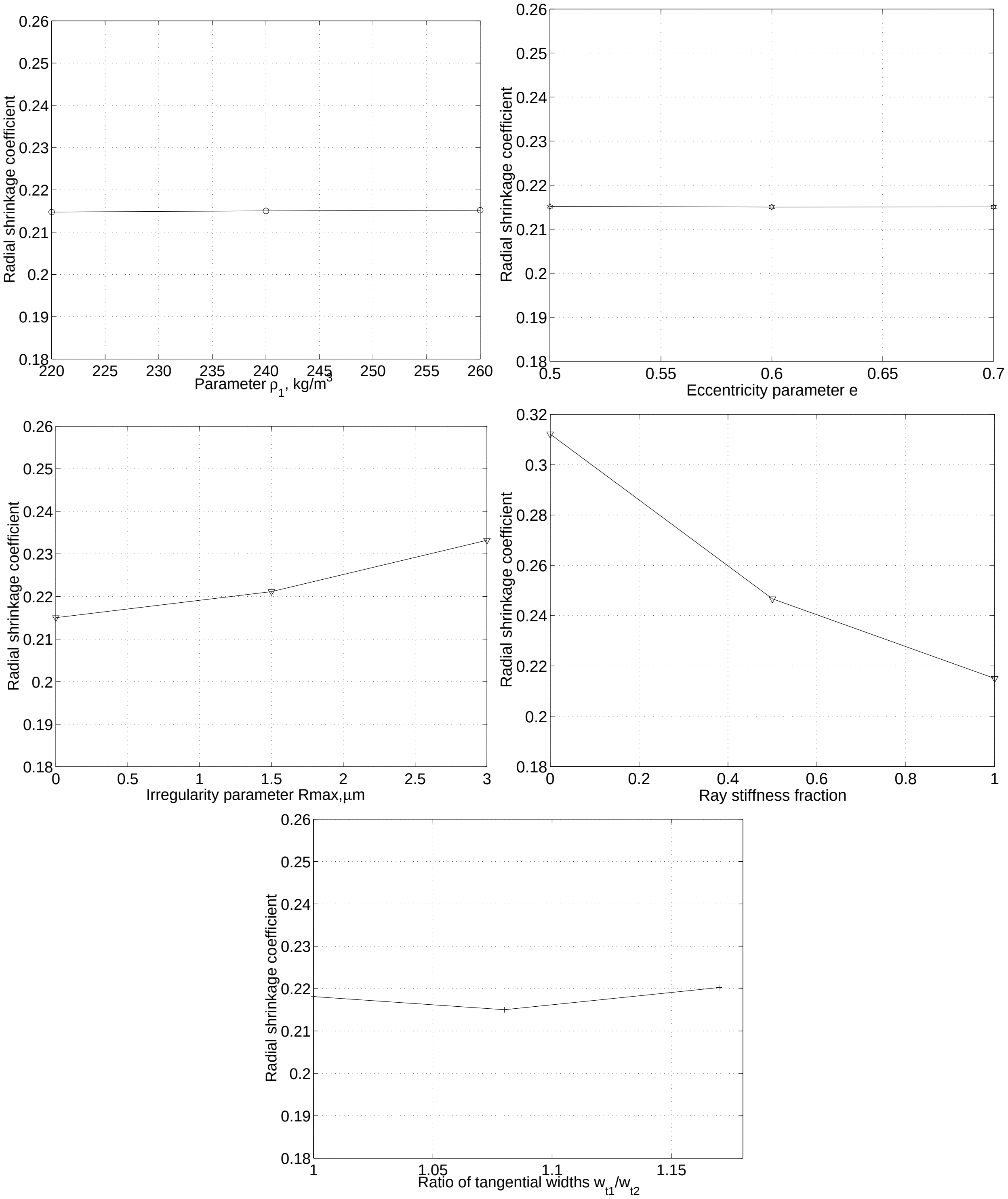

Figure B.11: *Hygroexpansion coefficient in the radial direction obtained from cell structures with varying geometry according to Table 6.1.*

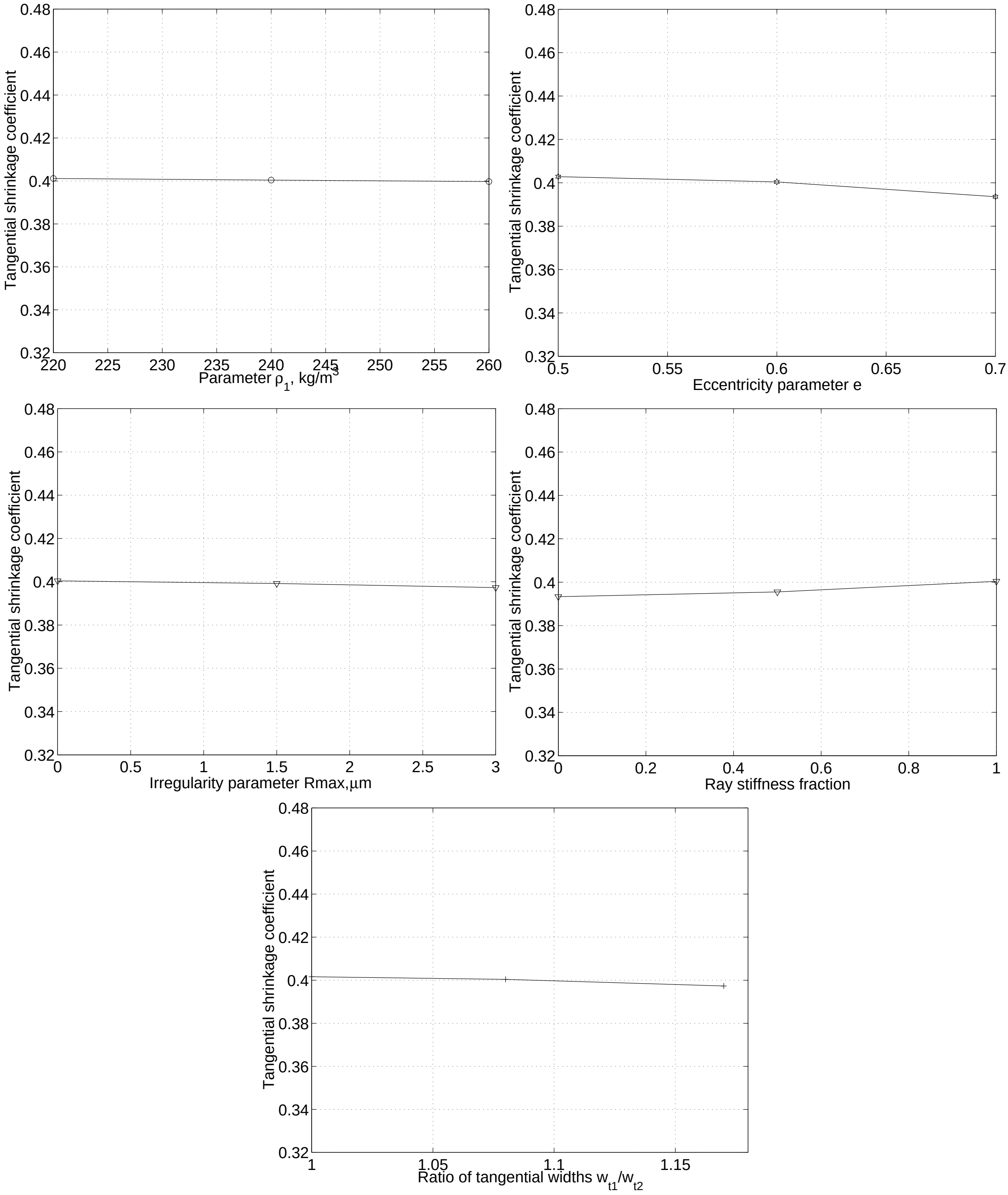

Figure B.12: *Hygroexpansion coefficient in the tangential direction obtained from cell structures with varying geometry according to Table 6.1.*